UNIVERSITA' DEGLI STUDI MILANO - BICOCCA
Scuola di dottorato in scienze

Dottorato in Fisica e Astronomia, Ciclo XXII
Coordinatore: Prof. Claudio Destri

TOWARD NEW INSIGHTS ON THE GAMMA RAY BURST PHYSICS: FROM X-RAY SPECTROSCOPY TO THE IDENTIFICATION OF CHARACTERISTIC TIME SCALES

Tutore: Prof. Guido Chincarini
Correlatore: Dott. Cristiano Guidorzi

Tesi di: Raffaella Margutti
Matricola n. 042114

Anno Accademico 2008-2009

CONTENTS

ABSTRACT

The PhD project is aimed at studying Gamma-Ray Burst (GRB) sources discovered by *Swift* from both the observational and theoretical point of view. It is basically divided into three parts: the first is dedicated to the development of a software able to automatically reduce *Swift* X-ray data; the second part contains the analysis and interpretation of three particularly interesting GRBs in the context of different theoretical models: the problems and the failure of most of them is shown. Finally, a third part is dedicated to the development of a temporal analysis alternative to the Fourier Transform: the Temporal Analysis in the Time Domain (TTD). Although optimized for GRB sources, this technique can be widely used to study the time properties of any source.

***Swift* GRB catalogue in the 0.3-10 keV energy band.** I present a homogeneous X-ray analysis of the GRBs for which the X-Ray Telescope (XRT) on board *Swift* did the follow up. The software is designed to automatically reduce and analyze the data. In particular, for each source the catalogue contains: count-rate light-curves in the 0.3-10 keV, 0.3-1 keV, 1-2 keV, 2-3 keV and 3-10 keV energy bands extracted in three different ways; hardness ratio information; time resolved spectral information; flux and luminosity calibrated light-curves in the different energy bands, where the calibration is done using the time resolved spectral information (this is the major improvement with respect to the existing *Swift*-XRT catalogue by Evans et al., 2009). Although written for GRB data, the software can be run on any source detected by XRT.

Observational constraints to the GRB theoretical models.
GRB 060904B, possible detection of Nickel emission: the detection of an extra component in the GRB 060904B X-ray spectra in addition to the standard single power law behavior is reported. This component can be fit with different models but the addition of a spectral line corresponding to Nickel emission provides the best correspondence: this would add a piece of information we still lack to the GRB-Supernova connection. I investigate the physical properties that the surrounding medium must have in order to produce a spectral feature that can explain the detected emission. I analyze and discuss how and if the detected spectral excess fits in different theoretical models developed to explain the nature of line emission during the afterglow phase of Gamma Ray Bursts (GRB) sources. Transmission and reflection models have been considered. The detected feature can be explained in a funnel scenario with typical opening angle $\theta \sim 5$ degrees, nickel mass $\sim 0.1\, M_{\odot}$ and $T = 10^6$ K. For $\theta \sim 20$ degrees, assuming the reprocessing material to be in the SuperNova (SN) shell, the detected emission implies a nickel mass $\sim 0.4\, M_{\odot}$ at $T \sim 10^7$ K and a metallicity ~ 10

times the solar value. If the giant X-ray flare that dominates the early XRT light-curve is identified as the ionizing source, the SN expansion began ~ 3000 s before the GRB event.

GRB 090111, extra soft X-ray emission and peculiar re-brightening: I present a detailed study of GRB 090111, focusing on its extra soft power-law photon index $\Gamma > 5$ at the very steep decay phase emission (power-law index $\alpha = 5.1$, steeper than 96% of GRBs detected by *Swift*) and the following peculiar X-ray re-brightening. The spectral analysis supports the hypothesis of a comoving Band spectrum with the the peak of the νF_ν spectrum evolving with time to lower values: a period of higher temporal variability in the 1-2 keV light-curve ends when the $E_{\rm peak}$ evolves outside the energy band. The X-ray re-brightening shows extreme temporal properties when compared to a homogeneous sample of 82 early flares detected by Swift. While an internal origin cannot be excluded, I show these properties to be consistent with the energy injection in refreshed shocks produced by slow shells colliding with the fastest ones from behind, well after the internal shocks that are believed to give rise to the prompt emission have ceased.

GRB 081028, an unusually late X-ray afterglow re-brightening: *Swift* captured for the first time a smoothly rising X-ray re-brightening of clear non-flaring origin after the steep decay in a long gamma-ray burst (GRB): GRB 081028. This offers the precious opportunity to study for the first time the rising phase which is likely present in all GRBs but is usually hidden by the prompt tail emission. This constitutes the first manifestation of what is later to give rise to the shallow decay phase. Contemporaneous optical observations reveal a rapid evolution of the injection frequency of a fast cooling synchrotron spectrum through the optical band, which disfavours the onset of the forward shock as the outflow decelerates as the origin of the observed re-brightening. I investigate alternative origins and show that the observations are consistent with the off-axis jet predictions. However, the high energy budget required by this interpretation suggests a different physical origin for the prompt and steep decay phases vs. the afterglow emission component. Strong spectral softening takes place from the prompt to the steep decay phase with the peak energy of the νF_ν spectrum evolving as fast as t^{-7}. I track the evolution of the spectral peak energy from the γ-rays to the X-rays and highlight the problems of the commonly assumed high latitude and adiabatic cooling interpretations. An abrupt switch-off of the central engine after the prompt emission is disfavored: the detected spectral evolution requires some forms of persistent central engine activity during the steep decay. Notably, a softening of both the high and low spectral slopes with time is also observed. I discuss the low on-axis radiative efficiency of GRB 081028 comparing its properties against a sample of *Swift* long GRBs with secure $E_{\gamma,\rm iso}$ measurements: the efficiency results are consistent with the different physical origin hypothesis of the prompt and re-brightening components.

Time in the Time Domain (TTD) analysis and short term GRB variability. The time variability in the afterglow and prompt light-curve can provide important clues to the nature of the source that powers the GRB emission and to its surrounding. The power spectrum analysis in the time domain

is developed starting from the findings of Li 2001: unlike the Fourier transform this is suitable to study the rms variations at different time scales. A complete characterization of the output of the technique is performed. Although optimized to study the GRB signal, the TTD is able to provide the the variability information of any kind of short, non-repetitive, non-stationary signals. The timing analysis of 252 15-150 keV light-curves of *Swift*-detected events, reveals the existence of three different classes of GRBs. Moreover, when the cosmological time dilation effect is considered, the distribution of the GRB characteristic variability time scales is found to cluster around 0.6-1 s. A showcase for the application of the TTD analysis to the GRB prompt emission is represented by the naked-eye GRB 080319B: this burst shows the presence of two characteristic variability time scales. Both undergo a remarkable evolution during the prompt emission and are strongly energy dependent. Different theoretical interpretations are discussed: none of them is able to account for all the observational findings.

The TTD analysis provides an unprecedented description of the temporal properties of the prompt emission: a full interpretation of its meaning and a robust connection to the physics and related models will be the next step of the research.

1. INTRODUCTION

This work is dedicated to the study of the most powerful explosions after the Big Bang: the Gamma Ray Bursts (GRB). Discovered in the late 60's and recognized to be of cosmic origin in 1973 [87], they outshine the gamma-ray sky for an interval of time between a few seconds and one thousand seconds, emitting an isotropic equivalent energy up to 10^{54} erg. A variety of physical models has been put forward to explain the nature of these explosions: the standard scenario consists of the fireball internal-external shock model, where a GRB is produced as a result of the dissipation of the kinetic energy of an ultra-relativistic flow in internal collisions. The long wavelength radiation emission, called afterglow visible up to days and weeks after the explosion instead arises when the flow is slowed down by shocks with the surrounding cirmcumburst matter (external shocks). Figure 1.3 shows an artist conception of the model. I refer the reader to [149] and references therein for a detailed overview of the model.

A series of review-papers and even some GRB books appeared in the literature: this, together with the conspicuous amount of published works give little sense to the effort of summarizing thousands of pages into a few ones. Instead I prefer to refer the reader to the most important works in whichever aspect of the GRB field when needed and to concentrate the attention of the following few sections on one of the most interesting aspects of the GRB observations: the temporal variability. To the temporal structure of the gamma ray signal are dedicated Sect. 1.1 and 1.2.

A complete summary of the GRB physics and observations can be found in [193], while the most recent observational results of the *Swift* [53] revolution are well summarized in [54]. A critical review of the standard scenario is given by [108]. The basic afterglow concepts are critically reviewed in [73].

Each chapter of the present work, while part of a unique work, is provided with its own introduction and conclusion section, so that the reader is not expected to read the whole thesis if interested in a particular aspect of the GRB field. Instead, each chapter can be thought as a stand-alone unit: in the introduction the reader will find everything is needed to understand the content of the correpsonding chapter.

The organization of this work is explained at the end of this chapter.

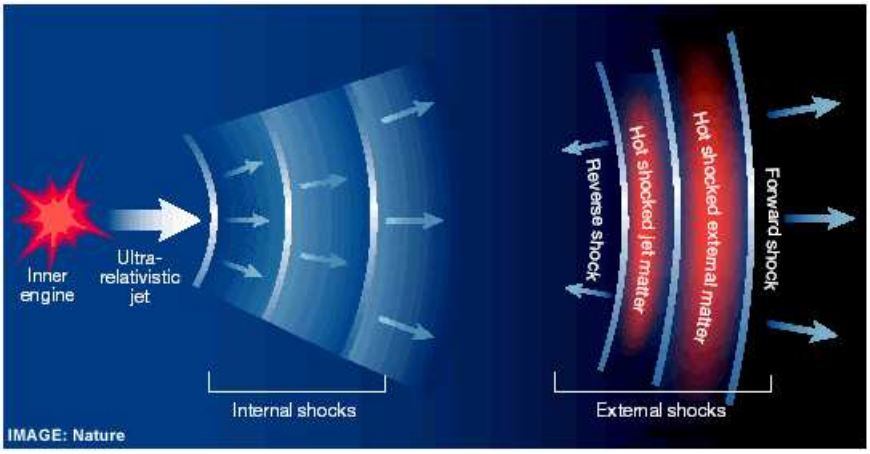

Fig. 1.1: Cartoon showing the basic features of the fireball internal external shock model.

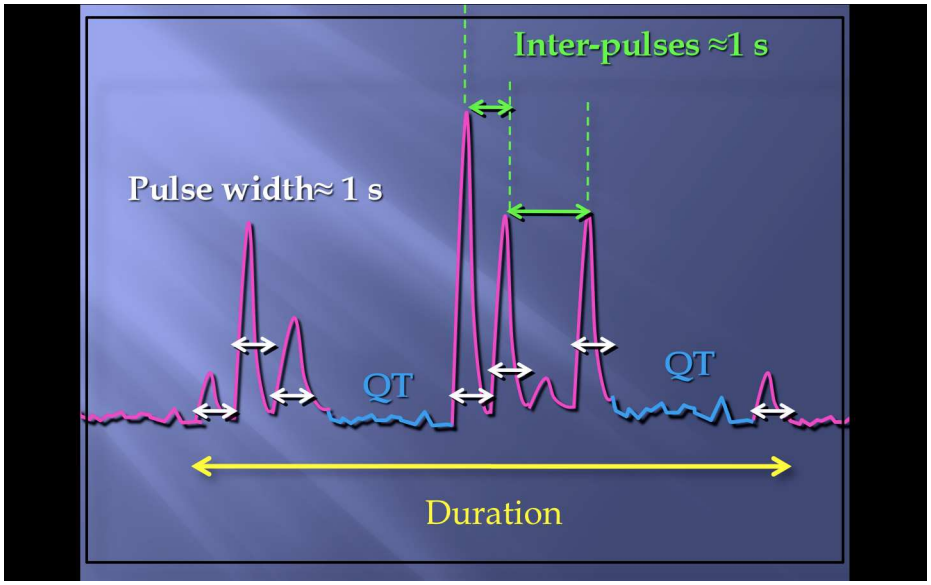

Fig. 1.2: Cartoon showing the four different observational time scales characterizing the GRB emission: the duration of the event; the width of each pulse; the interval of time between pulses and the quiescent times (QT).

1.1 Temporal structure of the GRB emission: observations

From the observational point of view, the GRB emission can be characterized using four different time scales (see Fig. 1.2):

- *The duration*: the duration of the burst usually expressed by the T_{90} parameter (which corresponds to the time interval covering from 5% to 95% of the total counts) spans more than 5 orders of magnitude: from less than 0.01 s up to $\sim$ 1000 s. This parameter defines two GRB populations: the long bursts with $T_{90} > 2$ s and the short ones, with $T_{90} < 2$ s [91].
- *The pulse width*: the bursts seem to be made up of individual pulses, with the pulse appearing to be the building block of the gamma-ray light curves. The distribution of the pulse widths is found to be a lognormal centered around 1 s observer frame: the 1 s time scale, therefore defines the typical duration of the single pulse emission. See e.g. [128].
- *The interval between pulses*: the interval between the pulses is also found to be lognormally distributed, with an excess for very long interval of times (Pareto-Levy tail). When this tail is not considered, the distribution is completely lognormal and centered around 1 s observer frame. 1 s can therefore be identified as the typical interval of time between two emission blocks (see e.g. [128]).
- *The quiescent times*: the excess of long intervals of the previous distribution is explained with the presence of quiescent times, long periods of several dozens of seconds with no observed activity. See e.g. [160].

To this group, another element has to be added, yet: the variability time scale or the time scale on which the signal is maximally variable. To the quantification of this time scale is dedicated the temporal analysis chapter of this work.

1.2 Temporal structure of the GRB emission: the standard model

Simple kinematic and geometrical considerations put important constraints on the temporal structure that is produced when the energy of a relativistic shell is converted into radiation. According to the standard internal shock scenario, 5 typical time scales should be able to describe the gamma ray emission (see e.g. [148] or [149]):

- *Radial time scale*: with reference to Fig. 1.3, the radial time is the observed interval of time from the arrival of the first to the last photon (A and D in Fig. 1.3), if most of the emission takes place between R and $2R$ and the emitting material is an infinitely thin relativistic shell with Lorentz factor γ:

$$T_{rad} = R/(2c\gamma^2) \tag{1.1}$$

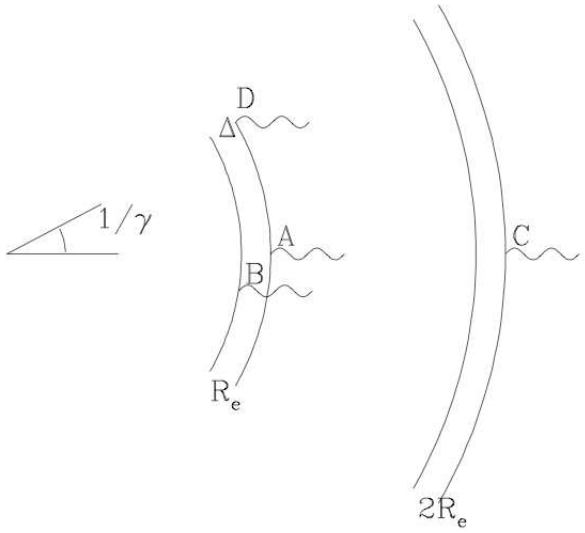

Fig. 1.3: Different time scales in terms of arrival times of photons A, B, C and D. From [148].

- *Angular time scale*: delay in the arrival of photons A and D (Fig. 1.3) emitted at the same time and at the same radius R caused by the different geometrical path. If the emitting source has an angular width larger than $1/\gamma$, this time scale represents the minimum observable variability time scale. In mathematical terms:

$$T_{ang} = R/(2c\gamma^2) \tag{1.2}$$

- *Intrinsic duration*: this time scale ΔT represents the intrinsic duration of the relativistic flow or the life time of the source that powers the flow. ΔT provides a natural lower limit to the observed duration.

- *Intrinsic variability* δt: this is the time scale on which the inner source varies and produces a variable flow. The relation with the observed variability is in this case much more complicated and depends on several factors.

- Cooling time scale: T_{cool} is the difference in the arrival time of photons while the shocked material which has a Lorentz factor γ cools measured in the observer frame. If $T^{'}_{cool}$ is the local cooling time, then T_{cool} can be expressed as:

$$T_{cool} = T^{'}_{cool}/\gamma \tag{1.3}$$

  (note the difference with respect to the cosmological time dilation effect). For synchrotron we have $T_{cool} \propto \nu^{-1/2}$.

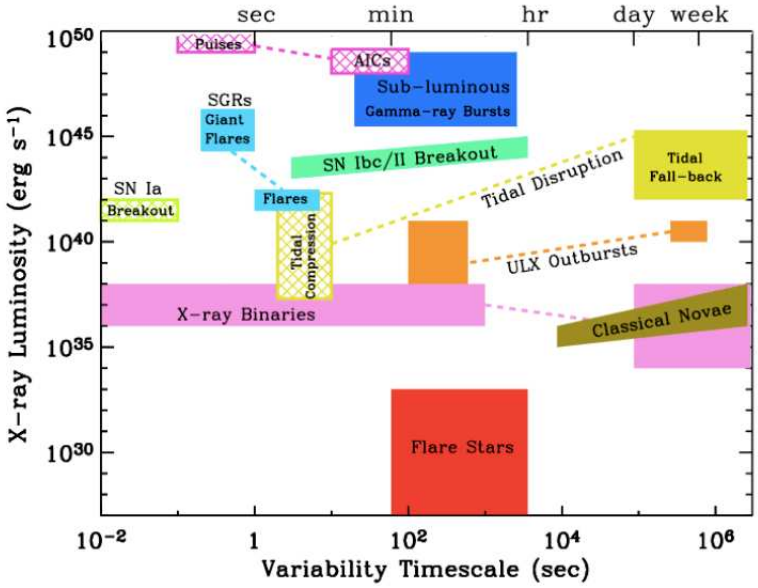

Fig. 1.4: Known (solid) or predicted (hatched) high energy transients in the local Universe ($d < 200$ Mpc). Transients with variability on multiple timescales are linked with dashed lines. From [184].

1.3 The dynamic sky

The time domain astronomy is expected to flourish in the next decade providing information on a variety of transients events that make our universe a dynamical universe (Fig. 1.4). The transients phase space has not been sampled yet, due to the lack of sensitive, wide field and triggering facilities dedicated to the search of transients in the sky, enabling rapid coordinated multi-wavelength follow-ups.

However, things are changing and dedicated transients "machines" are being (or have been) projected at different wavelengths: over the past two decades the population of local X-ray transients has been mapped by CGRO, Einstein, ROSAT, BeppoSAX and HETE-2. Currently, RXTE, Integral, Chandra, XMM, AGILE and Swift are providing the best available information on the variable X-ray sky. However, due to the limitations of the present instrumentation we are insensitive to the class of X-ray events with low volumetric rates, short lived or subluminous emission (like supernova shock breakout outbursts; tidal compression flares or accretion induced collapse outbursts). New facilities like EXIST[1] (Energetic X-ray Imaging Survey Telescope) are expected to populate that part

[1] EXIST would image and temporally resolve the entire sky every two 95-minutes orbits, detecting extremely faint high energy sources in the range 5-600 keV. See `http://exist.gsfc.nasa.gov/`.

of the phase plane in the X-ray regime, potentially discovering unknown classes of transients for which we lack both predictions and detections. This happens simultaneously to an on-going ground based technological effort in the radio (E-VLA, SKA pathfinders) and optical/IR regime to lift the veil on the dynamic Universe. In the optical band the PTF[2] (Palomar Transients Factory) is a key project which achieved first light in December 2008 with the unique goal to perform a systematic investigation of variables and transients in the optical sky. Among the operational facilities I list PanSTARRS[3]; imminent facilities are SkyMapper[4], VST[5], ODI[6]; future facilities include LSST[7] and SASIR in infrared [22]. To this category belongs the project in which I am involved: **The Sooner**, a 3-m robotic telescope characterized by a very rapid pointing; simultaneous multi-wavelength observations including photometry, spectroscopy and polarimetry; high temporal resolution observations. This experiment is expected to turn the exception of the naked-eye GRB 080319B into routine, with a long-range goal to witness the sequence of events thataccompany thecollapse of a massive star or the merging of degenerated objects. *The development of a timing analysis suitable to treat brief and highly non stationary transient events is the necessary theoretical counterpart to this technological effort.*

Transient emitters will be discovered by the synergistic coverage -from the discovery to the real time dissemination of trigger alerts to the community to allow a rapid follow up - of these multi-wavelength surveys and thanks to the cross-talk between them and non-electromagnetic surveys. The neutrino (e.g. ICECUBE) and gravitational wave telescopes (e.g. LIGO, VIRGO) suffer from poor localization and/or poor sensitivity: the electromagnetic localization of the event is therefore of primary importance. Multi-messenger astronomy is the future.

[2] The PTF is based around the Palomar 48-inch Oschin Schmidt telescope with a 96-million pixel detector and 7.8 square degrees field of view. See [92] for more details and visit `http://www.astro.caltech.edu/ptf/`

[3] Pan-STARRS: the Panoramic Survey Telescope & Rapid Response System is an innovative design for a wide-field imaging facility being developed at the University of Hawaii's Institute for Astronomy. See `http://pan-starrs.ifa.hawaii.edu/public/` for details.

[4] `http://www.mso.anu.edu.au/skymapper/`

[5] `http://www.eso.org/projects/vlt/`

[6] `http://www.astro.yale.edu/telescopes`

[7] `http://www.lsst.org/lsst`

The Sooner – (The large Robotic Telescope)

UNIMIB – INAF – MIUR – SINS
G. Chincarini, S. Covino, L. Mankiewicz,, M. Riva, F. Vitali, M. Zannoni,
On behalf of the CODEVISIR Collaboration

The study of the Universe can be characterized by two grand design themes: Weak Gravitation (Cosmology) and Strong Gravitation (compact relativistic objects). The challenge of Cosmology is the understanding of the evolution of the Universe as a whole and of its parts. The big unknowns are the understanding of Dark Matter, of Dark Energy and finally whether or not General Relativity still holds. On the other hand we have discovered that especially the phenomena related to the formation of black holes, neutron stars and relativistic stars in general are related to highly variable emission of electromagnetic energy and quite often to sudden bursts of electromagnetic energy likely accompanied (or preceded) by the emission of gravitational waves and neutrinos. This may occur in the collapse of massive stars, leading to GRBs and SNe with the final product of a Black Holes and Neutron Star respectively, and in the merging of relativistic objects: NS+NS and BH+NS.

We plan to open a new window of opportunity to study the variegated physics of very fast astronomical transients, particularly the one related to extreme compact objects. Our innovative approach is based on three cornerstones: 1) the design (the conceptual design has been already completed) of a 3m robotic telescope and related focal plane instrumentation characterized by the unique features: "No telescope points faster"; ii) simultaneous multi-wavelengths observations (photometry, spectroscopy & polarimetry); iii) high time resolution observations.
This experiment will turn the "exception" (like the optical observations of GRB 080319B) to "routine". **The long-range goal is also to witness, in the near future and in coordination with satellites, GWs and neutrinos facilities, the sequence of events that accompany the collapse of a massive star or the merging of degenerated objects.**

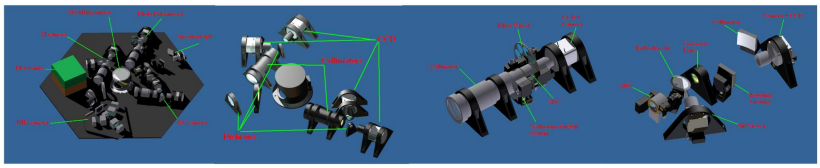

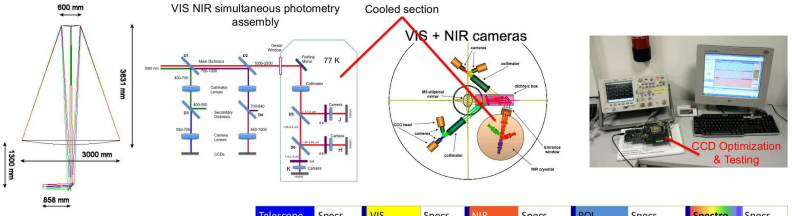

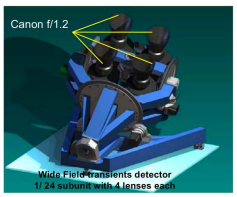

Telescope	Specs	VIS	Specs	NIR	Specs	POL	Specs	Spectro graph	Specs
Pointing Goal (spec)	60^0/30s (60^0/50s)	Filters	g, r, I, z	Filters	J, H, K	Type	Double Wollastone	Δλ	370-920
Tracking	0.2"/10m w/o Auto	High Time Res.	0.1 s	Cooling	ESO Standard	Atmosph. Corrector	TBD	Res.	R = 800
Primary Mirror	300 cm F/1.5	CCD Pixel 13.5 μ	2k x 2k	FPA Pixel 18 μ	2k x 2k 2RG HgCdTe	Filters	standard	Sim. Coverage	200 nm
Combined	F/10	Sampling	3.4 arcs/pix	Sampling	3.2 arcs/pix	Sampling	3.4 arcs/pix	Slit	1." x 4'
FOV	15 arcmin	FOV	10x10 arcmin	FOV	10 x 10	FOV	2x8 arcmin	CCD	1k x 1k

The CODEVISIR collaboration: *S. Benetti, C. Bonoli, F. Bortoletto, E. Cascone, G. Chincarini, P. Conconi, R. Cosentino, S. Covino, F. D'Alessio, P. D'Avanzo, V. De Caprio, M. Della Valle, N. Elias de La Rosa, A. Fernandez Soto, D. Fugazza, E. Giro, A. Gomboc, C. Guidorzi, D. Magrin,G. Malaspina, F. Mannucci, R. Margutti, R. Mazzoleni, E. Molinari, L. Nicastro, A. Riva, M. Riva, R. Salvaterra, M. Sperandio, P. Spanò, M. Stefanon, V. Testa, G. Tosti, F. Vitali, M. Zannoni; with the collaboration of C. Fryer and P. Kumar.*

Fig. 1.5: The Sooner project.

2. *SWIFT* GAMMA-RAY BURST CATALOGUE IN THE 0.3-10 KEV ENERGY RANGE

2.1 Introduction

The *Swift* [53] spacecraft has ushered in a new era of Gamma-Ray Burst (GRB) science. A key role was played by the X-Ray Telescope (XRT, [24]), which lead to the unexpected discovery of erratic X-ray re-brightenings known as flares ([30] and Chincarini in prep.); of the steep (see e.g., [189]) and of the shallow decay phases of the 0.3-10 keV light-curve (see e.g., [104]). As of June 2009, XRT detected the X-ray counterpart of $\sim 95\%$ of *Swift*-BAT triggers, providing temporal and spectral information starting from $\sim 60 - 90$ s after trigger and following the fading of the source down to the XRT threshold. This results in X-ray follow-ups typically lasting $\sim 10^6$ s (observer frame), with a record of $\sim 10^7$ s held by GRB 060729.

The production of a homogeneous catalogue contaning the temporal and spectroscopic information of *Swift* GRBs in the 0.3-10 keV range is therefore of primary importance. This chapter is devoted to the description of the software used to generate the dataset: the dataset comprises XRT observations of *Swift*-detected GRB as well as observations of non-*Swift* GRBs for which XRT did the follow-up.

2.2 Swift *data products*

Swift relies on two telemetry systems: the Tracking and Data Relay Satellite System (TDRSS) and the Malindi one. The TDRSS is used to telemeter data to the ground in real time so that both the spectral and temporal information reach the ground immediately after the explosion. While particularly useful for the XRT Burst Scientist (XBS) on duty at the moment of explosion being intended as quick-look products, these data are not fully calibrated and should not be used for scientific purposes. Malindi data instead comprise the full data set for a particular burst and are usually available from a few to several hours after the event. These data are designed to be the starting point of any kind of scientific analysis: I therefore concentrate on Malindi data, referring the reader to `http://www.swift.ac.uk/team/sper/sperproddoc.php` for details about the information that can be obtained from TDRSS data.

The data buffered on board (Level 0 files) are telemetred to the Malindi ground station (Kenya) $\sim 9 - 10$ times a day and then processed at the Swift

Data Center (SDC) at the Goddard Space Flight Center (GSFC) to obtain FITS files containing image and event data from the 3 *Swift* instruments (Level 1 files). Level 2 calibrated event lists and sky images are produced after data screening and coordinate transformation: these are the input of the catalogue builder software. The Level 2 products then go through the scripts for each instrument, leading to spectra, light-curves and combined sky images (Level 3 files). Event lists, exposure maps and sky images are first re-processed using the `xrtpipeline` within the latest *heasoft* release available at the time of the explosion of the GRB. I do not reprocess earlier GRB observations with the new release of the software. Data are screened and calibrated with standard screening and filtering criteria adopting the latest calibration files available in the *Swift* calibration database (CALDB) at the time of the analysis. Events characterised by:

(1) CCD temperature higher than $-50\,°C$;
(2) Central pixel energy lower than 0.3 keV;

are excluded from the final cleaned event lists in order to be less sensitive to the CCD dark current noise (1) and to the contribution of the Earth limb (2). When analyzing Window Time (WT) mode[1] data, only grades 0-2 are included[2], while for Photon Counting (PC) data events associated with grades higher than 12 are rejected (according to the *Swift* nomenclature, [24]).

The WT and PC cleaned event lists of different observations[3] are merged so that for each GRB a unique PC event list and WT event list is built. A unique instrument map file is created for PC data: this is a fits file, with a number of extensions equal to the number of the orbits of observation. For WT data this operation is not necessary since the WT mode has never been used after the first orbit. The attitude information of the spacecraft is collected in a unique attitude file with different extensions. The complete information of each *Swift* GRB observation is therefore stored into 5 files (Level 3 products):

(1) WT and PC cleaned event list files.
(2) WT and PC exposure map files: for each orbit of observation, these files contain information about the effective vignetted corrected exposure time of each pixel of the CCD.
(3) Attitude file.

The software is developed to basically produce three types of data products: count-rate light-curves, time resolved spectra and hardness ratios. The results from the spectral analysis are then used to produce flux calibrated light-curves. When the redshift information is available, the count-rate light-curves are transformed into luminosity curves. Only spectroscopically determined redshifts or photometric redshifts determined with a high level of confidence are

[1] We refer the reader to [80] for a comprehensive description of *Swift* read-out modes.
[2] See [24] for the definition of *Swift*-XRT grades.
[3] Malindi data are grouped into *observations*: each observation usually comprises data coming from different orbits but sharing the same ObsID.

used. The luminosity distance is computed according to standard cosmology: $H_0 = 70\,\mathrm{Km\,s^{-1}\,Mpc^{-1}}$, $\Omega_\Lambda = 0.7$, $\Omega_\mathrm{M} = 0.3$.

This chapter is organised as follows: Sect. 2.3.1 describes the different event extraction regions necessary for the following analysis, while Sect. 2.3.2 discusses the methods applied to correct for pile-up effects. The complete procedure of light curve extraction is outlined in Sect. 2.4. To the hardness ratio and to the spectral analysis of GRB data, are instead dedicated Sect. 2.5 and Sect. 2.6, respectively. Finally, the flux (and luminosity when possible) calibration of the GRB count-rate light curves is the subject of the last part of the chapter (Sect. 2.7). As of July 2009 the XRT catalogue comprises about 400 GRBs: the reader can follow the generation of the catalogue data products for GRB 081028 which is taken as example given the very good statistics, from Sect. 2.3 to Sect. 2.7. The results are summarized in Sect. 2.8.

The following analysis is partially done by using the XRTDAS software package. In particular, the time resolved spectral analysis of Sect. 2.6 is made via XSPEC 12. The additional automated processing described below is performed via custom IDL scripts.

2.3 Preparation for light-curve and spectra extraction

The creation of an X-ray light-curve and the extraction of an X-ray spectrum are in general reasonably easy tasks: however, both the fading nature of the GRBs signal and the way *Swift* is designed to carry out observations of a particular target, complicate and slow down the two processes. In the following I outline the different complications related to the XRT data analysis and detail how these complications are handled by the software:

1. **GRB soft X-ray fading:** standard X-ray light-curve generators like `xselect` or `lcurve` within the FTOOLS, assume that the source is stable and consequently give the possibility to rebin the data only using bins of uniform duration. For sources whose rate fades significantly (orders of magnitude) during the observation, this directly translates into having light-curve bins of very different statistical significance. At late times, long bin durations are required to detect the source, while using these bins at the beginning of the observation would result in the majority of cases in an excessive smoothing of the light-curve, losing in this way the particulars of the temporal structure of the emission. Alternatives are therefore required. The software is built to follow two different approaches: first, it produces light-curve with bins determined on the base of the number of source counts per bin; second, it gives the possibility to account for the background contribution in each bin, so that to assure a minimum source to background counts ratio in each bin. The two procedures are detailed in Sect 2.4. Moreover, the source fading count-rate requires to extract the GRB signal from different source regions to maximize the signal to noise ratio, as described in Sect. 2.3.1.

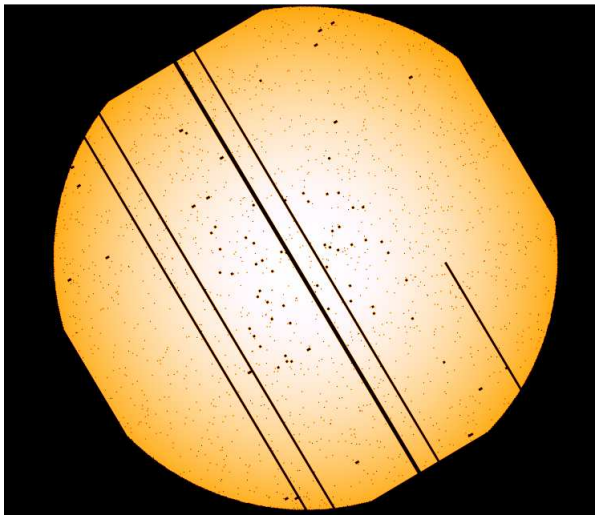

Fig. 2.1: Exposure map for one orbit of observation of the *Swift*-detected GRB 090807. The strips of damaged pixels and single bad pixels of the XRT CCD are apparent. Exposure maps are designed to account for bad columns and pixels, hot pixels, attitude variations and telescope vignetting when required.

2. ***Swift* observations:** The complete XRT data set of a particular target is made up of different *observations* sharing the same ObsID. Each observation comprises multiple *snapshots*. This is partially due to the fact that the unpredictable nature of GRB sources compels *Swift* to contemporary follow more than one target at a time; the other part of the story is linked to the low-Earth orbit of the spacecraft: once every $\sim$ 1800 s, for other $\sim$ 1800 s, the Earth is in between *Swift* and the target. The consequence is the un-ability to observe the fading GRB light-curves continuously, or from a practical point of view, the presence of many data gaps in a single light-curve. This directly translates into the necessity to combine snapshots and observations sometimes to build a unique spectral or light-curve bin where the source is detected. The software automatically accounts for the possible exposure fraction minor than one as described in Sect. 2.4.

3. **Point Spread Function (PSF) correction:** Once extracted from a particular region, the flux of the source has to be corrected for PSF losses, as described in Sect. 2.3.2. A complication arises from the progressive damage of the XRT CCD with time: apart from several detector columns flagged as "hot" after a micrometeorid struck the XRT on 2005 May 27th, there is currently a number of hot and bad pixels as shown in Fig. 2.1, which make the determination of the lost flux non trivial. For the light-curves, this is done using the `xrtmkarf` tool for WT data since they consist of a unique snapshot and the source has the same detector coordinates during the observation; PC data consist of several observations and snapshots

where the source is moving in detector coordinates: the hot pixels therefore occupy different positions in sky coordinates as time goes by and a dynamical correction for PSF losses must be applied: this is accomplished by using the `xrtlccorr` tool which provides a correction factor for each snapshot. This is another drawback arising from the way *Swift* observations are organized. Starting from the end of 2008, after the BAT trigger *Swift* automatically re-points the source maximizing the probability of having the source centroid away from the hot columns. However, for a few cases the bad columns intersect the source PSF, making the determination of the source best position inaccurate. For this reason the software uses as source position the best position delivered by the XRT team: these are the "enhanced positions" (see [44] and [42] for a detailed decription) made available by the XRT team within hours from the explosion. Using this method the attitude of the spacecraft is determined using serendipitous sources in the UVOT (*Swift* Ultraviolet and Optical Telescope, [167]) field of view to improve the on-board star trackers information. The result is a GRB position with a typical 90% error < 2" in the 90% of cases (see [44]).

4. ***Swift*-XRT readout-modes:** the XRT is designed to automatically switch the readout modes according to the source count-rate. A detailed description of the XRT readout modes is given by [80]. In particular, for count-rates higher than $\sim 1\,\mathrm{count\,s^{-1}}$ the spacecraft operates in WT mode where a spatial dimension is sacrified to have a high temporal resolution ($\sim 2 \times 10^{-3}\,\mathrm{s}$). For count-rates lower than $\sim 1\,\mathrm{count\,s^{-1}}$, data are acquired in PC mode: the spatial dimension is restored with the drawback of a lower temporal resolution (2.5s)[4]. For the majority of cases this means that the first part of the observation is carried out in WT mode and the second part in PC mode, when the source has faded enough. In a few cases the GRBs show re-brightenings which make the XRT toggling between the two readout modes, with partial overlaps between the two kinds of observation. Other times a rapid mode switching is induced by a rapid appearance and disappearance of hot pixels with high temperature or by photons scattered by the Earth atmosphere. The software is written to treat WT and PC mode data in a completely independent way both during the spectra and in the light-curve analysis. The different temporal resolutions directly translates into different pile-up regimes, as detailed in Sect. 2.3.2.

The phase of light-curve and spectra preparation consists of two major operational steps: first, the definition of the most appropriate regions of event extraction for the background and for the source in its different count-rate stages; second, the definition of the time intervals during which the source is affected

[4] For completeness: the XRT was originally designed to have a third readout mode for very high count-rates. This was the Photodiode mode, which was disabled soon after the meteoroid impact.

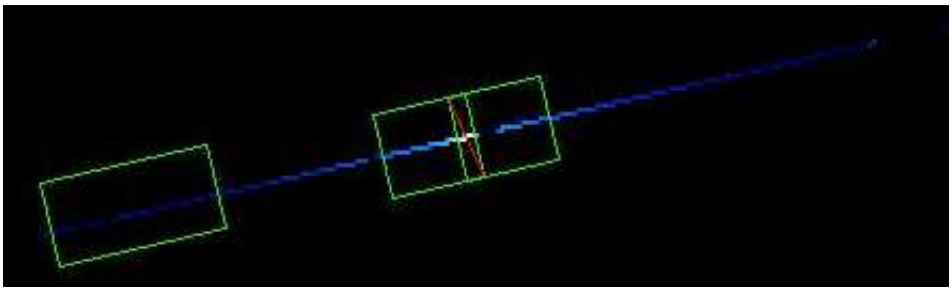

Fig. 2.2: In WT mode one spatial dimension is sacrified to gain higher temporal resolution with respect to the PC mode. In WT mode the source photons are collected by a unique strip of ~ 200 pixels (blue and light-blue pixels in the figure). Green empty boxes: left: WT background data extraction region (Region 3). Right: Region 1 and 2. The red line marks the central part of the region which is excluded to correct for pile-up.

by pile-up in WT and PC mode, respectively. The preparation phase ends with the definition of the appropriate region file "holes" as described in Sect. 2.3.1 and Sect. 2.3.2.

2.3.1 Event Extraction Regions

WT data are extracted in a 20×40 pixel region centered at the aferglow position along the WT strip of data (Region 1). When pile-up is present (see the following Sect.) the central part of the rectangular region is excluded from the analysis (Region 2). The size of this hole is determined as described in Sect. 2.3.2. WT background data are extracted within a rectangular box which is manually chosen to be far from serendipitous background sources (Region 3) (see Fig. 2.2).

For PC observations, events are selected within four different regions: first, PC data are extracted from a circular region centered at the enhanced position provided by the XRT team (Region 4). In most cases a radius of 20 pixel ($1\,\text{pixel} \sim 2.36''$) is used. The radius is chosen so as to contain $\sim 90\%$ of the total flux as determined by the `xrtmkarf` tool. Exceptions are however present: bright (faint) sources require radii greater (smaller) than the standard 20 pixel value; at the same time, also for bright sources, a region of event extraction smaller than usual is sometimes necessary to avoid contamination from serendipitous background sources. Typically, for the standard 20 pixel circle, the excluded flux fraction is $\sim 10\%$. The original radial distribution of radiation -and the total source flux- is recovered using the accurate information of the instrumental Point Spread Function (PSF) provided by [125].

As for WT observations, also in PC mode the central part of the circular region is excluded (and an annulus is used) when pile-up corrections need to be applied (Region 5). The size of the central hole is determined as decribed in Sect. 2.3.2. When the count-rate of the fading afterglow is lower than $0.01\,\text{count}\,\text{s}^{-1}$,

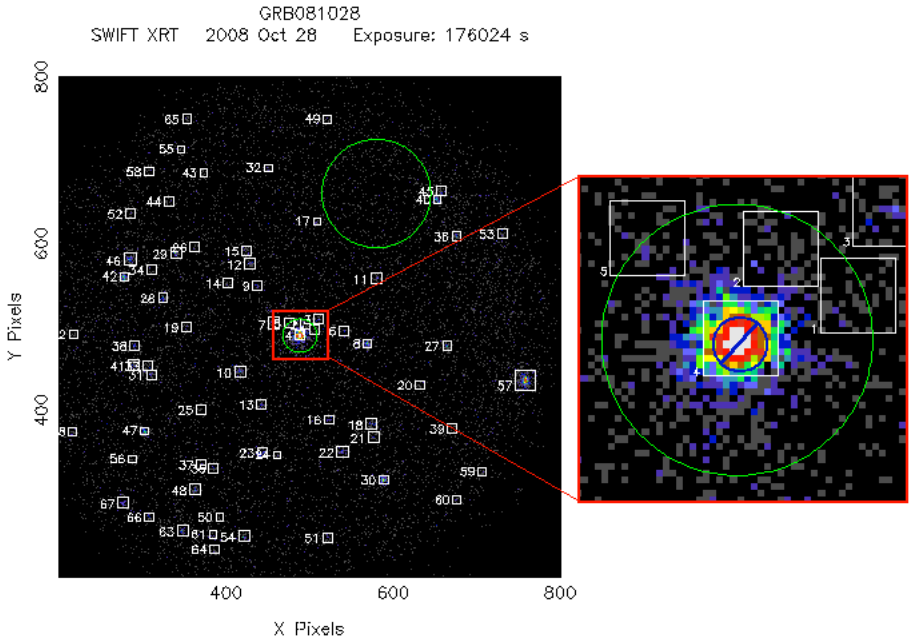

Fig. 2.3: XRT-PC mode field for GRB 081028. Any background source with a minimun $2\,\sigma$ significance is marked with a number. The background region in the upper right part of the panel (Region 7) is chosen in a source-free portion of the CCD. The green circle around the GRB source is Region 4; when pile-up is present, the events in the blue circle in the right panel are excluded (Region 5).

the source events need to be extracted from a smaller region: only in this way a high signal-to-noise (SN) ratio is guaranteed. This directly translates into the introduction of a third PC extraction region (Region 6): a circle with a typical 10 pixel radius. Finally, the PC background level is assessed exctracting the events from an annular region centered as close as possible to the GRB location and with an inner radius greater than 3/2 the radius of Region 4. When this is not possible, background data are selected within a circular region with size as big as possible. In both cases the background region (Region 7) is manually selected in a free-source portion of the soft X-ray sky. This is accomplished by reading the PC cleaned event list file with the `Ximage` package and localizing any source in the field with a minimum signal to noise equal to 2. Moreover $\frac{A_7}{A_4} \geq 8$ is required, where A_7 and A_4 stand for the area of Region 7 and 4, respectively. Figure 2.3 shows the extraction regions used for GRB 081028.

For each GRB, a background light-curve is produced following the procedure detailed in Sect. 2.4. If the resulting light-curve is not constant within errors, the assumed region of background events extraction is rejected and a new one is selected far from the previous location (in order to avoid the contamination

from the GRB photons).

2.3.2 *Pile-up correction*

The pile-up affects several X-ray observations, being originated by the arrival of more than one photon in the same CCD pixel or in adjacent CCD pixels in a time interval which is short compared to the CCD readout time. The problem is therefore not unique of *Swift*: however, the fading nature of GRB source requires the pile-up corrections to be applied in a dynamical way. The *Swift* observation mode (WT or PC) is automatically chosen with the aim of reducing the pile-up effects. In spite of this, pile-up if often present and pile-up corrections therefore need to be applied. The subject of pile-up corrections is extensively treated in [192] and in [138] for PC observations, while the WT pile-up correction is detailed in [166]. In particular:

1. Pile-up causes a group of low energy photons to be detected as a single high energy event: the obvious result is the distortion -generally speaking a hardening- of the orignal spectrum. In other words, an increase of the mean energy associated to each photon. See [166], their Fig. A1 for an example;

2. Pile-up causes a group of low-grade events to be detected as a single high-grade event. The result is first a deficit (excess) of low (high) grade events; second, but not less important, an apparent loss of flux, since higher grade events are usually associated with cosmic rays and therefore rejected.

The pile-up therefore reveals its presence in three different ways:

1. Distortion of the original Point Spread Function, PSF ([192]);

2. Distortion of the original spectrum ([166]);

3. Distortion of the grade distribution ([166]).

Each of these three manifestations is used to compute both the intervals of time and the radial portion of the PSF affected by pile-up. In general, intervals of time where the count-rate is higher than 150 count s^{-1} in WT mode or higher than 0.6 count s^{-1} in PC mode are considered at risk of pile-up.

For PC data, following [192], the software extracts the source events in an annulus whose inner radius r_i is derived comparing the observed to the nominal PSF. In this way the region mostly affected by pile-up is excluded from the analysis and the original signal is recovered from the external wings of the PSF, where pile-up effects are negligible. The central part of the nominal PSF is known within a relative error of $\sim 5\%$ ([125]). This error is properly propagated in the final uncertainty of PSF corrected data. The value of the radius r_i of the region that needs to be excluded from the analysis is computed as described below. Given an energy E and an off-angle θ, the nominal PSF profile is well modeled by a King function ([125]):

$$PSF(r) = \left[1 + \left(\frac{r}{r_c}\right)^2\right]^{-\beta} \tag{2.1}$$

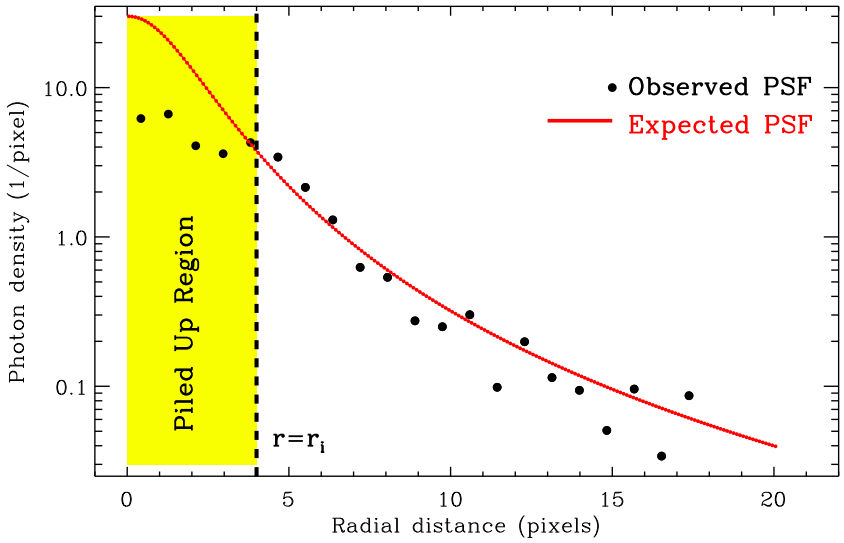

Fig. 2.4: Comparison of the observed and expected 0.3-10 keV PSF for GRB 061007 between 2 ks and 6 ks from trigger. The pile-up clearly affects the detector region for radial ditances minor than 4 pixels from the PSF centroid.

where:

$r_c \equiv r_c(E,\theta)$: core radius;
$\beta = \beta(E,\theta)$: slope.

The pile-up causes the centre of the observed PSF to underestimate the nominal PSF profile up to r_i. The comparison of the observed to the nominal PSF directly gives the outer radius of the region with distorted PSF, r_i (see Fig. 2.4 where I plot the results for GRB 061007: GRB 081028 is not affected by pile-up in PC mode). In most cases $r_i \sim 4$ pixels.

In order to compute the extension of the innermost region of the PSF affected by pile-up in WT mode, the WT light-curve of a particular GRB is first extracted without applying any pile-up correction. Events are selected within the standard rectangular 40×20 pixel region, as described in Sect. 2.3.1. The grade distribution of these events (an in particular of the intervals of time with the highest count-rate) is then computed: the size of the exclusion region is finally determined as the position at which the deficit of grade zero becomes negligible (a 4 pixel box for GRB 060614). A consistent result is always obtained computing the detected average energy per photon. Since the grade distribution proved to have a higher sensitivity than the average energy per photon method, the first method is used to compute r_i while the latter is used only as a consistency check.

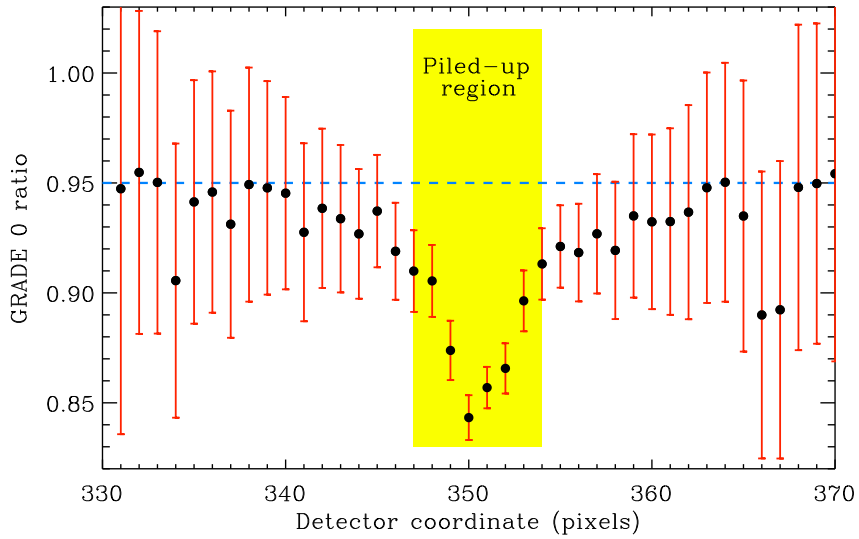

Fig. 2.5: Grade 0 ratio distribution for GRB 060614 0.3-10 keV events between 100 and 200 s from trigger. Shaded area: region strongly affected by pile-up. In this region a deficit of grade-0 photons is apparent.

Once determined $r_{\rm i}$, the correction for the lost flux is computed using the `xrtmkarf` and `xrtlccorr` tools for WT and PC modes respectively.

2.4 Light Curves Extraction

In overview: the software is able to produce source and background light-curves of any source detected within the XRT field of view and in any energy interval between 0.3 ad 10 keV. The source light-curve is rebinned using two different methods: a constant number of source counts or a constant signal-to-noise ratio. In order to be less sensitive to the Earth limb radiation effects, no event is extracted between 0.2 and 0.3 keV. WT and PC data reduction procedures are completely independent.

2.4.1 WT data

WT data are extracted from the appropriate region and in the specified energy band running the `xselect` tool. A first light-curve binned at constant intervals of time $\Delta t_{\rm WT}$ is derived using the `lcurve` tool: in principle, the time interval could be set to the minimum value allowed by the read out mode ($\sim$ 1.7 ms [24]). However, given the typical GRB maximum count rate in WT mode of the order of 100 count $\rm s^{-1}$ a longer mimimum bin time is required so that the count rate of each bin is representative of the source count rate at that time:

this is particularly important for the pile-up correction. $\Delta t_{\rm WT} = 1.0\,{\rm s}$ is used. This process occurs twice: once for non piled-up data, extracting the data from Region 1 (Sect. 2.3.1); once for piled-up data, using Region 2. In both cases, the obtained count rates are corrected for PSF losses and partial pixel exposure using the `xrtmkarf` tool. A unique list of corretected count rates bins with same duration is then built, replacing the data in the first list with those corrected for pile-up when necessary. These data are corected for pile-up, vignetting[5], partial pixel exposure and PSF losses. No background subtraction is necessary since the $0.3-10\,{\rm keV}$ background is of the order of a few $10^{-3}\,{\rm counts\,s^{-1}}$ to be compared to WT count rates which are $> 0.5\,{\rm count\,s^{-1}}$.

2.4.2 PC data

The reduction of PC data closely follows the WT mode data reduction of the previous paragraph. As before, events are extracted within Region 4, 5 and 6 of Sec. 2.3.1 and in a particular energy band included between 0.3 and 10 keV. Background events are instead selected from Region 7 in the same energy interval. Each of these operations requires the use of the `xselect` tool. A total of 4 filtered event lists is produced. A first light-curve binned at constant time intervals is obtained from each of these event list files by running the `xselect` tool with $\Delta t_{\rm PC} = 2.51\,{\rm s}$ (minimum value allowed by the readout mode, [24]).

The PSF and exposure corrections are performed in the following step, applying the `xrtlccorr` task to the ligth-curves just derived. It is important to underline that for background data no PSF correction needs to be applied and is accordingly not applied. Finally, a total background *un*-subtracted PC light-curve is derived starting from the three lists of vignetted, PSF and exposure corrected count rates just obtained:

1. List 1: events extracted from Region 4;
2. List 2: events extracted from Region 5;
3. List 3: events extracted from Region 6.

In particular, pile-up effects are removed replacing the count rates originally $\geq 0.6\,{\rm count\,s^{-1}}$ (pile-up threshold for PC acquired data) with the corrispondent values of List 2. At the same time a high signal-to-noise is guaranteed by switching to List 3 when the count rates recorded in List 1 are comparable to the background level of that particular GRB event. The resulting light curve is then verified to transition smoothly from Region 4 to 5 and from Region 5 to 6.

The background subtraction is dynamically performed accounting for the fact that in the previous step *all* the events (background + GRB) within the source region have been corrected for PSF losses, while only point source generated counts need to be corrected. For this reason, the background subtracted signal S is derived as follows:

$$S = \gamma\Big(O - \chi\frac{\alpha}{\beta}\,B\Big) \tag{2.2}$$

[5] Level 2 products were already corrected for vignetting. See Sect. 2.1

where:

O : Source count rate extracted from Region 4, 5 or 6;
B : Background count rate extracted from Region 7;
α : Background exposure correction factor;
β : Source exposure correction factor;
γ : Source PSF+exposure correction factor;
χ : Normalization factor accounting for the different areas of the extraction regions.

The final result is therefore a PC light curve binned at costant time intervals ($\Delta t_{\rm pc} = 2.51\,{\rm s}$) background subtracted and corrected for pile-up, partial pixel exposure, PSF losses and vignetting. The WT and PC mode constant bin duration light-curves constitute the Level 4 products of the pipeline.

I parenthetically note that the temporal analysis of the final chapter the requires the light-curves to be extracted in a pile-up free region and with the highest temporal resolution. This means that while the PC light-curves with constant bin duration $\Delta t_{\rm PC} = 2.51\,{\rm s}$ are ready to be used as input of the temporal analysis, the WT light-curve need to be re-extracted with a lower constant bin duration. $\Delta t_{\rm WT} = 0.007\,{\rm s}$ is chosen as a good compromise between a reasonable computing time and a good temporal resolution.

2.4.3 Light-curve rebinning

The light-curve is binned using two different methods.

1. **Constant number of photons:** a light-curve point is defined as the smallest number of bin with constant duration with at least C source re-contructed counts. The C value varies from 80 to 5 according to the statistics of the event. The default value is 25.

2. **Constant signal-to-noise ratio (SN):** a light-curve point is defined as the smallest number of bin with constant duration with a minimum SN=4. The SN is here defined as:

$$\mathrm{SN} = \frac{\mathrm{N_{s-b}}}{(\mathrm{N_s} + \mathrm{N_b})^{1/2}} \tag{2.3}$$

where:

$N_{\rm s-b}$: Background subtracted number of counts;
$N_{\rm s}$: Signal counts (before background subtraction);
$N_{\rm b}$: Background number of counts.

Swift data are not continuously collected, as described in Sec. 2.1: they are instead accumulated into different *snapshots* in different *observations*. This implies that: the effective exposure time of each light-curve bin can be lower than the interval of time covered by the bin; moreover, a single *snapshot* could contain not enough signal to satisfy the binning criterion. If at the end of a

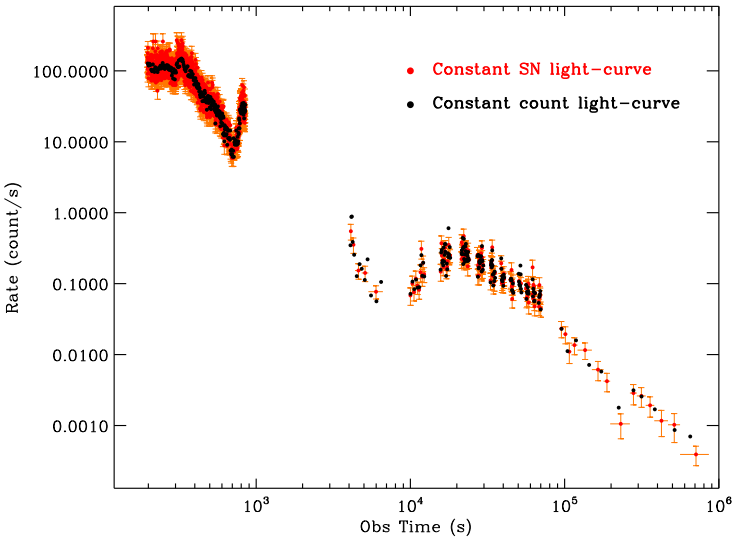

Fig. 2.6: 0.3-10 keV count-rate light-curve of GRB 081028. Red (black) points: data rebinned at constant SN ratio (number of counts). $1\,\sigma$ errors are reported for constant SN data only for the sake of clarity.

snapshot there are some events left over that do not comprise a full bin, its signal is simply merged to the previous bin of the same *snapshot*. Because of the fading nature of GRB sources, it is generally not possibile to build a full bin using all the events of a single *snapshot* at late times: in this case the signal coming from different consecutive *observations* is merged to satisfy the binning criterion. Finally, if the total number of detected photons associated with a particular GRB does not reach the fixed SN or count level, they are lowered to meet the source weakeness. However, no light-curve is extracted with less than 5 counts per bin or a signal-to-noise lower than 3. During the binning procedures the errors are calculated using the standard theory of error propagation. In the following, BT stands for the bin mean time.

The entire procedure can be applied to data extracted into different energy bands so that the source behaviour can be analysed in different wavelenghts regimes. For each GRB a constant SN light-curve is extracted in the $0.3-1$ keV (b1) band; $1-2$ keV (b2) band; $2-3$ keV (b3) band and $3-10$ keV (b4) band.

Figure 2.7 shows the final result for GRB 081028. Light-curves extracted at constant SN or number of counts are classified as "Level 5" products of the analysis. The data are finally written to ASCII files. For each bin the following information is stored into the files: observed time in seconds from the BAT trigger; bin duration; corrected count rate in count s^{-1}; $\pm 1\sigma$ uncertainty on the count rate; effective bin duration (this information is necessary to recover the original number of counts observed in that interval of time). For constant SN

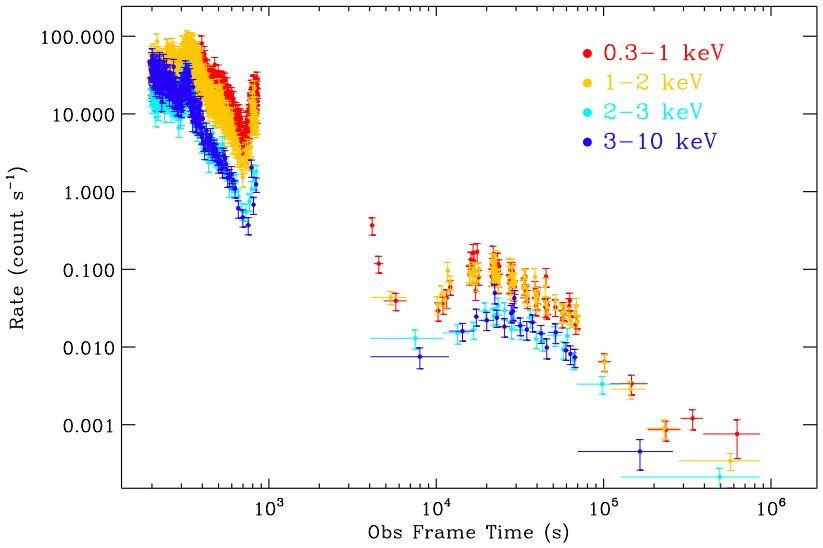

Fig. 2.7: Count rate light-curve of GRB 081028 extracted in different energy bands. In each band, the signal is then re-binned so as to achieve a minimum signal-to-noise ratio of 4.

light-curves another column is added to the respective ASCII files reporting the value of the SN reached in that bin.

2.5 *Hardness ratio analysis*

For weak sources for which the limited number of counts does not allow to extract even a single spectrum, the hasdness ratio (HR) analysis is the only way to quantify the spectral properties of the emission; for GRBs with higher statistics, the HR analysis provides a time resolved information on the spectral evolution of the source that the spectral analysis of Sec. 2.6 can not provide. The HR is here defined as:

$$\mathrm{HR(t)} = \frac{\mathrm{C_{\Delta E1}(t)}}{\mathrm{C_{\Delta E2}(t)}} \tag{2.4}$$

where:

- $C_{\Delta E1}$: Number of source counts in the energy band $\Delta E1$, in the time interval Δt centered at time t.
- $C_{\Delta E2}$: Number of source counts in the energy band $\Delta E2$, in the time interval Δt centered at time t.

As a first step, the $0.3 - 10$ keV light-curve needs to be extracted and binned at constant SN or number of counts as described in the previous section. Two

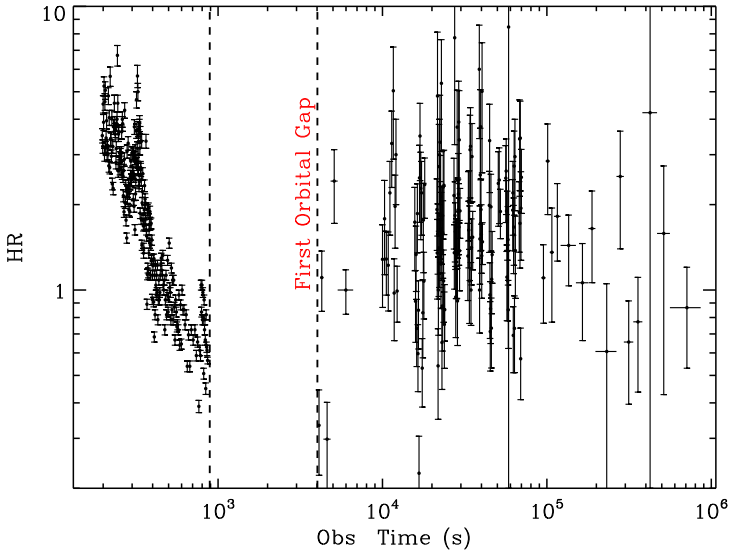

Fig. 2.8: Hardness ratio (HR) temporal evolution for GRB 081028 with $\Delta E_1 = (0.3 - 2)$ keV and $\Delta E_2 = (2 - 10)$ keV. A softening is apparent before the first orbital gap.

other light-curves are extracted filtering the original events in $\Delta E1$ and $\Delta E2$. These are then binned so that each of their bins begins and ends exactly when begins and ends the respective total light curve bin. In this way a HR value is obtained for each bin of the total light curve for which the number of counts in $\Delta E1$ and $\Delta E2$ is different from zero. The final result for GRB 081028 is shown in Fig. 2.8. The software automatically filters into 4 different energy bands: $0.3 - 1$ keV (b1); $1 - 2$ keV (b2); $2 - 3$ keV (b3) and $3 - 10$ keV (b4). In this way it is possible to obtain the HR in different $\Delta E1$ and $\Delta E2$ simply combining the information of these light-curves. The default choice is $\Delta E1 = 0.3 - 2$ keV; $\Delta E2 = 2 - 10$ keV.

* * *

For each GRB the following light-curve and hardness ratio files are available in the archive for Level 5 products:

1. $0.3 - 10$ keV light-curve ASCII file with constant number of counts bin and constant SN. WT and PC mode files are merged into a unique file.

2. Constant SN b1, b2, b3 and b4 light-curve files. WT and PC mode files are merged into a unique file.

3. Hardness ratio files: light-curve files in the energy bands b1, b2, b3 and b4 where the bin duration is defined by the total $0.3 - 10$ keV light-curve. WT and PC mode files are merged into a unique file.

Each of these files is accompanied by a plot.

2.6 Spectra Extraction

In addition to the temporal evolution of the source counts derived in the previous section, the time resolved spectral analysis of GRB sources gives us complemetary information. This Sect. is written with the aim of detailing the automatic spectra extraction procedure. While originally designed to run after the light-curve analysis, the spectral code is completely independent. As for the light-curve analysis, also in this case WT and PC data are considered separately. With reference to Fig. 2.9, the XRT data are divided into 5 epochs according

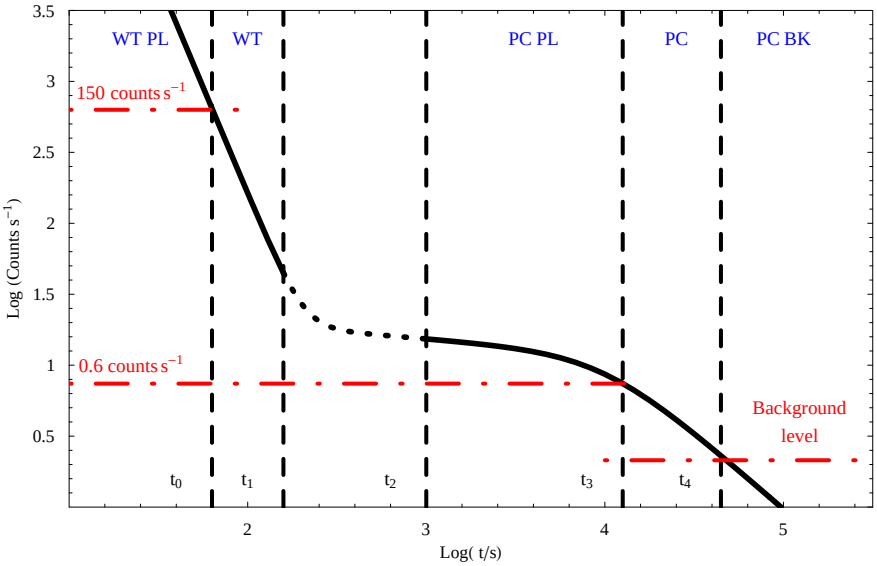

Fig. 2.9: Syntetic $0.3 - 10$ keV GRB light-curve. For the sake of clarity, the five epochs discussed in the main text are here explicitely drawn together with the assumed thresholds for WT and PC pile-up (red dot-dashed lines). The background level is also indicated.

to the count rate level. In particular:

1. For $t \leq t_0$ the source is observed in WT mode, with a count rate higher than 150 counts/s. Pile-up effects are here important (see Sect. 2.3.2). In this time interval events are therefore extracted within Region 2 using the `xselect` tool.

2. For $t_0 < t \leq t_1$ the read out mode is WT and no pile-up is present. In this case Region 1 is used.

3. For $t_2 < t \leq t_3$ pile-up effects are important in PC mode and events are consequtnly extracted in Region 5.

4. For $t_3 < t \leq t_4$ the source count rate is consistently higher than the background level but no pile-up correction needs to be applied. In this case the circular Region 4 is used as boundary for event extraction via `xselect`.

5. For $t > t_4$ the source count rate is comparable to the background level. In order to improve the S/N the smaller circular Region 6 is used as input of `xselect`.

Finally, an event list of background data is obtained filtering the original event files in Region 3 and 7 for WT and PC data respectively.

For each of the five epochs above a number of different spectra is extracted. The five epochs are processed separately. Each spectrum is required to have a minimum of 2000 photons before background subtraction. This binning scheme represents the best compromise bewtween a reasonably good signal-to-noise and a high temporal resolution. For faint soft-X afterglows (total number of photons between 1000 and 2000) the threshold for spectra extraction is lowered to 1000, while no spectral analysis is performed on GRBs with less than 100 counts in the $0.3 - 10$ keV energy band. For these GRBs, clues regarding the possible spectral evolution can only be derived from the hardness ratio analysis of Sect. 2.4. The last spectrum of each epoch generally collects the remaining photons: if their number is lower than 1/10 of the threshold for spectra extraction (2000 or 1000 photons), then the last spectrum is merged with the previous one. For each of the five modalities no spectrum is extracted if the photon number does not exceed 1/10 the selected threshold. In this case the spectral analysis stops and the spectral properties of the source are assessed using the HR analysis information.

Once the data have been divided into time intervals a source and a backgroud spectrum are generated using `xselect`. An exposure map and an Ancillary Response File (ARF) are also created for each time interval: the different extensions of the original PC exposure map file (Level 3 products) related to a particular time interval are combined weighting each extension according to its total exposure time to give a unique exposure file for that spectrum. This file is then used as input for `xrtmkarf` to generate the respective ARF file. When possible, the source spectra are binned using the `grppha` tool to ensure a minimum of 20 counts per energy bin, ignoring channels below 0.3 keV and above 10 keV.

After creating the source and backgroud spectra, the software is written to automatically model them using a photo-electrically absorbed power-law within `Xspec 12`. A redistribution matrix file (RMF) has to be provided: the latest available RMF file in the *Swift* CALDB at the time of the analysis has been used. The XRT spectral response is detailed in [62]. Each spectrum is fit using the model `(tbabs)*(pow)`. As a first run all the parameters of the model are left free to vary; if the GRB has a known redshift an extra neutral absorber at the source redshift is added to the previous model and the new fitting model becomes: `(tbabs)*(ztbabs)*(pow)`. The Galactic column density in the direction of the

burst is in this case frozen to the value found from the [85] map: this is done using the `NH` FTOOL. The parameters of the spectral model are the following:

(1) global normalization (free);
(2) galactic neutral Hydrogen column density (frozen);
(3) host galaxy neutral Hydrogen column density (free);
(4) source redshift (frozen);
(5) photon index (free).

The 90% confidence intervals of each parameter are computed using the `uncertainty` command within `Xspec 12`. The best fit parameters and the statistical information about each fit is saved in an ASCII file. This file contains for each fit: χ^2; degrees of freedom (dof); interval of time of extraction; best fit photon index and 90% c.l. errors; best fit Hydrogen column density (the total or the intrinsic one depending on the availability of the redshift information) provided with 90% c.l. errors; best fit spectrum normalization with 90% c.l. errors.

The temporal evolution of the spectral parameters can be easily derived: Fig. 2.10 and 2.11 show the results for GRB 081028:

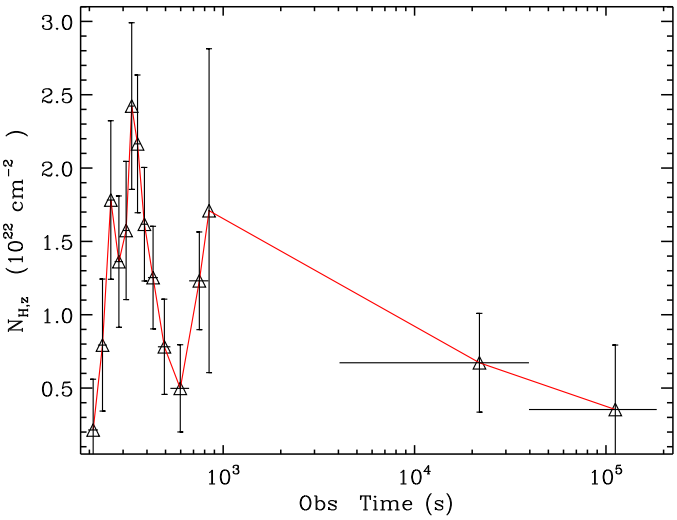

Fig. 2.10: Temporal evolution of the best fit intrinsic neutral hydrogen column density $N_{\mathrm{H,z}}$ obtained for GRB 081028. This kind of evolution is likely to be unrelated to the real behaviour: this is instead an artifact of the fitting procedure (see the main text for details).

Although designed to extract several spectra in different intervals of time, the software allows to extract a spectrum in an arbitrary time interval within the same epoch. The number of photons per spectrum can be modified as well.

It is often difficult to disentangle the contribution given to the observed 0.3-10 keV SED by two different model parameters, even when they have a

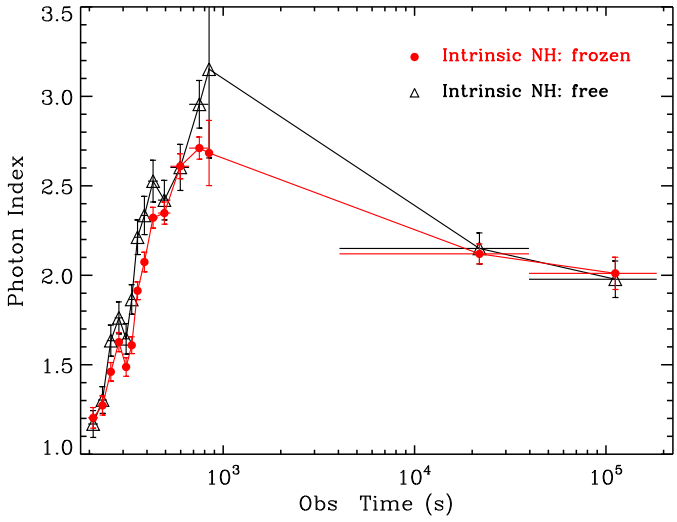

Fig. 2.11: Best fit spectral photon index as a function of time as observed for GRB 081028. Black points: photon index evolution obtained leaving $N_{\rm H,z}$ free to vary. Red points: result obtained for $N_{\rm H,z} = 0.52 \times 10^{22}$ cm^{-2}. This value has been obtained modelling the PC mode data in the time interval $(7 - 300) \times 10^3$ s, where no spectral evolution is taking place in the XRT energy range.

completely different physical role. In the case of a simple power-law model, a spurious positive correlation between the photon index and the intrinsic column density is generated by the combined effect of the fitting model and the limited energy band of the XRT. To avoid this effect, one of the two parameters must be frozen to a previously determined value. Since the intrinsic Hydrogen column is supposed to vary on timescales much shorter (see e.g. [147]) than the beginning of the XRT observation (which is ~ 60 s in the best cases), and given that a convincing proof of its time variability during the X-ray afterglow has not been provided yet[6], the temporal evolution of the photon index can be reconstructed in a proper way providing to the software a reliable estimate of the $N_{\rm H,z}$ (or $N_{\rm H}$ when the redshift is unknown). This value is later used by the software as frozen value for all the spectral fits of that particular GRB. The $N_{\rm H,z}$ (or $N_{\rm H}$) to be supplied is computed as follows: among the five epochs, the one

[6] A claim of NH variability is done in [26] for GRB 050904: however, the time interval with a lower intrinsic NH, and on which value strongly depends the claim of the variable NH, is dominated by important flaring activity. Since flares are known to have a Band spectrum, it is not clear if the superposition of intrinsically Band spectra can mimic an SPL spectrum with a lower NH. This hypothesis has not been tested in [26]: instead, a SPL fit is done and the resulting NH is assumed to be physical. The results presented in [26] must therefore be taken with caution until this possibility is first tested and than discarded as the source of the evolution.

with the best statistic (greatest number of source photons) is chosen. A unique spectrum containing much more than the usual 2000 photons is extracted in that particular time interval and then fit as before. The better statistics allows for a more refined determination of the parameter. A "time averaged" neutral Hydrogen column density is in this way obtained and used as input for the software. The time resolved spectral analysis is then re-run as before: the unique difference is that the neutral Hydrogen column is now an input instead of an output. Following the previous scheme, the spectral best fit parameters together with their 90% uncertainties and the statistical information about each fit is saved in an ASCII file. Fig. 2.11 explicitely compares the results of this second approach applied to GRB 081028. The software is written to receive as input any value of the Hydrogen column a scientist thinks to be the best estimate of the parameter. The default value is the "time averaged" value obtained as described above.

The ASCII files containing the time resolved spectral information of each source, belong to the Level 5 products of the software.

2.7 Flux and luminosity calibration of the count-rate light-curves

The spectral analysis of the previous section is used to convert the count-rate light-curves of Sect. 2.4 into flux and luminosity light-curves. A time resolved spectral analysis is in this case essential since the GRB are known to show strong spectral variations mainly during the steep decay. A showcase in this respect is GRB 081028 which is the subject of the extensive analysis of the next chapter: in that chapter is clearly shown that the count to flux converting factor undergoes a variation of a factor 2 during the the steep decay. Consequently, a flux conversion which does not account for the spectral evolution would have produced flux and luminosity light-curves which are wrong of that factor. *An accurate flux conversion is therefore of primary importance.*

For each spectrum, the absorbed and de-absorbed 0.3-10 keV flux is computed together with the model count-rate. A count-to-flux conversion factor is therefore computed from the best fit model for each time interval of the time resolved spectral analysis (see Fig. 2.12). This value is considered reliable if the respective χ^2/dof implies a P-value higher than 5%. The discrete set of count-to-flux conversion factors is then used to derive a continuous count-to-flux conversion factor through interpolation. Particular attention is devoted to the result of the extrapolation procedure, necessary when some of the bins of the original count rate light-curve fall outside the total time interval of spectra extraction. In this case the software allows the extrapolated factors to vary within a range of 10% from the nearest in time flux conversion factor directly calculated from the spectral analysis. Since the count-rate light-curves are already vignetted and PSF corrected, the flux conversion factor has to be de-corrected for this effects, so that the correction is not applied twice. The flux conversion factors in this way obtained are finally applied to the count rate light curves described in Sect. 2.4. The flux calibration is therefore dynamically performed,

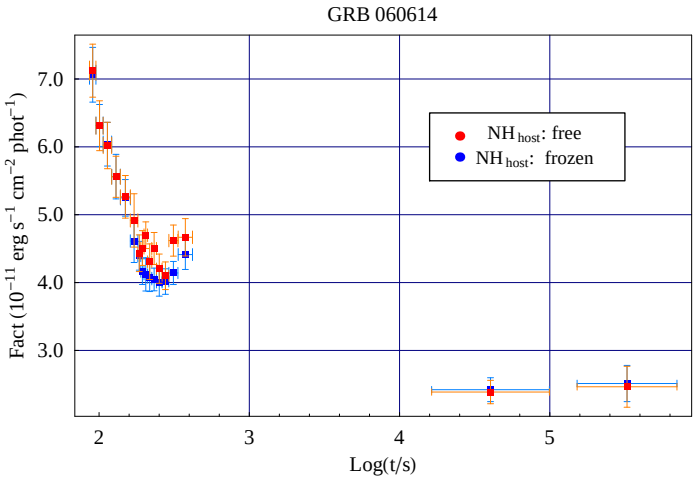

Fig. 2.12: Temporal evolution of the count rate-flux conversion factor calculated for GRB 060614. Red points: results from spectral fits performed letting the host galaxy neutral Hydrogen column density free to vary. Blue points: results from fits performed freezing the host galaxy neutral Hydrogen column density to its average value.

accounting for the spectral evolution with time of the source.

The complete procedure is applied to both the NH-free and NH-frozen set of spectra, so that each light-curve is calibrated in two different ways. The flux calibration is applied to the complete set of light-curves: to the total one extracted in the 0.3-10 keV band and to the four light-curves extracted in the b1, b2, b3 and b4 bands.

For bursts with known redshift, the flux units can be easily converted into luminosity units using the well known relation:

$$L(t) = \frac{F(t)}{4\pi D_{\rm L}^2} \tag{2.5}$$

where:

- $L(t)$ Luminosity as a function of time.
- $F(t)$ Flux as a function of time.
- $D_{\rm L}^2$ Luminosity distance. The standard Λ cosmology is used: $\Omega_{\rm m} = 0.3$, $\Omega_\Lambda = 0.7$ and $H = 0.7\,{\rm Km\,s^{-1}\,Mpc^{-1}}$.

The final result is shown in Fig. 2.13 and 2.14. Flux and Luminosity light curves are defined as "Level 6" products of the software. Finally, the catalogue includes some scripts to automatically convert the count-rate light-curve in any sub-energy band of the XRT using the spectral information of the spectral tables without re-running the `xrtpipeline`.

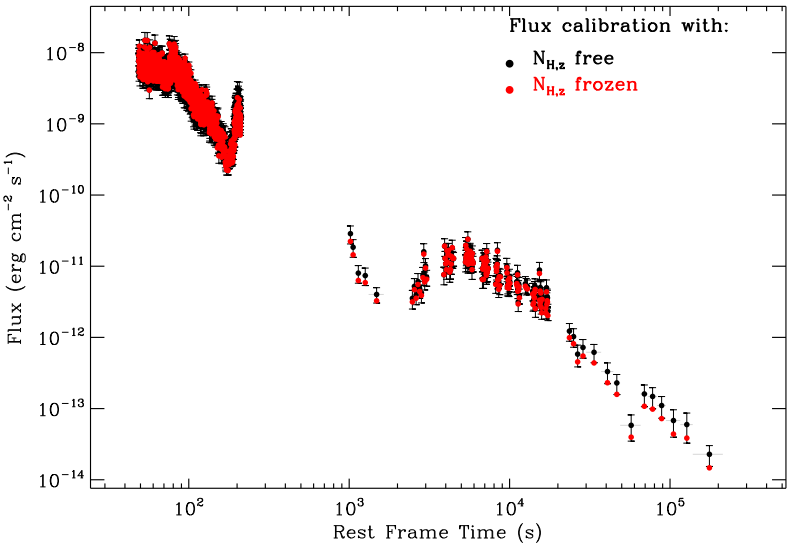

Fig. 2.13: Flux unit light-curve of GRB 081028. The original count-rate light-curve has been converted into a flux light-curve using the information coming from the time resolved spectral analysis.

2.8 Summary

Summary of the products of the analysis:

- **LEVEL 0 products**: Time-ordered telemetry data distributed by the Swift Data Center (SDC) at NASA/GSFC.
- **LEVEL 1 products**: Calibrated and quality flagged event lists.
- **LEVEL 2 products**: Cleaned, calibrated and quality flagged event list files: starting point of the present analysis.
- **LEVEL 3 products**: `xrtpipeline` products.
- **LEVEL 4 products**: Light-curves extracted at constant bin duration.
- **LEVEL 5 products**: Light-curves extracted at constant SN or counts in the total anergy band and in 4 XRT sub-energy bands; ASCII files with the time resolved spectral information; hardenss ratio analysis.
- **LEVEL 6 products**: Flux and luminosity calibrated light-curves in the total (0.3-10 keV) XRT energy bands and in the four sub-energy bands.

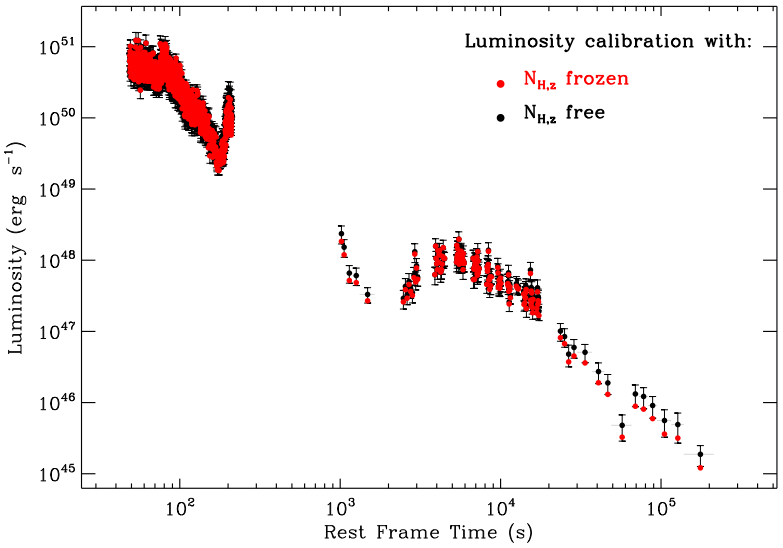

Fig. 2.14: Luminosity light-curve of GRB 081028. Eq. 2.5 has been used.

2.9 *Comparison to the XRT team official light-curve and spectra repository*

The writing of the automatic light-curve and spectra extraction software was begun before the XRT team official repository was available on line. While obviously sharing the basic scheme, the two automatic procedures differs in some way. The reader is referred to [42] and [44] for a detailed description of the production of the official catalogue. The two catalogues are not in competition, since they are both produced by XRT members. The following paragraph outlines both the advantages and drawbacks of my software when compared to the official one. OS stands for the Official Software while MS refers to "my software".

1. The OS uses 8 regions of event extraction to maximize the signal-to-noise, while the MS only uses 3. This produces more refined count light-curve when the count rate is around $10^{-3}\,\mathrm{count\,s^{-1}}$ and is the principal limitation of MS. Figure 2.15 shows the comparison between the two approaches and quantify the statements above. While the OS is more accurate then the MS, the MS is able to produce perfectly reliable curves. This is the major *drawback* of MS: I'm still working to improve the pipeline.

2. The OS combines the ARFs weighting their content according to the proportion of counts in the total source spectrum. The MS weights the ARFs according to their exposure. While the OS approach is the formally correct one (as shown by [44]), the approximate approach of the MS produces

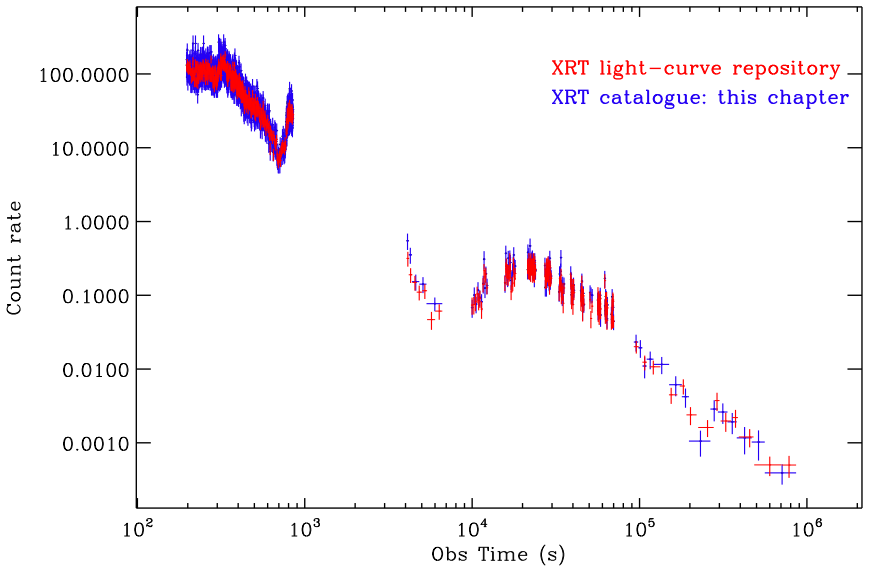

Fig. 2.15: Comparison between the official XRT light-curve of GRB 081028 (from the XRT light-curve repository, [42], [44]) and the count rate light-curve of the present catalogue. A perfect agreement is apparent.

spectral parameters estimates completely consistent with the outputs of the OS. The relative errors of the two procedures are also similar.

3. The spectral fits are always done using the Cash statistics by the OS, while the MS is written to use the χ^2 statistics. Since the MS is designed to fit spectra with 2000 or 1000 photons previously grouped to provide a minimum of 20 counts per bin, the χ^2 approach is completely reliable. When the number of photons in a spectrum is lower than 100, the MS automatically gives an error message. A word of caution: the OS provides best fit parameters obtained using the Cash statistics on very poor spectra, where the number of background counts could be as high as 10%, even if in these conditions the Cash approach cannot be applied, since it assumes that all the photons come from the source of interest.

4. The OS uses a tcl script SHAKEFIT to protect from the possible local minima during a fit. In the MS it is possible to understand if the fit has fallen into a local minimum only if the output shows unusual values of the parameters, where unusual means: unusual when compared to the values obtained for GRBs, but also unusual when compared to the temporal evolution of the spectral parameters of that particular event. The latter approach proved to be a very powerful tool to protect from local minima.

5. In the OS the flux conversion is done using a unique conversion factor and

is therefore not able to account for the spectral evolution of the source. The MS performs a dynamical flux conversion and is able to follow the spectral variations of the emission. This is particularly important during the first stages of the explosion. If the spectral evolution is not properly taken into account, the flux calibration can be wrong of a factor of 2-3, as shown for GRB 081028. This is the major *advantage* of the MS.

2.10 Chapter Acknowledgements

I am particularly grateful to Alberto Moretti who taught me to use the `xrtpipeline` and all the other FTOOLs from scratch; to Francesco Pasotti with whom the project of the automatic light-curve and spectra pipeline was carried out; to Cristiano Guidorzi and Pat Romano for their important suggestions every time we were in troubles with the software; to Guido Chincarini, who "kindly" pushed Francesco and I to conclude the project.

3. ANOMALOUS X-RAY EMISSION IN GRB 060904B: A NICKEL LINE?

3.1 Abstract

The detection of an extra component in GRB 060904B X-ray spectra in addition to the standard single power law behavior has recently been reported in the literature [126]. This component can be fit with different models; the addition of a spectral line provides the best correspondence. I investigate the physical properties that the surrounding medium must have in order to produce a spectral feature that can explain the detected emission. I analyze and discuss how and if the detected spectral excess fits in different theoretical models developed to explain the nature of line emission during the afterglow phase of Gamma Ray Bursts (GRB) sources. Transmission and reflection models have been considered. Given the high ($>> 1$) value of the Thomson optical depth, the emission is likely to arise in a reflection scenario. Within reflection models, the external reflection geometry fails to predict the observed luminosity. On the contrary, the detected feature can be explained in a funnel scenario with typical opening angle $\theta \sim 5$ degrees, nickel mass $\sim 0.1\, M_{\odot}$ and $T = 10^6$ K. For $\theta \sim 20$ degrees, assuming the reprocessing material to be in the SuperNova (SN) shell, the detected emission implies a nickel mass $\sim 0.4\, M_{\odot}$ at $T \sim 10^7$ K and a metallicity ~ 10 times the solar value. If the giant X-ray flare that dominates the early XRT light-curve is identified as the ionizing source, the SN expansion began ~ 3000 s before the GRB event.
These results have been published in Margutti et al., 2008, A&A, 480, 677 (highlight section).

3.2 Introduction

A direct observation of the Gamma-Ray Burst (GRB) central engines is not possible; however, it is possible to infer something about the nature of their progenitors if indirect probes of the physical conditions, structure and composition of the material at the GRB site can be found. X-Ray spectroscopy is such a probe (at least potentially).

The observation of emission features in the X-ray afterglow of Gamma-Ray Burst (GRB) events would be extremely powerful. The emission line radiation is supposed to be produced through reprocessing of the burst radiation: for this reason its luminosity, spectral shape and wavelength shift carry important infor-

GRB	z	Δt (s)	$L_{\rm line}$ (erg s^{-1})	ID	Sig.	Ref.
970508	0.835	$(2-5.6)\times10^4$	6×10^{44}	Fe Kα	2.7σ	[151]
970828	0.958	$(1.2-1.4)\times10^5$	5×10^{44}	FeXXVI Lyα	2.4σ	[207], [208]
921216	1.00	$(1.3-1.5)\times10^5$	8×10^{44}	FeXXVI Lyα	4.7σ	[152]
000214	0.47	$(4-1.5)\times10^4$	4×10^{43}	Fe Kα	3.2σ	[4]
011211	2.14	$(4-6.7)\times10^4$	6.4×10^{44}	Si XIV	...	[19],[161],[162]
			6.2×10^{44}	S XVI	...	
020813	1.254	$(7.6-1.5)\times10^5$	1.1×10^{44}	Si	...	[25]
			1.6×10^{44}	S XVI Lyα	3.3σ	
030227	~ 1.6?	$(7-\geq 8)\times10^4$	6×10^{44}	Si XIV	3.8σ	[200]
			4×10^{44}	S XVI	3.5σ	

Tab. 3.1: Summary of reported emission lines in the literature. Data have been collected from [173] and [20]. The significances reported have been estimated using the $F-$test.

mation not only about the geometry and structure of the surrounding medium but also about the physical conditions at the GRB site and the same GRB energetics. The total power and energy are obviously the main parameters for the construction of any reasonable theoretical model of GRB production: the importance of having an estimate (or even limits) of these parameters is therefore clear. The observation of emission features directly provides strict lower limits on the GRB emitted luminosity; lower limits that are independent of a number of assumptions, such as the density of the surrounding material and the degree of collimation of the burst radiation. The spectroscopical identification of the line emitting elements carries additional information about the burst progenitors: the presence of metal lines for example favours hypernova models ([203], citePaczynski) vs. compact mergers scenarios.

Detections of emission and absorption features in the GRB X-ray afterglows have been claimed in a number of observations (see Table 3.1). However the statistical significance and, hence, the realiability of these detections has been criticized by [173]: a large fraction of the claims are based on using the $F-$test, a statistical method that, when applied to emission features, gives both false positive and false negative (see [156] for details). As a consequence claims of line detection based on this method are not reliable. After a re-analysis of the data based on Monte Carlo simulations, Sako et al. [173] ruled out all of the reported features.

A bright emission feature was detected by [126] in the X-Ray afterglow of GRB 060904B ≈ 200 s (observer time) after the BAT trigger. For the reasons explained above, being aware of the warnings given by [156], [126] adopt entirely the statystical method described in [173] and [169] in order to assess the reality of the line emission: a multitrial significance of 3.2σ was derived. We refer the reader to [126] for details about the stastistical methods used.

Motivated by these data, we decided to perform a comprehensive analysis,

revisiting the various theoretical models developed to explain the claimed line emissions.

This work is organised as follows: in Sec. 3.3 we summarize the results of the [126] analysis: in this Sect. the reader will find all the numerical quantities of the observed parameters involved in the following discussion. The spectroscopic identification of the line emission is discussed in Sec. 3.4 while constraints to the theoretical models are derived in Sec. 3.5 starting from purely geometrical considerations. We discuss the relevant physical quantities in Sec. 3.6: particular attention will be payed to the physical processes responsible of the observed line broadening. We calculate in Sec. 3.7 lower limits to the total energy reservoir of the burst as derived from the observed line energy. Finally, the theoretical models able to account for the detected emission are discussed in Sec. 3.8: a complete derivation is given. Conclusions are drawn in Sec. 3.9

Throughout this chapter standard Λ cosmlogy is used: $\Omega_m = 0.3$, $\Omega_\Lambda = 0.7$, $h_0 = 0.7$.

3.3 Physical data

GRB060904B was detected by the Burst Alert Telescope (BAT) (*Swift* satellite) at 01:03:21 UT. The X Ray Telescope (XRT) began to observe the field 66 s after the BAT trigger. The burst is located at RA $15\,\mathrm{h}\,50\,\mathrm{m}\,58\,\mathrm{s}$, Dec $+44^\circ\,57'\,57''$, corresponding to a Galactic Hydrogen column density of $0.118 \times 10^{22}\mathrm{cm}^{-2}$.

From optical observations ([52]) we know that GRB 060904B lies at z=0.703, with a luminosity distance of 4.16 Gpc. The BAT and XRT light-curve of the prompt and afterglow emission of GRB 060904B is presented in Fig. 3.2, and 3.1.

The continuum emission of GRB 060904B in the 0.3-10 keV band is well fitted by an absorbed simple power law model. The temporal evolution of the photon index is show in Fig. 3.3.

A bright emission feature was detected by Moretti et al. [126] $\approx 200\,\mathrm{s}$ after the BAT trigger (see Fig. 3.4).

After a Monte Carlo analysis of the data, these authors report a multi-trial significance of $\sim 3.2\,\sigma$ (see [126] and references therein for details about the statistical method used). The physical properties of the emission feature are listed in Table 3.2. Such detection differs from previous claims because of the much larger energy involved (about three orders of magnitude higher, see [20], their Table 1 for a complete summary) and because of the time of the line detection: only $\approx 10^2\,\mathrm{s}$ after the BAT trigger. Previous observations (if real) report times as high as $10^4 - 10^5\,\mathrm{s}$ after the burst.

3.4 Spectroscopic identification

The line emission detected in GRB 060904B spectra is centered at $E_\mathrm{o} = 7.85^{+0.16}_{-0.25}\mathrm{keV}$ when a gaussian fit is performed (See Tab. 3.2). We interpret this emission to arise from the 2p-1s transition in Helium-like or Hydrogen-like Nickel (Tab.

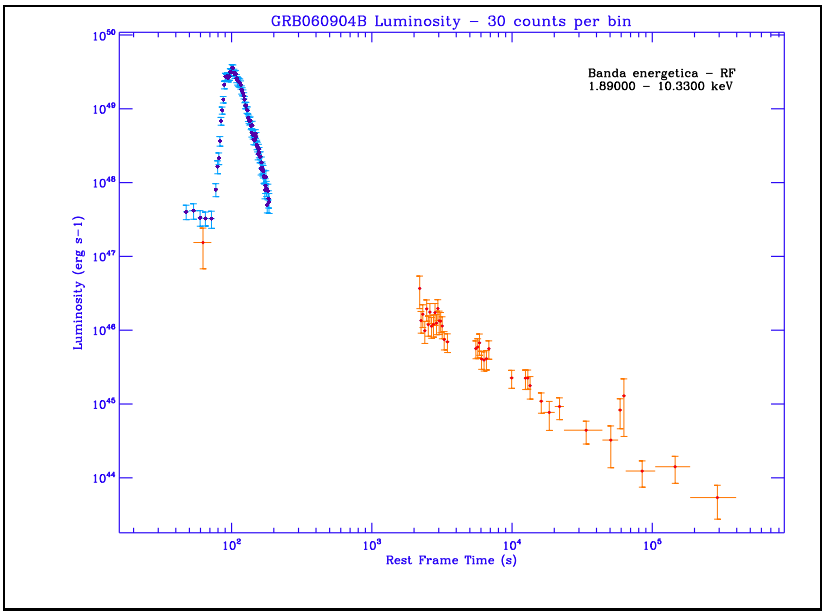

Fig. 3.1: XRT lightcurve of GRB 060904B. It is notable the observational gap between $\sim$ 200 and 2000 s after the trigger.

3.4). A highly ionized environment is therefore required. Parenthetically we note that such a highly ionized medium prevents the line from beeing produced by fluorescence.

Nickel is indeed expected to be present at the GRB location if the burst is accompanied by an (unobserved) SN explosion. An upper limit to the remnant age can be obtained considering that we do observe Nickel emission but we do not detect any Cobalt emission. Figure 3.5 shows the abundances of Nickel, Cobalt and Iron as a function of time since the SN explosion for a 40 $M_\odot$ star: a given Cobalt-Nickel relative abundance would therefore directly translate into a remnant age. If the emitted lines are produced via radiative recombination, then:

$$L_i = \frac{N_i \epsilon_i}{t_{\rm rec}} \tag{3.1}$$

where:

L_i : Line luminosity of a given element i;
ϵ_i : Energy associated with the transition;
$t_{\rm rec}$ Recombination time scale ;

$$\Rightarrow \frac{L_i}{L_j} = \left(\frac{N_i \epsilon_i}{N_j \epsilon_j}\right)\left(\frac{t_{\rm rec,i}}{t_{\rm rec,j}}\right) \tag{3.2}$$

If the physical conditions of emission of Nickel and Cobalt atoms are the same,

Tab. 3.2: Rest frame values of the physical quantities related to the line emission feature detected in GRB 060904B spectra (Moretti et al [126]).

$t^{*}_{\rm obs}$	138 s
Δt^{**}	≥ 47 s
Equivalent Width (EW)	~ 2 keV
Line width(σ_ν)	$0.5^{+0.35}_{-0.17}$ keV
Line centroid(E_0)	$7.85^{+0.16}_{-0.25}$keV
Luminosity ($\rm L_{line}$)	$1.10 \pm 0.18 \times 10^{47}$erg sec^{-1}

* First detection of the emission.

** Duration of the line emission. This is a lower limit on the real value of the parameter because of the presence of a gap of observations lasting $\sim$ 2000 s. See Fig. 3.1. Hence we can write: 138 s $< \Delta$t $<$ 2000 s.

*** Gaussian fit (1σ).

	Ni	Co	Fe
Neutral	7.478	6.930	6.404
He-like	7.806	7.242	6.701
H-like	8.102	7.526	6.973

Tab. 3.3: Centroid energies for kα emission lines arising from Nickel (Ni), Cobalt (Co) and Iron (Fe) in different ionization states. keV units are used.

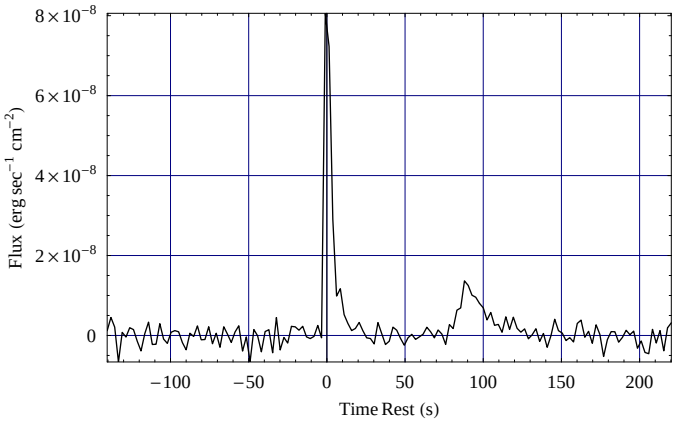

Fig. 3.2: BAT lightcurve of GRB 060904B

then from Eq. 3.2:

$$\frac{N_i}{N_j} = \frac{L_i}{L_j}\frac{\epsilon_i}{\epsilon_j} \tag{3.3}$$

$$\Rightarrow \frac{N_{\rm Co}}{N_{\rm Ni}} = \frac{L_{\rm Co}}{L_{\rm Ni}}\frac{\epsilon_{\rm Co}}{\epsilon_{\rm Ni}} \tag{3.4}$$

An upper limit to the luminosity of the (undetected) Cobalt emission lines can be derived calculating the luminosity of a simulated gaussian line with a width $\approx$ 0.5 keV (see Tab. 3.2) and a normalization corresponding to 3σ from the underlying continuum. In this case the Cobalt lines would be present but the high level of the underlying continuum prevented us from detecting such emission. The simulated line luminosities (upper limits to the real Cobalt emission) are shown in Fig. 3.6. We derive:

$$N_{\rm Co} \leq 1 \times N_{\rm Ni} \tag{3.5}$$

The upper limit to the remnant age is therefore $\approx$ 6 days. Assuming $v \approx 10^5\,{\rm Km\,s^{-1}}$ as the typical expansion velocity of the SN shell (see for example [143]), we derive the maximum distance travelled by the SN shell: $R_{\rm max} \approx 10^{15}$ cm.

3.5 Geometrical constraints

The detection of an emission feature in the afterglow spectra of GRB 060904B only $\sim$ 200 s after the BAT trigger, poses strong constraints on the possible location of the line-emitting material.

From purely geometrical considerations we have that the emitting material must be located within a distance R given by:

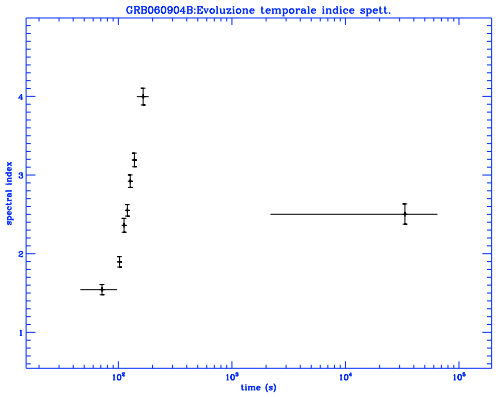

Fig. 3.3: Temporal evolution of the photon index with time (rest frame value).A single absorbed power law model (SPL) has been used.

$$R \leq \frac{c\, t_{\rm obs}}{1 - cos(\theta)} \simeq 4 \times 10^{12} \frac{t_{\rm obs}}{138\ {\rm s}} \frac{1}{1 - cos(\theta)}\ {\rm cm} \tag{3.6}$$

where:

- θ : angle between the line-emitting material and the line of sight at the GRB site;
- $t_{\rm obs}$: delay between the arrival of GRB and line photons (rest frame value).

We parenthetically note that for a time delay completely geometrical in origin, the strict equality would apply. It's notable that $R \geq 10^{16}$ requires $\theta \leq 1°$.

The implications of relation 3.6 will be explored under three different hypothesis:

a) No a-priori assumption about the delay between the GRB event and the SN explosion;
b) Contemporary GRB/SN explosion;
c) Delayed SN explosion.

Case A– If the line-emission originates from material ejected by an SN explosion, then from the non-detection of the Cobalto emission in the spectra of GRB 060904B we derive $t_{\rm remnant} \leq 6$ days (Sec. 3.4). Taking $v_{\rm remnant} \approx 10^9\,{\rm cm\,s^{-1}}$ as typical expansion velocity of the SN shell in the first days (see eg. [143]), we therefore find: $R_{\rm max} \approx 10^{15}$ cm, an order of magnitude inferior to the distances required by the distant reprocessor models [1] (see eg. [20]).

[1] During a SN explosion the phase subsequent to the time of shock emerge is roughly homologous, so that we can take the radius R of the expanding shell to be ([5]): $R \approx R_0 +$

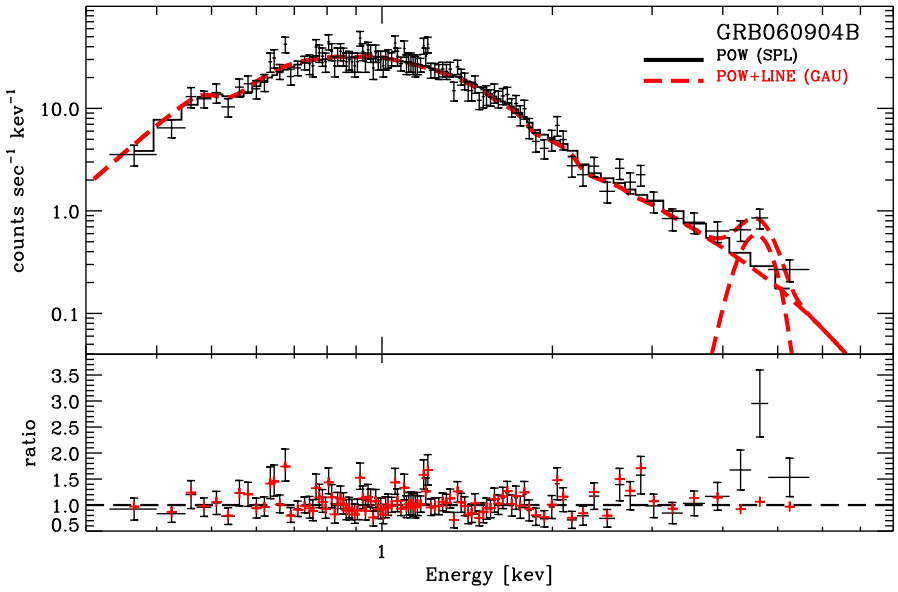

Fig. 3.4: Upper panel: GRB 060904B spectrum observed in the rest frame time interval $138 - 185$ s. Solid black line: best fit absorbed simple power-law model (SPL): photon index $\Gamma = 3.55^{+0.08}_{-0.08}$; neutral absorber column density at the source redshift $N_{\rm H,z} = (0.69^{+0.04}_{-0.04}) \times 10^{22}\,{\rm cm}^{-2}$. Dashed coloured line: best fit absorbed power-law plus gaussian model (GAU): $\Gamma = 3.67^{+0.10}_{-0.09}$; $N_{\rm H,z} = (0.74^{+0.05}_{-0.05}) \times 10^{22}\,{\rm cm}^{-2}$; the values of the parameters related to the gaussian component are reported in Tab. 3.2. The Galactic hydrogen column density $N_{\rm H,MW}$ has been fixed to the value reported in [36] along the GRB direction ([126]). Lower panel: ratio between the observed values and the model predicted values.

Case B– The maximum distance travelled by the SN shell material is $R_{\rm max} \approx 10^{11}$ cm, comparable to the radius of Wolf-Rayet stars, potential progenitors of GRB events. In this case, there is no value of the parameter θ able to link this distance to the measured time delay $t_{\rm obs}$ if this delay is purely geometrical. In this scenario the time delay can be therefore only partially due to geometrical reasons:

$$\Rightarrow t_{\rm obs} = t^{\rm G} + t^{\rm NG} \tag{3.7}$$

where:

$t^{\rm G}$: purely geometrical contribution;
$t^{\rm NG}$: not geometrical contribution.

$v_{\rm a} \times t$, where:

R_0 : Initial shell radius, comparable to the radius of the progenitor;
$v_{\rm a}$: Asymptotic fluid velocity $\approx 10^9$ cm s^{-1}.

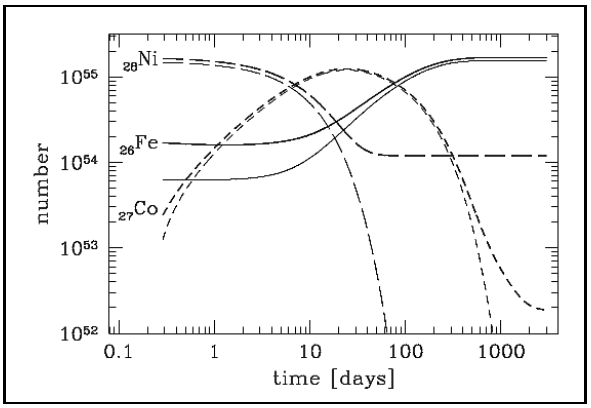

Fig. 3.5: Abundances of Nickel, cobalt and iron as a function of time since the SN explosion for a $40M_\odot$ star as modeled by [204]. Thik line: sum over all isotopes; thin line: A=56 isotope of each. (From [109])

If the time-scale of the emission process is negligible, then the photons responsible of the material excitation and of the subsequent line emission must be emitted $\sim 100\,\mathrm{s}$ after the beginning of the GRB event. Another possibility is that t^{NG} is dominated by the physics of the emission mechanism. In this case:

$$t^{\mathrm{NG}} \approx t^{\mathrm{mec}} \tag{3.8}$$

where the symbol t^{mec} stands for the time-scale of the emission process. In the case of the ionization/recombination process, we can express t^{mec} as the longer between the recombination and the ionization time-scales. The first is given by:

$$t_{\mathrm{rec}} = \frac{1}{\alpha_{\mathrm{r}}(Z,T)\, n_{\mathrm{e}}} \tag{3.9}$$

where:

$\alpha_{\mathrm{r}}(Z,T)$:	recombination coefficient;
n_{e} :	electron number density;
T :	electronic temperature.

In the temperature range from 3 K to 10^{10} K, α_{r} is well fitted by the formula ([195]):

$$\alpha_{\mathrm{r}} = a[(T/T_0)^{1/2}(1+(T/T_0)^{1/2})^{1-b}(1+(T/T_1)^{1/2})^{1+b}]^{-1} \tag{3.10}$$

where a, b, T_0 and T_1 are the fitting parameters. Table 3.4 shows the best fit values of these parameters for H-like and He-like Nickel.

The ionization time-scale is roughly given by:

$$t_{\mathrm{ion}} = \frac{4\pi R^2 \varepsilon_{\mathrm{ion}}}{L_{\mathrm{ion}} \sigma_{\mathrm{Ni}}} \tag{3.11}$$

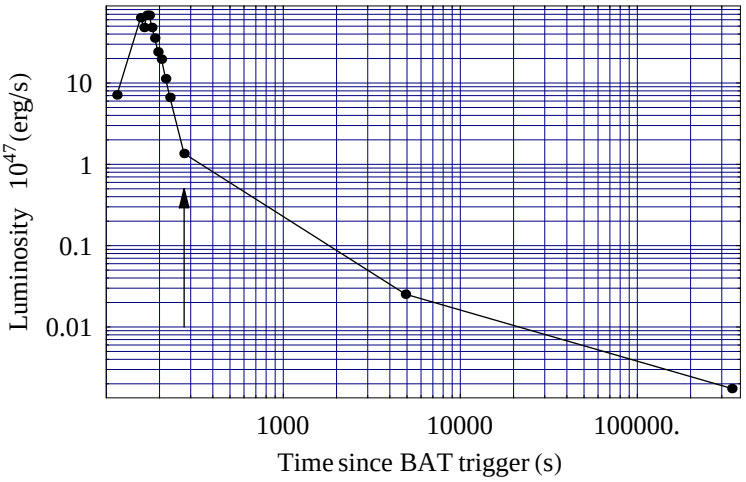

Fig. 3.6: Simulated Co line luminosity as a function of time (upper limits to the real undetected Cobalt emission) for GRB 060904B. A 7.2 keV He-like Co emission is assumed. The arrow indicates the time at which we detect the Nickel emission.

	a ($cm^3\ s^{-1}$)	b	T_0 (K)	T_1 (K)
Ni XXVII	1.676×10^{-9}	0.6861	3530	4.538×10^{8}
Ni XXVIII	3.002×10^{-9}	0.7581	1467	5.409×10^{8}

Tab. 3.4: Fit parameters of relation 3.10 for H-like Nickel (Ni XXVIII) and He-like Nickel (Ni XXVII). From [195]

where:

- R : Distance between the ionizing photon source and the line emitting material;
- $\varepsilon_{\rm ion}$: Typical energy of the ionizing photons. For numerical computation we assume $\varepsilon \sim \xi$ photoionization threshold energy of the atomic species involved. For H-like and He-like Nickel atoms $\xi \sim 10$ keV ([194]);
- $L_{\rm ion}$ Luminosity of the ionizing continuum. An upper limit to $t_{\rm ion}$ will be derived assuming $L_{\rm ion} \sim L_{\rm line}$, the luminosity of the observed line emission;
- $\sigma_{\rm Ni}$ Photoionization cross section of the atomic species involved, at the energy $\epsilon_{\rm ion}$. For H-like and He-like Nickel atoms: $\sigma(10\ {\rm keV}) \approx 10^{-20}\ {\rm cm}^{-2}$ (Fig. 3.8).

Combining Eq. 3.9 with Eq. 3.11 we derive:

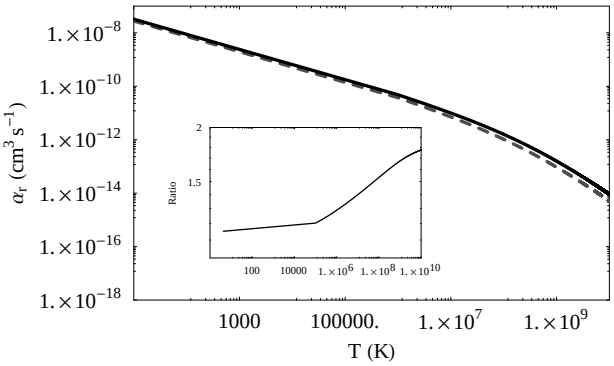

Fig. 3.7: Solid line: H-like Nickel radiative recombination rate coefficient; Dashed line: He-like Nickel radiative recombination rate coefficient. Insert: ratio between H-like and He-like Nickel radiative recombination rate coefficients.

$$\frac{t_{\rm ion}}{t_{\rm rec}} = \frac{\alpha_{\rm r}(Z,T) n_{\rm e} 4\pi R^2 \epsilon_{\rm ion}}{L_{\rm ion}\sigma_{\rm Ni}} \tag{3.12}$$

with:

$$n_{\rm e} = \frac{M}{V}\frac{1}{\mu_{\rm e} m_{\rm p}} \tag{3.13}$$

where:

- M : Total mass of the SN shell;
- V : Volume of the shell ($V \cong 4\pi R^2 \Delta R$);
- ΔR : Thickness of the shell;
- m_p Proton mass;
- μ_e Numerical coefficient linked to the chemical composition of the material. $\mu_e = 1.0\,, 1.2\,, 2.0$ for pure hydrogen, solar composition and no hydrogen, respectively.

$$\Rightarrow \frac{t_{\rm ion}}{t_{\rm rec}} = \frac{\alpha_{\rm r}(Z,T) M \epsilon_{\rm ion}}{\Delta R \mu_{\rm e} m_{\rm p} L_{\rm ion}\sigma_{\rm Ni}} \tag{3.14}$$

Figure 3.9 offers a graphic view of the previous relation: it is clear that $t_{\rm ion} \ll t_{\rm rec}$ for $T \geq 10^4$ K and for reasonable values of the other parameters involved: $1 \leq M/M_\odot \leq 40$ and $\Delta R \sim 10^{11}$ cm. We therefore conclude:

$$\Rightarrow t^{\rm mec} \approx \max(t_{\rm ion}, t_{\rm rec}) = t_{\rm rec} \tag{3.15}$$

Case C– From our observations we know that the maximum delay between the SN explosion and the GRB event is ~ 138s. As before:

$$t_{\rm obs} = t^{\rm G} + t^{\rm NG} \approx 138 \text{ s} \tag{3.16}$$

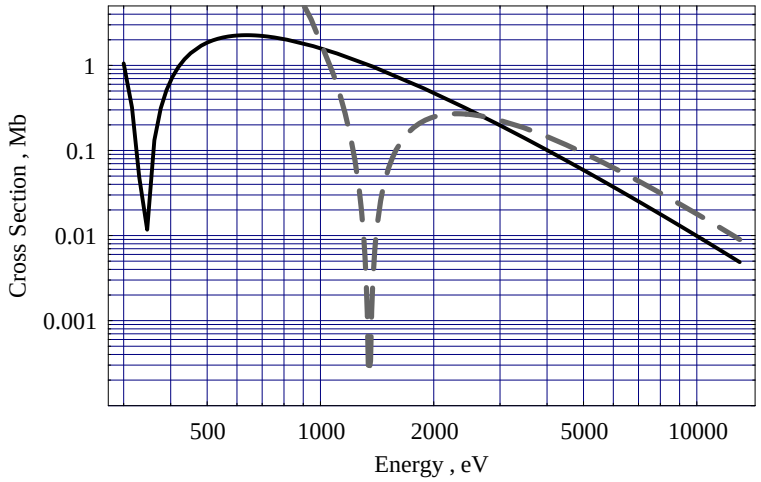

Fig. 3.8: Photoionization cross section as a function of the energy from [194] fit. Black solid line: Ni XXVIII (H-like); grey dashed line: Ni XXVII (He-like).

If $t^{\rm G} \ll t^{\rm NG}$, (a reasonable assumption, given the small distances that could be travelled by the shell material):

$$\Rightarrow t^{\rm NG} = t_{\rm ion} + t_{\rm rec} + \Delta t_{\rm GRB-SN} \approx 138 \text{ s} \tag{3.17}$$

where $\Delta t_{\rm GRB-SN}$ is the time delay between the two events. Beeing $t_{\rm ion} \ll t_{\rm rec}$ for $T \geq 10^4$ K (3.9) and for reasonable values of the other parameters involved we derive:

$$t_{\rm rec} + \Delta t_{\rm GRB-SN} \approx 138 \text{ s} \tag{3.18}$$

Obviously enough, the previous relation also implies:

$$t_{\rm rec} \leq 138 \text{ s} \Rightarrow n_{\rm e} \geq \frac{1}{138\,\alpha_{\rm r}(Z,T)} \text{ cm}^{-3} \tag{3.19}$$

This condition will be studied in detail in the following section.

In each of the three cases studied in this section, we can therefore exclude that the line emission originates in a distant reprocessor scenario ([20]), where the delay between the first arrival of GRB photons and the arrival of line photons is dominated by light travel time differences and distances are $\sim 10^{16}$ cm. This is not a surprising result: the observation of a line emission $\sim 10^2$ s (rest frame value) after the burst requires the line-emitting material to be within $\sim c\,t$ fro the burst site. For GRB 060904B :

$$c\,t \sim 10^{12} \text{ cm} \ll 10^{16} \text{ cm} \tag{3.20}$$

Moreover, we must also consider that if R is the SN shell radius, than the Nickel enriched material extends out only to a fraction of this distance [5]:

$$\frac{R_{\rm Ni}}{R} \approx 0.65 \tag{3.21}$$

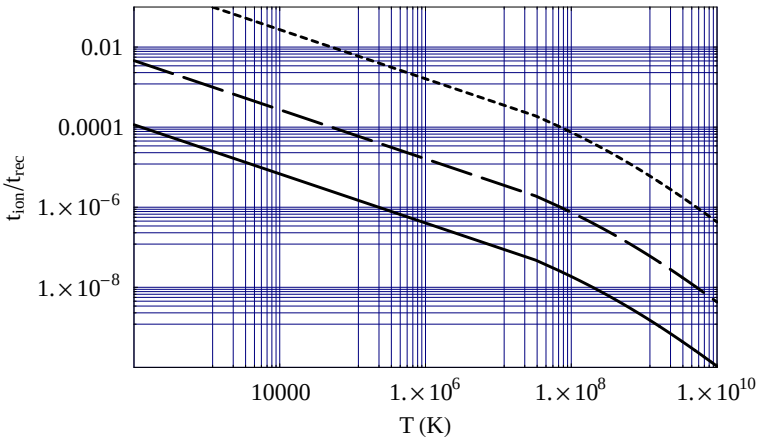

Fig. 3.9: Ionization to radiative recombination time scales as a function of the electron temperature for different values of the mass and thickness of the SN shell of material. Solid line: $M = 1\,M_\odot, \Delta R = 10^{11}$ cm; long-dashed line: $M = 40\,M_\odot, \Delta R = 10^{11}$ cm; short-dashed line: $M = 40\,M_\odot, \Delta R = 10^{9}$ cm. Solar composition ($\mu = 1.2$) is assumed.

3.6 Physical parameters and processes

3.6.1 Radiative recombination time-scale: the electron temperature and density parameter space

The emission feature detected in GRB 060904B is characterized by a luminosity of $L_{\rm line} = 1.1 \times 10^{47}$ erg s^{-1} (Tab. 3.2), implying an emission rate of Nickel line photons ($\dot{N}$) of:

$$\dot{N} = \frac{L_{\rm line}}{\epsilon_{\rm Ni}} \approx 10^{55}\ {\rm s}^{-1} \tag{3.22}$$

where $\epsilon_{\rm Ni}$ is the energy of the single line photons (7.8 and 8.1 keV for H-like and He-like Nickel atoms respectively).

Assuming the radiative recombination of H-like and He-like Nickel atoms to be the leading physical mechanism of the line emission, the line luminosity is given by:

$$L_{\rm line} = \frac{N_{\rm Ni}\,\epsilon_{\rm Ni}}{t^{\rm mec}} = \frac{N_{\rm Ni}\,\epsilon_{\rm Ni}}{\max(t_{\rm rec}, t_{\rm ion})} = \frac{N_{\rm Ni}\,\epsilon_{\rm Ni}}{t_{\rm rec}} = N_{\rm Ni}\,\epsilon_{\rm Ni}\,\alpha_{\rm r}(Z,T)\,n_{\rm e} \tag{3.23}$$

with:

$N_{\rm Ni}$: Number of emitting Nickel atoms.

$t_{\rm rec} > t_{\rm ion}$ (see Fig. 3.9) and Eq. 3.9 have been used.
The mass of pure Nickel involved in the emission process is therefore (see Fig. 3.10):

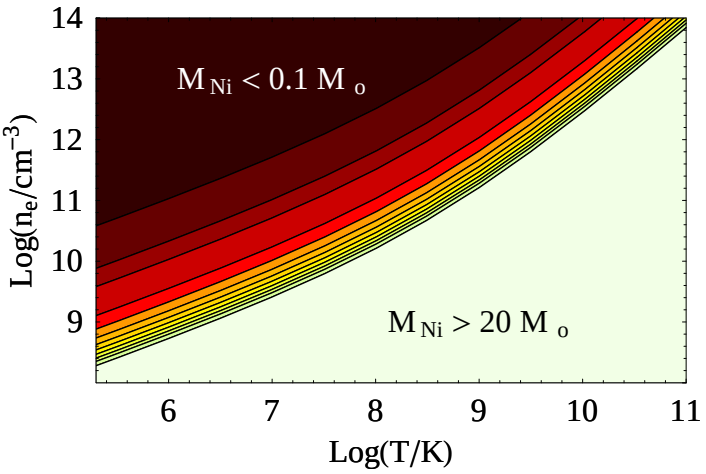

Fig. 3.10: Nickel mass according to relation 3.24. From the black to the white region, the solid lines mark $M_{\rm Ni} = 0.1, 0.5, 1, 3, 5, 7, 9, 11, 13, 15, 17, 20$ $\rm M_\odot$ GRB 060904B data have been used.

$$M_{\rm Ni} = 59\, m_{\rm p}\, N_{\rm Ni} = 59\, m_{\rm p}\, \frac{L_{\rm line}}{\epsilon_{\rm Ni}}\, t_{\rm rec} \tag{3.24}$$

where $m_{\rm p}$ is the proton mass.
An upper limit to this parameter can be derived in two different ways: first we consider that the recombination time cannot be longer than the time at which we first detect the Nickel emission, if GRB photons are supposed to be responsible of the material photoionization:

$$t_{\rm rec} \leq t_{\rm obs} \tag{3.25}$$

$$\Rightarrow M_{\rm Ni} \leq 59\, m_{\rm p}\, \frac{L_{\rm line}}{\epsilon_{\rm Ni}}\, t_{\rm obs} \tag{3.26}$$

Second, if we do observe the line emission for Δt (rest frame value), then using Eq. 3.22, the number of line photons emitted is $\sim \dot{N} \times \Delta t$. The maximum amount of Nickel mass is required when each Nickel atom emits only one photon; in other words, when each Nickel atom recombines only once in Δt:

$$\Rightarrow M_{\rm Ni} \leq 59\, m_{\rm p}\, \dot{N}\, \Delta t \tag{3.27}$$

Combining Eq. 3.26 with Eq. 3.27 we finally derive:

$$M_{\rm Ni} \leq 59\, m_{\rm p} \times \min\left[\frac{L_{\rm line}}{\epsilon_{\rm Ni}}\, t_{\rm obs}\,,\; \dot{N}\, \Delta t\right] \tag{3.28}$$

For GRB 060904B the previous relation implies:

$$M_{\rm Ni} < 20\ \rm M_\odot \tag{3.29}$$

Nickel masses as large as $\approx 20\,M_{\odot}$ are difficult to account for in any reasonable physical scenario. We therefore conclude that each Nickel atom recombines more than once in the observed Δt. For GRB 060904B this means: $t_{\rm rec} \leq 47$ s. Consequently models similar to our Case B with $t^{\rm NG} \sim t_{\rm rec}$ can be excluded for this event. Eq. 3.25 can be re-written as:

$$t_{\rm rec} \leq \min(t_{\rm obs}, \Delta t) \tag{3.30}$$

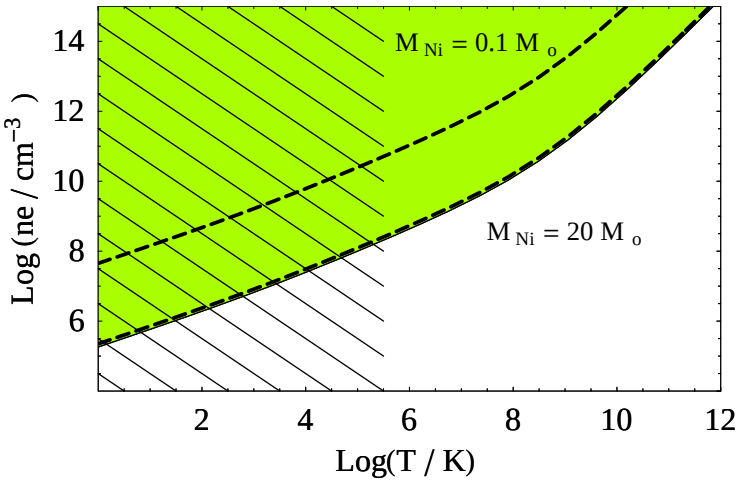

Fig. 3.11: Coloured area: electron number density-temperature parameter space according to relation 3.30 for GRB 060904B. The dashed lines mark the $0.1\,{\rm M}_{\odot} < M_{\rm Ni} < 20\,{\rm M}_{\odot}$ region. The shaded area represents the $T \leq 3.2 \times 10^5$ K region. The electron temperature is likely to be higher than this value at this stage of the SN explosion ([5]).

Using Eq. 3.9, Eq. 3.30 also translates into the condition:

$$n_{\rm e} \geq \frac{1}{\min(t_{\rm obs}\,,\,\Delta t)\alpha_{\rm r}(Z,T)} \tag{3.31}$$

The allowed parameter space for GRB 060904B is shown in Fig. 3.11.

A condition similar to Eq. 3.31 can be derived considering that if each Nickel atom produces K line photons, the required Nickel mass is:

$$M_{\rm Ni} = 59\,m_{\rm p}\frac{\dot{N}\,\Delta t}{K} \tag{3.32}$$

where $\Delta t \geq 47$ s for GRB 060904B (see Tab. 3.2).

$$\Rightarrow M_{\rm Ni} \geq \frac{22.4}{K}\ {\rm M}_{\odot} \tag{3.33}$$

Tab. 3.5: Nickel masses required by well studied hypernovae explosions associated with GRB events.

GRB	SN	$M_{\rm Ni}\,(\mathrm{M}_\odot)$
980425	1998 bw	0.4*
030329	2003 dh	0.4*
031203	2003 lw	0.6*
060218	2006 aj	0.2**

* [130]

** Nomoto, "Swift:unveiling the relativistic universe", Venice 2006.

If $M_{\rm Ni}$ is comparable to the Nickel masses implied by the well studied hypernovae explosions associated with GRB events (Tab. 3.5) we derive:

$$K \geq 45 \tag{3.34}$$

where $M_{\rm Ni} \approx 0.5 M_\odot$ has been used. This condition implies a limit on the recombination time, that cannot be longer than $\sim \Delta t/K$. For GRB 060904B:

$$t_{\rm rec} \leq 1\,\mathrm{s} \tag{3.35}$$

$$\Rightarrow n_{\rm e} \geq \frac{1}{\alpha_{\rm r}(Z,T)} \tag{3.36}$$

The electron temperature-number density parameter space is shown in Fig 3.12.

3.6.2 Thompson Optical Depth

The Thompson otpical depth of the SN shell is given by:

$$\tau_{\rm T} = \int n_{\rm e}\sigma_{\rm T} dx \approx n_{\rm e}\sigma_{\rm T}\Delta R \tag{3.37}$$

with:

$$n_{\rm e} = \frac{\rho}{\mu_{\rm e} m_{\rm p}} \tag{3.38}$$

where:

- $\sigma_{\rm T}$: Thompson cross section ($\approx 0.6 \times 10^{-24}\,\mathrm{cm}^{-2}$);
- ρ : Density of the matter;
- ΔR : Shell thickness;
- $\mu_{\rm e}$: Numerical coefficient linked to the chemical composition of the material.

$$\Rightarrow \tau_{\rm T} = \frac{1}{\mu_{\rm e} m_{\rm p}} \frac{\sigma_{\rm T}}{4\pi R^2} \Big(\frac{M_{\rm Ni}}{X}\Big) \tag{3.39}$$

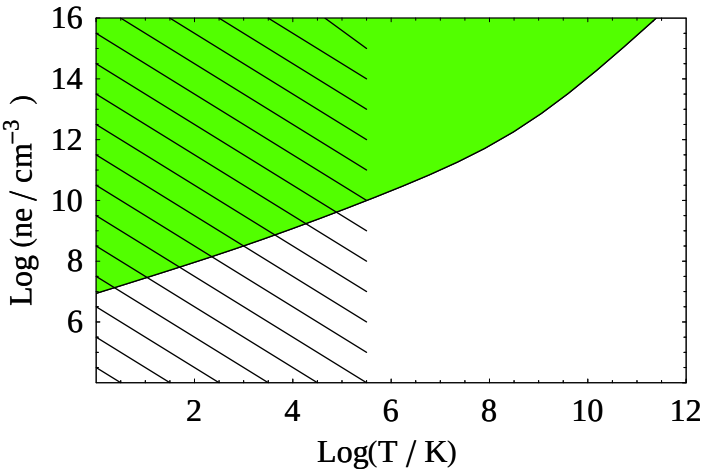

Fig. 3.12: Coloured area: electron number density-temperature parameter space according to relation 3.36 for GRB 060904B. In this case a total Nickel mass of $0.5\,M_\odot$ is assumed: the coloured area allows for the situation in which only a part of this mass effectively contributes to the observed emission. The shaded area represents the $T \leq 3.2 \times 10^5$ K region. The electron temperature is likely to be higher than this value at this stage of the SN explosion ([5]).

with:

$$X = \frac{M_{\rm Ni}}{M} \tag{3.40}$$

ratio between the Nickel mass and the total mass of the shell.
The geometrical constraints calculated in Sec. 3.5 have important implications on the scattering optical depth. In particular, according to relation 3.6, we derive:

$$\tau_{\rm T} \geq \frac{1}{\mu_{\rm e} m_{\rm p}} \frac{\sigma_{\rm T}}{4\pi} \Big(\frac{M_{\rm Ni}}{X}\Big) \Big(\frac{2}{c\, t_{\rm obs}}\Big)^2 \tag{3.41}$$

$R \sim 10^{12}$ cm has been used. Inserting $t_{\rm obs} \approx 138$ s for GRB 060904B, it is easy to show that $\tau_{\rm T} \gg 1$ for any reasonable choice of the parameters involved. The complete situation is shown in Fig.3.13.

The photoionization optical depth of H-like or He-like Nickel atoms is instead given by:

$$\tau_{\rm Ni} = \xi\, n_{\rm Ni} \sigma_{\rm Ni} \Delta R = \xi\, n_{\rm Ni} \sigma_{\rm Ni} \Big(\frac{\tau_{\rm T}}{n_{\rm e} \sigma_{\rm T}}\Big) \tag{3.42}$$

where:

- $n_{\rm Ni}$: Nickel number density;
- $\sigma_{\rm Ni}$: Nickel cross section ($\approx 10^{-20}\,{\rm cm}^{-2}$, see Fig. 3.8);
- ξ : Nickel abundance ratio (ionized to total).

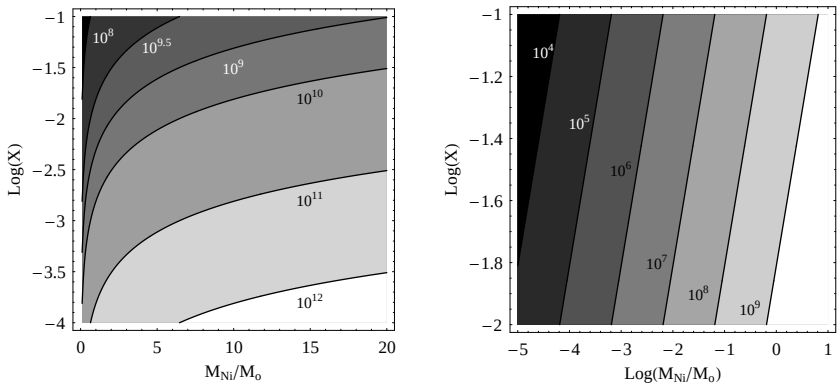

Fig. 3.13: Thompson optical depth contour plot in the Nickel mass-abundance parameter space according to Eq 3.41.

The subscript "Ni" stands for H-like or He-like Nickel.
Considering that:

$$\frac{n_{\rm Ni}}{n_{\rm e}} = \frac{X\mu_e}{59} \tag{3.43}$$

equation 3.42 transforms into:

$$\tau_{\rm Ni} = \frac{\xi\,\sigma_{\rm Ni}}{\sigma_{\rm T}}\frac{X\mu_{\rm e}}{59}\,\tau_{\rm T} \tag{3.44}$$

and for equation 3.41:

$$\tau_{\rm Ni} \geq \frac{\xi\sigma_{\rm Ni}M_{\rm Ni}}{59\pi\,m_{\rm p}(ct_{\rm obs})^2} \tag{3.45}$$

Results are shown in Fig. 3.14: $\tau_{\rm Ni} \geq 1$ is obtained for reasonable values of $M_{\rm Ni}$ and ξ.

While an efficient use of the H-like or the He-like Nickel ions requires $\tau_{\rm Ni} \geq 1$, a Thompson optical depth larger than one is a problem: if photons diffuse through a plasma cloud in which Thomson scattering is the predominant mechanism and if the cloud has a central photon source, then the average number of scatterings experienced by a photon will be $1/2\,\tau_{\rm T}^2$ (see for example [188]). With $\tau_{\rm T} \gg 1$, the line would be smeared in the continuum and no detection would be possible. We must therefore require the line photons not to have crossed such regions during their ways to us. This in turn implies that the electron clouds are not isotropically distributed around the GRB location, in order to allow the line photons to "freely" escape.

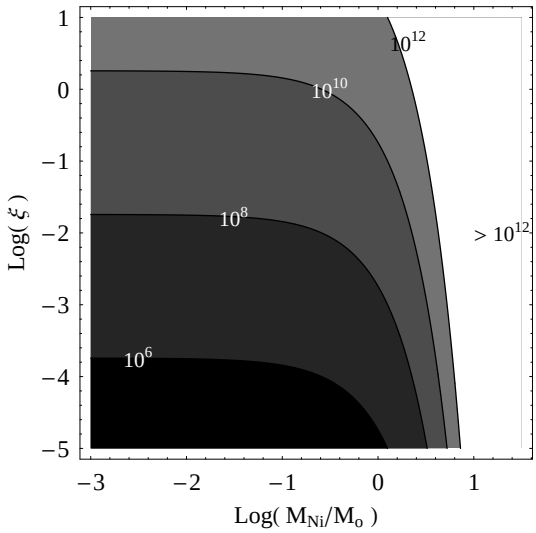

Fig. 3.14: Photoionization optical depth contour plot according to Eq 3.45.

3.6.3 Line width

For H-like Ni ions the Ly-α line has a radiative width [153]:

$$\gamma \approx \gamma_{\rm H} Z^4 \approx \text{ eV} \tag{3.46}$$

where $\gamma_{\rm H}$ is the Ly-α radiative width for Hydrogen atoms and Z is the number of electrons of the ion. The natural width is therefore much smaller than the observed value ($\approx$ 0.5 keV, see Table 3.2). In this paragraph we analyze and discuss the different physical processes that could lead to the observed line broadening.

Pure Thermal broadening

If the line profile results from the thermal motion of the emitting atoms and the distribution of speeds towards and away from an observer is given by the Maxwell distribution:

$$P(v)dv = \Big(\frac{m}{2\pi kT}\Big)^{1/2} \exp\Big(-\frac{mv^2}{2kT}\Big)dv \tag{3.47}$$

then the line profile is given by a normal distribution:

$$P(\lambda)d\lambda = \Big(\frac{mc^2}{2\pi kT\lambda_0^2}\Big)^{1/2} \exp\Big(-\frac{mc^2(\lambda-\lambda_0)^2}{2kT\lambda_0^2}\Big)d\lambda \tag{3.48}$$

with standard deviation:

$$\sigma_\lambda = \lambda_0 \Big(\frac{kT}{mc^2}\Big)^{1/2} \tag{3.49}$$

where:

k : Boltzmann constant;
T : Temperature of the emitting particle;
m : Mass of the emitting particle;
λ_0 : Centroid of the distribution.

For non-relativistic thermal velocities, the Doppler shift in frequency is expressed by:

$$\frac{v}{c} = \frac{\nu_0 - \nu}{\nu} \tag{3.50}$$

For $|\nu_0 - \nu| \ll 1$ we can make the approximations:

$$\frac{v}{c} \approx \frac{\nu_0 - \nu}{\nu_0} \tag{3.51}$$

$$\frac{dv}{c} \approx -\frac{\nu_0}{\nu^2}\, d\nu \tag{3.52}$$

The Doppler profile will now be a normal distribution in frequency with standard deviation:

$$\sigma_\nu = \nu_0 \Big(\frac{kT}{mc^2}\Big)^{1/2} \tag{3.53}$$

For GRB 060904B:

$$\begin{aligned} \sigma_\nu &= 0.5\,\mathrm{keV} \\ m &= 59 m_\mathrm{p} \\ \nu_0 &\approx 1.9 \times 10^{18}\ \mathrm{Hz} \end{aligned}$$

This would imply a temperature $T \approx 10^{12}$ K. This temperature would cause the recombination efficiency to drop, the time scale of the emission process becoming excessively long. Condition 3.25 would be in this case satisfied only for $n_\mathrm{e} \geq 10^{15}\,\mathrm{cm}^{-3}$. In particular $t_\mathrm{rec} < 47\,\mathrm{s}$ (see 3.6.1) for $n_\mathrm{e} \geq 3 \times 10^{15}\,\mathrm{cm}^{-3}$. For these reasons we exclude the broadening to be entirely thermal in origin.

Doppler broadening due to electron scattering and resonance broadening

The photon scattering by free electrons contribute to the broadening and distortion of the spectrum : when hot electrons scatter radiation the line profile will be Doppler-broadened and on average will shift toward higher frequencies. In particular, in high temperature gas the first scattering by an electron will produce an average frequency broadening given by [188]:

$$\frac{\Delta\nu}{\nu} \approx \Big(\frac{2KT}{mc^2}\Big)^{1/2} \tag{3.54}$$

where the symbol m stands for the electron mass.
For GRB 060904B we have: $\frac{\Delta\nu}{\nu} \approx 0.06$. In this case the line width could be explained by a single Compton scattering if the electron temperature is $\sim 10^7$ K. As a consequence, from Eq. 3.25 we derive $n_\mathrm{e} \geq 10^{10}$ cm^{-3}.

The doppler broadening resulting from electron scattering is more efficient by a factor of $(M_{\rm ion}/m_{\rm e})^{1/2} \approx 320$ than that due to resonance scattering ([153]). Moreover, the first scattering by an electron produces a Doppler width given by Eq. 3.54, sufficient to remove the resonance lines from resonance. For these reasons we don't consider the resonance scattering a physical process that efficiently contributes to the observed line broadening.

Multiple Scattering Broadening

Line photons can undergo numerous scatterings by free electrons before reaching the observer. As a result the line profile will change. In particular photons will naturally differ in the number of times they are scattered; this thing as well as the dispersion in the frequency shift when a photon is scattered (scattering processes are supposed to be not completely elastic), will give rise to complicated line profiles. For the limiting cases $kT_{\rm e} = 0$ and $kT_{\rm e} \gg h\nu_0$ with a large Thomson-scattering depth $\tau_{\rm T} \gg 1$ Syunyaev and Titarchuk ([188]) provide analytic expressions for the multiple scattering broadening.

The first cause of line broadening is the dispersion in the time of photon to escape from the scattering cloud; in other words the dispersion in the number of scatterings they underwent. In the case of a spherical cloud with the source in the center the convolution of the solution of the Kompaneets equation with the distribution of the photons over their time of escape from the cloud ([188]) gives:

$$\Delta\lambda_1 \approx \lambda_{\rm c}\, N_{\rm sc} \tag{3.55}$$

where $\lambda_{\rm c}$ is the Compton length:

$$\lambda_{\rm c} = \frac{h}{m_{\rm e}c} \tag{3.56}$$

The wavelenght shift in each scattering process is the second cause of the line broadening and leads to:

$$\Delta\lambda_2 \approx \lambda_{\rm c}\, N_{\rm sc}^{1/2} \tag{3.57}$$

With $N_{\rm sc} \gg 1$:

$$\Delta\lambda_1 \gg \Delta\lambda_2 \tag{3.58}$$

The thermal Doppler broadening becomes the third cause of the line broadening for scattering on electrons with the finite temperature $kT_{\rm e} > 0$ leading to a $\Delta\lambda_3$. From Sec. 3.6.3 we have:

$$\Delta\lambda_3 = \lambda_0 \left(\frac{kT_{\rm e}}{m_{\rm e}c^2}\right)^{1/2} \tag{3.59}$$

When the number of scatterings is large the line broadens as:

$$\frac{\Delta\lambda_4}{\lambda_0} = \frac{\Delta\nu}{\nu_0} \approx \left(\frac{2N_{\rm sc}\, kT_{\rm e}}{m_{\rm e}c^2}\right)^{1/2} \tag{3.60}$$

where $N_{\rm sc}$ stands for the number of scatterings suffered by a line photon. The Doppler broadening may be neglected as compared to $\Delta\lambda_2$ when ([154]):

$$kT_{\rm e} < \frac{(h\,\nu_0)^2}{2m_{\rm e}c^2} \tag{3.61}$$

If the previous condition is satisfied (cold plasma), then the broadening of the line would be $\approx \Delta\lambda_1 + \Delta\lambda_2$. For the $\approx$ 8 keV Nickel emission Eq. 3.61 translates into: $T_{\rm e} \ll 7 \times 10^5$ K. In this scenario, the observed GRB 060904B line broadening requires $N_{\rm sc} \approx 3 - 4$. However, the temperature constraint is difficult to account for at this very early stage of the SN explosion (see the previous section). We cannot therefore neglect the Doppler contribution. Before analyzing the thermal contribution is worth noting that the $N_{\rm sc}$ value just derived is an upper limit to the real number of scattering processes underwent by a photon.

Eq. 3.60 (multiple scattering doppler contribution) for GRB 060904B translates into:

$$\left(\frac{2N_{\rm sc}\,kT_{\rm e}}{m_{\rm e}c^2}\right)^{1/2} \approx 0.06 \tag{3.62}$$

The $N_{\rm sc} - T_{\rm e}$ relation obtained in this way is shown in Fig. 3.15.

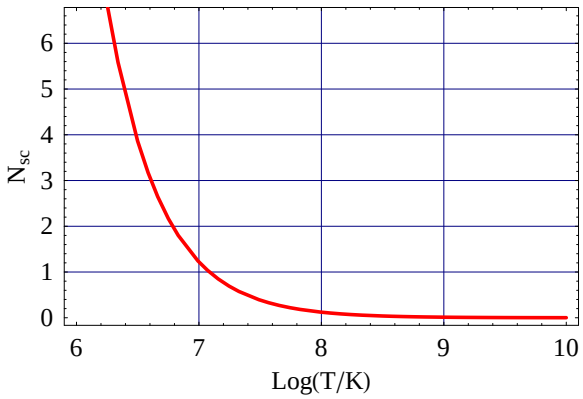

Fig. 3.15: Number of scatterings undergone by a line photon for GRB 060904B according to Eq. 3.62 as a function of the electron temperature.

The real situation is complex: the line profile results from Doppler broadening, thermal broadening, wavelength shift of the single photons each time they undergo a scattering process and dispersion of the number of scatterings underwent by the different photons. However we can get a rough estimate of the electron temperature as follows (assuming that the observed broadening comes from the multiple scattering process): the limited number of scatterings ($\approx 3 - 4$) required to explain the observed line broadening in absence of the thermal Doppler broadening, implicitly suggests that the real number of scattering processes suffered by each photon is not far from that value and that the

thermal contribution is not required to play a major role. From Fig. 3.16 it is clear that $T_e \preceq 10^7\,\mathrm{K}$. If the thermal Doppler broadening contributes $\approx 1/2$ to the observed value, then we get $T_e \approx 1 - 3 \times 10^6\,\mathrm{K}$. In general we can conclude that according to this scenario, the electron temperature is likely to be $\approx 10^6 - 10^7\,\mathrm{K}$.

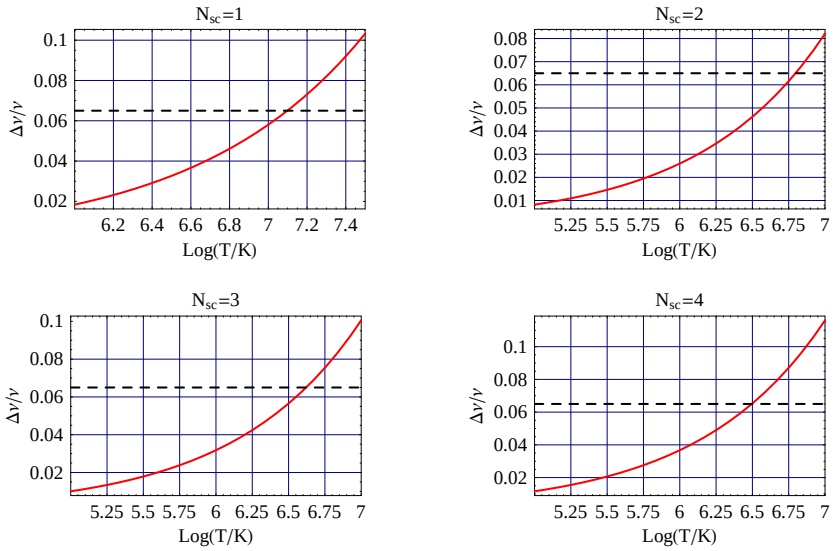

Fig. 3.16: Solid line: thermal Doppler broadening calculated according to Eq. 3.62 as a function of the electron temperature. $N_{sc} = 1$, $N_{sc} = 2$, $N_{sc} = 3$ and $N_{sc} = 4$ have been assumed. Dashed line: observed value.

Consequently, from the constraint on the recombination time we derived in Sec. 3.6.1, $n_e \succeq 10^8\,\mathrm{cm}^{-3}$ (see Fig. 3.17). If we require the line emitting material to be $M_{Ni} \sim 0.5\,M_\odot$ then $n_e \approx 10^9 - 10^{10}\,\mathrm{cm}^{-3}$. However it is important to underline that the Nickel mass we are speaking about is the *line emitting* mass different from the total Nickel mass. In particular geometries the line emitting material will be a small part of the total mass. As a consequence, much higher electron densities or temperatures are required in order to reproduce the observed emission (in other words, really small recombination times).

We parenthetically note that the number of scatterings a photon undergoes depends strongly on the geometry of emission assumed. In particular, for a funnel geometry McLaughlin et al., 2002 [109] showed that the average number of scatterings a photon will have on the way out of the cone if the photon does not wander into the wall and only stays on the surface, there is no absorption and the funnel, of opening angle θ_j, is infinite is:

$$\bar{N} = \frac{1 + \cos(\theta_j)}{1 - \cos(\theta_j)} \tag{3.63}$$

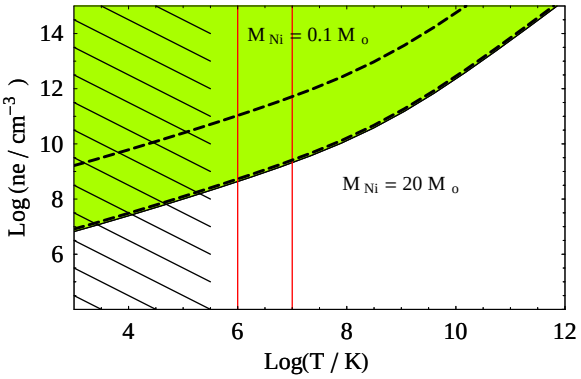

Fig. 3.17: Coloured area: electron number density-temperature parameter space for $t_{\rm rec} \leq 138$. The shaded area represents the $T \leq 3.2 \times 10^5$ K region. The electron temperature is likely to be higher than this value at this stage of the SN explosion ([5]). The red solid lines mark the 10^6 and 10^7 K regions.

(The number of scatterings for small angles is quite large. However reducing the cone height but keeping the rest of the semplifications this number is highly reduced).

Collisional broadening

The collisional line broadening is actually negligible for low-density environments, for which the coronal approximation would apply. The coronal approximation requires a steady-state low-density plasma where in absence of an external ionizing radiation source, collisional ionizations are balanced by radiative and dielectronic recombinations (while photoionization is negligible). In particular, the steady-state assumption implies that there is statistical equilibrium, the particles have Maxwellian energy distribution and that the ions and electrons have the same temperature. This condition can be fullfilled at the time we observe the line emission only if the electron-ion collision time $t_{\rm ei}$ is significantly shorter than $t_{\rm obs}$ (and also shorter than the cooling time of the plasma) [191]:

$$t_{\rm ei} \approx 10^5 T^{3/2} n_{\rm e}^{-1} \tag{3.64}$$

The electron number density-temperature parameter space calculated using Eq. 3.64 together with the condition $t_{\rm ei} \leq t_{\rm obs}/100$ is shown in Fig. 3.18. From this figure it is clear that the ion and electron temperature are likely to be different at the time of the emission; no collisional equilibrium has been reached yet.

From Eq. 3.31 electron number densities as high as $\sim 10^{16}\,{\rm cm}^{-3}$ are possible. Although these densities are rather high compared to those in stellar coronae, the effects are relatively small, because of the high temperature ($T \approx 10^{12}\,{\rm K}$)[191]. Consequently the low-density approximation can be used also in this case; the collisional contribution to the line broadening is therefore negligible under the conditions at hand.

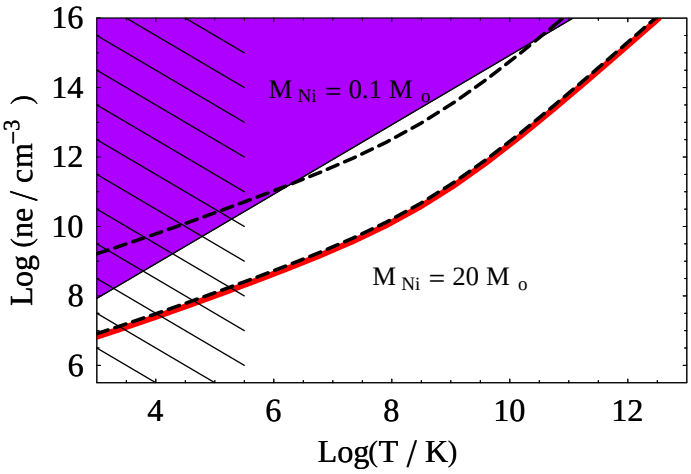

Fig. 3.18: Coloured area: electron number density-temperature parameter space calculated using Eq. 3.64 together with the condition $t_{\rm ei} \leq t_{\rm obs}/100$. The solid red line separates the $t_{\rm rec} < \Delta t$ region (upper panel, allwed region) from the $t_{\rm rec} < \Delta t$ region (lower panel) according to Eq. 3.31. The dashed lines mark the $0.1\,{\rm M}_\odot < M_{\rm Ni} < 20\,{\rm M}_\odot$ The shaded area represents the $T \leq 3.2\times10^5$ K. The electron temperature is likely to be higher than this value at this stage of the SN explosion [5].

Expanding Supernova Shell

In this paragraph we consider the possibility of a kinematical line broadening. In particular, in the framework of an expandig SN shell, the broadening of the line would be caused by the same expansion of the shell. From Table 3.2 the observed line width is $\sim 0.5\,{\rm keV}$ (rest frame value). In the non-relativistic limit this value would correspond to an expansion velocity of

$$v_{\rm Shell} = c\,\frac{\Delta\lambda}{\lambda_0} \approx 25\,000\ {\rm Km\,s^{-1}} \tag{3.65}$$

In the relativistic limit the expansion velocity is linked to the line width by:

$$\frac{\Delta\lambda}{\lambda_0} = \left(\frac{1-\beta}{1+\beta}\right)^{1/2} - 1 \tag{3.66}$$

where:

λ_0 : Line centroid (rest frame value);
$\Delta\lambda$: Line width (rest frame value);
β : v/c.

In the relativistic limit the GRB 060904B line emission implies: $v_{\rm Shell} \approx 24\,000\,{\rm Km\,s^{-1}}$.

Note that: first, the expansion velocities have been calculated under the assumption that we see a large fraction of the remnant ($\theta = 90°$, see Fig. (to

insert)). Consequently they provide lower limits to the real expansion velocities for the $\theta < 90^\circ$ models. Second, if the line profile is symmetrical then we must conclude that blue-shifted and red-shifted line photons have reached us. Consequently, in the framework of an expanding SN shell this means that some of the detected line photons result from the emission of material located in the back of the expanding shell. On the contrary if the line profile is asymmetrical, then only blu-shifted or red-shifted photons have reached the observer. In the former scenario (blu-shifted photons only) the line photons have been produced in the front side of the remnant while something prevented the back side photons from reaching the observer or being detected (for example, with $\tau_{\rm T} \gg 1$ the line photons would be smeared in the continuum. See Sec.3.6.2). The latter situation (red-shifted photons only) requires the photons to have been emitted by material in the back side of the remnant, the front side beeing previously evacuated by the burst itself. Unfortunately the quality of the present data does not permit a detailed anlysis of the the line profile. However in both cases we must require the line of sight to the burst location to be evacuated of matter in order to have a small Thompson opacity (see Sec. 3.6.2) and to permit the existence of the observed long-lasting afterglows ($\approx 5 \times 10^5$ s for GRB 060904B).

Expansion velocities of $\approx$ 25 000 Km s^{-1} are therefore required if the line broadening is totally kinematic in origin. Such velocities are indeed observed during the first stages of SNe and associated GRB HNe explosions, as shown in Fig. 3.19.

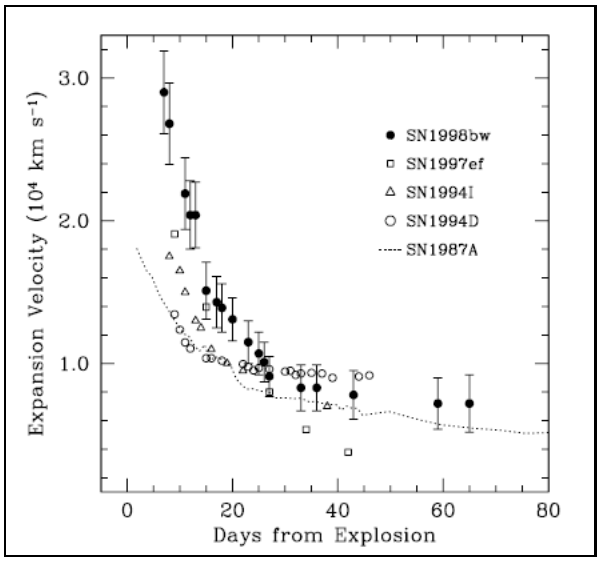

Fig. 3.19: Si II λ6355 expansion velocity of SN 1998bw compared with SN 1994D, SN 1994I and SN 1997ef. For comparison the photospheric expansion velocities deduced from the H absorption minima of SN 1987A are also plotted. (From [143]).

3.7 Line Energetics

3.7.1 Line collimation

The luminosity of the line detected in GRB 060904B spectra and reported in Table 3.2 has been calculated assuming an isotropic line emission. However, even for isotropically produced photons, it is possible that geometrical or physical factors produce an effective collimation of the emission. The result is the amplification of the observed flux by the factor $4\pi/\Omega_{\rm line}$ with respect to the isotropic emission. Conversely, the line luminosity reported would be an overestimate to the "real" luminosity $L_{\rm real}$:

$$L_{\rm real} = \frac{\Omega_{\rm line}}{4\pi} L_{\rm line} \tag{3.67}$$

In this paragraph we quantify the possibility of a line photo collimation. Particular attention will be payed to the collimation of photons produced by geometrical factors, in reference to a funnel geometry.

Ghisellini et al. 2002 [58] showed that for a funnel of height R and opening angle θ_j after $N_{\rm sc}$ scatterings, the total number of photons emitted in the direction of the observer will be enhanced by a factor:

$$F(\theta) = \Sigma[1 - P_{\rm lost}(\theta)]^{N_{\rm sc}} \tag{3.68}$$

$$\Rightarrow \lim_{N_{sc}\to\infty} F(\theta) = \frac{1}{P_{\rm lost}(\theta)} \tag{3.69}$$

with:

$$\begin{cases} P_{\rm lost} = 0.5 + P_{\rm esc}(\theta) & \text{(for electron scattering)} \\ P_{\rm lost} = P_{\rm esc}(\theta) & \text{(for a resonant line)} \end{cases} \tag{3.70}$$

where:

$P_{\rm lost}(\theta)$: Total probability for a photon to be lost ;
$P_{\rm esc}(\theta)$: Total probability for a photon to exit the funnel.

For a photon scattered at a distance Rz ($0 \leq z \leq 1$) from the funnel opening the total probability to exit the funnel is ([58]):

$$P_{\rm esc}(\theta) = \int_0^1 (1-z) P_{\rm esc}(z,\theta)\, dz \tag{3.71}$$

beeing:

$$P_{\rm esc}(z,\theta) = \frac{1 - \cos[\mathrm{atan}(\sin\theta/z)]}{2} \tag{3.72}$$

It is assumed that the funnel walls radiate and scatter the line uniformly; that half of the photons will be scattered deeper into the funnel walls than towards the observer; that resonant photons scattered in this direction are rescattered by ions and redirected towards the open space.

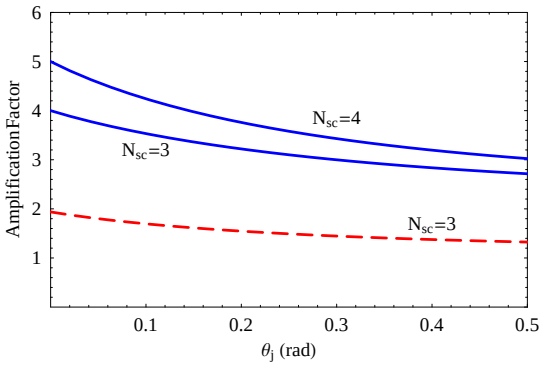

Fig. 3.20: Line luminosity amplification factor as a function of the funnel opening angle θ_j (funnel geometry assumed). Red solid lines: result of Eq. 3.68 for a resonant line for $N_{\rm sc} = 3$ (lower line) and $N_{\rm sc} = 4$ (upper line). Blue dashed line: result of Eq. 3.68 for electron scattering. Only the 3 scattering amplification is shown, beeing very similar to the 4 one (and to the infinite one).

Figure 3.20 shows the results of Eq. 3.68 for electron scattering and for a resonant line. $N_{\rm sc} = 3$ and $N_{\rm sc} = 4$ have been used (see Sec. 3.6.3). While for a resonant line a factor of amplification of ~ 5 can be achieved for really small funnel opening angles, if electron scattering is important (as it is in our case: $\tau_T \gg 1$, from Sec. 3.6.2), the amplification of the line can be at most a factor of two. If this is the case then we are overestimating the real line luminosity by the same factor:

$$\Rightarrow (0.6 \leq L_{\rm real} \leq 1.1) \times 10^{47}\,{\rm erg\,s^{-1}} \tag{3.73}$$

3.7.2 Line Efficiency

A strict lower limit to the ionizing continuum energy comes from the line luminosity itself. For GRB 060904B we do observe a line emission for ≈ 47 s. Consequently the illuminating continuum must satisfy the condition:

$$E_{\rm ill} \geq L_{\rm line} \times \Delta t \tag{3.74}$$

or, considering the possibility of the line photon collimation discussed above:

$$E_{\rm ill} \geq L_{\rm real} \times \Delta t \tag{3.75}$$

where:

- $E_{\rm ill}$: Energy of the illuminating continuum;
- $L_{\rm line}$: Luminosity associated with the line emission under the assumption of isotropical emission;
- $L_{\rm real}$: Luminosity associated with the line emission corrected for the possible line photon collimation (see Sec. 3.7.1).

$$\Rightarrow E_{\rm ill} \geq 3 \times 10^{48}\,{\rm erg} \tag{3.76}$$

For the total energy $E_{\rm ion}^{\rm tot}$ of the illuminating and (ionizing) continuum the condition is therefore:

$$E_{\rm ill}^{\rm tot} \geq 2 \times E_{\rm ill} \approx 10^{49}\,{\rm erg} \tag{3.77}$$

where the factor 2 in the previous equation corresponds to consider two-sided jets with the line emitting material visible on only one side. It is important to underline that Eq. 3.77 provides a lower limit to the energy of the ionizing continuum first because it is unlikely for the efficiency of the line emission to be close to 1 (see the rest of the paragraph); second because we detect a line emission for 47 s but the duration of the line emission is likely to be greater than this value (remember for GRB 060904B the observational gap between ~ 200 and ~ 2000 s).

If $L_{\rm ill}$ is the luminosity of the continuum that illuminates the line emitting material, then the efficiency $\eta_{\rm line}$ in producing the line can be defined as:

$$\eta_{\rm line} = \frac{E_{\rm line}}{E_{\rm ill}} = \frac{L_{\rm line}}{L_{\rm ill}} \frac{\Delta t_{\rm line}}{\Delta t_{\rm ill}} \tag{3.78}$$

where:

$\Delta t_{\rm line}$: Duration of the line emission;
$\Delta t_{\rm ill}$: Duration of the line emitting material illumination.

Taking $\Delta t_{\rm line} \sim \Delta t_{\rm ill}$ for GRB 060904B from Eq. 3.78 we have:

$$L_{\rm ill} \sim \frac{L_{\rm line}}{\eta_{\rm line}} \tag{3.79}$$

The really high optical depths calculated in Sec. 3.6.2 favour models in which the line originates in reflection and practically exclude the possibility of the transmission mechanism (see Sec.3.8 for a detailed discusssion). For this reason, in the following, we will concentrate on the efficiency in the production of line photons by the reflection mechanism. In this models the line emission efficiency can be estimated as the ratio of the energy in the photons absorbed by the line emitting atoms in the layer of the material with $\tau_{\rm Ni} \sim 1$ (see Sec. 3.6.2) to the total energy of the continuum photons (considering that the energy of the line photon is lower than that of the photoionizing one)[98]:

$$\eta_{\rm line} \sim \frac{h\nu_{\rm line} \int_{\nu_0}^{\nu_{max}} \frac{L(\nu)}{h\nu} \left(\frac{\nu}{\nu_0}\right)^{-3} d\nu}{\int_{\nu_{\rm min}}^{\nu_{\rm max}} L(\nu) d\nu} \tag{3.80}$$

Figure 3.21 shows the line production efficiency for $h\nu_{\rm line} \approx 8$ keV He-like or H-like Nickel emission for a power law continuum spectrum as a function of the spectral index. It is notable that the reprocessing efficiency for Nickel is $\approx 5\%$ at most.

The plotted results are upper limits to the real efficiencies (the ionization parameter and the effects of Auger autoionization are neglected). We refer to

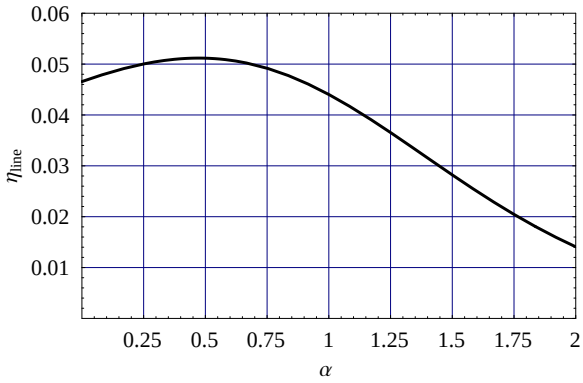

Fig. 3.21: Reprocesing efficiency for H-like or He-like NIckel emission as a function of the spectral index α according to Eq.3.80. $h\nu_0 = 10\,\mathrm{keV}$, $h\nu_{\rm min} = 1\,\mathrm{keV}$ and $h\nu_{\rm max} = 50\,\mathrm{keV}$ have been used.

[58] and [99] for a complete numerical treatment. However, [98] found that the approximate analytical calculus returns results within a factor of two when compared to the complete numerical one. Consequently we consider $\eta_{\rm line} \approx 1\%$ a good estimate of the Nickel reprocessing efficiency. We parenthetically note that the line efficiency calculated above doesn't account for geometrical factors. For GRB 060904B we therefore obtain:

$$L_{\rm ill} \approx 6 \times 10^{48}\,\mathrm{erg\ s^{-1}} \tag{3.81}$$

The previous relation has been calculated considering the line luminosity corrected for collimation to be $\approx 0.6 \times 10^{47}\,\mathrm{erg\ s^{-1}}$ (see Sec. 3.7.1).

$$\Rightarrow L_{\rm ill}^{\rm tot} \approx 10^{49}\,\mathrm{erg\ s^{-1}} \tag{3.82}$$

A factor of 2 has been applied for the two-sided jets geometry.

$$E_{\rm ill}^{\rm tot} = L_{\rm ill}^{\rm tot} \Delta t_{\rm ill} \sim L_{\rm ill}^{\rm tot} \Delta t \tag{3.83}$$

where:

- $\Delta t_{\rm ill}$: Interval of time during which the reprocessing material has been illuminated by the ionizing photons;
- Δt : Interval of time during which we observe the line emission ($\sim 47\,\mathrm{s}$).

$$\Rightarrow E_{\rm ill}^{\rm tot} \approx 5 \times 10^{50}\,\mathrm{erg\,s^{-1}} \tag{3.84}$$

If instead there is no collimation, then we obtain:

$$E_{\rm ill}^{\rm tot} \approx 10^{51}\,\mathrm{erg\,s^{-1}} \tag{3.85}$$

3.7.3 Limits on the total GRB energy

The emission line energy provides us with a powerful tool that can be used to derive lower limits to the total enegy radiated by the burst and to the total energy reservoir of the fireball. The energy radiated in $\gamma-$rays E_γ is linked to the two sided isotropic line emission by:

$$E_\gamma \geq 2\frac{E_{\rm line}}{\eta_x \eta_{\rm line}} \tag{3.86}$$

where:

$E_{\rm line} = L_{\rm line}\Delta t$	Isotropic energy contained in the observed line emission;
$\eta_{\rm line}$	Reprocessing efficiency;
$\eta_{\rm x}$	Fraction of the burst spectrum in the $X-$ray band;

The factor 2 considers the two-sided jet emission.
The previous relation trasforms into:

$$E_\gamma \geq 2\frac{E_{\rm line}}{\eta_x \eta_{\rm line}}\frac{\Omega_{\rm line}}{4\pi} \tag{3.87}$$

if we allow for the possibility of line photons collimation. From the previous section we know $\eta_{\rm line} \approx 1\%$; the bolometric correction $\eta_{\rm x}$ can be estimated using a Band [7] spectrum with typical values of the parameters: this yields $\eta_{\rm x} \approx 0.1$. Finally, the line collimation factor has been estimated in Sec. 3.7.1: we found $\Omega_{\rm line}/4\pi \approx 1/2$ for $\theta \leq 5^\circ$.

Indicating with the symbol η_γ the efficiency of converting the kinetic energy into $\gamma-$rays, the total energy reservoir in the form of kinetic energy of the fireball is given by:

$$E = \frac{E_\gamma}{\eta_\gamma} \tag{3.88}$$

The value of the parameter η_γ is very uncertain: in the conventional internal+exernal shock GRB model $\eta_\gamma \approx 1\% - 5\%$ ([212]); however, allowing for an extremely inhomgeneous velocity of the ejecta shell $\eta_\gamma \approx 40\%$ (see [89], [90]); A more recent study by Zhang et al. 2007 [216] derive for 32 GRB detected by *Swift* with early X-ray afterglow data, $\eta_\gamma < 10\%$ at the end of the shallow decay phase; and $\eta_\gamma > 90\%$ at the deceleration time of the fireball (We refer to [216] for more details). It is worth noting that the derivation of η_γ sensitively depends on many physical parameters of the burst itself and its environment.

Now, if we compute the total radiated energy from Eq. 3.87, using $E_{\rm line} = L_{\rm line}\Delta t \approx 5 \times 10^{48}$ erg, we obtain:

$$E_\gamma \geq 10^{52}\Big(\frac{\Omega_{\rm line}}{4\pi}\Big)\Big(\frac{0.1}{\eta_{\rm x}}\Big)\Big(\frac{0.01}{\eta_{\rm line}}\Big)\,{\rm erg} \tag{3.89}$$

The isotropic energy emitted in photons is therefore $\approx 10^{52}$ erg.

The total energy reservoir in the form of kinetic energy of the fireball can be estimated using Eq. 3.88:

$$E \geq 10^{53}\Big(\frac{\Omega_{\rm line}}{4\pi}\Big)\Big(\frac{0.1}{\eta_{\rm x}}\Big)\Big(\frac{0.01}{\eta_{\rm line}}\Big)\Big(\frac{0.1}{\eta_\gamma}\Big)\,{\rm erg} \tag{3.90}$$

3.7.4 Independent $E_\gamma^{\rm iso}$ estimate

For GRB 060904B no peak energy has been detected. However it is possible to estimate this parameter starting from the $15-150$ keV power-law photon index. [215] show that:

$$\mathrm{Log(E_p)} = (2.76 \pm 0.07) - (3.61 \pm 0.26)\mathrm{Log}(\Gamma) \tag{3.91}$$

with:

$E_{\rm p}$: Peak energy in keV ;
Γ : $15-150$ keV photon index.

[113] (*http* : *//www.mpe.mpg.de/tilde jcg/grb*060904.*html*) report $\Gamma = 1.70 \pm 0.14$. Inserting this value in Eq. 3.91, this relation gives $E_{\rm p} \approx 85$ keV. Taking cosmological corrections into account it is now possible to estimate the value of the intrinsic peak energy $E_{\rm p,i}$. We derive $E_{\rm p,i} \approx 145$ keV ($z = 0.703$ has been used). Finally, using the revised Amati06 relation ([2]):

$$\left(\frac{E_{\rm p,i}}{\rm keV}\right) = 95^{+11}_{-9} \left(\frac{E_\gamma^{\rm iso}}{10^{52}\,\rm erg}\right)^{0.49^{+0.06}_{-0.05}} \tag{3.92}$$

$$\Rightarrow E_\gamma^{\rm iso} \approx 2 \times 10^{52}\,\rm erg \tag{3.93}$$

This is the order of magnitude of the isotropic energy radiated by GRB 060904B. It is worth noting that this estimate agrees with the previous one (Eq. 3.89). Using Eq. 3.84 we derive for GRB 060904B:

$$\frac{E_{\rm ill}^{\rm tot}}{E_{\rm iso}} \approx 0.01 \tag{3.94}$$

The line emission detected in GRB 060904B therefore requires a fraction of the order of $\approx 1\%$ of the isotropic energy of the burst to have illuminated the line emitting material.

3.7.5 The ionizing source, the ionization factor ξ and the metallicity of the SN ejecta

The emission feature detected in GRB 060904B spectra is characterised by a large $EW = 2$ keV. For a line production efficiency of $\sim 1\%$,(see [99]) we expect an underlying 1-10 keV continuum luminosity $L_{1-10\,\rm keV} \geq 100\,L_{\rm line}$ if this is to be identified with the ionizing source. From the *Swift* XRT light curve we derive $L_{1-10\,\rm keV} = 4 \times 10^{48} \rm erg\,s^{-1}$ at $t \sim 160$ s, time at which we detect the emission feature. The *detected* underlying continuum is therefore *not* physically linked to the line emission.

The $1-10$ keV rest frame luminosity as a function of time from the GRB onset is reported in Table 3.6. This table shows that the detected luminosity is actually higher than $100 L_{\rm line} \sim 10^{49}\,\rm erg\,s^{-1}$ in the time interval $100-130$ s. Assuming that the continuum illuminating the reprocessing material is similar

	Δt (s)	Γ	$L_{1-10\,\mathrm{keV}}$ ($\mathrm{erg\,s^{-1}}$)	$R^2 n$ $\xi = 10^4$ ($\mathrm{cm^{-1}}$)
1	$46 - 97$	$1.61^{+0.11}_{-0.11}$	$8^{+0.4}_{-0.5} \times 10^{48}$	$8^{+0.4}_{-0.5} \times 10^{44}$
2	$97 - 107$	$1.93^{+0.11}_{-0.10}$	$4^{+0.2}_{-0.2} \times 10^{49}$	$4^{+0.2}_{-0.2} \times 10^{45}$
3	$107 - 117$	$2.36^{+0.15}_{-0.14}$	$3^{+0.2}_{-0.2} \times 10^{49}$	$3^{+0.2}_{-0.2} \times 10^{45}$
4	$117 - 123$	$2.56^{+0.12}_{-0.11}$	$2^{+0.1}_{-0.1} \times 10^{49}$	$2^{+0.1}_{-0.1} \times 10^{45}$
5	$123 - 131$	$2.81^{+0.12}_{-0.12}$	$2^{+0.1}_{-0.1} \times 10^{49}$	$2^{+0.1}_{-0.1} \times 10^{45}$
6	$131 - 145$	$3.15^{+0.15}_{-0.14}$	$1^{+0.1}_{-0.1} \times 10^{49}$	$1^{+0.1}_{-0.1} \times 10^{45}$
7	$145 - 185$	$3.75^{+0.19}_{-0.17}$	$4^{+0.2}_{-0.2} \times 10^{48}$	$4^{+0.2}_{-0.2} \times 10^{44}$
8	$185 - 64600$	$2.22^{+0.15}_{-0.14}$	$2^{+0.2}_{-0.3} \times 10^{45}$	$2^{+0.2}_{-0.3} \times 10^{41}$

Tab. 3.6: Rest frame isotropic $1 - 10\,\mathrm{keV}$ luminosity of GRB 060904B as a function of time from the GRB event. The XRT data have been splitted into different intervals of time, so that a minimum number of ≈ 2000 photons is containd in each spectrum. A SPL model has been assumed. Δt: interval of time; Γ: photon index (90% CI are listed); R: scale distance; n:particle density; ξ:ionization factor. For the interval of time containing the emission feature (point 7) only the SPL contribution has been reported.

to the observed radiation, it is therefore possible to explain the detected emission feature requiring the ionizing emission to be isotropic and the reprocessing material to have a large covering factor. In this scenario the time delay between the arrival of direct continuum photons and the observation of the claimed line emission Δt_{D} is explained in terms of light travel time effects. We assume that the ionizing photons are produced at $t \sim 100\,\mathrm{s}$ or at a travelled distance of $R \sim 3 \times 10^{12}\,\mathrm{cm}$. At this distance they interact with the SN material (see Fig. 3.22). An estimate of the funnel opening angle θ is therefore given by:

$$(R + R_{\mathrm{p}})\,\theta \sim c\Delta t_D \tag{3.95}$$

where R_{p} is the progenitor radius. With $\Delta t_{\mathrm{D}} \sim 40\,\mathrm{s}$, the previous relation translates into $\theta \sim 22^\circ$, 17° and 5° for $R_{\mathrm{p}} = 10^{11}, 10^{12}$ and $10^{13}\,\mathrm{cm}$. Moreover, assuming a typical expansion velocity $v_{\mathrm{shell}} \sim 10^9\,\mathrm{cm\,s^{-1}}$, we have:

$$v_{\mathrm{shell}}(t + t_{\mathrm{SN}}) \sim ct \tag{3.96}$$

where the symbol t_{SN} stands for the time delay between the GRB and the beginning of the SN expansion: for $t_{\mathrm{SN}} > 0$ the SN event happened before the GRB explosion. For $t \sim 100\,\mathrm{s}$ the previous relation implies $t_{\mathrm{SN}} \sim 3000\,\mathrm{s}$.

In this work we considered an efficiency of production of line photons by the reflection mechanism of the order of 1%. However, we know that the line production effciency is a strong function of the ionization parameter ([99]) ξ here defined as:

$$\xi = \frac{4\pi D_{\mathrm{L}}^2 F_{[1-10]}}{R^2 n} \tag{3.97}$$

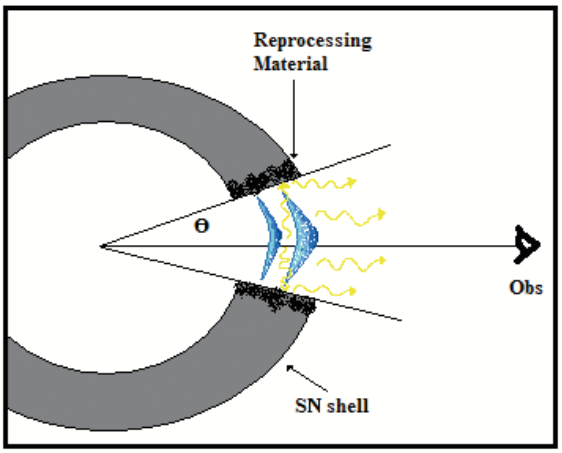

Fig. 3.22: Sketch of the geometry assumed for the production of the ionizing photons.

where F_{1-10} is the $1-10\,\mathrm{keV}$ ionizing flux; D_L is the luminosity distance ($\sim 4150\,\mathrm{Mpc}$ for $z = 0.703$); R is the distance of the reprocessing material and the symbol n stands for the particle density. Table 3.6, last column, lists the quantity nR^2 for $\xi = 10^4$; the $1-10\,\mathrm{keV}$ luminosity is derived from the XRT light curve. For a total shell mass of $10\,\mathrm{M}_\odot$ (order of magnitude of the stimated mass ejected by HNe explosion, see e.g. [116], [117], [118]) and a scale distance $R \sim 10^{12}\,\mathrm{cm}$ ($\sim v_\mathrm{shell} \times t_\mathrm{SN}$) we obtain $nR^2 \approx 10^{45}\,\mathrm{cm}^{-1}$, value we actually derive from the observed XRT luminosity between 100 and 130 s for $\xi = 10^4$. At this very high value of the ionization parameter, Ni line production efficiencies $\approx 1\%$ can be obtained only for higher than solar metallicities ([99]). In particular, the SNR associated with GRB 060904B must have a metallicity of the order of ten times the solar value.

3.8 The Models

We can divide the models we consider into transmission and reflection models. Transmission models require the lines to be produced by an optically thin medium ($\tau_\mathrm{T} \leq 1$). In SubSec. 3.6.2 we found $\tau_\mathrm{T} \gg 1$. Moreover, the large equivalenth width of the X-ray line in GRB 060904B (2 keV, Tab. 3.2) favours reflection models, where the ionizing flux is efficiently reprocessed in line photons. In trasmission models this happens only for a particular fine tuning of the parameters (emitting material and free electron densities) [197]. For these reasons we will discuss in detail only models in which the line originates in reflection.

Reflection models require the presence of a dense, optically thick, anisotropically distributed material surrounding the burst site. The material must be dense and optically thick in order to efficiently reprocess the continuum into

line photons, while the distribution is required to be anisotropic in order to have a clean path where the line photons can propagate and reach the observer. Different geometries are possible. However, apart from the geometry, in all reflection models the ionizing flux illuminates a thick piece of material and only photons scattered towards the observer and not absorbed by the thick medium are detected (the others beeing re-scattered or absorbed by the surrounding material). Consequenlty only a superficial layer of the whole material effectively contributes to the line emission. We require this layer to have:

- $\tau_{\rm T} \sim 1$ (In order to avoid excessive Compton broadening of the line, see SubSec. 3.6.3);
- $\tau_{\rm Ni} > 1$ (To efficiently absorb the continuum).

where:

$\tau_{\rm T}$: Thompson optical depth;
$\tau_{\rm Ni}$: Photoionization optical depth of H-like or He-like Nickel atoms.

Fig. 3.14 shows that $\tau_{\rm Ni} \geq 1$ is obtained for reasonable values of $M_{\rm Ni}$ and ξ. The second condition is therefore automatically fulfilled. On the contrary, the $\tau_{\rm T} \sim 1$ requirement directly translates into:

$$V_{\rm em} \approx S\,\Delta R \tag{3.98}$$

$$\tau_{\rm T} = n_{\rm e}\,\sigma_{\rm T}\,\Delta R \sim 1 \tag{3.99}$$

$$\Rightarrow V_{\rm em} = \frac{S}{\sigma_{\rm T} n_{\rm e}} \tag{3.100}$$

where:

$V_{\rm em}$: Volume of the material effectively contributing to the line emission;
S : Emitting surface;
ΔR : Material thickness;
$\sigma_{\rm T}$: Thompson cross section;
$n_{\rm e}$: Electron number density.

The line luminosity can be therefore written as:

$$L_{\rm line} = \frac{n_{\rm Ni}\,V_{\rm em}\epsilon_{\rm Ni}}{t_{\rm rec}} = \frac{n_{\rm Ni}\epsilon_{\rm Ni}}{t_{\rm rec}}\Big(\frac{S}{n_{\rm e}\sigma_{\rm T}}\Big) = \frac{n_{\rm Ni}\,\epsilon_{\rm Ni} S\,\alpha_{\rm r}(Z,T)}{\sigma_{\rm T}} \tag{3.101}$$

where:

$n_{\rm Ni}$: Number density of *emitting* Nickel atoms;
$\epsilon_{\rm Ni}$: Energy of a single line photon;
$\alpha_{\rm r}(Z,T)$: Recombination coefficient.

In this paragraph we consider how and if the observed emission detected in GRB 060904B fits into the reflection models that appeared in the literature (see e.g. [197]). In particular three alternative geometries will be discussed: a funnel geometry, a slab geoemtry and an external reflection geometry (3.23).

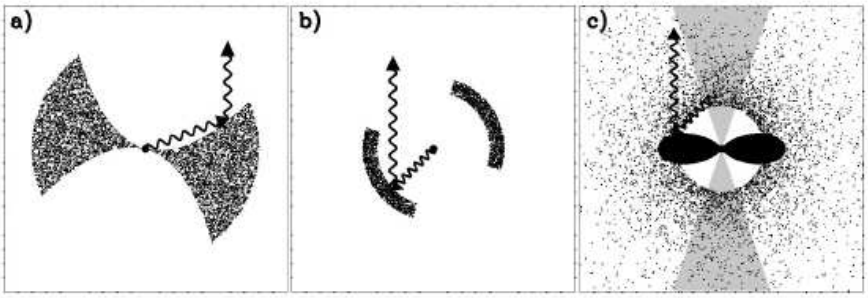

Fig. 3.23: Picture of the three geometries discussed. *(a)* A funnel excavated in a supernova remnant produeces the line emission in reflection. *(b)* The internal parts of a young receding supernova remnant. *(c)* Some equatorial material exploding simultaneously with the burts is illuminated by burst photons scattered by the preburst stellar wind. (From [197]).

3.8.1 Shell geometry

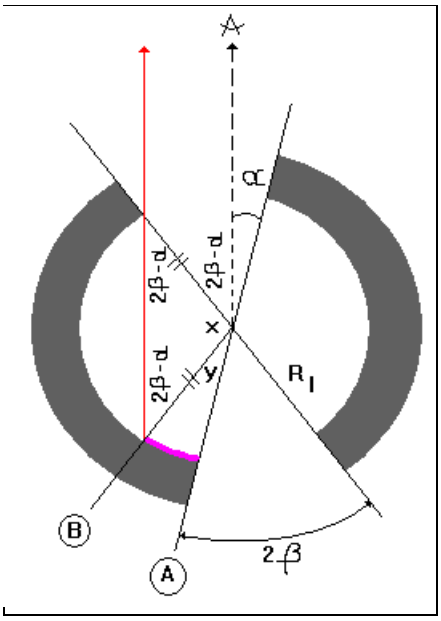

Fig. 3.24: Cartoon of the internal reflection model. The shell material is provided by a young and receding supernova remnant. Note that only radiation reflected by the coluored part of the shell can reach the observer.

The reflecting material is in this case provided by the internal parts of the SN remnant. As before we expect the shell to have an expansion velocity of a few $\sim$ 10 000 $\mathrm{Km\,s^{-1}}$. The illumination comes from a point source located

at the GRB position. This model therefore requires the presence of a isotropic ionizing source able to illuminate the line emitting material with a luminosity of the order $10^{49}\,\mathrm{erg\,s^{-1}}$ ([98]). This source is different from the observed GRB prompt emission if this emission is supposed to be collimated. The essential geometry of the model is portrayed in Fig. 3.24. From purely geometrical considerations it is possible to show that:

$$x = \pi - 4\beta + 2\alpha \tag{3.102}$$

$$x + y + 2\beta = \pi \quad \Rightarrow y = 2(\beta - \alpha) \tag{3.103}$$

with $-\beta < \alpha < \beta$ and $\beta < \pi/2$ (see Fig. 3.24). The maximum delay between the GRB event and the arrival of the reflected photons (if completely due to geometrical reasons) is obtained for photons scattered at position "A" and is given by:

$$ct_{\mathrm{obs}}^{max} = R_{\mathrm{I}}(1 + \cos(\alpha)) \tag{3.104}$$

while the minimum delay (position "B") is given by:

$$ct_{\mathrm{obs}}^{min} = R_{\mathrm{I}}(1 + \cos(\alpha - 2\beta)) \tag{3.105}$$

Substituting in the previous equation $ct_{\mathrm{obs}}^{\mathrm{min}} \sim t_{\mathrm{obs}}$, time at which we detect the line emission ($\approx 117\,\mathrm{s}$) we find:

$$R_{\mathrm{I}} = \frac{3.5 \times 10^{12}\,\mathrm{cm}}{1 + \cos(\alpha - 2\beta)} \tag{3.106}$$

(see Fig. 3.25)

$$\Rightarrow R_{\mathrm{I}} \leq 3.5 \times 10^{12}\,\mathrm{cm} \tag{3.107}$$

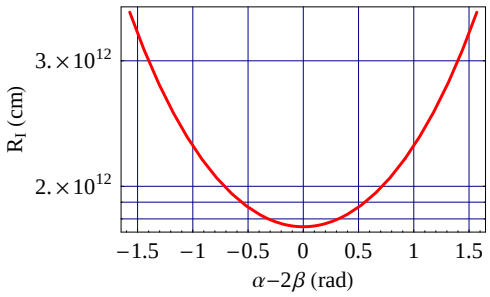

Fig. 3.25: Internal radius of the remnant as a function of the $\alpha - 2\beta$ quantity. See Eq. 3.106

We start again from Eq. 3.101:

$$L_{\mathrm{line}}^{tot} = \frac{n_{\mathrm{Ni}} V_{\mathrm{em}} \epsilon_{\mathrm{Ni}}}{t_{\mathrm{rec}}} = n_{\mathrm{Ni}} V_{\mathrm{em}} \epsilon_{\mathrm{Ni}} \alpha_{\mathrm{r}}(Z,T) n_{\mathrm{e}} \tag{3.108}$$

with:

$$V_{\rm em} = 4\pi R_{\rm I}^2 \Delta R_{\rm em} \frac{\Omega_{\rm m}}{4\pi} \tag{3.109}$$

where $\Omega_{\rm m}$ is the solid angle covered by the emitting material.
Assuming $\tau_{\rm T} = 1$ the emitting volume can be re-written as:

$$V_{\rm em} = R_{\rm I}^2 \Delta R_{\rm em} \Omega_{\rm m} = \frac{R_{\rm I}^2 \Omega_{\rm m}}{n_{\rm e}\sigma_{\rm T}} \tag{3.110}$$

$$L_{\rm line}^{\rm tot} = \frac{n_{\rm Ni}\,\epsilon_{\rm Ni}\,\alpha_r(Z,T)\Omega_{\rm m} R_{\rm I}^2}{\sigma_{\rm T}} \tag{3.111}$$

This is the *total* luminosity produced by the material. However, due to geometrical reasons, only a fraction of the line photons reach the free space in the direction of the observer. We assume this fraction to be $\approx \frac{\Omega_{\rm free}}{4\pi}$. If β is the half opening angle of the funnel excavated in the SN shell then:

$$\frac{\Omega_{\rm free}}{4\pi} = 1 - \cos\beta \tag{3.112}$$

$$\Rightarrow L_{\rm line} = (1-\cos\beta)\Big(\frac{\rm n_{Ni}\,\epsilon_{Ni}\,\alpha_r(Z,T)\Omega_m R_I^2}{\sigma_{\rm T}}\Big) \tag{3.113}$$

The number density of Nickel atom $n_{\rm Ni}$ is given by:

$$n_{\rm Ni} = \frac{M_{\rm Ni}^*}{V}\frac{1}{59 m_{\rm p}} = \frac{M_{\rm Ni}^*}{R^2 \Delta R\,\Omega_{\rm m}}\frac{1}{59 m_{\rm p}} \tag{3.114}$$

In the previous equation the symbol ΔR stands for the shell width.
Our final relation is therefore:

$$L_{\rm line} = \frac{M_{\rm Ni}^* \epsilon_{\rm Ni}\alpha_{\rm r}(Z,T)}{59 m_{\rm p}\Delta R \sigma_{\rm T}}(1-\cos\beta) \tag{3.115}$$

The previous relation tacitly assumes $t_{\rm rec} > t_{\rm rec}$ or:

$$\frac{t_{\rm rec}}{t_{\rm rec}} = \frac{1}{n_{\rm e}\sigma_{\rm T}}\frac{L_{\rm ion}\sigma_{\rm Ni}}{\epsilon_{\rm ion} 4\pi R^2} > 1 \tag{3.116}$$

Pasting:

$$n_{\rm e} = \frac{M}{V}\frac{1}{\mu_{\rm e} m_{\rm p}} = \frac{M_{\rm Ni}^*}{X}\frac{1}{R^2 \Delta R \Omega_{\rm m} \mu_{\rm e} m_{\rm p}} \tag{3.117}$$

with $\Omega_{\rm m} = 4\pi\,\cos\beta$
into Eq. 3.116 we have:

$$\frac{t_{\rm rec}}{t_{\rm rec}} = \frac{L_{\rm ion}\sigma_{\rm Ni}}{\epsilon_{\rm ion}\alpha_r}\frac{X\,\Delta R \mu_{\rm e} m_{\rm p}}{M_{\rm Ni}^*}\cos\beta > 1 \tag{3.118}$$

The system of equations that defines our shell model is therefore:

$$\begin{cases} L_{\rm line} = \frac{M^*_{\rm Ni}\epsilon_{\rm Ni}\alpha_{\rm r}(Z,T)}{59 m_{\rm p}\Delta R \sigma_{\rm T}}(1-\cos\beta) \\ \frac{L_{\rm ion}\sigma_{\rm Ni}}{\epsilon_{\rm ion}\alpha_r}\frac{X\,\Delta R \mu_{\rm e} m_{\rm p}}{M^*_{\rm Ni}}\cos\beta > 1 \\ R_{\rm I} = \frac{3.5\times10^{12}\,{\rm cm}}{1+\cos(\alpha-2\beta)} \\ -\beta < \alpha < \beta \\ \beta < \pi/2 \end{cases} \tag{3.119}$$

The free variables of the system are:

β Half opening angle of the funnel excavated in the SN remnant. In order to reduce the parameter space we consider $\beta \sim \theta_{\rm j}$, the jet opening angle. Solutions with $\beta < 20^\circ$ (0.3 rad) will be preferred (see the previous section).

$M^*_{\rm Ni}$ Total Nickel mass. We expect this parameter to be $< 1 M_\odot$. In particular, if the presence of the Nickel emission is related to the explosion of an (undetected) SN similar to other well studied SNe associated with GRB events, then we expect $M^*_{\rm Ni} \approx 0.4\,M_\odot$ (see Table 3.5).

X Metallicity ($M^*_{\rm Ni}/M$).

ΔR Shell thickness. If the observed duration Δt of the line emission is required to be comparable to the time needed by the source photons to cross the SN shell, then $\Delta R \geq 10^{12}$ cm.

T Electron temperature. Results will be calculated for $T_{\rm e} = 10^6, 10^7, 10^8, 10^9$ K

(see Table 3.7 for the values of the parameters used).
In order to find the possible solutions of the system 3.119, we start analysing the second relation shown. Considering that $M_{\rm Ni^*}/X = M$, this relation can be re-written as follows:

$$M < \frac{L_{\rm ion}\sigma_{\rm Ni}\Delta R \mu_{\rm e} m_{\rm p}}{\epsilon_{\rm ion}\alpha_{\rm r}}\cos\beta \tag{3.120}$$

Results are shown in Fig 3.26 for different values of the electron temperature. At the same time, we can derive from the first equation of the system the total Nickel mass required to explain the observed line emission. We require the Nickel mass in this way obtained to satisfy the condition plotted in Fig. 3.26 for a given metallicity (X parameter of the system 3.119). Results are shown in Fig. 3.27. We note that:

- Small opening angles β requires the metallicity to be consistently higher than solar (10 to 100 times the solar value); in particular if $\beta \sim \theta_{\rm j}$, jet opening angle, (see Table 3.8) then we expect $\beta \approx 0.1 - 0.3$ rad;

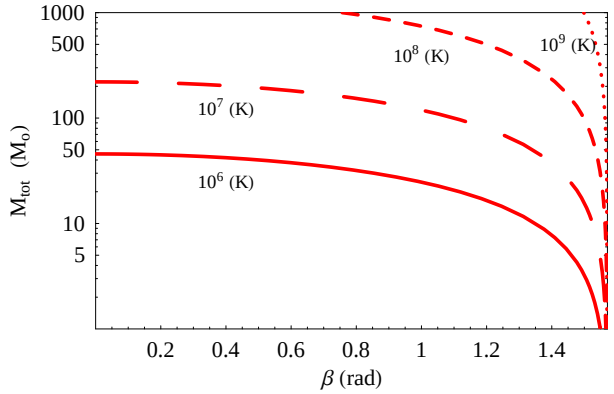

Fig. 3.26: Upper limits to the total mass of the shell as a function of the opening angle for different electron temperatures. Eq. 3.120 with $\Delta R = v_{\rm shell} \times t_{\rm obs} \approx 3.5 \times 10^{11}$ cm has been used. The SN explosion is supposed to be contemporary to the GRB event.

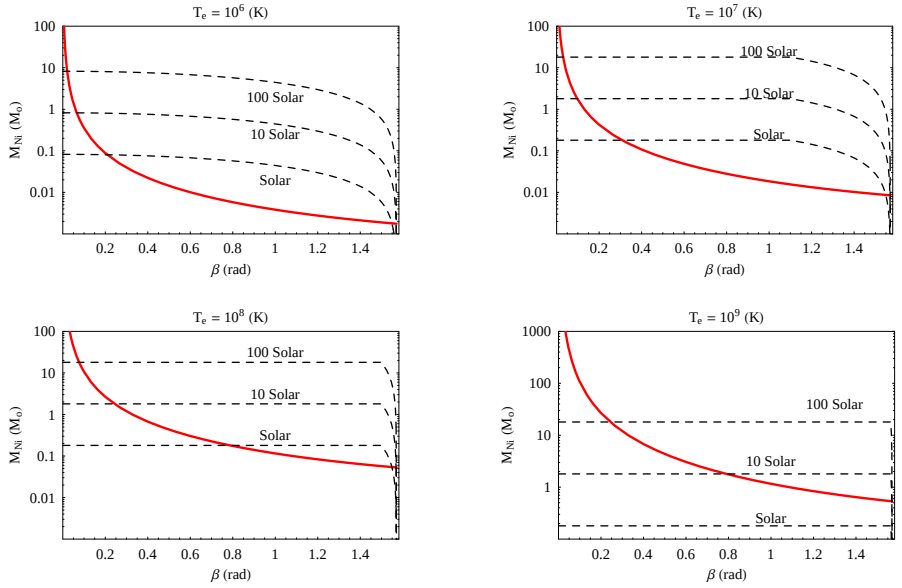

Fig. 3.27: Red solid line: total Nickel mass as a function of the shell opening angle according to Eq. 3.115 for different electron temperatures. $\Delta R = v_{\rm shell} \times t_{\rm obs} \approx 3.5 \times 10^{11}$ cm has been used. Dashed lines: upper limits to the parameter calculated from Eq. 3.120 assuming the total mass of the shell to be less than $100\,M_\odot$.

- For $T_e = 10^9$ K, $\beta \approx 0.3$ rad is obtained only for metallicity higher than 100 times solar;
- Assuming $M^*_{Ni} \approx 0.4\,M_\odot$ (see Table 3.5), we derive $\beta = 0.1, 0.2, 0.6$ and 2.3 rad for $T_e = 10^6, 10^7, 10^8, 10^9$ K respectively;

To conclude, the Nickel emission detected in GRB 060904B can be accounted for by this model for $M^*_{Ni} \approx 0.4\,M_\odot$, $\beta \approx 0.2$ rad and $T_e = 10^7$ K. (Higher electron temperatures require $\beta \gg 0.1$ rad). In this scenario, the line broadening can be explained by a single scattering process. The metallicity is sensitively higher than solar. However, one of the problems with this model is that the reflected photons must have a clean path from the back of the shell to the observer, a condition which is difficult to justify at the very early stages of a SN explosion.

3.8.2 External reflection models

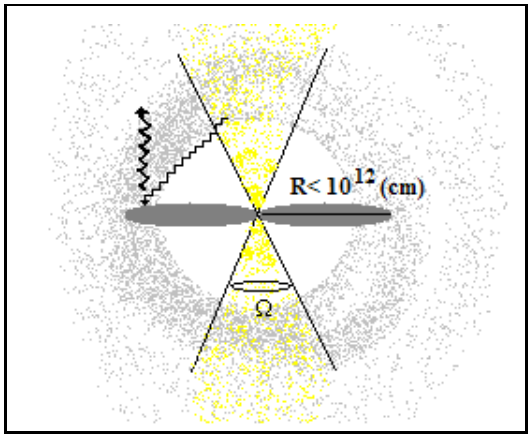

Fig. 3.28: Cartoon of the "external reflection model". Note the line emitting material ejected along the progenitor's equator and the presence of a wind produced material surrounding the burst location.

According to the "external reflection models", the line emitting material is back-illuminated by burst or afterglow photons scattered by the preburst stellar wind. We will assume that the line emitting material has been ejected at subrelativistic speeds along the progenitor's equator in a simultaneous SN-GRB explosion. Consequently, the equatorial line emitting material has a radius $\sim 3 \times 10^{12}$ cm at most. A picture of this model is presented in Fig. 3.28. For a complete discussion of the model see e.g. [197]. Massive star progenitors are always surrounded by dense material produced by strong winds. Under the assumption of a spherical geometry, the electron density of the wind material is

given by:

$$n_{\rm e,w} = \frac{dM_{\rm shell}}{4\pi r^2\, dr}\frac{1}{\mu_{\rm e} m_{\rm p}} \tag{3.121}$$

$$dM_{\rm shell} = \dot{m}_{\rm w} dt \tag{3.122}$$

$$dr = v_{\rm w} dt \tag{3.123}$$

with:

$dM_{\rm shell}$: Mass of the shell wind material;
$\dot{m}_{\rm w}$: Mass-loss rate;
$v_{\rm w}$: Wind velocity.

$$\Rightarrow n_{\rm e,w} = \frac{\dot{m}_{\rm w}}{4\pi r^2 v_{\rm w}}\frac{1}{\mu_{\rm e} m_{\rm p}} \tag{3.124}$$

Electrons of the wind material scatter back a fraction of the burst and afterglow photons. At the same time, the burst photons accelerate the electrons, decreasing in this way the efficiency of the back scattering process since the Klein-Nishina cross section of relativistic photons is always less than the Thomson cross section of non relativistic ones. For simplicity we will assume that each electron scatters photons until it reaches $\Gamma_{\rm e} \approx 2$. If $L_{\rm scatt}$ is the luminosity scattered by elctrons at rest with the photon source, then from relativistic arguments it is possible to show that (see e.g. [100]):

$$L_{\rm w} = \frac{1-\beta_{\rm e}}{\Gamma_{\rm e}^2} L_{\rm scatt} \tag{3.125}$$

where $L_{\rm w}$ is the luminosity back-scattered by electron moving outward from the source with ve5locity $\beta_{\rm e}$ and Lorentz factor $\Gamma_{\rm e}$. A rough evaluation of $L_{\rm scatt}$ is given below. For a given chemical compositon the number of barions per electron is $\mu_{\rm e}$. Because of the Coulomb interaction, the dynamics of the free electrons is coupled with the dynamics of the barions. As a consequence, the burst photons have to accelerate the couple electron+barions (and not only the single electron) to relativistic speeds before the efficiency of the back-scattering process significantly drops down. Then we assume that each electron scatters a total energy $\approx \mu_{\rm e} m_{\rm p} c^2$ and that only after all these scatterings the electron and the associated barions become relativistic. For 0.5 MeV photons, the number of scatterings is therefore:

$$N_\gamma = \mu_{\rm e}\frac{m_{\rm p}}{m_{\rm e}} \approx 2000 \tag{3.126}$$

If this is the case, a given shell of wind material at a distance r and from the photon source and thickness Δr would scatter a total energy:

$$E_{\Omega,r} = (4\pi r^2 \Delta r\, n_{\rm e,w})(\mu_{\rm e}\frac{m_{\rm p}}{m_{\rm e}})\frac{\varepsilon_{511}}{2}\frac{\Omega}{4\pi} \tag{3.127}$$

where:

Ω : Jet opening angle;
ε_{511} : Assumed mean energy of the incident photons (≈ 0.5 MeV).

The factor of two acounts for the energy loss of the scattered photon due to the recoil of the scattering electron. The time scale Δt of emission of this energy is given by:

$$\Delta t \sim \frac{2\Delta r}{c} \tag{3.128}$$

since the photon has to travel twice the width of the shell.

$$\Rightarrow L_{\rm scatt} = cr^2 n_{\rm e,w} \mu_{\rm e} \frac{m_{\rm p}}{m_{\rm e}} \frac{\varepsilon_{511}}{4} \Omega \tag{3.129}$$

Note that the scattered luminosity is indipendentent of r, since in each shell with thickness Δr there are an equal number of electrons (a density profile $\sim r^{-2}$ has been assumed). However, this is true as long as each electron is able to scatter ≈ 2000 photons. The density of electrons in a shell $n_{\rm e,w} \sim r^{-2}$, while their cross section is constant ($\sigma_{\rm T}$). As a consequence there will be a critical radius r^* beyond which the condition $N_\gamma \geq 2000$ is no more fulfilled. This condition can be re-written as:

$$\frac{E_{\rm GRB}}{\varepsilon_{511}} \frac{\sigma}{\Omega r^2} \geq \mu_{\rm e} \frac{m_{\rm p}}{m_{\rm e}} \tag{3.130}$$

where $E_{\rm GRB}$ is the energy emitted in photons by the GRB event (allowing for collimation) and σ is the electrons cross section.

$$r \leq \left(\frac{E_{\rm GRB}}{\Omega\, \varepsilon_{511}} \frac{m_{\rm e}}{\mu_{\rm e} m_{\rm p}} \sigma \right)^{1/2} \tag{3.131}$$

The previous equation can be expressed as a function of the isotropic energy of the burts event as follows:

$$r \leq \left(\frac{E_{\gamma,\rm ISO}}{4\pi\, \varepsilon_{511}} \frac{m_{\rm e}}{\mu_{\rm e} m_{\rm p}} \sigma \right)^{1/2} \approx 2 \times 10^{15} \left(E_{\gamma,\rm ISO,53} \right)^{1/2} \text{ cm} \tag{3.132}$$

where $E_{\gamma,\rm ISO,53}$ is the isotropic energy of the burst emitted in photons in units of 10^{53} erg. The numerical value of the Thomson cross section has been used in order to get an upper limit to the critical radius. For times $t > 2r^*/c$ the line emitting material is illuminated by burst photons scattered beyond the critical radius. As a consequence, the number of back scattered photons $\sim t^{-2}$ ($n_{\rm e,w} \sim r^{-2}$, $t \sim r$). The back-scattered luminosity as a function of the time is plotted in Fig. 3.29. (Note that in this derivation the GRB event has been considerated a single pulse of energy without temporal structure.) Its maximum value is reached during the constant $L_{\rm scatt}$ epoch and it is therefore given by Eq. 3.129.

From Sec. 3.7 we know that for GRB 060904B $E_{\gamma,\rm ISO} \approx 2 \times 10^{52}$erg.

$$\Rightarrow r^* \approx 10^{15}\,\text{cm} \tag{3.133}$$

$$\Rightarrow t_2 \approx 7 \times 10^4\,\text{s} \tag{3.134}$$

Pasting Eq. 3.124 into Eq. 3.129 we obtain:

$$L_{\rm scatt} = \frac{\Omega \varepsilon_{511}}{16\pi m_{\rm e}} \frac{\dot{m}_{\rm w}}{v_{\rm w}} \tag{3.135}$$

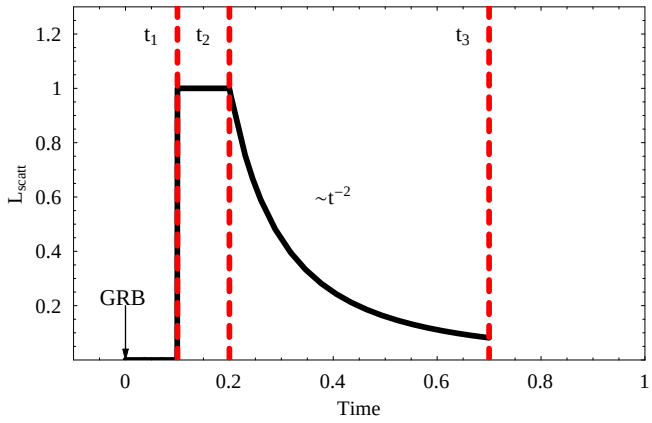

Fig. 3.29: Back-scattered luminosity as a function of the time. The luminosity is normalized to its maximum value while the time is given in units of some maximum time of observation. $t_1/2 = R_{\rm I}/c$ is the beginning of the back-scattering process; $t_1 = R_{\rm I}/c$ marks the arrival of the back scattered photons to the reprocessing material site. Note that this time must be of the order of the observed delay between the GRB event and the line detection. For GRB 060904B this implies $R_{\rm I} \approx 1.5 \times 10^{12}$ cm. $t_2 = 2r^*/c$ marks the end of the constant $L_{\rm scatt}$ epoch. Finally, $t_3 = 2R_{\rm o}/c$ marks the arrival of the last back-scattered photons to the reprocessing material site. $R_{\rm I}$ and $R_{\rm o}$ are the internal and external radius of the wind material.

or

$$L_{\rm scatt} \approx 3 \times 10^{55}\,\Omega\Big(\frac{\dot{m}_{\rm w}}{{\rm M}_\odot {\rm yr}^{-1}}\Big)\Big(\frac{{\rm cm\,s}^{-1}}{v_{\rm w}}\Big)\ {\rm erg\,s}^{-1} \tag{3.136}$$

Inserting $v_{\rm w} = 10^7$ cm and $\dot{m}_{\rm w} = 10^{-5}\,{\rm M}_\odot\,{\rm yr}^{-1}$, typical values of the wind velocity and mass-loss rate, we finally derive:

$$L_{\rm scatt} \approx 3 \times 10^{43}\,\Omega\Big(\frac{\dot{m}_{\rm w,-5}}{v_{\rm w,7}}\Big) \approx L_{\rm w} \tag{3.137}$$

since $\frac{1-\beta_{\rm e}}{\Gamma_{\rm e}^2} \approx 1$ (see Fig. 3.30). In the previous expression $v_{\rm w} = 10^7 v_{\rm w,7}\,{\rm cm\,s}^{-1}$ and $\dot{m}_{\rm w} = 10^{-5}\dot{m}_{\rm w,-5}\,{\rm M}_\odot{\rm yr}^{-1}$.

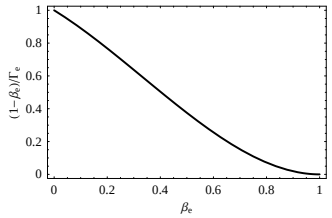

Fig. 3.30: $L_{\rm w} - L_{\rm scatt}$ conversion factor as a function of the electron β parameter.

On the other hand, due to geometrical (not all back-scattered photons will be re-directed towards the reprocessing material) and physical reasons (not all photons have enough energy to ionize the atoms), only a fraction of this luminosity will actually ionize the reprocessing material. We can therefore write:

$$L_{\rm ion} = f\, L_{\rm w} \tag{3.138}$$

with $f \leq 1$.

$$\Delta E_{\rm line} \leq L_{\rm ion} \Delta t_{\rm ion} \tag{3.139}$$

where:

$\Delta E_{\rm line}$: Energy emitted in line photons;
$\Delta t_{\rm ion}$: Interval of time during which the line emitting material is illuminated by the ionizing photons.

(The previous equation accounts for the possibility of non-radiative de-excitation).

$$\Rightarrow \Delta E_{\rm line} \leq f\, L_{\rm w} \Delta t_{\rm ion} \tag{3.140}$$

On the other hand, $f_{\rm max} = 1$, $\Delta t_{\rm ion-max} = t_{obs} = 138$s.

$$\Rightarrow \Delta E_{\rm line} \leq 138\, L_{\rm w} \tag{3.141}$$

$$L_{\rm w-max} \approx L_{\rm scatt}(\Omega = 4\pi) \approx 4 \times 10^{44} \Big(\frac{\dot{m}_{\rm w,-5}}{v_{\rm w,7}} \Big) \,{\rm erg\,s^{-1}} \tag{3.142}$$

$$\Rightarrow \Delta E_{\rm line} \leq 4 \times 10^{46} \Big(\frac{\dot{m}_{\rm w,-5}}{v_{\rm w,7}} \Big) \,{\rm erg} \tag{3.143}$$

It is notable that $L_{\rm w-max}$ is already more than 2 orders of magnitude *lower* than the observed line luminosity and ≈ 4 orders of magnitude lower than the expected ionizing luminosity: [98] show that in optimal conditions a reprocessing efficiency of $\approx 1\%$ at most can be reached, so that for the emission feature detected in GRB 060904B $L_{\rm ion} \geq 10^{49}{\rm erg\ s^{-1}}$ is required. A fine tuning of the progenitor wind velocity $v_{\rm w} = 10^7 v_{\rm w,7}\,{\rm cm\,s^{-1}}$ and of the mass-loss rate $\dot{m}_{\rm w} = 10^{-5} \dot{m}_{\rm w,-5}\,{\rm M_\odot yr^{-1}}$ is therefore required to explain the observed line luminosity. For this reason we consider this scenario unlikely.

3.8.3 Funnel geometry

In this case a funnel excavated in the SN shell produces the line emission in reflection. We do not require the emitting material to have been accelerated by the radiation pressure. In Sec. 3.4 we showed that for GRB 060904B the SN explosion dates back to no more than a few days before the GRB event. Consequently we expect expansion velocities of the shell as high as $\sim 10\,000$ Km s^{-1} even without the help of the radiation pressure.

Constant density material

In the most realistic scenario the funnel walls are not straigth (as in a cone geometry) but curved instead, and can be therefore efficiently illuminated by a central ionizing flux source. Assuming a cone geometry for simplicity (see Fig. 3.31), the emitting surface S is given by:

$$S = \pi R^2 \sin(\theta) \tag{3.144}$$

The meaning of the parameters R and θ is clear from Fig. 3.31. In particular we underline that R is the maximum distance between the line emitting material and the source of the ionizing photons. For the volume V occupied by the

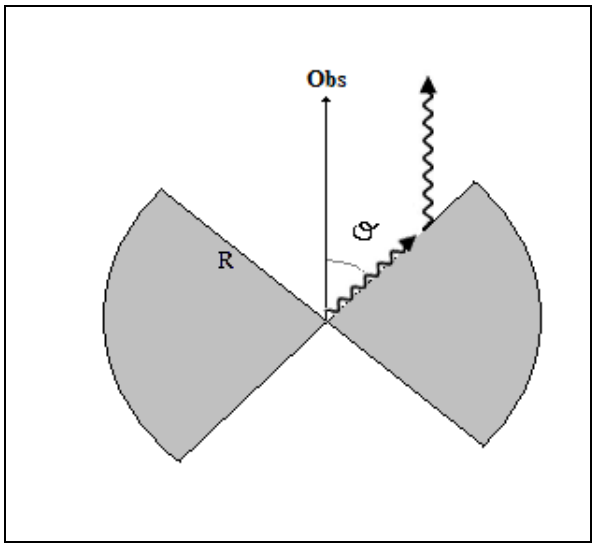

Fig. 3.31: Cone geometry for the funnel excavated model.

material we have:

$$V = \frac{4}{3}\pi R^3 \cos(\theta) \tag{3.145}$$

$$\Rightarrow n_{\rm Ni} = \frac{M^*_{\rm Ni}}{59\, m_{\rm p}\, V} = \frac{M\, X}{59\, m_{\rm p} \frac{4}{3}\pi R^3 \cos(\theta)} \tag{3.146}$$

where:

- $M^*_{\rm Ni}$: Total Nickel mass (differently from $M_{\rm Ni}$ which stands for the actually *emitting* Nickel mass);
- X : Ratio between the Nickel and the total mass of the material surrounding the burst;

Pasting Eq. 3.146 and Eq. 3.144 into Eq. 3.101 we get:

$$L_{\rm line} = \frac{3\,\epsilon_{\rm Ni}\alpha_{\rm r}(Z,T)}{236\, m_{\rm p}\sigma_{\rm T}} \left(\frac{M^*_{\rm Ni}}{R} {\rm tg}(\theta) \right) \tag{3.147}$$

On the other hand, Eq. 3.101 implicitly assumes the time scale of the emission process to be the recombination time scale. In particular this implies that $t_{\rm rec} > t_{\rm ion}$. If we allow for the possibility of a collimation of the ionizing continuum, then the ionization time scale can be written:

$$t_{\rm ion} = \frac{\Omega R^2 \epsilon_{\rm ion}}{L_{\rm ion}\sigma_{\rm Ni}} \tag{3.148}$$

We assume the collimation angle of the ionizing photons to be $\sim \theta$, funnel opening angle.

$$\Rightarrow \Omega = 2\pi(1 - {\rm Cos}(\theta)) \tag{3.149}$$

For the funnel-cone geometry the condition $t_{\rm rec} > t_{\rm ion}$ becomes:

$$\frac{t_{\rm rec}}{t_{\rm ion}} = \frac{4\pi}{3\Omega}\frac{L_{\rm ion}\sigma_{\rm Ni}\mu_{\rm e}m_{\rm p}}{\varepsilon_{\rm ion}\alpha_{\rm r}(Z,T)}\Big(\frac{R\,X}{M^*_{\rm Ni}}\cos(\theta)\Big) > 1 \tag{3.150}$$

(Eq. 3.11 has been used).
The system of equations to solve is therefore:

$$\begin{cases} L_{\rm line} = \frac{3\,\epsilon_{\rm Ni}\alpha_{\rm r}(Z,T)}{236\,m_{\rm p}\sigma_{\rm T}}\Big(\frac{M^*_{\rm Ni}}{R}{\rm tg}(\theta)\Big) \\ \frac{4\pi}{3\Omega}\frac{L_{\rm ion}\sigma_{\rm Ni}\mu_{\rm e}m_{\rm p}}{\varepsilon_{\rm ion}\alpha_{\rm r}(Z,T)}\Big(\frac{R\,X}{M^*_{\rm Ni}}\cos(\theta)\Big) > 1 \\ R < \frac{c\,t_{\rm obs}}{1-\cos(\theta)} \end{cases} \tag{3.151}$$

Where the third equation comes from the geometrical constraints discussed in Sec. 3.5. (Note that the electron temperature dependence is carried by the recombination coefficient $\alpha_{\rm r}(Z,T)$). Eliminating $M^*_{\rm Ni}$ from the first and second equation we get:

$$\frac{2\sin(\theta)}{1-\cos(\theta)} > 236\frac{L_{\rm line}}{L_{\rm ion}}\frac{\sigma_{\rm T}}{\sigma{\rm Ni}}\frac{\epsilon_{\rm ion}}{\epsilon_{\rm Ni}}\frac{1}{\mu_{\rm e}\,X} \tag{3.152}$$

We can therefore re-write the previous system of equations as:

$$\begin{cases} L_{\rm line} = \frac{3\,\epsilon_{\rm Ni}\alpha_{\rm r}(Z,T)}{236\,m_{\rm p}\sigma_{\rm T}}\Big(\frac{M^*_{\rm Ni}}{R}{\rm tg}(\theta)\Big) \\ \frac{2\sin(\theta)}{1-\cos(\theta)} > 236\frac{L_{\rm line}}{L_{\rm ion}}\frac{\sigma_{\rm T}}{\sigma{\rm Ni}}\frac{\epsilon_{\rm ion}}{\epsilon_{\rm Ni}}\frac{1}{\mu_{\rm e}\,X} \\ R < \frac{c\,t_{\rm obs}}{1-\cos(\theta)} \end{cases} \tag{3.153}$$

This system of equations defines our simplified funnel geometry model with line photons produced by reflection. For the numerical evaluation of the system we used for each variable the values reported in Table 3.7.

Before discussing the results of this model, it is important to underline that the Nickel mass which appears in the prevoius equations $M^*_{\rm Ni}$ refers to the *total* Nickel mass present. The line emitting Nickel material is only a part of this value and in this work is indicated as $M_{\rm Ni}$.

Substituting the numerical values indicated, it is easy to show that the second relation is always fulfilled provided that the metallicity is higher than ≈ 0.04 the solar value, or $X \geq 0.00008$ (see Fig. 3.32).

Figure 3.33 shows the results of our calculation. In particular we note that:

$L_{\rm line}$	$1.10 \times 10^{47}\,{\rm erg\,s^{-1}}$	$L_{\rm ion}$	$10^{49}\,{\rm erg\,s^{-1}}$
$\epsilon_{\rm Ni}$	$8\,{\rm keV}$	$\epsilon_{\rm ion}$	$10\,{\rm keV}$
$\mu_{\rm e}$	1.2	$m_{\rm p}$	$1.67 \times 10^{-24}\,{\rm g}$
$\sigma_{\rm T}$	$0.6 \times 10^{-24}\,{\rm cm^2}$	$\sigma_{\rm Ni}$	$10^{-20}\,{\rm cm^2}$
$t_{\rm obs}$	$138\,{\rm s}$	$\alpha_{\rm r}$	from Eq. 3.10

Tab. 3.7: Numerical values of the parameters that appear in the funnel geometry model.

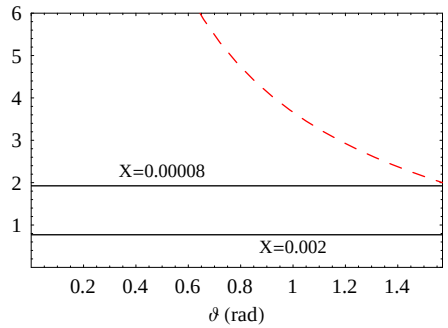

Fig. 3.32: Dashed line: $\frac{2\sin(\theta)}{1-\cos(\theta)}$. Solid lines: $236\frac{L_{\rm line}}{L_{\rm ion}}\frac{\sigma_{\rm T}}{\sigma_{\rm Ni}}\frac{\epsilon_{\rm ion}}{\epsilon_{\rm Ni}}\frac{1}{\mu_{\rm e}\,X}$. The value of the metallicity parameter X used are reported in the figure.

1. High electron temperature models ($T_{\rm e} \geq 10^8\,{\rm K}$) require total Nickel mass $\sim 10\,{\rm M_\odot}$. Even for one hundred solar metallicities this would imply a $\geq 100\,{\rm M_\odot}$ stellar progenitors. Such models are therefore excluded. Consequently, a completely thermal broadening of the line is equally excluded.

2. The electron temperature is likely to be in the range $10^6 - 10^7$ K in good agreement with what we found in Sec. 3.6.3. The line width is in this scenario interpreted as a consequence of multiple scattering process, with $N_{\rm sc} \sim 1 - 3$. However, because of the great uncertainty affecting the measured broadening of the line $\sigma_\nu = 0.50^{+0.35}_{-0.17}$ electron temperatures comparable with $\approx 10^8\,{\rm K}$ are also possible: in this case the observed broadening can be explained by a single scattering process (see Sec. 3.6.3).

3. The total Nickel mass required to reproduce the line emission observed in GRB 060904B is likely to satisfy the condition $M^*_{\rm Ni} \leq 1{\rm M_\odot}$ (see Table 3.5).

4. If $M^*_{\rm Ni} \approx 0.4\,{\rm M_\odot}$ (Nickel mass implied by hypernovae explosions associated with GRB, see Table 3.5) and $R \sim 10^{12}\,{\rm cm}$ then for $T_{\rm e} = 10^6\,{\rm K}$ we derive $\theta \approx 1°$; for $T_{\rm e} = 10^7\,{\rm K}$ $\theta \approx 5°$, while $\theta \approx 27°$ for $T_{\rm e} = 10^8\,{\rm K}$ where θ is the funnel opening angle. If the GRB photons are supposed to be the source of ionization of the line emitting material, then indicating with θ_j

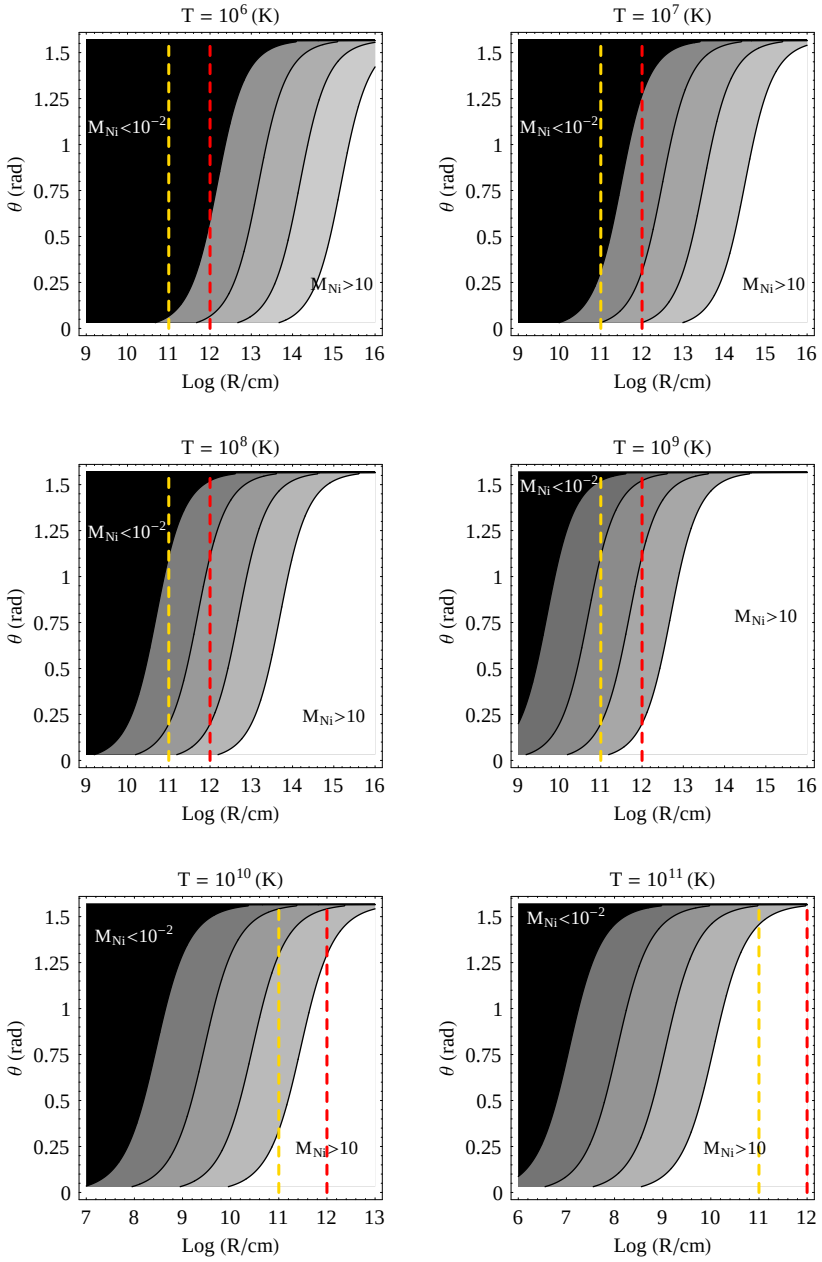

Fig. 3.33: Nickel mass contour plot according to equations 3.153 for different temperatures. In each plot, from left to right the black solid lines mark the $M_{\rm Ni} = 10^{-2}\,{\rm M}_\odot$, $10^{-1}\,{\rm M}_\odot$, $1\,{\rm M}_\odot$ and $10\,{\rm M}_\odot$ regions. Red dashed line: $R = 10^{12}$ cm, order of magnitude of the distance between the ionizing photons source and the reprocessing material derived from geometrical cosiderations (See Sec. 3.5). Orange dashed line: $R = 10^{11}$ cm, $R_{\rm max}$ according to our "Case B" and "C".

GRB	θ_j	References
970508	16.7°	[51]
970828	4.1°	[51]
980703	8.4°	[220]
991216	2.9°	[51]
000926	4.6°	[220]

Tab. 3.8: Jet opening angles for different GRB events. For GRB 980703 and GRB 000926 *initial* values of the jet opening angle are provided. These values have been derived from observed jet break times. We refer the reader to the reported references for more details.

the jet opening angle it is reasonable to expect: $\theta_j \sim \theta$. The value of the jet opening angle calculated by [51] for GRB 970508, GRB 970828 and GRB 991216 is shown in Table 3.8.

5. For small funnel opening angles, a factor of 2 of line photons collimation (and subsequent amplification) with respect to the isotropic emission has been calculated in Sec. 3.7.1. Applying this small correction to the line luminosity value we obtain the situation shown in Fig. 3.35. Consequently we derive $\theta_j(T_\mathrm{e} = 10^6\,\mathrm{K}) \approx 0.5°$ and $\theta_j(T_\mathrm{e} = 10^7\,\mathrm{K}) \approx 2°$.

6. The electron density n_e can be expressed as:

$$n_\mathrm{e} = \frac{M}{V}\frac{1}{\mu_\mathrm{e} m_\mathrm{p}} = \frac{M_\mathrm{Ni}}{X}\frac{3}{4\pi R^3 \cos(\theta)}\frac{1}{\mu_\mathrm{e} m_\mathrm{p}} \tag{3.154}$$

According to our model: $R \approx 10^{12}\,\mathrm{cm}$, $\cos(\theta) \approx 1$, $M_\mathrm{Ni} \approx 0.4\,\mathrm{M}_\odot$.

$$\Rightarrow n_\mathrm{e} \approx \frac{10^{20}}{X}\,\mathrm{cm}^{-3} \tag{3.155}$$

Our model therefore requires electron densities as high as $10^{23}\,\mathrm{cm}^{-3}$,$10^{22}\,\mathrm{cm}^{-3}$ and $10^{21}\,\mathrm{cm}^{-3}$ for solar metallicity, ten solar metallicity and one hundred solar metallicity respectively. (We note that these value would correspond to free electron densities, parameter which appears in the expression of the recombination time, only if the material is completely ionized). These are really high values: however, [197] conclude $n_\mathrm{e} \geq 10^{10}\,\mathrm{cm}^{-3}$ for $R = 6 \times 10^{15}\,\mathrm{cm}$. Our distances are $\sim \times 10^{-4}$ the distances implied by the Vietri et al. 2001 [197] model: consequently we expect electron densities $\sim 10^{12}$ times higher. We note that [190] find a typical value of $n_\mathrm{e} \sim 10^{20}\mathrm{cm}^{-3}$ for the electron densities in nearby reprocessor scenarii.

We therefore conclude that the line emission we detect in GRB 060904B spectra can be explained in our constant density- funnel geometry model for:

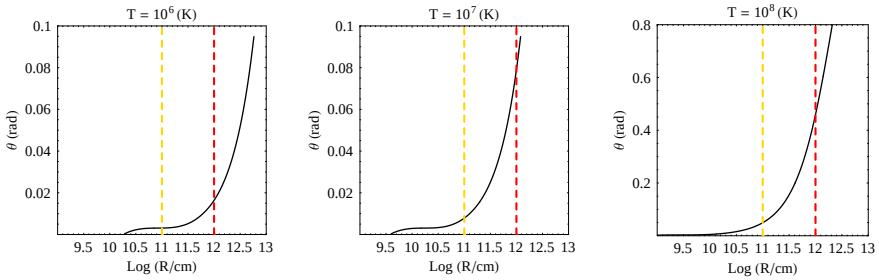

Fig. 3.34: Nickel mass contour plot according to equations 3.153 for $T_e = 10^6$ K, $T_e = 10^7$ K and $T_e = 10^8$ K. In each plot, the black solid line marks the $M^*_{Ni} = 0.4\,M_\odot$. Red dashed line: order of magnitude of the distance between the ionizing photons source and the reprocessing material derived from geometrical cosiderations (See Sec. 3.5). Orange dashed line: $R = 10^{11}$ cm, R_{max} according to our "Case B" and "C".

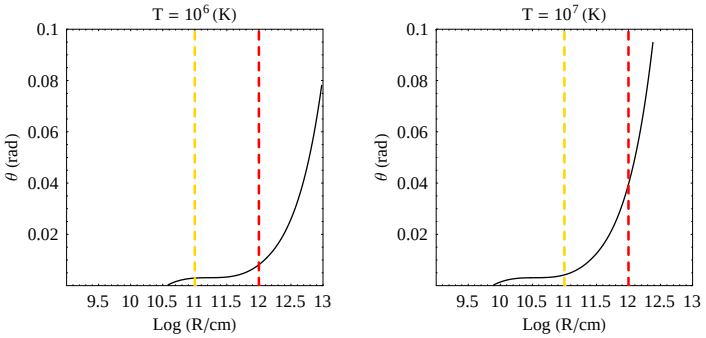

Fig. 3.35: Nickel mass contour plot according to equations 3.153 for $T_e = 10^6$ K, $T_e = 10^7$ K . In each plot, the black solid line marks the $M^*_{Ni} = 0.4\,M_\odot$. Red dashed line: order of magnitude of the distance between the ionizing photons source and the reprocessing material derived from geometrical cosiderations (See Sec. 3.5). Orange dashed line: $R = 10^{11}$ cm, R_{max} according to our "Case B" and "C". With respect to Fig. 3.34, a factor of 2 coming from the line photon collimation (see Sec. 3.7.1) effect has been considered. Hence in this case we considered $L_{line} = 1.10 \times 10^{47}/2$.

$M_{Ni} \approx 0.4\,M_\odot$, $T_e \sim$ a few 10^7 K, $\theta_j \sim$ a few 3°, $R \approx 10^{12}$ cm, $n_e \approx 10^{21}$ cm^{-3} [2]. The line emission is produced by reflection; each photon undergoes an average

[2] However we are far from the quantistic limit. We can obtain a rough estimate of the critical (quantistic limit) electron density as follows:

$$\Delta x\,\Delta p \approx \hbar \Rightarrow n_e \sim (\Delta x)^{-3} \approx \left(\frac{\Delta p}{\hbar}\right)^3 \tag{3.156}$$

$$\Delta p \approx m_e v \tag{3.157}$$

number of scatterings $N_{\rm sc} \leq 2$ before reaching the oberver: this is the principle source of the detected line broadening.

Stratification

The geometry of the model is shown in Fig. 3.36.

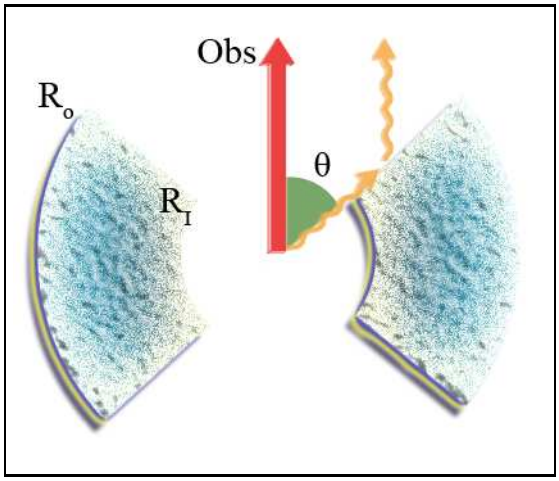

Fig. 3.36: Sketch of the geometry assumed for the reflecting material for the funel model disussed in the text.

As before, the geometry is given by funnel excavated line emitting material, but we allow the density to vary with the radius of the shell. In particular, we consider a power-law density profile [3]

$$n_{\rm e} = n_{\rm I}\Big(\frac{r}{R_{\rm I}}\Big)^{-\alpha} \tag{3.160}$$

where:

$n_{\rm I} \equiv n_{\rm e}(R_{\rm I})$;	
$R_{\rm I}$	Internal radius of the shell;
α	Power law index.

As before:

$$L_{\rm line} = \frac{n_{\rm Ni} V_{\rm em} \epsilon_{\rm Ni}}{t_{\rm rec}} = n_{\rm Ni} V_{\rm em} \epsilon_{\rm Ni} n_{\rm e} \alpha_{\rm r}(Z,T) \tag{3.161}$$

with

$$v \approx \left(\frac{kT_{\rm e}}{m_{\rm e}}\right)^{1/2} \tag{3.158}$$

$$n_{\rm e}^{crit} \approx 10^{30}{\rm cm}^{-3} \tag{3.159}$$

[3] The density profile of the outer layers of a SNR can be approximated by a power-law. The power-law index varies with time. See e.g. [16],[40] and references therein for a complete discussion.

$$\Rightarrow dL_{\rm line} = \left(n_{\rm Ni}\epsilon_{\rm Ni}n_{\rm e}\alpha_{\rm r}\right) dV_{\rm em} \tag{3.162}$$

For $\tau_{\rm T} = 1$, $dV_{\rm em}$ can be re-written as:

$$dV_{\rm em} \sim \Delta R\, dS = \frac{1}{\sigma_{\rm T} n_{\rm e}}\, dS \tag{3.163}$$

In the geometry of emission chosen, the unit surface dS is given by:

$$dS = 2\pi r \sin(\theta) dr \tag{3.164}$$

with θ= funnel opening angle.

$$\Rightarrow dL_{\rm line} = \frac{\epsilon_{\rm Ni}\alpha_{\rm r}}{\sigma_{\rm T}} 2\pi r \sin(\theta) n_{\rm Ni}(r) dr \tag{3.165}$$

On the other hand:

$$n_{\rm Ni} = \frac{dM^{*}_{\rm Ni}}{dV}\frac{1}{59 m_p} = \frac{dM}{dV}\frac{1}{\mu_{\rm e} m_{\rm p}}\frac{X\mu_{\rm e}}{59} = n_{\rm e}\frac{\mu_{\rm e} X}{59} \tag{3.166}$$

where:

- $M^{*}_{\rm Ni}$ Total Nickel mass (different from the actually emitting nickel mass in this work indicated as $M_{\rm Ni}$);
- V Total volume;
- X Ratio of the Nickel to the total mass.

Consequently, according to our model the observed line luminosity is given by:

$$L_{\rm line} = \frac{\mu_{\rm e} X}{59\sigma_{\rm T}}\epsilon_{\rm Ni}\, 2\pi\, \alpha_{\rm r} \sin(\theta) \int_{\rm R_I}^{\rm R_o} {\rm r}\, {\rm n_e(r)}\, {\rm dr} \tag{3.167}$$

or

$$L_{\rm line} = \frac{\mu_{\rm e} X}{59\sigma_{\rm T}}\epsilon_{\rm Ni}\, 2\pi\, \alpha_{\rm r} \sin(\theta) {\rm n_I R_I^{\alpha}} \int_{\rm R_I}^{\rm R_o} {\rm r}^{1-\alpha}\, {\rm dr} \tag{3.168}$$

This is the first equation that defines our model. However it is better to express the "internal" electron density $n_{\rm I}$ as a function of a more intuitive variable, like the total mass of the shell M or the total Nickel mass $M^{*}_{\rm Ni}$. To do this, it is enough to consider that the total mass M of the shell is related to the various parameters of the model by (Eq. 3.166):

$$dM = n_{\rm e}(r)\mu_{\rm e} m_{\rm p} dV(r) \tag{3.169}$$

where:

$$dV(r) = 2 \times 2\pi r^2 \cos(\theta) {\rm dr} \tag{3.170}$$

$$\Rightarrow M = 4\pi\mu_{\rm e} m_{\rm p} \cos(\theta) \int_{\rm R_I}^{\rm R_o} {\rm r}^2 {\rm n_e(r)} {\rm dr} \tag{3.171}$$

or

$$M = 4\pi\mu_{\rm e} m_{\rm p} \cos(\theta) {\rm n_I R_I^{\alpha}} \int_{\rm R_I}^{\rm R_o} {\rm r}^{2-\alpha}\, {\rm dr} \tag{3.172}$$

The total Nickel mass is therefore given by:

$$M^*_{\rm Ni} = X\,M = X\Big(4\pi\mu_{\rm e}m_{\rm p}\cos(\theta){\rm n_I R_I^\alpha}\int_{\rm R_I}^{\rm R_o}{\rm r}^{2-\alpha}\,{\rm dr}\Big) \tag{3.173}$$

Calculating the quantity $n_{\rm I}R_{\rm I}^\alpha$ from the previoud equation, and pasting in Eq. 3.168 we finally derive:

$$L_{\rm line} = M^*_{\rm Ni}\frac{\epsilon_{\rm Ni}\,\alpha_r(Z,T)}{118\sigma_{\rm T}m_{\rm p}}{\rm tg}(\theta)\frac{\int_{\rm R_I}^{\rm R_o}{\rm r}^{1-\alpha}{\rm dr}}{\int_{\rm R_I}^{\rm R_o}{\rm r}^{2-\alpha}{\rm dr}} \tag{3.174}$$

In order to write the second equation, we consider that the condition $t_{\rm rec} > t_{\rm ion}$ translates into:

$$\frac{t_{\rm rec}}{t_{\rm ion}} = \frac{L_{\rm ion}\sigma_{\rm Ni}}{\Omega\epsilon_{\rm ion}\alpha_{\rm r}(Z,T)}\frac{1}{n_{\rm I}R_{\rm I}^\alpha\,r^{2-\alpha}} > 1 \tag{3.175}$$

where Ω allows for the possibility of a collimation of the ionizing photons. Taking the collimation angle of the ionizing photons to be $\sim\theta$, (funnel opening angle):

$$\Omega = 2\pi(1-\cos(\theta)) \tag{3.176}$$

$$\Rightarrow \frac{t_{\rm rec}}{t_{\rm ion}} = \frac{L_{\rm ion}\sigma_{\rm Ni}}{2\pi(1-\cos(\theta))\epsilon_{\rm ion}\alpha_{\rm r}({\rm Z,T})}\frac{1}{n_{\rm I}R_{\rm I}^\alpha\,r^{2-\alpha}} > 1 \tag{3.177}$$

As before, we want to express the previous relation as a function of the mass contained in the shell. Using Eq. 3.173 to define the quantity $n_{\rm I}R_{\rm I}^\alpha$ and substituting in Eq. 3.177 the final result is:

$$\frac{t_{\rm rec}}{t_{\rm ion}} = \Big(\frac{L_{\rm ion}\sigma_{\rm Ni}}{\epsilon_{\rm ion}\alpha_{\rm r}}\frac{2\cos(\theta)}{(1-\cos(\theta))}\frac{\mu_{\rm e}m_{\rm p}}{M}\frac{1}{r^{2-\alpha}}\int_{R_{\rm I}}^{R_{\rm o}} r^{2-\alpha}\,dr\Big) > 1 \tag{3.178}$$

The system of equation that defines our funnel model with stratification is therefore:

$$\begin{cases} L_{\rm line} = M^*_{\rm Ni}\frac{\epsilon_{\rm Ni}\,\alpha_r(Z,T)}{118\sigma_{\rm T}m_{\rm p}}{\rm tg}(\theta)\frac{\int_{\rm R_I}^{\rm R_o}{\rm r}^{1-\alpha}{\rm dr}}{\int_{\rm R_I}^{\rm R_o}{\rm r}^{2-\alpha}{\rm dr}} \\ \frac{L_{\rm ion}\sigma_{\rm Ni}}{\epsilon_{\rm ion}\alpha_{\rm r}}\frac{2\cos(\theta)}{(1-\cos(\theta))}\frac{\mu_{\rm e}m_{\rm p}}{M}\frac{1}{r^{2-\alpha}}\int_{R_{\rm I}}^{R_{\rm o}} r^{2-\alpha}\,dr > 1 \\ R_{\rm o} - R_{\rm I} \approx c\Delta t \end{cases} \tag{3.179}$$

where in the last equation the duration Δt of the line eission is required to be comparable to the time needed by the source photons to cross the SN shell. The value of the different parameters used to evaluate the previous conditions are

listed in Table 3.7. The free variables of the system are:

- θ Funnel opening angle. If the burst photons are supposed to be the ionizing source of the line emitting material then $\theta \sim \theta_{\rm j}$, jet opening angle. Values of this parameter are listed in Table 3.8: it is important to underline that these values have been derived from observed jet break times.
- $M^*_{\rm Ni}$ Total Nickel mass. We expect $M^*_{\rm Ni} < 1\,M_\odot$. In particular, if the undetected SN associated with GRB 060904B is similar to other well studied SNe associated with GRB events then $M^*_{\rm Ni} \approx 0.4\,M_\odot$ is expected (see Table 3.5);
- X Metallicity ($M^*_{\rm Ni}/M$);

- $R_{\rm o}$ Outer radius of the shell. From the previous considerations (see Sec. 3.7.5) we expect $R_{\rm o}$ to be comparable with 3×10^{12} cm;
- $R_{\rm I}$ Internal radius of the shell. This parameter is supposed to be comparable to the radius of the stellar progenitor. In order to reduce the parameter space, two different values of this parameter will be considered: $R_{\rm I} = 10^{11}$ cm and $R_{\rm I} = 10^{12}$ cm;
- α Mass density power law index. The mass density of a SNR can be approximated by a power-law in radius for radii greater than some critical value, while at radii less than critical the density is roughly constant. However, at small times from the SN explosion the density profile is nearly constant within $R_{\rm o}$. At this distance the density undergoes a rapid cutoff (see Fig. 3.37). For this reason we will consider only small values of the α parameter: in particular the model will be explored for $\alpha = 0$ and $\alpha = 1$.
- $T_{\rm e}$ Electron temperature. Results will be calculated for $T_{\rm e} = 10^6, 10^7$ and 10^8 (K).

Model with $\alpha = 0$

The $R_{\rm o} - \theta$ parameter space as calculated from the first of the relation in the system 3.179 is shown in Fig. 3.39 for different electron temperatures and internal radius of the shell $R_{\rm I}$. In Fig. 3.38 we show the the upper limits to the total mass of the shell calculated from 3.178: it is clear that for small angles this relation doesn't give us any practical constraint. However it is worth noting that as the temperature rises, the recombination time increases, so that at a fixed funnel opening angle, more Ni is needed (and hence more mass in the SN shell) to fullfil the $t_{\rm rec} = t_{\rm ion}$ requirement. Consequently the condition $t_{\rm rec} > t_{\rm ion}$ will be satisfied by a more extended range of SN shell masses: for example, for $R_{\rm I} = 10^{11}$ cm, $R_{\rm o} = 10^{12}$ cm, $T = 10^7$ K we derive $M \leq 100\,{\rm M}_\odot$ with $\theta \leq 1.45$ rad. For GRB-associated HNe, the ejected mass reported in the literature ([116], [117], [118]) is however about one order of magnitude smaller. For this reason we expect $M \sim 10\,{\rm M}_\odot$.

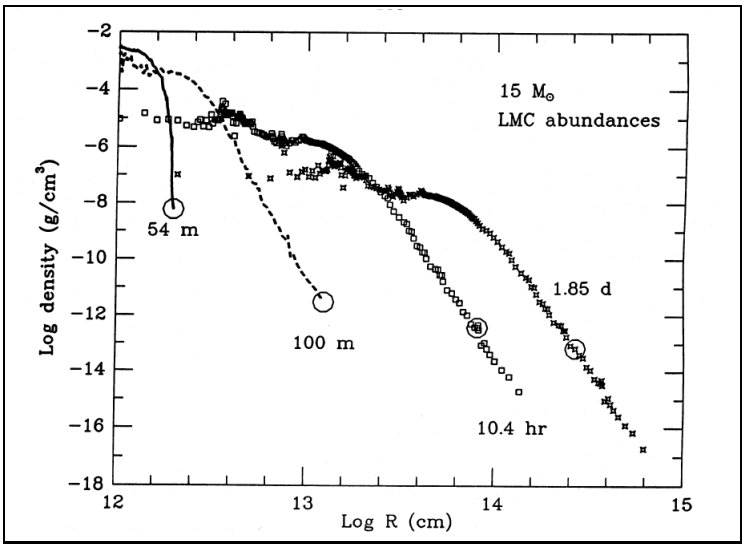

Fig. 3.37: Density vs. radius for SN 1987A at various istants in time. From [6].

Instead interesting conclusions can be drawn from the other figure:

- Figure 3.39 presents the variation of the total Ni mass required to explain the detected emission as a function of the funnel opening angle and the outer radius of the shell. Results are shown for different values of the internal radius and temperature. The stratification index has been fixed to 0. As the temperature rises, the required total Ni mass increases: this is due to the dependence of the recombination time on the temperature. On the other hand the increase of the funnel opening angle requires the detected emission to be explained by a smaller amount of Ni mass. This can be understood by considering that the density of the matter in the SN shell is a monotonic increasing function of θ. Consequently $t_{\rm rec}$ is a decreasing function of the funnel opening angle. The dependence of $M^*_{\rm Ni}$ on the matter density manifests itself also through the parameter $R_{\rm o}$: the increase of the outer shell radius requires $M^*_{\rm Ni}$ to increase, in order to reproduce the luminosity of the detected emission feature. Finally, increasing $R_{\rm I}$, $M^*_{\rm Ni}$ decreases.

- High electron temperature ($\geq 10^9$ K) models require total Nickel mass as high as $\sim 10\,M_\odot$ or $\theta \geq 60^\circ$ at $t \sim 10^2$ s after the GRB onset. The first condition would imply a mass of the shell remnant $\geq 100\,{\rm M}_\odot$ even under the assumption of one hundred solar metallicity. For this reason, consistently with Sect. 3.6 we consider unlikely the $T \geq 10^9$ K scenario.

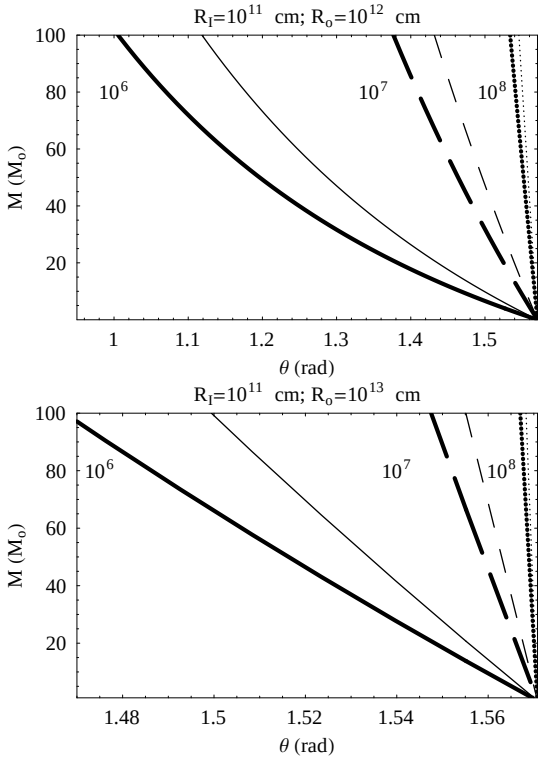

Fig. 3.38: Upper limits to the total mass of the shell derived from equation 3.178 evaluated at $r = R_o$ as a function of the funnel opening angle. Solid lines: $T = 10^6$ K; dashed lines: $T = 10^7$ K; dotted lines: $T = 10^8$ K. Thick lines: $\alpha = 0$; thin lines: $\alpha = 1$.

- A line broadening completely thermal in origin is therefore excluded. If $T_e \approx 10^6$ K a multiple scattering process with $N_{sc} \sim 2$ can be invoked. However, if $T_e \sim 10^7 - 10^8\,(K)$, then a single Compton scattering would be enough to explain the observed broadening (we refer to Sec. 3.6.3 for details);
- If the funnel opening angle θ is to be identified with the jet opening angle θ_j, then $\theta \sim 60^\circ$ at $t \sim 10^2$ s after the GRB onset is difficult to justify: [97], starting from theoretical considerations, drew the conclusion that GRBs have $\theta_j \sim 1^\circ$; from the observational point of view, a typical $\theta_j \sim 5^\circ$ is derived from the afterglow jet break data ([211]).

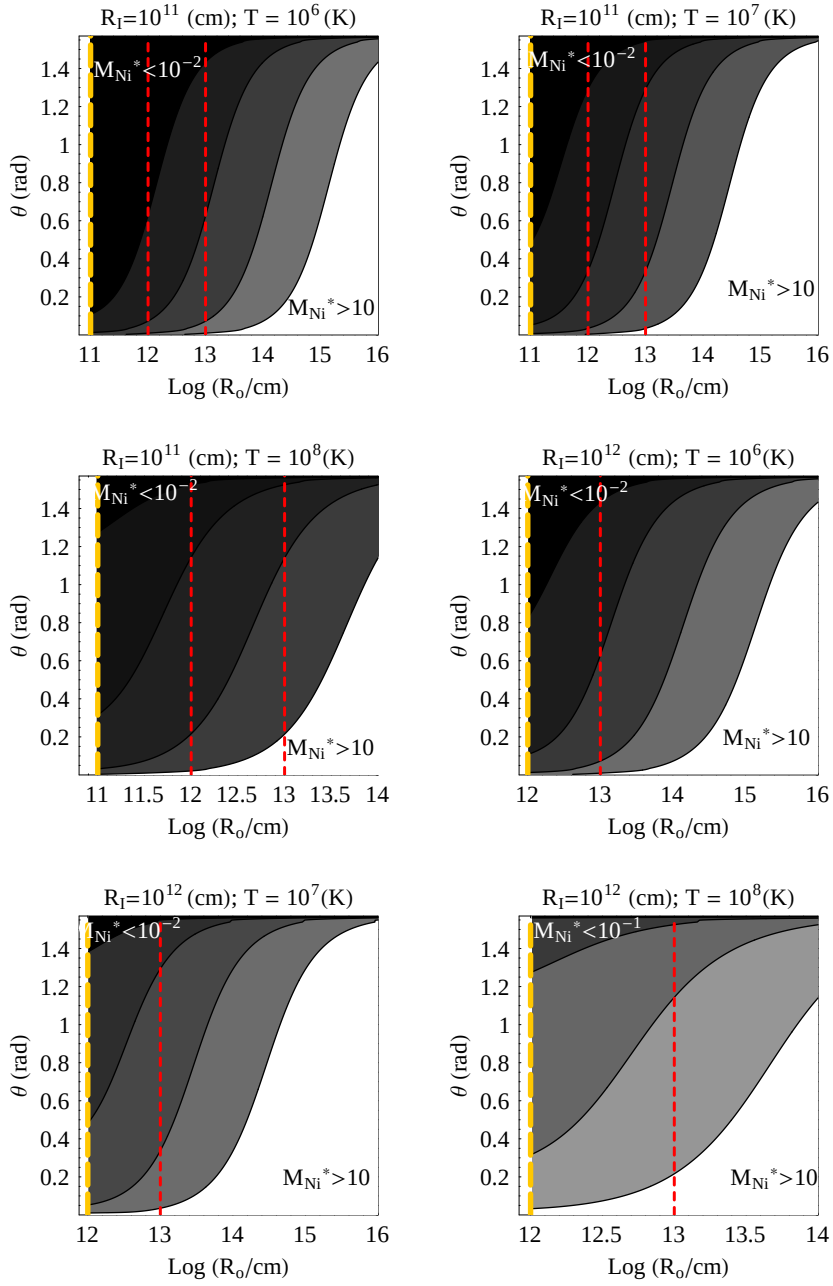

Fig. 3.39: Nickel mass contour plot according to equations 3.179 for different the different temperatures indicated, $R_{\rm I} = 10^{11}$ cm and $\alpha = 0$ In each plot, from left to right the black solid lines mark the $M_{\rm Ni} = 10^{-2}\,{\rm M}_\odot$, $10^{-1}\,{\rm M}_\odot$, $1\,{\rm M}_\odot$ and $10\,{\rm M}_\odot$ regions. Red dashed lines: $R = 10^{12}$ cm and $R = 10^{13}$ cm. Orange dashed line: $R_{\rm I} = 10^{11}$ cm or $R_{\rm I} = 10^{12}$ cm.

- If $\theta \sim 5^\circ$ (~ 0.1rad) the detected emission implies a total Ni mass of the order of $0.1\,M_\odot$ for $R_I = 10^{11}$ cm, $R_o = 10^{12}$ cm and $M^*_{Ni} \geq 1\,M_\odot$ for $R_o = 10^{13}$ cm, with M_{Ni^*} increasing from $T = 10^6$ to 10^7 K. Such high values of Ni mass suggest that the line emitting material is a SN remnant. (Note that up to this point no ad hoc assumption about the presence of the SN event has been made.) The same conclusion is reached using $R_I = 10^{12}$ cm: in this case $\theta \sim 0.1$ rad favours $T \sim 10^6$ K (see Fig. 3.39). We underline that in this scenario the giant flare that dominates the early XRT ligth curve can not be identified with the ionizing source: in Sect. 3.7.5 we derived $\theta \geq 5^\circ$. An undetected source of ionization is therefore required. Alternatively, non geometrical factors must be invoked to explain the delay between the arrival of direct continuum photons and line photons.

- However, in most cases *Swift* data do not support the existence of jet breaks: using high quality multi-wavelength data [35] concluded that no convincing case of achromatic break has been detected in *Swift* afterglows (the achromatic behaviour was not robustly established in the pre-*Swift* era). The same conclusion has been reached by [141], [201] and [23] in independent studies. Alternatively, the funnel opening angle might not be directly linked to the jet opening angle: in other words, the naive expectation $\theta \sim \theta_j$ might be wrong. These reasons drive us to explore the prediction of the reflection model for bigger θ.

- Moreover, in Sect. 3.7.5 we showed that the restarted activity of the GRB central engine might be the source of the observed line emission if the ionizing radiation is nearly isotropic and the material intercepts most of the ionizing flux. In that section we also showed that under the assumption that the reprocessing material is a SNR expanding at $v_{shell} \sim 10^9 \mathrm{cm\,s^{-1}}$, we obtain $\theta \sim 22^\circ$, 17° and 5° for progenitor radii of the order of 10^{11}, 10^{12} and 10^{13} cm respectively. In this scenario the SN shell expansion began ~ 3000 s before the first GRB emission detected by BAT. Consequently, at $t \sim 100$ s we have $R_o \sim R_p + 3 \times 10^{12}$ cm. With $M^*_{Ni} = 0.4 M_\odot$, we find that the detected emission requires $T \sim 10^7$ K for $\theta \sim 20^\circ$ (0.3 rad) regardless of the internal radius assumed. No prediction can be made about the stratification index.

- Applying the line photon collimation correction factor calculated in Sec. 3.7.1, our funnel opening angle estimates would be lowered by a factor of two. With reference to Fig. 3.20 we applied the correction only to $\theta < 10^\circ$.

- We move now to consider the internal electron density $n_{\rm I}$. Vietri et al. 2001 [197] report $n_{\rm e} \approx 10^{10}\,{\rm cm}$ for $R \approx 6 \times 10^{15}\,{\rm cm}$. Our distances are $\sim 10^{-3} - 10^{-4}$ the value reported by [197]. For this reason we expect electron densities $10^{9} - 10^{12}$ times higher. (This is only a very rough estimate). From Eq. 3.173 it is easy to show that:

$$n_{\rm I} = \frac{M^{*}_{\rm Ni}}{4\pi\mu_{\rm e} m_{\rm p} X R_{\rm I}^{\alpha} \cos(\theta) \int_{\rm R_I}^{\rm R_o} {\rm r}^{2-\alpha}{\rm dr}} \tag{3.180}$$

For $\alpha = 0$, $M^{*}_{\rm Ni} = 0.4\,{\rm M}_{\odot}$, $R_{\rm I} = 10^{11}\,{\rm cm}$ and $R_{\rm o} = 3 \times 10^{12}\,{\rm cm}$ ($v_{\rm shell} \times t_{\rm SN} = 10^{9} \times 3000\,{\rm cm}$) we obtain $n_{\rm I} X = 4 \times 10^{18}$, 4×10^{18}, $7 \times 10^{18}\,{\rm cm}^{-3}$ for $T = 10^{6}$, 10^{7} and $10^{8}\,{\rm K}$ respectively. Using instead $R_{\rm I} = 10^{12}\,{\rm cm}$, $R_{\rm o} = 10^{13}\,{\rm cm}$ and leaving the value of the other parameters unchanged we have: $n_{\rm I} = 10^{17}$, 10^{17}, $5 \times 10^{17}\,{\rm cm}^{-3}$ for $T = 10^{6}$, 10^{7} and $10^{8}\,{\rm K}$ respectively.

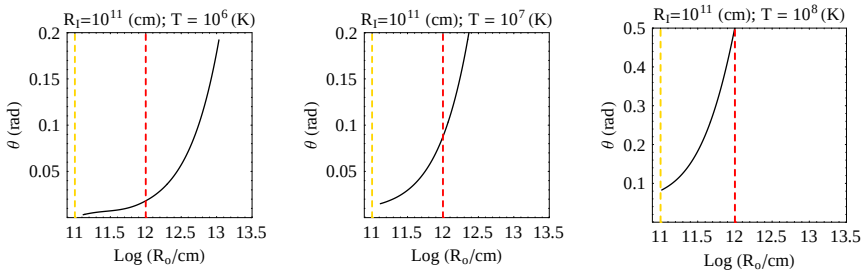

Fig. 3.40: Nickel mass contour plot according to Eq. 3.179 for $\alpha = 0$, $R_{\rm I} = 10^{11}\,{\rm cm}$ and different electron temperatures. Black solid line: $M^{*}_{\rm Ni} = 0.4\,{\rm M}_{\odot}$; red dashed line: $R_{\rm o} = 10^{12}\,{\rm cm}$, order of magnitude of the distance between the ionizing photons source and the reprocessing material derived from geometrical considerations see Sec. 3.5; orange dashed line: $R_{\rm I} = 10^{11}\,{\rm cm}$.

Models with $\alpha \,! = 1$

For small α (i.e. $\alpha < 1$) the model is not particularly sensitive to the variation of this parameter. Only for $\alpha \geq 1$ the differences become important. In particular it is easy to show that increasing α (i.e. increasing the importance of the stratification) we can reproduce the detected line emission with smaller funnel opening angles. Obviously, the models with internal radius $R_{\rm I} = 10^{11}\,{\rm cm}$ are more sensitive to the change of the stratification index α.

The dependence of the model on the value of the stratification index α is clear from Fig. 3.42 and 3.43: at a fixed outer radius, $\alpha = 1$ requires smaller values of the funnel opening angle and higher values of the internal electron density. While the $\theta - R_{\rm o}$ relation is nearly insensitive to the variation of this parameter,

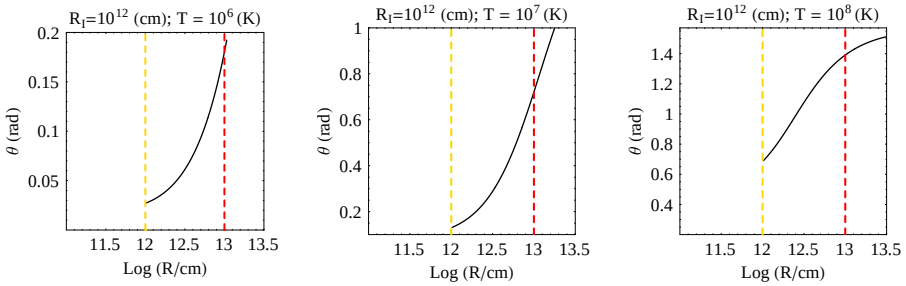

Fig. 3.41: Nickel mass contour plot according to Eq. 3.179 for $\alpha = 0$, $R_{\rm I} = 10^{12}$ cm and different electron temperatures. Black solid line: $M^{*}_{\rm Ni} = 0.4\,{\rm M}_{\odot}$; red dashed line: $R_{\rm o} = 10^{13}$ cm, order of magnitude of the distance between the ionizing photons source and the reprocessing material derived from geometrical considerations see Sec. 3.5; orange dashed line: $R_{\rm I} = 10^{12}$ cm.

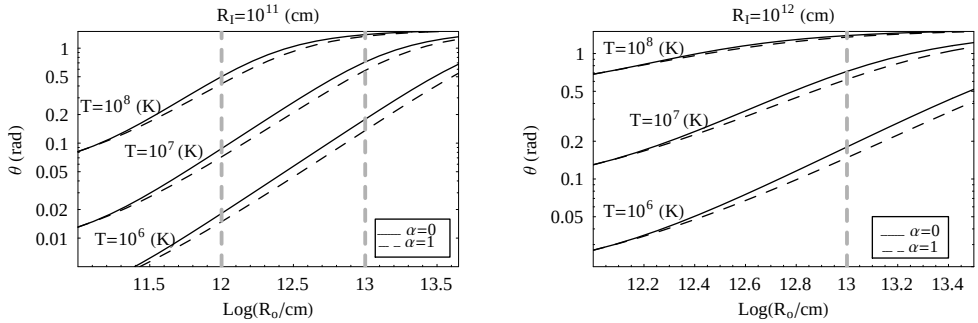

Fig. 3.42: Funnel opening angle (θ) versus outer shell radius ($R_{\rm o}$) according to Eq. 3.179. A total Ni mass $M^{*}_{\rm Ni} = 0.4\,{\rm M}_{\odot}$ has been assumed (see the text for explanations). Results are shown for $R_{\rm I} = 10^{11}$ cm (left panel) and $R_{\rm I} = 10^{12}$ cm (right panel). In both panels the realtion is shown for three different temperatures: 10^6 K (bottom), 10^7 K and 10^8 K (top). Solid (dashed) black lines correspond to $\alpha = 0$ ($\alpha = 1$). Dashed grey lines: $R_{\rm o} = 10^{12}, 10^{13}$ cm.

as α increases from 0 to 1, $n_{\rm I}$ increases by a factor $\approx 10^1 - 10^2$ (Fig. 3.43). Figure 3.42 shows the variations of the characteristic quantities of the problem assuming a total Ni mass of 0.4 $\rm M_{\odot}$: for $T = 10^6$ K, $R_{\rm I} = 10^{11}$ cm, $R_{\rm o} = 10^{12}$ cm the model requires $\theta \approx 0.02$ rad ($\alpha = 0$). Increasing the electron temperature to 10^7 K (10^8 K) and keeping $\alpha = 0$, the opening angle increases to 0.07 rad (0.34 rad). The corresponding internal electron density is $n_{\rm I} \approx 10^{20}\,{\rm cm}^{-3}$.

3.9 Conclusions

Moretti et al. 2007 [126] recently reported the detection of a spectral feature statistically not consistent with the standard single power law behaviour in

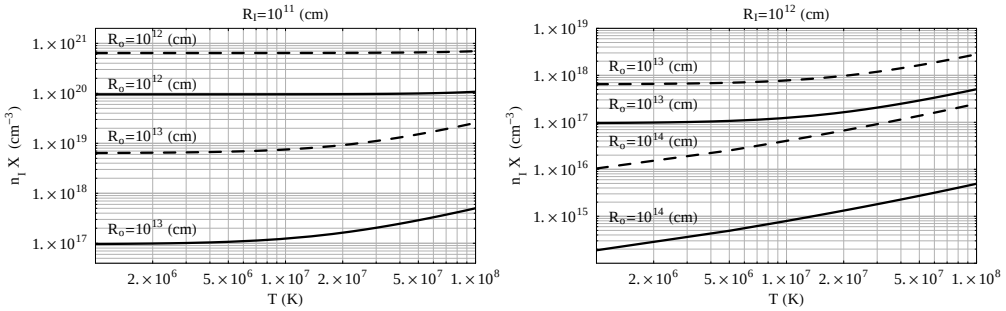

Fig. 3.43: Internal electron density $n_{\rm I}$ times the Ni abundance ratio $X = M^*_{\rm Ni}/M$ as a function of the temperature. A total Ni mass $M^*_{\rm Ni} = 0.4\,{\rm M}_\odot$ has been assumed (see the text for explanations). Left (right) panel: $R_{\rm I} = 10^{11}\,{\rm cm}$ ($R_{\rm I} = 10^{12}\,{\rm cm}$). In both panels results are shown for different values of the outer radius of the SN shell $R_{\rm o}$. Solid (dashed) lines: $\alpha = 0$ ($\alpha = 1$).

GRB 060904B spectra. The emission has been detected $\approx 10^2\,{\rm s}$ after the onset of the GRB, lasted more than 48 s with an isotropic luminosity of $\approx 10^{47}\,{\rm erg\,s^{-1}}$ (three orders of magnitude grater than the previous claimed detections). From the spectroscopical point of view, the detected feature can be interpreted as He-like or H-like Ni emission. Given the poor statistics it is not possible to discuss the line profile.

The peculiarity of the detection motivated us to explore in detail the theoretical implications of the presence of highly ionised Ni emitting $\approx 10^2\,{\rm s}$ after the burst. Given the typical $\tau_{\rm T} \gg 1$ (Sect. 3.6) only reflection models have been considered. Within these models, the external reflection scenario fails to predict the observed luminosity when standard values of the wind velocity and mass loss rate of the progenitor star are used. On the other hand, *if* this is Ni line emission, the detected feature can be interpreted in a funnel scenario with the line produced in reflection and typical Ni masses of the order of $0.1\,{\rm M}_\odot$ for $\theta = \theta_j \sim 5^\circ$, $T \sim 10^6\,{\rm K}$. Such high values of Ni masses strongly suggest the presence of a SN explosion associated with the GRB event. Alternatively, *if* the reprocessing material is a SNR and *if* the giant X-ray flare that dominates the early XRT light curve is the ionizing source, the expansion of the SN shell began $\approx 3000\,{\rm s}$ before the GRB detection, $M^*_{\rm Ni} \sim 0.4\,{\rm M}_\odot$, $\theta \sim 20^\circ$ and $T \sim 10^7\,{\rm K}$. These models imply mean electron densities $n_{\rm e} \sim 10^{21}\,{\rm cm^{-3}}$ for ten times solar metallicity ($X \sim 10^{-2}$).

Finally, GRB jets might be structured, with angle-dependent energy per solid angle and Lorentz Γ factor as well: power-law jets or Gaussian jets have been recently proposed in the literature (see e.g. [210]). Unfortunately, the jet angular structure is still unknown: for this reason no assumption has been made about the angular distribution of the jet energy. As a consequence, our results have been calculated assuming that the detected radiation is representative of the whole emitted radiation, regardless of the direction of emission. However,

it is important to underline that in the most realistic situation the emission properties of the ionizing continuum are likely to change with θ.

In conclusion, starting from simple analytical models, we presented a consistent scenario in which the line emission can in principle arise. Given the importance of the claim, the subject certainly calls for a deeper study.

4. GRB090111: EXTRA SOFT STEEP DECAY EMISSION AND PECULIAR RE-BRIGHTENING

4.1 Abstract

I present a detailed study of GRB 090111, focusing on its extra soft power-law photon index $\Gamma > 5$ at the very steep decay phase emission (power-law index $\alpha = 5.1$, steeper than 96% of GRBs detected by *Swift*) and the following peculiar X-ray re-brightening. Our spectral analysis supports the hypothesis of a comoving Band spectrum with the the peak of the νF_ν spectrum evolving with time to lower values: a period of higher temporal variability in the 1-2 keV light-curve ends when the $E_{\rm peak}$ evolves outside the energy band. The X-ray re-brightening shows extreme temporal properties when compared to a homogeneous sample of 82 early flares detected by Swift. While an internal origin cannot be excluded, I show these properties to be consistent with the energy injection in refreshed shocks produced by slow shells colliding with the fastest ones from behind, well after the internal shocks that are believed to give rise to the prompt emission have ceased.

4.2 Introduction

The unprecedented fast re-pointing capability of Swift ([53]) has ushered in a new era in the study of Gamma Ray Bursts (GRB) sources. A canonical picture of the X-ray afterglow light-curve emerged (see e.g. [134]), with five different components describing the overall structure observed in the majority of events: an initial steep decay, a shallow-decay plateau phase, a normal decay, a jet-like decay component as well as randomly occuring flares.

The steep decay phase smoothly connects to the prompt emission (e.g. [189]), with a typical temporal power law decay index between 2 and 4 ([44]): this strongly suggests a common physical origin. The observed spectral softening with time challenges the simplest version of the most popular theoretical model for this phase, the High Latitude Emission (HLE) model ([50]; [93]): according to this scenario, steep decay photons originate from the delayed prompt emission from different viewing latitudes of the emitting area ([214]) and are expected to lie on a simple power law (SPL) spectral model. The $0.3 - 10\,$keV spectrum of the steep decay phase is generally consistent with the expected SPL behaviour with a typical photon index $\Gamma \sim 2$ (see [44]); however, a careful inspection of the GRBs with the best statistics reveals that alternative explanations are required

(see e.g. [218]; [157]). Deviations from the SPL spectral model are therefore of particular interest.

Flares have been found to be a common feature of early X-ray afterglows: with a typical duration over occurrence time $\Delta t/t \sim 0.1$ ([30]) and a Band spectrum ([7]) reminiscent of the typical spectral shape of the prompt emission ([46]), they are currently believed to be related to the late time activity by the central engine. In spite of the growing statistics their origin is still an open issue.

I analyse and discuss how and if the extra soft ($\Gamma > 5$) steep decay emission of GRB 090111 fits into different theoretical models; particular attention will be devoted to the possible link with the detected soft prompt $15 - 150$ keV emission. After the steep decay, the GRB 090111 $0.3 - 10$ keV light-curve shows a peculiar re-brightening, with extreme properties when compared to typical X-ray flares: alternative explanations are discussed. The paper is organised as follows: observations are described in Sect. 4.3; the details of the data analysis are reported in Sect. 4.4. Our results are discussed in Sect. 4.5. Conclusions are drawn in Sect. 4.6. Uncertainties and upper limits are quoted at the 90% confidence level (c.l.) unless otherwise stated.

4.3 Swift observations

The Swift Burst Alert Telescope (BAT; [8]) triggered and located GRB 090111 at 23:58:21 UT on 2009-01-11. The spacecraft immediately slewed to the burst allowing the X-ray Telescope (XRT; [24]) and the UV/Optical Telescope (UVOT, [167]) to collect data starting 76.6 s and 86 s after the trigger, respectively. A refined position was quickly available:
R.A.(J2000)=$16^{\rm h}46^{\rm m}42.14^{\rm s}$, Dec.(J2000)=$+00°04'38.2$" with a 90% error radius of 1.7 arcsec ([45]). No source was detected by the UVOT at the X-ray afterglow position [81]. No prompt ground based observation was reported, probably due to the vicinity (46°) to the Sun.

The data were processed with the HEASOFT v. 6.6.1 package and corresponding calibration files: standard filtering and screening criteria were applied. BAT data analysis was based on the event data recorded from -240 s to 960 s. XRT data were acquired in Windowed Timing (WT) mode until around 150 s; after that time the XRT automatically switched to the Photon Counting (PC) mode to follow the decaying source photon flux. Between $\sim 150 \sim 690$ s PC data were affected by pile-up: in this time interval an annular region of events extraction with the exclusion radius estimated following the prescriptions of [125] was used instead of a circular region. The resulting $0.3 - 10$ keV light-curve is shown in Fig. 4.2: the chosen data binning assures a minimum signal to noise ratio (SNR) equal to 4; when single orbit data were not able to fulfil this requirement, data coming from different orbits were merged to build a unique data point.

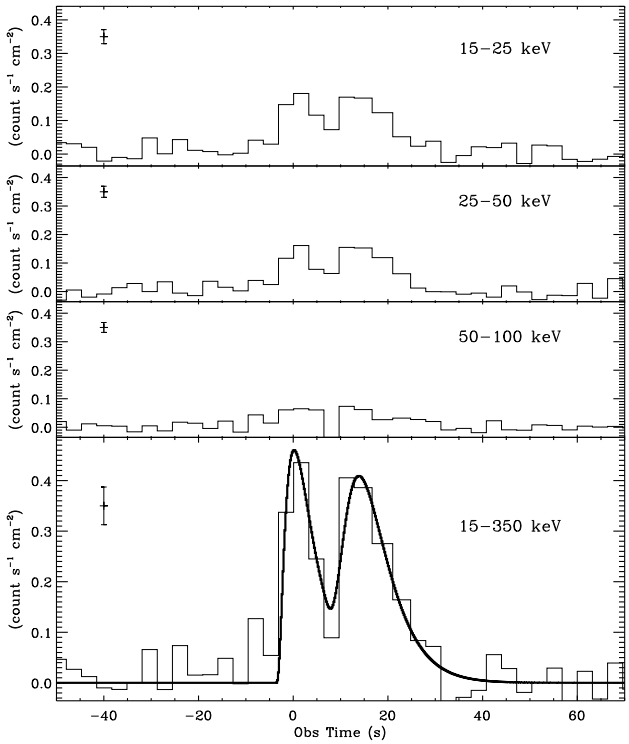

Fig. 4.1: BAT mask weighted light-curve in different energy bands (binning time of 3.2 s). No signal is detected above 100 keV. Bottom panel, solid black line: $15 - 350$ keV light-curve best fit. The typical 1σ error size is also shown in each panel.

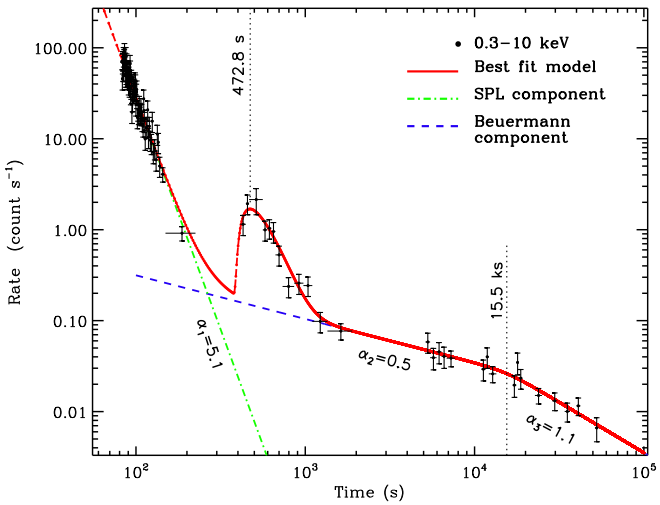

Fig. 4.2: XRT $0.3-10\,\mathrm{keV}$ light-curve with best fit superimposed.

4.4 Analysis and results

The BAT light curve (Fig. 4.1) shows a double-peaked structure with $T_{90}(15-350\,\mathrm{keV}) = 24.8 \pm 2.7\,\mathrm{s}$ ([185]). It can be fit using two [133] profiles peaking at $t_{\mathrm{peak},1} = 4.2 \pm 1.2\,\mathrm{s}$ and $t_{\mathrm{peak},2} = 9.3 \pm 1.1\,\mathrm{s}$; the two structures are characterised by a $1/e$ rise and decay times $t_{\mathrm{rise},1} = 2.6 \pm 0.5\,\mathrm{s}$, $t_{\mathrm{decay},1} = 6.6 \pm 0.5\,\mathrm{s}$, $t_{\mathrm{rise},2} = 4.5 \pm 0.4\,\mathrm{s}$, $t_{\mathrm{decay},2} = 8.8 \pm 1.3\,\mathrm{s}$ and a width $w_1 = 9.1 \pm 1.0\,\mathrm{s}$ and $w_2 = 13.3 \pm 1.6\,\mathrm{s}$. The amplitude is $A_1 = 0.46 \pm 0.13\,(\mathrm{count\,s^{-1}\,cm^{-2}})$ and $A_2 = 0.38 \pm 0.04\,(\mathrm{count\,s^{-1}\,cm^{-2}})$. The parameters are defined following [133], while their uncertainty is computed accounting for their covariance and quoted at 68% c.l.

The time averaged BAT spectrum can be fit by a soft single power-law photon index $\Gamma = 2.37 \pm 0.18$ with a total fluence $S(15-150\,\mathrm{keV}) = (6.2 \pm 1.1) \times 10^{-7}\,\mathrm{erg\,cm^{-2}}$ ($\chi^2/\mathrm{dof} = 55.92/56$). The fluence ratio $S(25-50\,\mathrm{keV})/\mathrm{S}(50-100\,\mathrm{keV}) = 1.29 \pm 0.20$ (68% c.l.) places GRB 090111 at the boundary between X-Ray Rich (XRR) and X-Ray Flash (XRF) events according to the classification of [171]. The BAT data alone are not able to constrain the E_{p} parameter (peak energy of the νF_ν spectrum): however, fixing the low energy photon index α_{B} of a Band model at -1 (typical value for both GRBs and XRFs, see e.g. [170]) I derive $E_{\mathrm{p}} < 32\,\mathrm{keV}$. Using the $E_{\mathrm{p}} - \Gamma$ relation developed by [172] we have $E_{\mathrm{p}} < 27\,\mathrm{keV}$, in agreement with the previous result.

The X-ray light-curve (Fig.4.2) exhibits a steep decay which is best fit by a simple power law with index $\alpha_1 = 5.1 \pm 0.2$ ($\alpha_1 = 4.6 \pm 0.2$) and $T_0 = 0$ s ($T_0 = 9.3$ s, peak time of the second prompt pulse). This is followed by a re-brightening which dominates the light-curve between 420 and 900 s. During this time period no detection can be reported in the 15-150 keV energy range. After the re-brightening the light curve flattens to a simple power law index $\alpha_2 =$

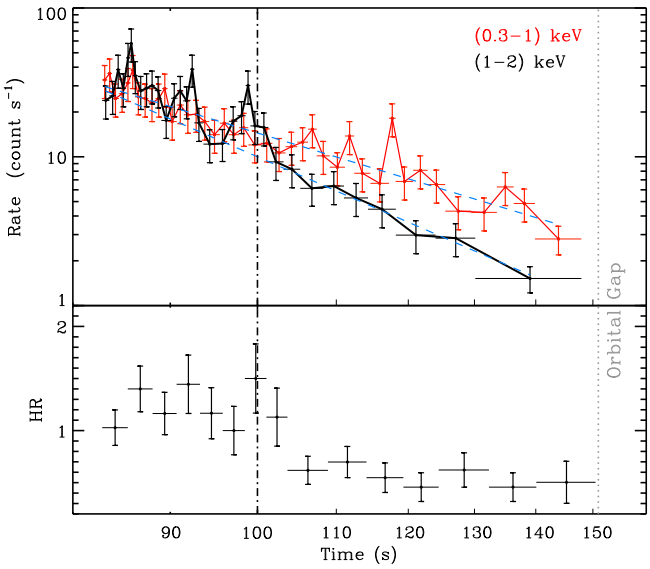

Fig. 4.3: Upper panel: red (black) points: $0.3-1$ keV ($1-2$ keV) XRT light-curve rebinned at constant signal to noise ratio SNR $= 4$. Blue dashed lines: best fit simple power law models. Lower panel: hardness ratio HR $= (1-10)$keV$/(0.3-1)$keV evolution with time. The dashed-dotted vertical line marks the beginning of the HR decrease.

0.5 ± 0.2, while starting from 15 ks the count rate decays as $\alpha_3 = 1.1 \pm 0.3$ (Fig. 4.2). The re-brightening can be fit adding a [133] component with amplitude $A = 1.53 \pm 0.23$ count s^{-1}, start time $t_s = 370$ s (χ^2/dof $= 84.8/93$) and rise and decay times $t_{rise} = 69.3 \pm 8.9$ s $t_{decay} = 212.3 \pm 37.5$ s; a width $w = 281.6 \pm 39.2$ s; a peak time $t_{peak} = 472.8 \pm 21.0$ and an asymmetry parameter $k = 0.51 \pm 0.04$ of [133]. This implies a T_{90} of ~ 675 s. In this time interval, the light-curve experiences a re-brightening to underlying continuum fluence ratio $S_{reb}/S_{cont} \sim 4.7$, while the relative flux variability is $\Delta F/F = 14.2 \pm 2.1$ (where ΔF is the re-brightening contribution to the total flux at t_{peak} and F is underlying power-law flux at the same time). All uncertainties related to the light-curve fitting are quoted at 68% c.l.

The steep decay spectrum ($77\,\mathrm{s} < t < 150\,\mathrm{s}$) can be modelled using an absorbed simple power-law with photon index $\Gamma = 5.1 \pm 0.4$ and neutral hydrogen column density $N_{H,0} = (4.9 \pm 0.8) \times 10^{21}$ cm^{-2} in excess of the Galactic value in this direction which is 6.5×10^{20} cm^{-2}, [85] (χ^2/dof $= 68.77/49$).While a pure black body emission model is ruled out, the addition of a black body component statistically improves the fit: however, the data are not able to simultaneously constrain the black body temperature and intrinsic absorption so that only rough 2σ limits can be quoted: $0.2\,\mathrm{keV} < \mathrm{kT_b} < 0.8\,\mathrm{keV}$, $(0.5 < \mathrm{N_{H,0}} < 5) \times 10^{22}$ cm^{-2}. The X-ray data can alternatively be fit by simultaneously modelling

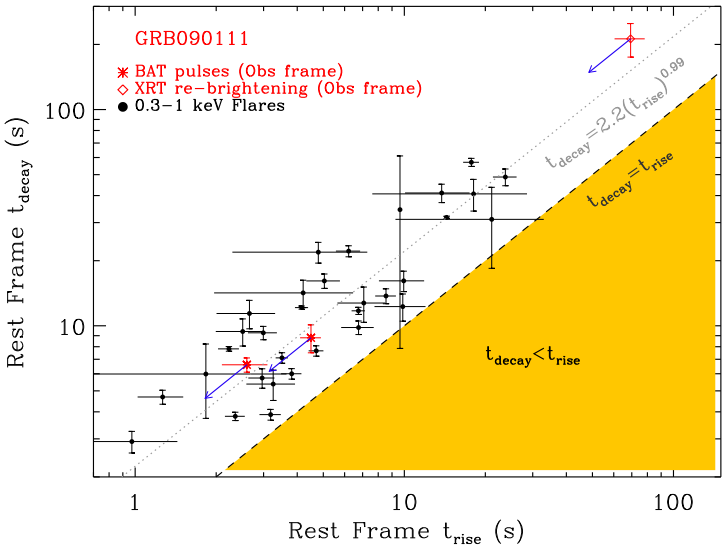

Fig. 4.4: Decay time versus rise time for a sub-sample of 32 early time flares identified in the 0.3-10 keV energy range in GRBs with red-shift (Chincarini et al.2009 in prep.) and for GRB090111. The blue arrows track the shift of the data when the red-shift correction is applied. The black dashed line corresponds to the $t_{\rm decay} = t_{\rm rise}$ locus, while the best fit power-law model is indicated with a grey dotted line: $t_{\rm decay} = (2.2 \pm 0.1) t_{\rm rise}^{(0.99 \pm 0.02)}$ (1σ c.l.).

the Galactic and host absorption at the proper redshift. I find two sets of allowed parameters: the first is for a close GRB with $\rm N_{H,z} = (0.63^{+0.14}_{-0.09}) \times 10^{22}\,cm^{-2}$, $z = 0.5^{+0.2}_{-0.3}$ and $\Gamma = 4.4 \pm 0.2$ (χ^2/dof = 40.5/49, Pval = 80%). The second solution is for a distant and heavily absorbed GRB: $\rm N_{H,z} = (8.8^{+2.8}_{-6.1}) \times 10^{22}\,cm^{-2}$, $z = 3.8^{+0.2}_{-0.3}$ and $\Gamma = 4.0 \pm 0.2$ (χ^2/dof = 48.6/49, Pval = 49%). The fit is not able to constrain the redshift parameter: however the detection of $N_{\rm H,z}$ in excess of the Galactic value (at $z = 0$) suggests $z < 1.8$ according to the [74] relation.

Spectral evolution is apparent from Fig. 4.3, with the $(1-2)\,$keV$/(0.3-1)\,$keV hardness ratio starting to decrease 100 s after the trigger: it is interesting to note that this corresponds to the end of a period of higher temporal variability detected in the $1-2\,$keV light-curve. This kind of variability is not seen in the $0.3-1\,$keV data. A comparison of the light-curves extracted in the two energy bands reveals a depletion of high energy photons with time: while the $0.3-1\,$keV best fit simple power-law decay index is $\alpha_1 = 4.3 \pm 0.3$, the continuum higher energy ($1-2\,$keV) photon flux decay is steeper, being modelled by $\alpha_2 = 5.6 \pm 0.5$.

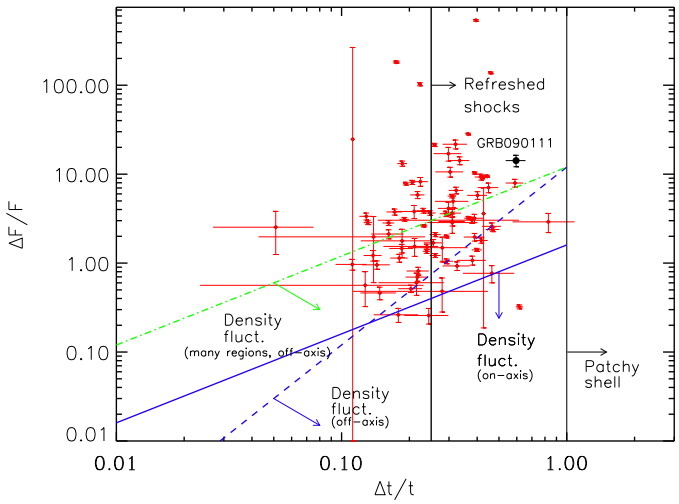

Fig. 4.5: Relative variability flux ($\Delta F/F$) kinematically allowed regions as a function of relative variability time scale $\Delta t/t$ for a sample of 81 early ($t_{\rm peak,obs} < 1000$ s) flares identified in 54 different GRBs (Chincarini et al. 2009 in prep.). The three limits shown have been computed according to Eq. 7 and A2 of Ioka et al. 2005. The position of GRB 090111 is marked with a filled black dot.

4.5 Discussion

4.5.1 Unusual spectral properties

GRB 090111 shows a very steep ($\alpha = 5.1 \pm 0.2$, 68% c.l.) and soft decay (spectral index $\beta = 4.1 \pm 0.4$): out of 295 GRB X-ray light-curves showing the canonical steep-shallow-normal decay transition analysed by [44], only 11 (4%) events are characterised by an initial power law index steeper than the one observed in GRB 090111. Such a high value suggests that this is the beginning of the tail of a flare whose onset was missed by the XRT. The spectral analysis leads to the same conclusion: out of 1242 time resolved XRT spectra of *Swift*-GRB in the time period April 2005 - September 2008, we found the existence of very soft absorbed simple power-law photon indices $\Gamma > 5$ in GRB050714B, GRB050822 and GRB060512: in each of these cases, the soft spectral emission is linked to flare activity in the XRT light-curve. (The three bursts also show a soft BAT prompt emission, with a time averaged 15-150 keV photon index $\Gamma \sim 2.4 - 2.5$). If this is the case, the comoving spectrum is likely to be a Band spectrum whose $E_{\rm peak}$ evolves to lower values.

Both the BAT prompt photon index steeper than 2, and the XRT photon index $\Gamma > 4$ steeper than the typical Band low-energy photon index $\alpha_{\rm B} \sim -1$ (see e.g. [86], [170]) suggest that in both cases the observed emission is dominated by the beta portion of the comoving Band spectrum. It is interesting

to note that fixing $\alpha_B \sim -1$ in the prompt spectrum we obtain $28\,\mathrm{keV} < \mathrm{E_{peak}} < 30\,\mathrm{keV}$ at 3σ level for a high energy photon index $-5 < \beta_\mathrm{B} < -4$ which matches the unusual value of the high energy photons index measured in XRT. This establishes a spectral connection between the XRT steep decay and the prompt emission, provided that the E_peak had shifted well inside the XRT energy range by the beginning of the observation as found in other GRBs and XRFs (e.g. GRB060614, [111]; XRF 050416A, [112]). At the same time the very soft emission observed extends the distribution in β_B to very low values: only $\sim 10\%$ of the spectra of 156 BATSE GRBs either have $\beta_\mathrm{B} < -4$ or do not have any high energy component (see e.g. [86]).

During the steep decay spectral evolution is apparent (Fig. 4.3, lower panel). I split the steep decay phase into two time intervals, taking 100 s as dividing line as suggested by the hardness ratio evolution. A simultaneous fit of the two spectra with an absorbed cut-off power-law model (with E_peak as a free parameter of the fit) shows that for each $(N_\mathrm{H,z}, z)$ couple there exists a statistically acceptable solution with $E_\mathrm{peak,1} = 1.0^{+0.2}_{-0.1}\,\mathrm{keV}$ and $E_\mathrm{peak,2} < 0.3\,\mathrm{keV}$, where the subscripts 1 and 2 refer to the first ($t < 100\,\mathrm{s}$) and second ($t > 100\,\mathrm{s}$) time interval, respectively. This suggests that the detected spectral evolution can be linked to the evolution of the E_peak to lower values. It is worth noting that the higher temporal variability characterising the 1-2 keV signal in the first 100 s (Fig. 4.3) disappears as the peak energy evolves outside the energy band.

4.5.2 Peculiar re-brightening: a flare?

Interpreting the X-ray re-brightening as onset of the afterglow, it is possible to infer the initial Lorentz factor Γ_0 of the fireball from the light-curve peak time (see [124] and references therein). For a homogeneous surrounding medium with particle density $n_0 = 1\,\mathrm{cm}^{-3}$, radiative efficiency $\eta = 0.2$ we have $\Gamma_0 \sim 180(1+z)^{3/8}(E_\gamma/10^{53}\mathrm{erg})^{1/8}$. From $z < 1.8$ we derive an intrinsic peak energy $E_\mathrm{p,i} < 84\,\mathrm{keV}$ and isotropic energy $E_\mathrm{iso} < 9 \times 10^{51}\,\mathrm{erg}$ (well within the 2σ region of the [2] relation). This translates into a conservative upper limit $\Gamma_0 < 100$: this is lower than what is commonly found for normal GRBs ($\Gamma_0 \sim 500$, see e.g. [124]), and consistent with the less-Lorentz-boosted interpretation of XRRs and XRFs (see [217] for a review). A similar result has been found for other XRFs: see e.g. XRF080330 ([79]).

In the context of off-axis emission, it is worth noting that the X-ray re-brightening experienced by GRB 090111 is a sharp feature, reaching a flux contrast $\Delta F/F \sim 14$ during a rising time of only $\sim 70\,\mathrm{s}$. [70] showed that both on-axis and off-axis decelerating jets can only produce smooth bumps in the afterglow emission. We therefore consider this hypothesis unlikely.

A much more likely explanation is suggested by Fig. 4.4 where the temporal properties of the GRB 090111 BAT pulses and of the XRT re-brightening are shown to be consistent with the best fit relation found for the intrinsic properties of 32 0.3-10 keV early time flares (Chincarini et al. 2009, in prep.). This fact, together with the consistency with the typical $t_\mathrm{rise}/t_\mathrm{decay} \sim 0.3 - 0.5$ ([132]) found for prompt pulses, would suggest a common internal shock origin.

Alternatively the bump could be due to refreshed shocks ([163]). Following the calculations of [83] we plot in Fig. 4.5 the $\Delta F/F$ and $\Delta t/t$ values for the X-ray bump of GRB 090111 together with the values coming from a homogeneous analysis of 82 early ($t_{\rm peak} < 1000\,$s) flares identified in 54 different GRBs by Chincarini et al. 2009 in prep.: all the flares (including the GRB 090111 bump) were fit using the same [133] profile, defining the width of each pulse as the time interval between the $1/e$ intensity points. Figure 4.5 shows the kinematically allowed regions for bumps produced by density fluctuations ([199]; [101]; [37]) seen on-axis, off-axis and by many regions according to eq. 7 and A2 in [83]; bumps due to patchy shells ([120]; [94]) occupy the $\Delta t > t$ region, while refreshed shocks account for the $\Delta t > t/4$ area. From this figure it is apparent that the X-ray bump of GRB 090111 lies in the refreshed shocks region: density fluctuations are ruled out.

4.6 Conclusions

GRB 090111 shows an extra soft $\Gamma > 5$ steep decay emission. This is likely due to an intrinsic Band spectrum whose low energy power law is missed because of the limited energy range of the XRT. The peak energy of the spectrum evolves through the XRT band producing a softening trend testified by the different light-curve decay behaviours in different energy bands. It's interesting to note that the period of higher temporal variability in the 1-2 keV light-curve ends when the $E_{\rm peak}$ shifts outside the energy band. The steep decay is followed by an X-ray re-brightening whose peculiar temporal properties made it worth a detailed study. While the temporal properties of the re-brightening are consistent with an internal origin, with $\Delta t/t \sim 0.6$ and $\Delta F/F \sim 14$ the bump lies in the refreshed shocks region of Fig. 4.5. Density fluctuations are ruled out. Finally, with a fluence ratio $S(25-50\,{\rm keV})/{\rm S}(50-100\,{\rm keV}) = 1.29 \pm 0.20$ (68% c.l.) I propose this event to be classified as XRR 090111.

5. GRB081028

GRB081028 paves the way to a different physical origin of the prompt plus steep decay phases vs late afterglow emission components and reveals the persistent activity of the central engine during the steep decay.

5.1 Abstract

Swift captured for the first time a smoothly rising X-ray re-brightening of clear non-flaring origin after the steep decay in a long gamma-ray burst (GRB): GRB 081028. This offers the precious opportunity to study for the first time the rising phase which is likely present in all GRBs but is usually hidden by the prompt tail emission. This constitutes the first manifestation of what is later to give rise to the shallow decay phase. Contemporaneous optical observations reveal a rapid evolution of the injection frequency of a fast cooling synchrotron spectrum through the optical band, which disfavours the onset of the forward shock as the outflow decelerates as the origin of the observed re-brightening. We investigate alternative origins and show that the observations are consistent with the off-axis jet predictions. However, the high energy budget required by this interpretation suggests a different physical origin for the prompt and steep decay phases vs. the afterglow emission component.

Strong spectral softening takes place from the prompt to the steep decay phase with the peak energy of the νF_ν spectrum evolving as fast as t^{-7}. We track the evolution of the spectral peak energy from the γ-rays to the X-rays and highlight the problems of the commonly assumed high latitude and adiabatic cooling interpretations. An abrupt switch-off of the central engine after the prompt emission is disfavored: the detected spectral evolution requires some forms of persistent central engine activity during the steep decay. Notably, a softening of both the high and low spectral slopes with time is also observed. We discuss the low on-axis radiative efficiency of GRB 081028 comparing its properties against a sample of *Swift* long GRBs with secure $E_{\gamma,\mathrm{iso}}$ measurements: the efficiency results are consistent with the different physical origin hypothesis of the prompt and re-brightening components.

5.2 Introduction

Gamma ray bursts (GRBs) are transient events able to outshine the γ-ray sky for a few seconds to a few minutes. The discovery of their optical [144] and X-ray [31] long-lasting counterparts represented a breakthrough for GRB science. Unfortunately, due to technological limitations, the X-ray observations were able to track the afterglow evolution starting hours after the trigger: only after the launch of the *Swift* satellite in 2004 [53] was this gap between the end of the prompt emission and several hours after the onset of the explosion filled with X-ray observations. A canonical picture was then established (see e.g., [134]), with four different stages describing the overall structure of the X-ray afterglows: an initial steep decay, a shallow-decay phase, a normal decay and a jet-like decay stage. Erratic flares are found to be superimposed mainly to the first and second stage of emission. An interesting possibility is that the four light-curve phases instead belong to only two different components of emission (see e.g., [201]): the first, connected to the activity of the central engine giving rise to the prompt emission, comprises the flares ([30] and references therein) and the steep-decay phase; the second is instead related to the interaction of the outflow with the external medium and manifests itself in the X-ray regime through the shallow, normal and jet-like decay. Observations able to further characterise the two components are therefore of particular interest.

The smooth connection of the X-ray steep decay light-curve phase with the prompt γ-ray emission strongly suggests a common physical origin ([189]; [135]): the High Latitude Emission (HLE) model ([50]; [93]) predicts that steep decay photons originate from delayed prompt emission from different viewing latitudes of the emitting area, giving rise to the $\alpha = \beta + 2$ relation (where α is the light-curve decay index and β is the spectral index). No spectral evolution is expected in the simplest formulation of the HLE effect in the case of a simple power-law prompt spectrum. Observations say the opposite: significant variations of the photon index have been found in the majority of GRBs showing a steep decay phase (see e.g., [214]); more than this, the absorbed simple power-law (SPL) has proved to be a poor description of the spectral energy distribution of the GRBs with the best statistics [1]. A careful analysis of these events has shown their spectra to be best fit by an evolving Band function [7], establishing the link between steep decay and prompt emission photons also from the spectral point of view (see e.g., GRB 060614, [111]; GRB 070616, [187]): caused by the shift of the Band spectrum, a temporal steep decay phase and a spectral softening appear simultaneously (see e.g. [218], [157]). In particular, the peak energy of the νF_ν spectrum is found to evolve to lower values, from the γ-ray to the soft X-ray energy range. Both the low (as observed for GRB 070616) and the high-energy portion of the spectrum are likely to soften with time, but no observation is reported to confirm the high energy index behaviour during the prompt and steep decay phase. The observed spectral evolution with time is an unvaluable

[1] The limited $0.3 - 10\,(\mathrm{keV})$ spectral coverage of the Swift X-Ray Telescope, XRT [24] and the degeneracy between the variables of the spectral fit can in principle lead to the identification of an SPL behaviour in intrinsically non-SPL spectra with poor statistics.

footprint of the physical mechanisms at work: observations able to constrain the behaviour of the spectral parameters with time are therefore of primary importance.

By contrast, no spectral evolution is instead observed in the X-ray during the shallow decay phase (see e.g. [105]) experienced by most GRBs between $\sim 10^2$ s and $10^3 - 10^4$ s. Unexpected discovery of the *Swift* mission, the shallow decay is the first light-curve phase linked to the second emission component. A variety of theoretical explanations have been put forward. The proposed models include: forward shock emission continuously fed by the central engine [141]; energy injection [213]; reverse shocks (see e.g., [55]); time dependent micro-physical parameters [84]; off-axis emission [68]; dust scattering [183]. The predictions of all these models can only be compared to observations tracking the flat and decay phase of the second emission component, since its rise is usually missed in the X-ray regime, being hidden by the tail of the prompt emission.

GRB 081028 is the first and unique event for which *Swift* was able to capture the rise of the second emission component [2]: the time properties of its rising phase can be constrained for the first time while contemporary optical observations allow to track the evolution of a break energy of the spectrum through the optical band. GRB 081028 is also one of the lucky cases showing a spectrally evolving prompt emission where the evolution of the spectral parameters can be studied from γ-rays to X-rays, from trigger time to ~ 1000 s. A hard to soft spectral evolution is clearly taking place beginning from the prompt emission and extending to the steep decay phase as already found for other *Swift* GRBs (GRB 060614, [111]; GRB 070616, [187], are showcases in this respect). Notably, for GRB 081028 a softening of the high-energy spectral slope is also observed.

The chapter is organised as follows: *Swift* and ground-based observations are described in Sect. 5.3; data reduction and preliminary analysis are reported in Sect. 5.4, while in Sect. 5.5 the results of a detailed spectral and temporal multi-wavelength analysis are outlined and discussed in Sect. 5.6. Conclusions are drawn in Sect. 5.7.

The phenomenology of the burst is presented in the observer frame unless otherwise stated. The convention $F(\nu, t) \propto \nu^{-\beta} t^{-\alpha}$ is followed, where β is the spectral index, related to the photon index Γ by $\Gamma = \beta + 1$. All the quoted uncertainties are given at 68% confidence level (c.l.): a warning is added if it is not the case. Standard cosmological quantities have been adopted: $H_0 = 70\,\mathrm{Km\,s^{-1}\,Mpc^{-1}}$, $\Omega_\Lambda = 0.7$, $\Omega_\mathrm{M} = 0.3$.

[2] There are a hand-full of events detected by *Swift* experiencing an early X-ray rise of non-flaring origin. Among them: GRB 070328; GRB 070714B; GRB 080205; GRB 080229A; GRB 080721 (see [139] and references therein). However, in none of these cases an X-ray steep decay has bee observed. A smooth rise in the X-rays has been observed in the short GRB 050724.

5.3 Observations

GRB 081028 triggered the *Swift* Burst Alert Telescope (BAT; [8]) on 2008-10-28 at 00:25:00 UT [76]. The spacecraft immediately slewed to the burst allowing the X-ray Telescope (XRT; [24]) to collect photons starting $T + 191$ s after the trigger: a bright and fading X-ray afterglow was discovered. The UV/Optical Telescope (UVOT, [167]) began observing at $T + 210$ s. In the first orbit of observations, no afterglow candidate was detected in any of the UVOT filters in neither the individual nor co-added exposures. A careful re-analysis of the acquired data revealed the presence of a source with a White band magnitude 20.9 at $\sim T + 270$ s (this paper). A refined position was quickly available thanks to the XRT-UVOT alignment procedure and the match of UVOT field sources to the USNO-B1 catalogue (see [59] for details): R.A.(J2000)=$08^{\rm h}07^{\rm m}34.76^{\rm s}$, Dec.(J2000)=$+02°18'29.8$" with a 90% error radius of 1.5 arcsec [43]. Starting at $\sim T + 9$ ks the X-ray light-curve shows a remarkable re-brightening [77]: this was later detected in ground-based NIR and optical observations.

The Telescope a Action Rapide pour les Objetcs Transitoires (TAROT; [88]) began observing 566.4 s after the trigger under poor weather conditions: no variable source was detected down to $R \sim 17.4$.

The optical afterglow was discovered by the Gamma-Ray Burts Optical and Near-Infrared Detector (GROND; [63]). The observations started 20.9 ks after the trigger: the afterglow was simultaneously detected in the $g'r'i'z'JHK$ bands [33] with the following preliminary magnitudes: $g' = 19.9 \pm 0.1$; $r' = 19.3 \pm 0.1$; $i' = 19.2 \pm 0.1$; $z' = 19.1 \pm 0.1$; $J = 19.0 \pm 0.15$; $H = 18.7 \pm 0.15$; $K = 19.0 \pm 0.15$, with a net exposure of 264 s and 240 s for the $g'r'i'z'$ and the JHK bands respectively. Further GROND observations were reported by [34] 113 ks after the trigger with 460 s of total exposures in $g'r'i'z'$ and 480 s in JHK. Preliminary magnitudes are reported below: $g' = 21.26 \pm 0.05$; $r' = 20.49 \pm 0.05$; $i' = 20.24 \pm 0.05$; $z' = 19.99 \pm 0.05$; $J = 19.6 \pm 0.1$. The source showed a clear fading with respect to the first epoch, confirming its nature of GRB afterglow.

The Nordic Optical Telescope (NOT) imaged the field of GRB 081028 ~ 6 hr after the trigger and independently confirmed the optical afterglow with an R band magnitude $R \sim 19.2$ [136].

An UV/Optical re-brightening was discovered by the UVOT starting $T +$ 10 ks contemporary to the X-ray re-brightening. The afterglow was detected in the v, b and u-band filters [182]. The UVOT photometric data-set of GRB 081028 is reported in Tab. 5.1. We refer to [155] for a detailed description of the UVOT photometric system.

The rising optical afterglow was independently confirmed by the Crimean telescope for Asteroid Observations (CrAO) and by the Peters Automated Infrared Imaging Telescope (PAIRITEL; [21]). CrAO observations were carried out starting at $\sim T + 1$ ks and revealed a sharp rising optical afterglow peaking after $T + 9.4$ ks: $R = 21.62 \pm 0.07$ at $t = T + 1.8$ ks; $I = 21.32 \pm 0.09$ at $t = T + 3.6$ ks; $I = 21.43 \pm 0.09$ at $t = T + 5.5$ ks; $I = 21.20 \pm 0.08$ at $t = T + 7.5$ ks; $I = 20.66 \pm 0.05$ at $t = T + 9.4$ ks [168].

PAIRITEL observations were carried out 40 ks after the trigger: the after-

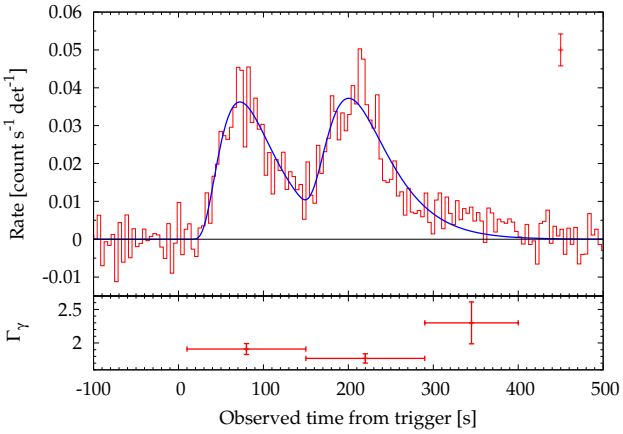

Fig. 5.1: Top panel: BAT 15-150 keV mask weighted light-curve (binning time of 4.096 s). Solid blue line: $15-150$ keV light-curve best fit using Norris et al., 2005 profiles. The typical 1σ error size is also shown. *Bottom panel:* best fit photon index Γ_γ as a function of time.

glow was simultaneously detected in the J, H, and Ks filters with a preliminary photometry $J = 17.7 \pm 0.1$, $H = 17.0 \pm 0.1$ and $Ks = 16.1 \pm 0.1$ [122].

A spectrum of GRB 081028 was taken with the Magellan Echellette Spectrograph (MagE) on the Magellan/Clay 6.5-m telescope at $\sim T + 27$ ks for a total integration time of 1.8 ks. The identification of absorption features allowed the measure of the redshift $z = 3.038$, together with the discovery of several intervening absorbers including Ly-alpha, SII, NV, SiIV, CIV and FeII [12].

According to [181] the Galactic reddening along the line of sight of GRB 081028 is $E(B-V) = 0.03$. [3]

5.4 Data Reduction and preliminary analysis

5.4.1 Swift-*BAT* data

BAT data have been processed using standard Swift-BAT analysis tools within *heasoft* (v.6.6.1). The burst has been detected in the part of the BAT field of view that was 85% coded. The ground-refined coordinates provided by [9] have been adopted in the following analysis. Each event recorded by BAT is mask-tagged using the *batmaskwtevt* at the source position. The BAT detector quality map is obtained by processing the nearest-in-time enable/disable map of

[3] [39] argue that the far-IR analysis of [181] overestimates the real $E(B-V)$ by a factor of $\sim 25\%$ and suggest scaling the previous value by that factor. We obtain $E(B-V) = 0.02$. The results presented in this paper do not depend on this correction: with this comment in mind, the [181] value $E(B-V) = 0.03$ is used throughout the paper.

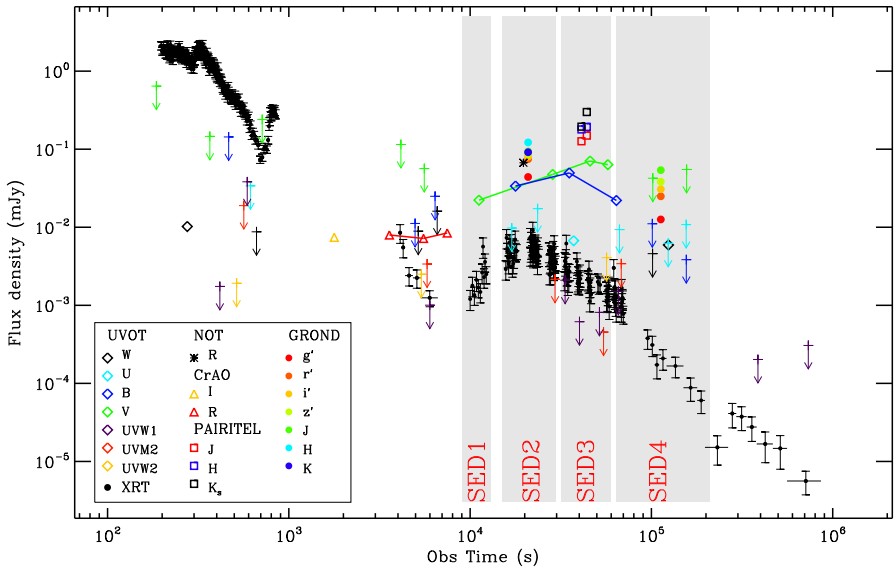

Fig. 5.2: Complete data set for GRB 081028 starting 200 s after the trigger including X-ray (XRT, 0.3-10 keV), UV/visible/NIR (UVOT, GROND, PAIRITEL, CrAO, NOT) observations. The arrows indicate 3σ upper limits of UVOT observations. The shaded regions indicate the time intervals of extraction of the SEDs.

the detectors. The mask-weighted background subtracted $15-150$ kev is shown in Fig. 5.1, top panel.

The mask-weighting procedure is also applied to produce weighted, background subtracted counts spectra using the tool *batbinevt*. The required corrections has been applied: in particular, since the response matrix depends on the position of the source in the BAT field of view, an updated detector response matrix is created using the *batupdatephakw* and *batdrmgen* tools, while we correct for systematics as a function of energy using *batphasyserr*. Before fitting the spectra, we group the energy channels requiring a 3σ threshold on each group; the threshold has been lowered to 2σ for spectra with poor statistics. The spectra are fit within *Xspec* v.12.5 with a simple power-law with pegged normalisation (*pegpwrlw*). The best fit photon indices resulting from this procedure are shown in Fig. 5.1, bottom panel. There is a hint of spectral evolution in the prompt component in the bottom panel of this figure: the best fit photon index evolves to slightly higher values, leading to a progressive softening of the emission with time.

5.4.2 Swift-*XRT data*

XRT data have been processed with the latest version of the *heasoft* package available at the time of writing (v. 6.6.1) and corresponding calibration files: standard filtering and screening criteria have been applied. In particular we use grades 0-2 and 0-12 in Windowed Timing (WT) and Photon Counting (PC) modes respectively. The first orbit data have been completely acquired in WT mode reaching a maximum count rate $\sim 140\,\mathrm{counts\,s^{-1}}$. We extract WT events in a box-shaped region of 40x20 pixels along the image strip. For count-rates between $100\,\mathrm{counts\,s^{-1}}$ and $140\,\mathrm{counts\,s^{-1}}$ we expect the source to be slightly affected by pile-up [166]: for this reason, we exclude a central box of 2x20 pixels from the original source region in the corresponding time intervals. The size of the exclusion region is determined from the study of the distortion of the grade 0 distribution. The study of the distortion of the mean energy associated to each photon gives consistent results. WT background photons are extracted from a 40x20 box region with no sources. Starting from $\sim 10\,\mathrm{ks}$ *Swift*-XRT switched to PC mode to follow the fading of the source. Events are then extracted using different region shapes and sizes in order to maximize the signal-to-noise (SN) ratio: in particular, starting from 560 ks the source detection is optimized using the tool SOSTA within *Ximage*. Since the maximum PC mode recorded count rate is $\sim 0.3\,\mathrm{count\,s^{-1}}$ there is no need for pile-up correction. The background is estimated from an annular region of inner and outer radii of 45 and 90 pixels away from any source detected at 2σ significance during the entire PC observation of GRB 081028. The resulting 0.3-10 keV light-curve is shown in Fig. 5.2: the displayed data binning assures a minimum SN equals to 4 (10) for PC (WT) data. In this way the strong variability of WT data can be fully appreciated without losing information on the late time behaviour. When single-orbit data are not able to fulfil the signal-to-noise requirement, data coming from different orbits are merged to build a unique data points.

We performe automatic time resolved spectral analysis accumulating signal over time intervals defined to contain a minimum of $\sim$ 2000 photons each. Exposure maps are created merging the original instrument maps belonging to the same interval of time as created by the *xrtpipeline*. For each spectrum an Ancillary Response File (ARF) is built using the *xrtmkarf* task within *heasoft*. The spectral channels are then grouped to provide a minimum of 20 counts per bin. A background spectrum is also produced extracting events from the background region. The *nh* FTOOL is used to determine the neutral Hydrogen Galactic column density in the direction of the burst which turned out to be $3.96 \times 10^{20}\,\mathrm{cm^{-2}}$ (weighted average value from the [85] map). Spectral fitting is done within *Xspec* (v.12.5) using a photo-electrically absorbed simple power law -SPL- model (*tbabs*ztbabs*pow*). The Galactic absorption component is frozen at the Galactic value together with the redshift, while we leave the intrinsic column density free to vary during the first run of the program. A count-to-flux conversion factor is worked out from the best fit model for each time interval for which we are able to extract a spectrum. This value is considered reliable if the respective χ^2/dof (Chi-square over degrees of freedom) implies a

P-value (probability of obtaining a result at least as extreme as the one that is actually observed) higher than 5%. The discrete set of reliable count-to-flux conversion factors is then used to produce a continuum count-to-flux conversion factor through interpolation. This procedure produces flux and luminosity light-curves where the possible spectral evolution of the source is properly taken into account (Fig. 5.2). In the case of GRB 081028 this is particularly important: the simple power law photon index evolves from $\Gamma \sim 1.2$ to $\Gamma \sim 3$ during the steep decay phase (Fig. 5.6) inducing a variation of a multiplicative factor ~ 1.7 in the count-to-flux conversion factor. As a second run, we remove one degree of freedom from the spectral fitting procedure noting the absence of spectral evolution during the X-ray re-brightening (see Sect.5.5.4). This gives the possibility to obtain a reliable estimate of the intrinsic neutral Hydrogen column density $N_{\rm H,z}$ of GRB 081028: the PC spectrum accumulated over the time interval $10 - 652$ ks can be adequately fit by an absorbed SPL model with best fit photon index $\Gamma = 2.09 \pm 0.07$ and $N_{\rm H,z} = (0.52 \pm 0.25) \times 10^{22}\,{\rm cm}^{-2}$ (90% c.l. uncertainties are provided). The flux-luminosity calibration procedure is then re-run freezing the intrinsic absorption component to this value.

5.4.3 Swift-*UVOT data*

The UVOT contains three optical and three UV lenticular filters, which cover the wavelength range between $(1600 - 6000)10^{-8}$ cm, in addition to a clear white filter that covers the wavelength range between $(1600 - 8000)10^{-8}$ cm [155]. The data available to download at the *Swift* data archive are reduced by the science data centre at Goddard Space Flight Center, and photometric analysis can be carried out immediately on the level 2 products, which are already in sky co-ordinates and aspect corrected. Source photometric measurements were extracted from the UVOT imaging data using the tool UVOTMAGHIST (v1.0) with a circular source extraction region with a 3" radius. In order to remain compatible with the effective area calibrations, which are based on 5" aperture photometry [155], an aperture correction was applied. The background was taken from a circular source-free region close to the target with a 10" radius. The UVOT photometric data-set of GRB 081028 is reported in Tab. 5.1.

5.4.4 Ground-based observations

GRB 081028 was observed at $\sim T + 6$h with the Bessel R filter using the coronagraphic PolCor camera built for high contrast, high spatial resolution imaging mounted on the 2.5 m NOT at La Palma, Canary Islands. Because of the very poor sky conditions only 519 frames out of 9000 can be used, for a total exposure of 51.9 s. The average time for the observations is estimated to be 05:53:00 UT. Image reduction is carried out by following standard procedures.

PAIRITEL responded automatically to the *Swift* trigger and began simultaneous J, H, K_s band observations of the GRB at 11:26:23 UT. A total of 472 individual 7.8 s exposures were obtained under moderate conditions (seeing $\sim 3''$) for a total exposure time of ∼3682 sec. The data are reduced and analysed

	Pulse 1	Pulse 2
$t_{\rm peak}$ (s)	72.3 ± 3.5	202.7 ± 3.3
$t_{\rm s}$ (s)	5.4 ± 17.5	125.6 ± 18.1
$t_{\rm rise}$ (s)	32.6 ± 3.7	36.4 ± 4.1
$t_{\rm decay}$ (s)	63.4 ± 8.1	70.0 ± 5.2
w (s)	96.0 ± 7.9	105.4 ± 6.2
k	0.32 ± 0.09	0.31 ± 0.07
A (count s^{-1} det^{-1})	$(3.6 \pm 0.2)10^{-2}$	$(3.5 \pm 0.2)10^{-2}$
Fluence (erg cm^{-2})	$(1.81 \pm 0.14)10^{-6}$	$(1.83 \pm 0.11)10^{-6}$
χ^2/dof	171/114	

Tab. 5.1: Best fit parameters and related quantities resulting from the modelling of the prompt 15-150 keV emission with two Norris et al., 2005 profiles. From top to bottom: peak time, start time, $1/e$ rise time, $1/e$ decay time, $1/e$ pulse width, pulse asymmetry, peak count-rate and statistical information. The χ^2 value mainly reflects the partial failure of the fitting function to adequately model the peaks of the pulses (see Norris et al., 2005 for details).

using the standard PAIRITEL pipeline. Photometry calibration is done against the 2MASS system. The resulting fluxes and magnitudes are consistent with the values reported by [122]: however, this work should be considered to supersede the previous findings. The ground-based photometric data-set of GRB 081028 is reported in Tab. 5.2

5.5 Analysis and results

5.5.1 Temporal analysis of BAT (15-150 keV) data

The mask-weighted light-curve consists of two main pulses peaking at $T + 7.23$ s and $\sim T + 202.7$ s followed by a long lasting tail out to $\sim T + 400$ s. In the time interval $T - 100$ s $T + 400$ s, the light-curve can be fit by a combination of two [133] profiles (Fig. 5.1, top panel) with best fit parameters and related quantities reported in Table 5.1: the parameters are defined following [133]; we account for the entire covariance matrix during the error propagation procedure. The GRB prompt signal has a T_{90} duration of 264.3 s, from T+52.3 s up to T+317.2 s, and a $T_{50} = (135.1 \pm 7.3)s$.

The temporal variability of this bursts has been characterised in two different ways. First, following [165] we compute a variability measure Var$(15 - 150\,\mathrm{keV}) = (5.0 \pm 0.14) \times 10^{-2}$. Second, we adopt the power spectrum analysis in the time domain ([102]; [103]) : unlike the Fourier spectrum, this is suitable to study the rms variations at different time-scales. See [115] and Margutti et al. in prep. for details about the application of this technique to the GRB prompt emission. In particular, we define the fractional power density (fpd) as the ratio between the temporal power of the signal subtracted bythe contribution of the noise and the mean count rate squared. This quantity is demonstrated to show a peak at the characteristic time scales of variability of the signal. We assess the significance of each fpd peak via Monte Carlo simulations. The fpd

Interval	Model	$t_{\rm start}$ (s)	$t_{\rm stop}$ (s)	Γ, α	$E_{\rm p}$ (keV)	Fluence (erg cm^{-2})	χ^2/dof	P-value
T_{90}	Pl	52.9	317.2	1.82 ± 0.09	–	$(3.3 \pm 0.20) \times 10^{-6}$	31.8/31	43%
	Cutpl	52.9	317.2	1.3 ± 0.4	65^{+42}_{-11}	$(3.15 \pm 0.20) \times 10^{-6}$	25.8/30	69%
Total	Pl	0.0	400.0	1.89 ± 0.09	–	$(3.7 \pm 0.20) \times 10^{-6}$	37.4/32	23%
	Cutpl	0.0	400.0	1.3 ± 0.4	55^{+20}_{-9}	$(3.45 \pm 0.19) \times 10^{-6}$	30.1/31	51%
Pulse 1	Pl	10.0	150.0	1.91 ± 0.13	–	$(1.60 \pm 0.12) \times 10^{-6}$	18.0/24	80%
	Cutpl	10.0	150.0	1.1 ± 0.6	49^{+18}_{-9}	$(1.47 \pm 0.11) \times 10^{-6}$	12.0/23	97%
Pulse 2	Pl	150.0	290.0	1.77 ± 0.11	–	$(1.79 \pm 0.11) \times 10^{-6}$	33.8/29	25%
	Cutpl	150.0	290.0	1.22 ± 0.45	69^{+87}_{-14}	$(1.47 \pm 0.11) \times 10^{-6}$	29.3/28	40%

Tab. 5.2: Best fit parameters derived from the spectral modelling of 15-150 keV data using a power law with pegged normalisation (Pl, *pegpwrlw* within *Xspec*) and a cut-off power-law model with the peak energy of the νF_ν spectrum as free parameter (Cutpl). From left to right: name of the interval of the extraction of the spectrum we refer to throughout the paper; spectral model used; start and stop time of extraction of the spectrum; best fit photon index Γ for a Pl model or cutoff power-law index for a Cutpl model; best fit peak energy of the νF_ν spectrum; fluence; statistical information about the fit.

of GRB 081028 shows a clear peak around 70 s (time scale related to the width of the two [133] profiles). Below 70 s the fpd shows a first peak at $\Delta t \sim 2\,$s and then a second peak at $\Delta t \sim 6\,$s, both at 1σ c.l. The signal shows power in excess of the noise at 2σ c.l. significance for time scales $\Delta t \geq 32\,$s.

5.5.2 Spectral Analysis of BAT (15-150 keV) data

We extract several spectra in different time intervals and then fit the data using different models to better constrain the spectral evolution of GRB 081028 in the 15-150 keV energy band. In particular, a first spectrum is extracted during the T_{90} duration of the burst; a second spectrum is accumulated during the entire duration of the 15-150 keV emission; finally, the signal between 10 s and 290 s from trigger has been split into two parts, taking 150 s as dividing time, to characterise the spectral properties of the two prompt emission pulses. The resulting spectra are then fit using a simple power-law and a cut-off power-law models within *Xspec*. The results are reported in Table 5.2. The measured simple power law photon index around 2 suggests that BAT observed a portion of an intrinsically Band spectrum [7]. Consistently with this scenario, the cut-off power law model always provides a better fit which is able to constrain the peak energy value ($E_{\rm p}$, peak of the νF_ν spectrum) within the BAT energy range. This results in a low energy photon index ~ 1.2, a quite typical value when compared to the distribution of low energy Band photon indices reported by [86]. The temporal evolution of the $E_{\rm p}$ parameter from the first to the second pulse of the prompt emission can also be appreciated. Section 5.5.6 is entirely devoted to the analysis of this topic.

A spectrum extracted in a 6.016 s time interval around the peak of the emission can be fit by a power-law with pegged normalisation of photon index $\Gamma = 1.59 \pm 0.23$ (90% c.l.). The fit is not able to constrain the $E_{\rm p}$ parameter;

n_2	c	n_1	a	b	d_1
$10^{18.3\pm5.5}$	-5.2 ± 1.5	1.2 ± 1.1	-4.5 ± 3.3	2.1 ± 0.1	2.4 ± 2.0
$10^{29.9\pm6.5}$	-7.60 ± 1.8	0.31 ± 0.02	-1.8 ± 0.3	1.3 ± 0.1	0.1
$t_{\rm br_1}$ (ks)	n_3	e	d_2	$t_{\rm br_2}$ (ks)	χ^2/dof
15.5 ± 6.3	–	–	–	–	164.8/145
19.5 ± 0.7	0.06	2.3 ± 0.1	0.05	62	147.1/143

Tab. 5.3: Best-fit parameters of the XRT light-curve modelling starting from 3 ks after the trigger. The first (second) line refers to Eq. 5.1 (Eq. 5.2).

however, a 90% c.l. lower limit can be quoted: $E_{\rm p} > 64\,{\rm keV}$ (χ^2/dof = 12.3/16). The peak flux in the 15-150 keV energy range is $(2.91 \pm 0.25) \times 10^{-8}\,{\rm erg\,cm^{-2}\,s^{-1}}$ while the 15-150 keV peak photon flux is $(0.40 \pm 0.05) \times 10^{-8}\,{\rm ph\,cm^{-2}\,s^{-1}}$.

The best fit parameters of the cut-off power-law model applied to the total spectrum of Table 5.2 imply $E_{\rm iso}(1 - 10^4\,{\rm keV}) = (1.1 \pm 0.1) \times 10^{53}\,{\rm erg}$. The respective rest frame peak energy is $E_{\rm p,i} = (1+z)E_{\rm p} = 222^{+81}_{36}\,{\rm keV}$, placing GRB 081028 within the 2σ region of the Amati relation [2].

The burst is characterised by an isotropic $10^2 - 10^3$ keV (rest frame) $L_{\rm iso} = (2.85 \pm 0.25) \times 10^{51}\,{\rm erg\,s^{-1}}$. This information together with the variability measure of the previous paragraph (${\rm Var}(15 - 150\,{\rm keV}) = (5.0 \pm 0.14) \times 10^{-2}$), makes GRB 081028 perfectly consistent with the luminosity variability relation (see [164]; [75]; [165]).

5.5.3 Temporal analysis of XRT (0.3-10 keV) data

This section is devoted to the study of the temporal properties of the X-ray emission. The XRT (0.3-10 keV) light-curve consists of two parts: a steep decay phase with flares and variability superimposed ($100\,{\rm s} < {\rm t} < 7000\,{\rm s}$), followed by a remarkable re-brightening with smoothly rising and decaying emission between 7 ks and 1000 ks. The two light-curve phases are studied separately.

GRB 081028 is one of the rare cases in which the XRT caught the prompt emission. The light-curve shows a flat phase up to $t \sim 300\,{\rm s}$ followed by a steep decay. Starting from $\sim 690\,{\rm s}$ the light-curve is dominated by a flare which peaks at 800 s but whose decaying phase is temporally coincident with the orbital data gap. The steep decay behaviour before the flare is inconsistent with the back-extrapolation of the post orbital data gap power-law decay, as shown in Fig. 5.3. The strong spectral evolution detected by the XRT (Sect. 5.5.4) requires a time resolved flux calibration of the light-curve before the light-curve fitting procedure. In the time interval $320\,{\rm s} < {\rm t} < 685\,{\rm s}$ the 0.3-10 keV light-curve best fit is given by a simple power-law with $\alpha = 3.6 \pm 0.1$ (χ^2/dof = 768.3/736). Figure 5.4 shows the different temporal behaviour of the detected signal when split into different energy bands: harder photons decay faster. The 0.2-1 keV light-curve decays following a power-law with index $\alpha \approx -2.5$; the decay steepens to $\alpha \approx -3.5$ $\alpha \approx -3.8$ for the 1-2 keV and 2-10 keV signal,

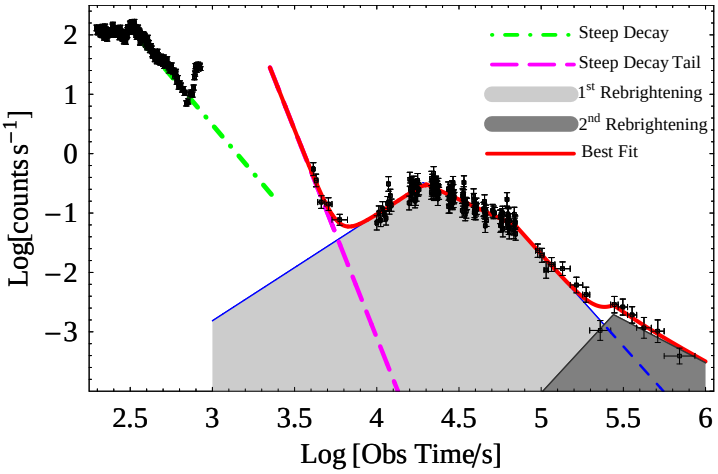

Fig. 5.3: 0.3-10 keV X-ray afterglow split into different components. Green dot-dashed line: steep decay; purple long dashed line: pre-rebrightening component; light grey region: first re-brightening component; dark grey region: second re-brightening component; red solid line: best fit model. See Sect. 5.5.3 for details.

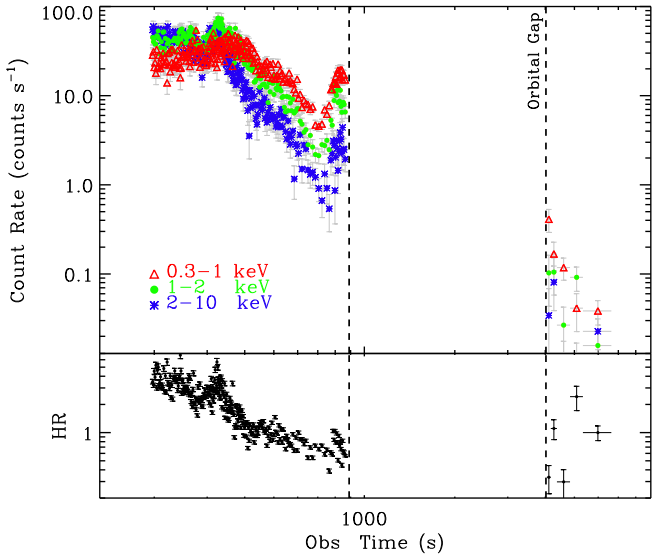

Fig. 5.4: Upper panel: steep decay portion of GRB 081028 X-ray afterglow. The XRT signal has been split into 3 energy bands so that the different temporal behaviour can be fully appreciated. Lower panel: $(0.3-1\,\mathrm{keV})/(1-10\,\mathrm{keV})$ hardness ratio evolution with time. The signal clearly softens with time. In both panels, the vertical black dashed lines mark the orbital data gap.

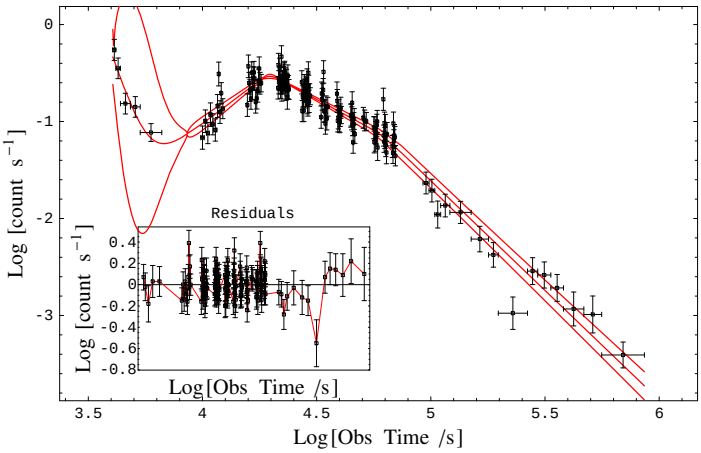

Fig. 5.5: XRT 0.3-10 keV count-rate light-curve of GRB 081028 starting from 3 ks with best fit model (Eq. 5.2, Table 5.3) and 1σ confidence intervals superimposed. *Insert:* residuals with respect to the best-fit model.

respectively.

During the re-brightening there is not evidence for spectral evolution in the X-ray regime (see Sect. 5.5.4). For this reason we model the count-rate light-curve instead of the flux calibrated one: this gives the possibility to obtain a fully representative set of best fit parameters [4] determined with the highest level of precision. The count-to-flux calibration introduces additional uncertainty inherited by the spectral fitting procedure. Starting from 3 ks (the inclusion of the last part of the steep decay is necessary to model the rising part of the re-brightening), the count-rate light-curve can be modelled by a power-law plus Beuermann function [14] where the smoothing parameter d_1 is left free to vary:

$$n_2 \cdot t^{c} + n_1 \left[\left(\frac{t}{t_{br_1}} \right)^{\frac{a}{d_1}} + \left(\frac{t}{t_{br_1}} \right)^{\frac{b}{d_1}} \right]^{-d_1} \tag{5.1}$$

The best fit parameters are reported in Table 5.3. The drawback of this model is that the best-fit slopes are asymptotic values and do not represent the actual power-law slopes. While due to the smooth transition between the rising and decaying phases, this makes the comparison between observations and model predictions difficult. Freezing d_1 to 0.1 to have a sharp transition results in an unacceptable fit (P-value$\sim 10^{-4}$) and suggests a light-curve steepening around 50 ks. The possibility of a break is investigated as follows: we select data points starting from 20 ks and fit the data using a simple power-law (SPL) or a broken power-law (BPL) model. Given that the SPL and BPL models are nested models and the possible values of the second model do not lie on the boundary of definition of the first model parameters [156], we can apply an F-test: with a

[4] This is in general not true in cases of strong spectral evolution as shown in the first part of this section.

probability of chance improvement $< 2\%$, we find moderate statistical evidence for a break in the light-curve at 62 ks. The final fitting function is given by Eq. 5.2:

$$\begin{cases} n_2 \cdot t^{\mathrm{c}} + n_1 \left[\left(\frac{t}{t_{\mathrm{br1}}} \right)^{\frac{a}{d_1}} + \left(\frac{t}{t_{\mathrm{br_1}}} \right)^{\frac{b}{d_1}} \right]^{-d_1} & t < 40\,\mathrm{ks} \\ f \cdot n_3 \left[\left(\frac{t}{t_{\mathrm{br_2}}} \right)^{\frac{b}{d_2}} + \left(\frac{t}{t_{\mathrm{br_2}}} \right)^{\frac{e}{d_2}} \right]^{-d_2} & t > 40\,\mathrm{ks} \end{cases} \tag{5.2}$$

where f is function of the other fitting variables and assures the continuity of the fitting function at 40 ks. The light-curve of GRB 081028 fits in this case with $\chi^2/\mathrm{dof} = 147.1/143$ and an P-value=39%: the best fit parameters are reported in Table 5.3 while a plot of the result is provided by Fig. 5.5. The fit of the flux-calibrated light-curve gives completely consistent results. The model predicts $F_{\mathrm{X,p}} = (1.53 \pm 0.08) \times 10^{-11}\,\mathrm{erg\,cm^{-2}\,s^{-1}}$, where $F_{\mathrm{X,p}}$ is the flux at the peak of the re-brightening.

Count-rate drop around 250 ks

The drop of the count-rate around 250 ks is worth attention: the statistical significance of this drop is discussed below. We select data with $t > 60$ ks. These data can be fit by a simple power-law with index $\alpha = 1.9 \pm 0.2$ ($\chi^2/\mathrm{dof} = 11.0/12$, P-value=53%). According to this model the drop is not statistically significant (significance $\sim 2.6\sigma$). However, this model under-predicts the observed rate for $t < 60$ ks: an abrupt drop of the count-rate during the orbital gap at 80 ks would be in this case required. Alternatively there is not any kind of switch-off of the source during the orbital gap and the flux around 80 ks joins smoothly to the flux component at $t < 60$ ks, as portrayed in Fig. 5.5. A careful inspection of the figure reveals the presence of a non random distribution of the residuals of the last 14 points: while this fit is completely acceptable from the χ^2 point of view, a run test shows that the chance probability of this configuration of residuals is less than 0.1%. This calls for the introduction of a new component to model the partial switch-off and re-brightening of the source around 250 ks. A possible description of the light-curve behaviour for $t > 20$ ks (peak time of the main re-brightening) is represented by a Beuermann plus Beuermann function with smoothing parameters frozen to give sharp transitions; the first decaying power-law index is frozen to $b = 1.3 \pm 1.3$ while the break time of the first Beuermann component is frozen to $t_{\mathrm{br_2}} = 62$ ks as reported in Table 5.3. The light-curve decays with $\alpha_2 = 3.1 \pm 0.2$ ($\alpha_3 = 1.5 \pm 0.7$) for 60 ks $<$ t $<$ 250 ks ($t > 316$ ks), see Fig. 5.3. This additional component accounts for $\sim 10\%$ of the total re-brightening $0.3 - 10$ keV energy which is $\sim 1.1 \times 10^{52}$ erg.

5.5.4 Spectral Analysis of XRT (0.3-10 keV) data

The very good statistics characterising the X-ray afterglow of GRB 081028 gives us the possibility to do a temporally resolved spectral analysis as described in Sect. 5.4.2. Figure 5.6 shows the dramatic evolution of the photo-electrically absorbed simple power-law photon index with time during the first 1000 s of

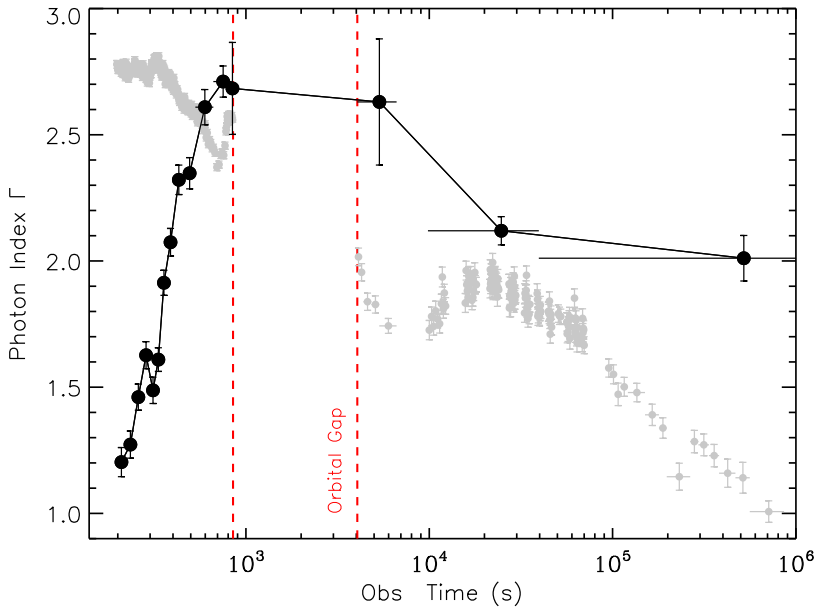

Fig. 5.6: 0.3-10 keV light-curve (grey points, arbitrary units) with best fit 0.3-10 keV photon index superimposed. Each point comes from the fit of a spectrum consisting of ~ 2000 photons: the model *tbabs*ztbabs*pow* within *Xspec* with the intrinsic column density $N_{\rm H,z}$ frozen to 0.52×10^{22} cm^{-2} has been used. An exception is represented by the first data points after the orbital gap: see Sect. 5.5.4 for details. The vertical red dashed lines mark the time interval of the first orbital gap. An abrupt change of the spectral properties of the source temporally coincident with the onset of the re-brightening is apparent.

observation, with Γ evolving from 1.2 to 2.7. The intrinsic neutral Hydrogen column density $N_{\rm H,z}$ has been frozen to $0.52 \times 10^{22}\,{\rm cm}^{-2}$ for the reasons explained below. If left free to vary, this parameter shows an unphysical rising and decaying behaviour between 200 s and 600 s.

The temporal behaviour of the light-curve in the time interval $4 - 7.5$ ks (after the orbital gap, see Fig. 5.3) physically connects these data points with the steep decay phase. We test this link from the spectroscopic point of view. The 0.3-10 keV spectrum extracted in this time interval contains 133 photons. Spectral channels have been grouped so as to have 5 counts per bin and then weighted using the Churazov method [32] within *Xspec*. A fit with a photo-electrically absorbed power-law (*tbabs*ztbabs*pow* model) gives $\Gamma = 2.63 \pm 0.25$, (90% c.l., χ^2/dof = 25.6/23, P-value=32%), confirming that this is the tail of the steep decay detected before the orbital gap as shown by Fig. 5.6.

The light-curve re-brightening around 7 ks translates into an abrupt change of the 0.3-10 keV spectral properties (Fig. 5.6), with Γ shifting from 2.7 to 2. The possibility of a spectral evolution in the X-ray band during the re-brightening is investigated as follows: we extracted three spectra in the time intervals 7-19.5 ks (spec1, rising phase); 19.5-62 ks (spec2, pre-break decaying phase); 62- end of observations (spec3, post-break decaying phase). A joint fit of these spectra with an absorbed simple power-law model (*tbabs*ztbabs*pow* model) where the intrinsic Hydrogen column density is frozen to $0.52 \times 10^{22}\,{\rm cm}^{-2}$ (see Sect. 5.4.2) and the photon index is tied to the same value, gives $\Gamma = 2.04 \pm 0.06$ with χ^2/dof = 118.0/167. Thawing the photon indeces we obtain: $\Gamma_1 = 2.13^{+0.14}_{-0.14}$; $\Gamma_2 = 2.03^{+0.07}_{-0.07}$; $\Gamma_3 = 2.00^{+0.13}_{-0.12}$ (χ^2/dof = 115.8/165). Uncertainties are quoted at 90% c.l.. The comparison of the two results implies a chance probability of improvement of 22%: we conclude that there is not evidence for spectral evolution during the re-brightening in the 0.3-10 keV energy range. The same conclusion is reached from the study of the $(1-10\,{\rm keV})/(0.3-1\,{\rm keV})$ hardness ratio.

5.5.5 *Spectral Energy Distribution during the re-brightening: evolution of the break frequency*

The re-brightening properties can be constrained through the study of the temporal evolution of the spectral energy distribution (SED) from the optical to the X-ray. We extract 4 SEDs as indicated by the shaded bands in Fig. 5.2:

1. SED 1 at $t \sim 10\,{\rm ks}$ corresponds to the rising portion of the X-ray re-brightening and includes XRT, UVOT and CrAO observations;

2. SED 2 is extracted at $t \sim 20\,{\rm ks}$, peak of the X-ray re-brightening. It includes XRT, UVOT, GROND and NOT observations;

3. SED 3 at $t \sim 41\,{\rm ks}$ describes the afterglow spectral energy distribution during the decaying phase of the re-brightening, before the detected light-curve break. It includes X-ray data from ~ 30 ks to ~ 62 ks, UVOT and PAIRITEL observations;

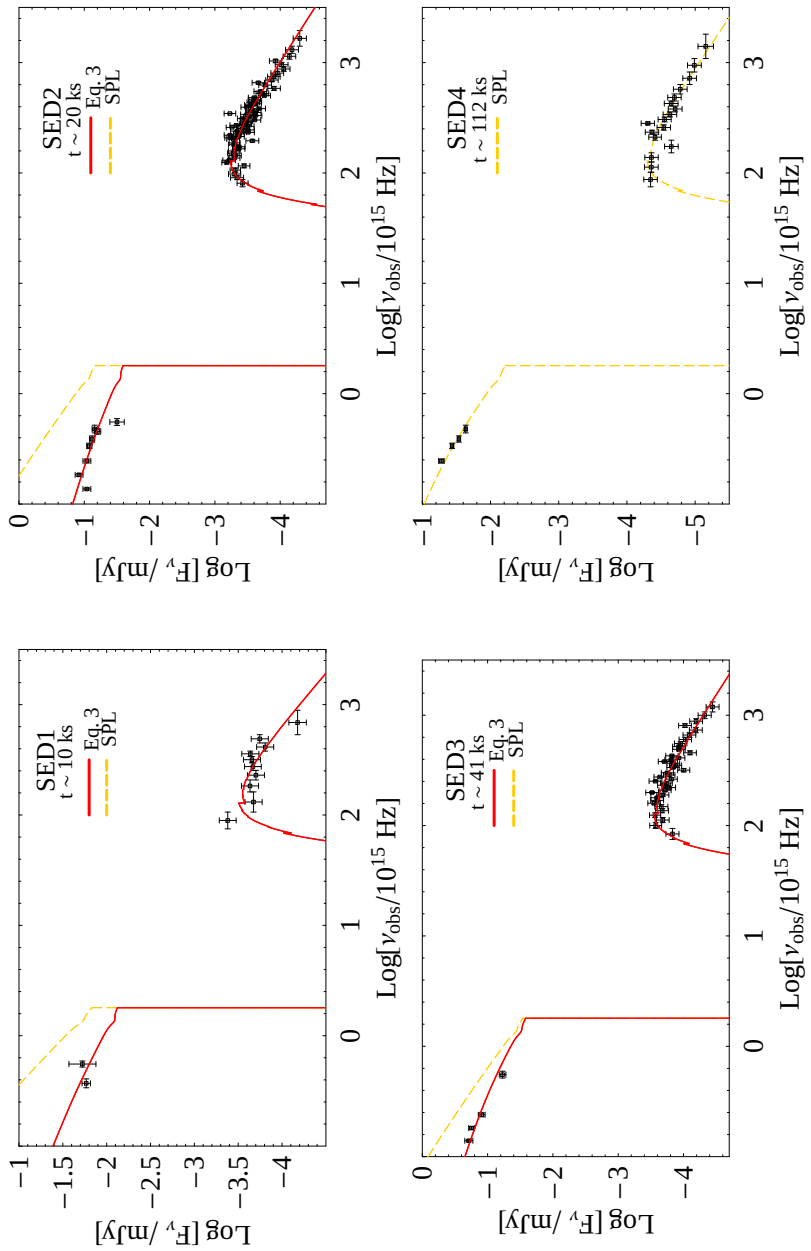

Fig. 5.7: Observer-frame SED1, SED2, SED3 and SED4 from optical to X-ray extracted at $t \sim 10$ ks, $t \sim 20$ ks, $t \sim 41$ ks and $t \sim 112$ ks, respectively. Red solid line: photo-electrically absorbed unextinguished model corresponding to Eq.5.3. This proved to be the best fit model for SED1, SED2 and SED3. Orange dashed line: photo-electrically absorbed unextinguished simple power law. This is the best fit model for SED4. For all SEDs a SMC profile at the redshift of the source is assumed. The best fit parameters are reported in Table 5.4.

4. SED 4 corresponds to the post-break decaying portion of the re-brightening, at $t \sim 112$ ks and includes XRT and GROND observations.

When necessary, optical data have been interpolated to the time of extraction of the SED. Uncertainties have been propagated accordingly.

At a redshift of 3.038, we expect some contamination in the spectrum from absorption systems located between the Earth and GRB 081028 [110]. This means that the g' filter of GROND and all UVOT filters but the v band are marginally or strongly affected by Lyman absorption: these filters are consequently excluded from the following analysis.

The Galactic and intrinsic absorption at wavelengths shorter than the Lyman edge are modelled using the photo-electric cross-sections of [127]. We adopt the analytical description of the Galactic extinction by [145], while the host galaxy absorption is assumed to be modelled by a Small Magellanic Cloud-like law (from [145]).

An absorbed simple power-law model from the optical to the X-ray range is not able to account for SED 1, SED 2 and SED 3 (Fig. 5.7), while it turned out to be the best model for SED 4. For the three SEDs a satisfactory fit is given by a broken power-law with X-ray spectral index $\beta_x \sim 1$; optical spectral index $\beta_o \sim 0.5$ and $N_{\mathrm{H,z}}$ consistent with the value reported in Sect. 5.4.2 ($0.52 \times 10^{22}\,\mathrm{cm}^{-2}$). The best fit break frequency is found to evolve with time to lower values following a power-law evolution with index $\alpha \sim 2$. This evolution is faster than expected for the cooling frequency of a synchrotron spectrum (see e.g. [175]; [67]): in the following, we identify the break frequency with the injection frequency. We freeze the Galactic contribution to give $E(B-V) = 0.03$ [181], while leaving the intrinsic component free to vary.

The broken power-law model has been then refined as follows. [64] showed that under the assumption of synchrotron emission from a relativistic blast wave that accelerates the electrons to a power law distribution of energies $N(\Gamma_e) \propto \Gamma_e^{-p}$, it is possible to derive a physically motivated shape of spectral breaks. Interpreting the break frequency as the injection frequency in the fast cooling regime, the broken power-law model reads (see [67], their Eq. 1):

$$F_\nu = F_{\mathrm{n}} \Big[\Big(\frac{\nu}{\nu_b} \Big)^{-s\beta_1} + \Big(\frac{\nu}{\nu_b} \Big)^{-s\beta_2} \Big]^{-1/s} \tag{5.3}$$

where ν_{b} and F_{n} are the break frequency and the normalisation, respectively; $\beta_1 = -0.5$ and $\beta_2 = -p/2$ are the asymptotic spectral indices below and above the break under the conditions above; $s \equiv s(p)$ is the smoothing parameter: in particular, for an interstellar (wind) medium $s = 3.34 - 0.82p$ ($s = 3.68 - 0.89p$) ([64], their Table 2). The free parameters of the final model are the following: normalization of the spectrum F_{n}; break frequency ν_{b}; power-law index of the electron distribution p and intrinsic neutral Hydrogen column density $N_{\mathrm{H,z}}$ (the host reddening has been frozen to 0). The ISM or wind environments give perfectly consistent results. We choose to quote only ISM results for the sake of brevity. For SED 4 we use an absorbed simple power-law with spectral index $-p/2$. The four SEDs are first fit separately; as a second step we perform a

SED	Par.	Value
1,2,3,4	p	1.97 ± 0.03
1	$\mathrm{Log}_{10}(\nu_\mathrm{b}/10^{15}\mathrm{Hz})$	2.0 ± 0.1
2	$\mathrm{Log}_{10}(\nu_\mathrm{b}/10^{15}\mathrm{Hz})$	1.4 ± 0.1
3	$\mathrm{Log}_{10}(\nu_\mathrm{b}/10^{15}\mathrm{Hz})$	0.4 ± 0.1
χ^2/dof	134.7/138	
P-value	56%	

Tab. 5.4: Best fit parameters for the simultaneous fit of SED1, SED2, SED3 and SED4. For SED1, SED2 and SED3 the emission model is expressed by Eq. 5.3, while for SED4 we used a simple power-law with spectral index $p/2$. The spectral normalisations and break frequencies have been left free to take different values in different spectra. The intrinsic neutral Hydrogen column value is found to be consistent with the value inferred from the X-ray spectra.

contemporary fit where only the spectra normalisation and break frequency are free to take different values in different spectra. We find fully consistent results with improved uncertainties thanks to the tighter constraints imposed by the contemporary fit. The best fit results are reported in Table 5.4 and portrayed in Fig. 5.7.

The spectral break frequency ν_b evolves with time to lower values, as shown in Fig. 5.8. The consistency of SED4 optical and X-ray data with a simple power-law model with index $-p/2$, suggest that the break frequency has crossed the optical band by the time of extraction of SED4. This translates into $\mathrm{Log}_{10}(\nu_\mathrm{b}/10^{15}\mathrm{Hz}) < -0.33$ for $t > 112\,\mathrm{ks}$. The decrease of the break frequency with time can be modelled by a simple power-law function: this leads to an acceptable fit ($\chi^2/\mathrm{dof} = 1.4/1$, P-value=24%) with best fit index $\alpha = 2.6 \pm 0.2$. Using $t_0 = 2$ ks as zero time of the power-law model we obtain: $\alpha = 2.3 \pm 0.2$ ($\chi^2/\mathrm{dof} = 2.1/1$, P-value=15%)

The fit implies a limited rest frame optical extinction which turns out to be $E(B-V)_\mathrm{z} \sim 0.03$. A $3-\sigma$ upper limit can be derived from the joint fit of the four SEDs, leaving all the parameters but the one related to the optical extinction free to vary. The upper limit is computed as the value which increases the χ^2 by a $\Delta\chi^2$ corresponding to a 3 σ c.l.. This procedure leads to: $A_{V,z} < 0.22$.

5.5.6 *Peak energy evolution with time*

The consistency of the prompt BAT spectrum with a cut-off power-law (Sect. 5.2) and the spectral variability detected in the XRT energy range (Sect. 5.5.4, Fig. 5.6) suggests a peak of the νF_ν spectrum moving through the bandpass. To follow the spectral evolution, we time slice the BAT and XRT data into 14 bins covering the 10-851 s time interval. The spectra are then fit within *Xspec* using a Band function (*ngrbep*) or a cut-off power-law (*cutplep*) with E_p as free parameter; alternatively a simple power law is used. Each model is absorbed by a Galactic (hydrogen column density frozen to $3.96 \times 10^{20}\,\mathrm{cm}^{-2}$) and intrinsic component ($N_{\mathrm{H,z}}$ frozen to $0.52 \times 10^{22}\,\mathrm{cm}^{-2}$, see Sect. 5.5.4). When possible

Interval	t_i (s)	t_f (s)		Model	$\alpha_{\rm B}$	$\beta_{\rm B}(\Gamma)$	$E_{\rm p}$ (keV)	χ^2/dof	P-value
3	203	222	BAT+XRT	Cutpl	1.19 ± 0.05	—	$61.0^{+20.0}_{-11.9}$	100.4/112	77%
				Pl	—	1.37 ± 0.02	—	147.3/114	2%
4	222	247	BAT+XRT	Cutpl	1.28 ± 0.06	—	$41.5^{+17.1}_{-9.4}$	80.5/101	93%
				Pl	—	1.44 ± 0.03	—	108.2/102	31%$^+$
5	247	271	BAT+XRT	Cutpl	1.38 ± 0.17	—	$16.1^{+9.6}_{-4.9}$	77.4/88	78%
				Pl	—	1.54 ± 0.04	—	96.5/89	3%$^+$
6	271	300	BAT+XRT	Cutpl	1.57 ± 0.07	—	$12.5^{+4.5}_{-2.7}$	129.8/91	1%
				Pl	—	1.76 ± 0.03	—	158.6/92	0.001%
7	300	323	XRT	Cutpl	1.20 ± 0.16	—	$5.2^{+3.7}_{-1.3}$	77.1/81	60%
				Pl	—	1.49 ± 0.05	—	87.6/82	32%
8	323	343	XRT	Cutpl	0.82 ± 0.18	—	$2.9^{+0.3}_{-0.3}$	78.7/83	61%
				Pl	—	1.61 ± 0.05	—	149.8/84	0.001%
9	343	371	XRT	Cutpl	1.38 ± 0.17	—	$2.0^{+0.3}_{-0.3}$	94.3/84	15%
				Pl	—	1.91 ± 0.05	—	131.2/82	0.1%
10	371	405	XRT	Band	~ 1.10	$2.3^{+0.1}_{-0.2}$	< 1.1	82.4/77	31%
				Cutpl	1.81 ± 0.016	—	$1.0^{+0.3}_{-0.9}$	102.4/78	3%
				Pl	—	2.07 ± 0.06	—	109.7/79	1%
11	405	456	XRT	Pl	—	2.3 ± 0.06	—	100.1/78	5%
12	456	530	XRT	Pl	—	2.3 ± 0.06	—	103.3/79	3%
13	530	664	XRT	Pl	—	2.6 ± 0.07	—	98.1/76	5%
14	664	838	XRT	Pl	—	2.7 ± 0.06	—	89.3/73	7%
15	838	851	XRT	Pl	—	2.7 ± 0.18	—	15.7/10	1%

Tab. 5.5: Best fit parameters derived from the spectral modelling of XRT and BAT data using photo-electrically absorbed models (*tbabs*ztbabs* within *Xspec*). Three different models have been used: a simple power-law (Pl); a cut-off power law and a Band function both with the peak energy of the νF_ν spectrum as free parameter. From left to right: name of the interval of the extraction of the spectrum we refer to throughout the paper (intervals 1 and 2 correspond to Pulse 1 and Pulse 2 of Table 5.2); start and stop time of extraction of each spectrum; energy range of the fit: "XRT+BAT" stands for a joint BAT-XRT data fitting; model used; best fit low and high energy photon indices for a Band or Cutpl power-law or best fit photon index Γ for a Pl model; statistical information about the fit. The $^+$ symbol indicates an apparent trend in the residuals of the fit.

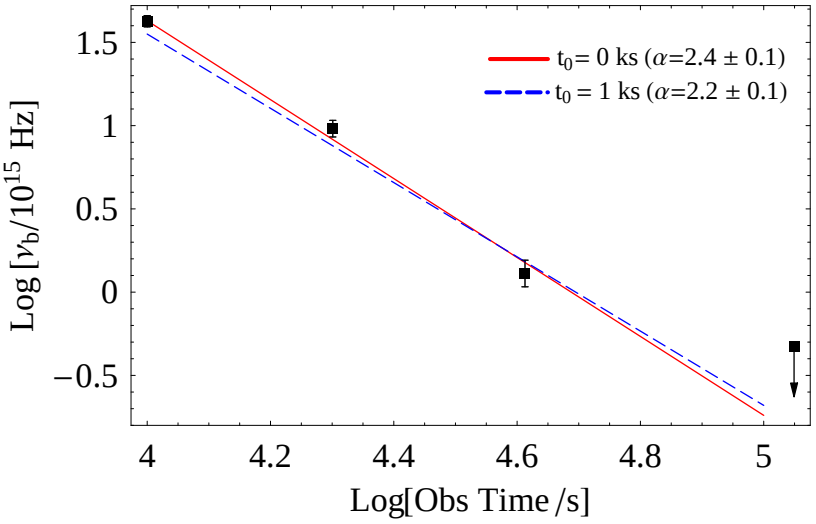

Fig. 5.8: Spectral break frequency (See Eq. 5.3) evolution with time as found from a simultaneous fit of SED1, SED2, SED3 and SED4 with best fit models superimposed. Red solid line (blue dashed line): simple power-law with zero time t_0=0 ks (2 ks) and best power-law index $\alpha = 2.6$ (2.3). The satisfactory fit of SED4 with a simple power-law provides the upper limit shown.

we take advantage of the contemporary BAT and XRT observations performing a joint BAT-XRT spectral fit. The normalisation for each instrument is always tied to the same value. The best fit parameters are reported in Table 5.5: the simple power law model gives a poor description of the spectra up to $\sim 400\,s$, when the curvature of the spectra requires for a cut-off power-law or a Band function. In particular, this is the case when the high energy slope enters the XRT bandpass. The $E_{\rm p}$ parameter is well constrained and evolves to lower energies with time; at the same time both the high and low energy photon indices are observed to gradually vary, softening with time (Fig. 5.9). The $E_{\rm p}$ decay with time can be modelled by a simple power-law starting ~ 200 s after trigger: $E_{\rm p} \propto (t - t_0)^{\alpha}$. The best fit parameters are reported in Table 5.6.

The uncertainty of the inter-calibration of the BAT and XRT has been investigated as possible source of the detected spectral evolution as follows. For each time slice, we multiply the fit model by a constant factor which is frozen to 1 for the BAT data. For XRT, this factor is left free to vary between 0.9 and 1.1, conservatively allowing the XRT calibration to agree within 10% with the BAT calibration. The best fit parameters found in this way are completely consistent with the ones listed in Table 5.5. The inter-calibration is therefore unlikely to be the main source of the observed evolution.

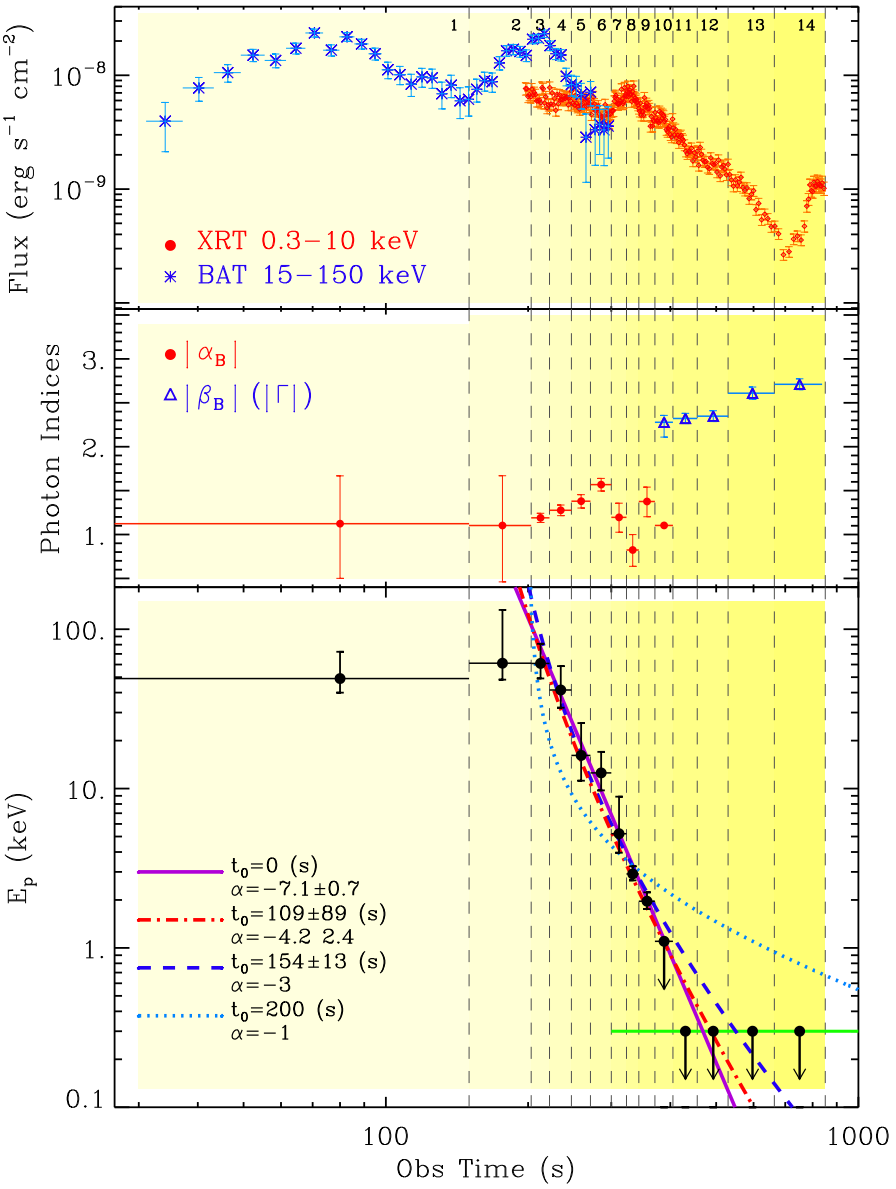

Fig. 5.9: Time resolved combined analysis of XRT and BAT data. Upper panel: BAT 15-150 keV and XRT 0.3-10 keV flux light-curves. No extrapolation of the BAT data into the XRT energy range has been done. The vertical dashed lines mark the intervals of extraction of the spectra: these are numbered according to Table 5.5, first column. Central panel: best fit photon indices evolution with time. Lower panel: best fit $E_{\rm p}$ parameter as a function of time. The decay has been fit with a simple power-law model starting from 200 s from trigger: $E_{\rm p}(t) \propto (t - t_0)^{\alpha}$. Starting from 405 s is likely to be outside the XRT energy range: $E_{\rm p} < 0.3\,$keV (solid green line).

t_0	α	χ^2/dof	Model
0 (s)	-7.1 ± 0.7	1.7/4	—
109 ± 89 (s)	-4.2 ± 2.4	2.5/5	—
154 ± 13 (s)	-3	3.2/4	Adiabatic cooling
200 (s)	-1	42.1/4	High latitude emission

Tab. 5.6: Best fit parameters and statistical information for a simple power-law fit to the $E_{\rm p}$ decay with time starting from 200 s after trigger: $E_{\rm p} \propto (t - t_0)^{\alpha}$.

5.6 Discussion

In GRB 081028 we have the unique opportunity to observe a smoothly rising X-ray afterglow after the steep decay: this is the first (and unique) long GRB *Swift*-XRT light-curve where a rise is seen at $t \geq 10$ ks with completely different properties when compared to typical X-ray flares [30]. At this epoch, canonical X-ray light-curves (e.g., [134]) typically show a shallow decay behaviour with flares superimposed in a few cases (Chincarini et al., in prep.): only in GRB 051016B a rising feature is detected at the end of the steep decay. [5] In the latter the sparseness of data does not allow to draw firm conclusions, so that a flare origin of the re-brightening cannot be excluded.

The very good statistics of GRB 081028 allows us to track the detailed spectral evolution from γ-rays to X-rays, from the prompt to the steep decay phase: this analysis fully qualifies the steep decay as the tail of the prompt emission. At the same time, it reveals that the steep decay and the following X-ray re-brightening have completely different spectroscopic properties (Fig. 5.6): this, together with the temporal behaviour, strongly suggests that we actually see two different emission components overlapping for a small time interval, as was first suggested by [134].

The small overlap in time of the two components is the key ingredient that observationally allows the detection of the rising phase: this can be produced by either a steeper than usual steep decay or a delayed onset of the second component. We tested both possibilities comparing GRB 081028 properties against a sample of 32 XRT light-curves of GRBs with known redshift and for which the steep-flat-normal decay transitions can be easily identified. While 63% of the GRBs are steeper than GRB 081028 ($\alpha_1 \sim 2$), no GRBs in the sample shows a rest frame steep-to-flat transition time greater than 1 ks, confirming in this way the "delayed-second-component" scenario. Alternatively, the peculiarity of GRB 081028 could reside in a steeper than usual rise of the second component: unfortunately this possibility cannot be tested.

5.6.1 Spectral evolution during the prompt and steep decay emission

The evolution of the peak energy $E_{\rm p}$ of the νF_ν spectrum from the γ-ray to the X-ray band described in Sect. 5.5.6 offers the opportunity to constrain the mechanism responsible for the steep decay emission.

[5] See the *Swift*-XRT light-curve repository, [44]

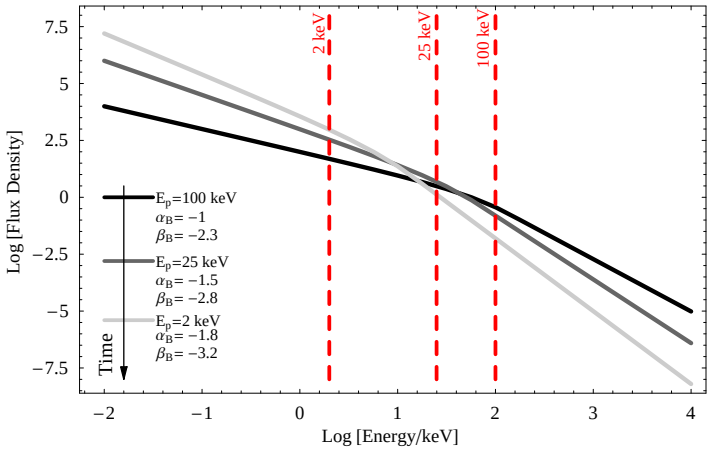

Fig. 5.10: Qualitative description of the spectral evolution with time detected in GRB 081028 from the prompt to the steep decay phase: the peak energy ($E_{\rm p}$) moves to lower energies while both the high and low energy components soften with time.

Spectral evolution through the prompt and steep decay phase has been noted previously, with the $E_{\rm p}$ tracking both the overall burst behaviour and individual prompt pulse structures (see e.g., [146] for a recent time resolved spectral analysis of prompt pulses). In particular, [206] find $E_{\rm p} \propto t^{\sim -3}$ for GRB 060904A; [111] model the prompt to steep decay transition of GRB 060614 with a Band (or cut-off power-law) spectral model with $E_{\rm p}$ evolving as $t^{\sim -2}$, while [61] and [60] report on the evolution of the $E_{\rm p}$ through the XRT energy band during single X-ray flares in GRB 050822 and GRB 051117, respectively. A decaying $E_{\rm p}$ was also observed during the 0.3-10 keV emission of GRB 070616 [187].

The detection of strong spectral evolution violates the prediction of the curvature effect in its simplest formulation as found by [214] in 75% of the analysed GRBs tails: this model assumes the instantaneous spectrum at the end of the prompt emission to be a simple power-law of spectral index β and predicts the $\alpha = 2 + \beta$ relation, where β is not supposed to vary (see e.g., [50]; [93]). The curvature effect of a comoving Band spectrum predicts instead $E_{\rm p} \propto t^{-1}$ and a time dependent $\alpha = 2 + \beta$ relation (see e.g., [56]; [218]): from Fig. 5.9, lower panel and Table 5.6 it is apparent that the observed $E_{\rm p} \propto t^{-7.1 \pm 0.7}$ is inconsistent with the predicted behaviour even when we force the zero time of the power-law fit model to be $t_0 = 200$ s, peak time of the last pulse detected in the 15-150 keV energy range, as prescribed by [104]. However, a more realistic version of the HLE might still fit the data: a detailed modelling is beyond the scope of this paper and will be explored in a future work.

The adiabatic expansion cooling of the gamma-ray producing source, which lies within an angle of $1/\gamma$ (where γ is the Lorentz factor of the fireball) to the observer line of sight, has also been recently proposed as a possible mechanism

responsible for the steep decay [38]. This process gives a faster temporal evolution of the break frequency as it passes through the X-ray band: typically $E_{\rm p} \propto t^{-3}$. Two fits to the data have been done, the first fixing the break evolution to t^{-3} and the other one leaving t_0 and the break temporal evolution as free parameters. Both fits are consistent with the adiabatic cooling expectation and set t_0 close to the beginning of the last pulse in the BAT light-curve (see Table 5.6). However, the adiabatic expansion cooling of a thin ejecta predicts a light-curve decay that is linked to the spectral index β by the relation $\alpha = 3\beta + 3$, where α is the index of the power-law decay. Since $\alpha_{\rm obs} \sim 3.6$ this would imply $\beta \sim 0.2$ which is much harder than observed (Sect. 5.5.4). This makes the adiabatic cooling explanation unlikely.

Both the curvature effect and the adiabatic model assume an abrupt switch-off of the source after the end of the prompt emission: the inconsistency of observations with both models argues against this conclusion and favours models where the X-ray steep decay emission receives an important contribution from the continuation of the central engine activity. In this case, the steep decay radiation reflects (at least partially) the decrease in power of the GRB jet. An interesting possibility is given by a decrease of power originating from a decrease in the mass accretion rate [95].

Alternatively, the observed spectral softening could be caused by cooling of the plasma whose cooling frequency identified with $E_{\rm p}$ decreases with time as suggested by [214].

While the spectral peak is moving, we also observe a softening of the spectrum at frequencies both below and above the peak when our data allow to constrain the low and high energy slopes of a comoving Band spectrum. A softening of the low energy index in addition to the $E_{\rm p}$ evolution has been already observed in the combined BAT+XRT analysis of GRB 070616 ([187], their Fig. 5). This result is consistent with the finding that while short GRBs have a low energy spectral component harder than long GRBs (i.e., $|\alpha_{\rm B,short}| < |\alpha_{\rm B,long}|$), no difference is found in the $\alpha_{\rm B}$ distribution of the two classes of GRBs when only the first 1-2 s of long GRB prompt emission is considered [57]: this proves the soft evolution of the $\alpha_{\rm B}$ parameter with time during the γ-ray prompt emission of long GRBs. Our analysis extends this result to the X-ray regime and indicates the softening of both the high and low spectral components from the prompt to the steep decay phase. The overall spectral evolution is qualitatively represented in Fig. 5.10.

5.6.2 Prompt efficiency

An important factor of GRBs in the context of the fireball model is their efficiency of conversion of the total initial energy into gamma-rays. Assuming that all energy not radiated in gamma-rays ends up in the kinetic energy $E_{\rm k}$ of the afterglow, the important parameters are the energy radiated in gamma-rays, E_γ, the kinetic energy of the afterglow, $E_{\rm k}$ and a parameter $f \equiv E_{\rm k}(10\ {\rm hr})/E_{\rm k,0}$ ([72]; [47], hereafter FP06) that accounts for energy injection during the shallow decay phase (since energy injection is the most common explanation for this

phase), where $E_{\rm k,0}$ is the initial kinetic energy of the afterglow, before energy injection. The efficiency of the prompt emission thus reads:

$$\epsilon_\gamma \equiv \frac{E_\gamma}{E_{\rm k,0}+E_\gamma} = \frac{f\tilde{\epsilon_\gamma}}{1+(f-1)\tilde{\epsilon_\gamma}} \tag{5.4}$$

where $\tilde{\epsilon_\gamma} \equiv E_\gamma/(fE_{\rm k,0}+E_\gamma) = E_\gamma/(E_{\rm k}(10\ {\rm hr})+E_\gamma)$.

All the listed quantities are isotropic equivalent quantities. This can be calculated with a good estimate of $E_{\rm k}(10\ {\rm hr})$ that can be obtained from the X-ray luminosity at 10 hours if the X-ray frequency ν_X is above both ν_m and ν_c (FP06; [107], hereafter LZ04). This is the case for GRB081028 (see Sect. 5.6.4) which shows an isotropic X-ray luminosity of $L_{\rm x,iso}(\,10\,{\rm hr},{\rm obs}) \sim (6.3\pm1.0)\times 10^{47}\,{\rm erg\,s^{-1}}$. The calculation of the kinetic energy is done using equation (9) of FP06: unlike LZ04, they integrate their model over the observed energy band $0.3-10$ keV and consider the effect of inverse Compton cooling:

$$\begin{aligned} E_{\rm k}(10\ {\rm hr}) = R\,L_{X,46}^{4/(p+2)}\Big(\frac{1+z}{2}\Big)^{(2-p)/(p+2)} \times \\ \times\epsilon_{\rm B,-2}^{-(p-2)/(p+2)}\epsilon_{\rm e,-1}^{4(1-p)/(p+2)}(1+Y)^{4/(p+2)} \end{aligned} \tag{5.5}$$

where $R = 9.2\times10^{52}[t(10\,{\rm hr})/{\rm T_{90}}]^{\frac{17\epsilon_e}{16}}$ erg, ϵ_B is the fraction of the downstream (within the shocked region) internal energy going into the magnetic field; Y is the Compton parameter which for fast cooling reads $Y \approx [(1+4\epsilon_e/\epsilon_B)^{1/2}-1]/2$ [178], and ϵ_e is the fraction of the internal energy that is given just behind the shock front to relativistic electrons that form a power-law distribution of energies: $N_{\rm e} \propto \gamma_{\rm e}^{-p}$ for $\gamma_{\rm max} > \gamma_{\rm e} > \gamma_{\rm min}$. The convention $Q_x = Q/10^x$ has been adopted in cgs units. This implies we need to make some assumptions on the microphysical parameters ϵ_e, ϵ_B and Y. For the latter, as the afterglow is likely to be in fast cooling (see Sect. 5.6.4), then $Y > 1$ and we take $Y \sim (\epsilon_e/\epsilon_B)^{1/2}$ following FP06. [119] showed that during the prompt emission it is most likely that $\epsilon_e \approx \sqrt{\epsilon_B}$. The values of the microphysical parameters being poorly constrained (Sect. 5.6.4), we set $\epsilon_e = 0.3$ and $\epsilon_B = 0.1$, which is consistent with the values obtained in subsection 5.6.4 (see equation (5.15) when $\xi_e < 1$ and equation (5.16) and the paragraph below it). Taking $p \sim 2$, we thus obtain $E_{\rm k}(10\ {\rm hr}) = 1.3\times10^{55}$ erg. Combined with the observed isotropic gamma-ray energy of the prompt emission $E_\gamma = 1.1\times10^{53}$ ergs, we have $\tilde{\epsilon_\gamma} = 8.6\times10^{-3}$ (corresponding to a ratio $E_{\rm k}(10\ {\rm hr})/E_\gamma \approx 116$): this is low, even compared to the values obtained by FP06 (their values being between 0.89 and 0.01 - see their Table 1), which are already lower than previous estimates by LZ04. Now returning to the efficiency including energy injection, we can obtain an estimate of $E_{\rm k,0}$ by using the previous formula but at the peak of the re-brightening and taking their parameter $R = 9.2\times10^{52}$ (thus ignoring energy radiative losses since the end of the prompt emission), which with its peak luminosity $L_{\rm peak} = 1.2\times10^{48}$ erg s^{-1} gives an initial kinetic energy injected into the afterglow $E_{\rm k,0} = 1.16\times10^{55}$ erg and then an efficiency of the prompt emission $\epsilon_\gamma = 9.4\times10^{-3}$. The conclusion that the efficiency of the prompt emission of GRB 081028 is small compared to other bursts stays.

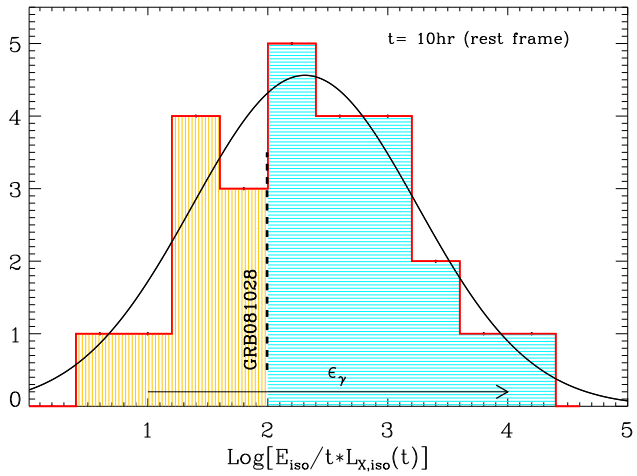

Fig. 5.11: Distribution of $E_\gamma/tL_X(t)$ with $t = 10\,\mathrm{hr}$ rest frame, for the sample of 31 long GRBs detected by *Swift* with E_γ provided by Amati et al. (2008). Black solid line: Gaussian best fit to the distribution. The dashed black line marks the position of GRB 081028 in the distribution, while the black solid arrow is pointed to the direction of increase of the radiative efficiency parameter ϵ_γ.

However, many assumptions enter here, making the final result quite uncertain, independent of the energy injection problem. We thus turn to comparison of fluences, as done by [216], which are good estimates of the prompt and afterglow energies and require no assumption to be calculated and compared. Moreover, their sample consists of *Swift* bursts only, which allows direct comparison with GRB 081028. The prompt $1 - 10^4\,\mathrm{keV}$ gamma-ray fluence[6] of GRB 081028 is $S_\gamma \sim 8 \times 10^{-6}\,\mathrm{erg\,cm^{-2}}$ and its afterglow X-ray fluence, calculated by $S_\mathrm{X} \sim t_\mathrm{peak} F_\nu(t_\mathrm{peak})$ to be consistent with [216] method, is $S_\mathrm{X} \approx 3\times10^{-7}\mathrm{erg\,cm^{-2}}$, so that their ratio is $S_\gamma/S_\mathrm{X} \approx 26.7$, placing GRB 081028 in the lower part of Fig. 6 of [216]. Compared to their sample of 31 *Swift* bursts, the $15-150$ keV fluence of GRB081028, which is $3.2 \times 10^{-6}\mathrm{erg\,cm^{-2}}$ is well within their range of values (spanning from $S_\mathrm{X,min} \approx 8 \times 10^{-8}\mathrm{erg\,cm^{-2}}$ to $S_\mathrm{X,max} \approx 1.5 \times 10^{-5}\mathrm{erg\,cm^{-2}}$; sixth column of their table 1), whereas its X-ray fluence is higher than most of them (see columns 6-9 of their table 2). It thus means that whereas GRB 081028 released as much energy in its prompt emission as most bursts, more kinetic energy was injected in its outflow. This gives a lower efficiency than most of the GRBs analysed by [216], consistent with the scenario above. Figure 5.11 clearly shows that this is likely to be extended to other *Swift* long GRBs: at late afterglow epoch the X-ray band is above the cooling frequency and the X-ray luminosity is a good probe of the kinetic en-

[6] Depending on the high energy slope of the Band spectrum, we have $S_\gamma \sim 6.6 \times 10^{-6}\,\mathrm{erg\,cm^{-2}}$ for $\beta_\mathrm{B} = -2.5$ and $S_\gamma \sim 9.5 \times 10^{-6}\,\mathrm{erg\,cm^{-2}}$ for $\beta_\mathrm{B} = -2.1$.

ergy. In particular $E_{\rm k} \propto L_{\rm x,iso}$ (see Eq. 5.5): this means that high (low) values of the ratio $E_\gamma/L_{\rm x,iso}$ are linked to high (low) values of radiative efficiency.

Finally, we point out that this conclusion was drawn from observed values, i.e. the burst is always considered on-axis. An off-axis viewing angle changes the above conclusion as discussed in see Sect. 5.6.4.

5.6.3 Afterglow modelling

This subsection is devoted to the analysis of the X-ray re-brightening in the framework of a number of different theories put forward to explain the shallow decay phase of GRB afterglows.

According to the dust scattering model [183] the shallow phase is due to prompt photons scattered by dust grains in the burst surroundings: this models predicts a strong spectral softening with time and a non-negligible amount of dust extinction which are usually not observed [180]. Both predictions are inconsistent with our data.

A spherical flow is expected to give rise to a peak of emission when the spectral peak enters the energy band of observation (see e.g., [67]): the SED analysis of Sec. 5.5.5 clearly shows that $E_{\rm p}$ was already below the X-ray band during the X-ray rising phase, well before the peak, thus ruling out the passage of the break frequency through the X-ray band as an explanation of the peak in the X-ray light-curve.

[177] argue that the reverse shock has a much lower temperature and is consequently expected to radiate at lower frequencies than the forward shock, even if it contains an amount of energy comparable to the GRB itself, making a reverse shock origin of the X-ray re-brightening unlikely. However, following [55], in the case of ejecta having a tail of Lorentz factor decreasing to low values, if a large amount of the energy dissipated in the shock (ϵ_e near its equipartition value) is transferred to only a fraction of electrons (typically $\xi_e \sim 10^{-2}$), then the reverse shock radiates in X-rays. In this case, it can also produce a plateau or re-brightening, the latter being more often obtained in a constant density external medium, that qualitatively agrees with the GRB 081028 afterglow.

Alternatively, the detected light-curve peak could be the onset of the afterglow: in this scenario, the rising (decaying) flux is to be interpreted as pre-deceleration (post-deceleration) forward shock synchrotron emission. The observed break frequency scaling $\nu_{\rm b} \propto t^{-2.6\pm0.2}$ is inconsistent with the expected cooling frequency evolution $\nu_{\rm c} \propto t^{-1/2}$ or $\nu_{\rm c} \propto t^{1/2}$ for an ISM or a wind environment, respectively (see e.g. [67]). We therefore consider a fast cooling scenario where $\nu_{\rm b} \equiv \nu_{\rm m}$. The initial afterglow signal from a thick shell is likely to overlap in time with the prompt emission [177], so that it would have been difficult to see the smoothly rising X-ray re-brightening of GRB 081028. For this reason only the onset of the forward shock produced by thin shells will be discussed. Following [177], the observed peak of the X-ray re-brightening implies a low initial fireball Lorentz factor $\gamma_0 \sim 75(n_0\epsilon_{\gamma,0.2})^{-1/8}$, where $n_0 = n/(1\,{\rm cm}^{-3})$ is the circumburst medium density and $\epsilon_{\gamma,0.2} = \epsilon_\gamma/0.2$ is the radiative efficiency. Since the X-ray frequencies are always above the injection frequency $\nu_{\rm m}$, the X-

ray light-curve should be proportional to $t^2\gamma(t)^{4+2p}$: during the pre-deceleration phase this means $F_X \propto t^2$ for an ISM and $F_X \propto t^0$ for a wind; The ISM scaling is consistent with the observed power-law scaling $\propto t^{1.8\pm0.3}$ if a sharp transition between the rising and the decaying part of the re-brightening is required. The asymptotic value of the power-law index during the rising phase is instead steeper than 2, as indicated by the fit of the re-brightening where the smoothing parameter is left free to vary: $\propto t^{4.5\pm3.3}$ (see Table 5.3 for details). The injection frequency is expected to scale as $\nu_m \propto \gamma(t)^{4-k}t^{-k/2}$, where the density profile scales as R^{-k}. This implies that for radii $R < R_\gamma$ (or $t < t_\gamma$) $\nu_{\rm m} \propto t^0$ for an ISM and $\nu_{\rm m} \propto t^{-1}$ for a wind, while for $R > R_\gamma$ ($t > t_\gamma$) the fireball experiences a self-similar deceleration phase where $\gamma \propto t^{-3/8}$ for an ISM and $\gamma \propto t^{-1/4}$ for a wind, and $\nu_{\rm m} \propto t^{-3/2}$ in both cases. R_γ is the radius where a surrounding mass smaller than the shell rest frame mass by a factor γ_0 has been swept up; t_γ is the corresponding time: for GRB 081028 $t_\gamma \sim 20$ ks (observed peak of the re-brightening). While for $t > t_\gamma$ the observed evolution of the break frequency is marginally consistent with $t^{-3/2}$, it is hard to reconcile the observed $\nu_{\rm m} \propto t^{-\alpha}$ with $\alpha \sim 2.6 - 2.4$ decay with the expected constant behaviour or $\propto t^{-1}$ decay for $t < t_\gamma$. This argument makes the interpretation of the re-brightening as onset of the forward shock somewhat contrived. Moreover, the identification of $t = 20$ ks with the deceleration time is also disfavoured by the earlier very flat optical light-curve. An alternative explanation is discussed in the next subsection.

5.6.4 *Afterglow modelling: the off-axis scenario*

For a simple model of a point source at an angle of θ from the line of sight, moving at a Lorentz factor $\gamma \gg 1$ with $\gamma \propto R^{-m/2}$, where R is its radius, the observed time is given by:

$$t = \frac{R}{2c\gamma^2}\left(\frac{1}{1+m} + \gamma^2\theta^2\right) \tag{5.6}$$

The peak in the light curve occurs when the beaming cone widens enough to engulf the line of sight, $\gamma(t_{\rm peak}) \sim 1/\theta$, so that before the peak $t \approx R\theta^2/2c \propto R$. We consider an external density that scales as R^{-k} (with $k < 4$) for which $m = 3-k$. When the line of sight is outside the jet aperture, at an angle θ *from the outer edge of the jet*, the emission can be approximated to zeroth order as arising from a point source located at an angle θ from the line of sight [68]. We have:

$$\frac{t_0}{t} \sim \frac{\nu}{\nu_0} = \frac{1-\beta}{1-\beta\cos\theta} \equiv a_{\rm aft} \approx \frac{1}{1+\gamma^2\theta^2} \tag{5.7}$$

where $\beta = (1-\gamma^{-2})^{1/2} = v/c$ and the subscript 0 indicates the $\theta = 0$ (on-axis) condition. The observed flux is given by

$$F_\nu(\theta, t) \approx a_{\rm aft}^3 F_{\nu/a}(0, at) \tag{5.8}$$

and peaks when $\gamma \sim 1/\theta$. In the following we use the notations $a_{\rm aft} \approx 1/(1+\gamma^2\theta^2)$; a for the particular case where $\gamma = \Gamma_0$ (where Γ_0 is the initial Lorentz

factor of the fireball): $a \approx 1/(1+\Gamma_0^2\theta^2)$; and a subscript "$*$" for the cases when $\theta = \Delta\theta$, $\Delta\theta$ being the jet opening angle.

For $t \ll t_{\rm peak}$, $\gamma\theta \gg 1$ and therefore $a_{\rm aft} \approx (\gamma\theta)^{-2} \propto \gamma^{-2} \propto R^{3-k} \propto t^{3-k}$. In this condition the local emission from a spherically expanding shell and a jet would be rather similar to each other, and the usual scalings can be used for an on-axis viewing angle (e.g., [67]):

$$\nu_{m,0} \propto R^{-3(4-k)/2} \propto t^{-3/2} \tag{5.9}$$

$$\nu_{c,0} \propto R^{(3k-4)/2} \propto t^{(3k-4)/(8-2k)} \tag{5.10}$$

with respective off-axis frequencies:

$$\nu_m \approx a\,\nu_{m,0} \propto R^{(k-6)/2} \propto t^{(k-6)/2} \tag{5.11}$$

$$\nu_c \approx a\,\nu_{c,0} \propto R^{(2+k)/2} \propto t^{(2+k)/2} \tag{5.12}$$

For $t > t_{\rm peak}$, $a_{\rm aft} \approx 1$ and $\nu \approx \nu_0$, so that the break frequencies have their familiar temporal scaling for a spherical flow (eq. 5.9 and 5.10)[7].

For a uniform external medium ($k = 0$), $\nu_c \propto t$ and $t^{-1/2}$ before and after the peak, respectively, while for a stellar wind environment ($k = 2$) the corresponding temporal scalings are t^2 and $t^{1/2}$. In both cases this is inconsistent with the observed rapid decrease in the value of the break frequency ($\nu_{\rm b} \propto t^{-2.6}$) unless we require a very sharp increase in the magnetic field within the emitting region due to a large and sharp increase in the external density [129]. We consider this possibility unlikely (see Sect. 5.6.3).

Alternatively, the break frequency could be ν_m, for a fast cooling spectrum where ν_c is both below ν_m and below the optical. In this case, for $t < t_{\rm peak}$ we have $\nu_m \propto t^{-3}$ (t^{-2}) for a $k = 0$ ($k = 2$) environment; after the peak $\nu_m \propto t^{-3/2}$ independent of k. Since we observe $\nu_{\rm b} \propto t^{-2.6\pm0.2}$ (or $\nu_{\rm b} \propto (t-t_0)^{-2.3\pm0.1}$ with $t_0 = 2\,{\rm ks}$) over about a decade in time around the light-curve peak, this is consistent with the expectations for a reasonable value of k.

Constraints on the model parameters are derived as follows: given that we see only one break frequency in our SEDs, which we identify with $\nu_{\rm m}$, we must require $\nu_{\rm c} < \nu_{\rm opt} (\approx 10^{15}\,{\rm Hz})$. The tightest constraints are derived at $t_{\rm peak}$, when $\nu_{\rm c}$ reaches its maximum value (it increases with time before $t_{\rm peak}$ and decreases with time after $t_{\rm peak}$ for $k < 4/3$). From [67], their Table 2, spectral break 11, this means:

$$\epsilon_B^{3/2} n_0 E_{k,54}^{1/2} (1+Y)^2 > 10^{-3} \tag{5.13}$$

where $n_0 = n/(1\ {\rm cm}^{-3})$ is the external medium density; $E_{k,54} = E_{\rm k,iso}/(10^{54}\ {\rm ergs})$ is the isotropic kinetic energy; Y is the Compton parameter which for fast cooling reads $Y \approx [(1+4\epsilon_e/\epsilon_B)^{1/2} - 1]/2$, [178]. Assuming equipartition ($\epsilon_e = \epsilon_B = 1/3$), $Y \approx 0.62$, Eq. 5.13 translates into:

$$n_0 \gtrsim 2 \times 10^{-3} E_{k,54}^{-1/2} \tag{5.14}$$

[7] While these expressions are derived for a spherical flow, they are reasonably valid even after the jet break time $t_{\rm jet}$ as long as there is relatively very little lateral expansion as shown by numerical simulations (see e.g., [66]; [219] and references therein).

For an efficiency of conversion of the kinetic to gamma-rays energy $\epsilon_\gamma = 1\%$ (which roughly agrees with the values obtained in subsection 5.6.2) the observed $E_{\gamma,\rm iso} = 1.1 \times 10^{53}\,$erg (see Sect. 5.5.2) implies: $n_0 \gtrsim 6 \times 10^{-4}$.

Using the best fit simple power-law models for the break frequency evolution with time of Sect. 5.5.5 we have $\nu_{\rm b}(112\,{\rm ks}) \sim 1.5 \times 10^{14}\,{\rm Hz}$. Following [67], their Table 2, spectral break 9, this means (a value that roughly agrees with the results for a range of values for p derived below is adopted):

$$\left(\frac{\bar{\epsilon}_e}{\xi_e}\right)^2 \epsilon_B^{1/2} \sim 2 \times 10^{-3}\, E_{k,54}^{-1/2} \tag{5.15}$$

where $\bar{\epsilon}_e = \epsilon_e \gamma_m / \langle\gamma_e\rangle$. The value of p is $p = 1.97 \pm 0.03$ with intrinsic reddening $E(B-V)_z = 0.03$ ($\chi^2/{\rm dof} = 135/138$). Freezing the intrinsic reddening to $E(B-V)_z = 0.06$ gives $p = 2.03 \pm 0.02$ ($\chi^2/{\rm dof} = 140.8/139$) while freezing it to $E(B-V)_z = 0.08$ gives $p = 2.08 \pm 0.02$ ($\chi^2/{\rm dof} = 158.6/139$). We thus take $p = 2.0 \pm 0.1$. In particular, we calculate the range of values obtained for the microphysical parameters in the three cases $p = 2.1$, $p = 2$ and $p = 1.9$ since the expression of $\bar{\epsilon}_e$ changes when $p > 2$, $p = 2$ and $p < 2$ [72]:

$$\frac{\bar{\epsilon}_e}{\epsilon_e} = \begin{cases} \approx (p-2)/(p-1) & p > 2 \\ 1/\ln(\gamma_{\rm max}/\gamma_{\rm min}) & p = 2 \\ (2-p)/(p-1)(\gamma_{\rm min}/\gamma_{\rm max})^{2-p} & p < 2 \end{cases} \tag{5.16}$$

$\gamma_{\rm max}$ is obtained by equating the acceleration and cooling times of an electron, and is $\gamma_{\rm max} = \sqrt{3q_e/(\sigma_T B'(1+Y))}$. Calculating the magnetic field value by $B' = \gamma_{\rm aft} c \sqrt{32\pi\epsilon_{\rm B} n m_p}$ and assuming $n_0 = 1\ {\rm cm}^{-3}$, $\epsilon_e = 0.3$, $\epsilon_B = 0.1$ and $\gamma_{\rm aft} = 30$ we obtain $\gamma_{\rm max} \sim 10^7$. Taking $\gamma_{\rm min} \sim 500$ (obtained for $p \sim 2.1$), $(\gamma_{\rm min}/\gamma_{\rm max}) \sim 5 \times 10^{-5}$ (given the way this ratio appears in equation (5.16) - either in a logarithm or with a power $2 - p = 0.1$ in our case - the dependence of the ratio $\bar{\epsilon}_e/\epsilon_e$ on it is very weak, and variations in its value have only a small effect). Then, since for $p = 2.1$, $(p-2)/(p-1) \sim 0.1$, and for $p = 2$, $1/\ln(\gamma_{\rm max}/\gamma_{\rm min}) \sim 0.1$, for $p \geq 2$ we obtain $(\epsilon_e/\xi_e)^2 \epsilon_B^{1/2} \sim 0.2$. From the equipartition value - giving the maximum possible values $\epsilon_e/\xi_e = \epsilon_B = 1/3$ - we obtain an upper limit on the fraction of accelerated electrons: $\xi_e \lesssim 0.3$. For $p = 1.9$ we have $(2-p)/(p-1)(\gamma_{\rm min}/\gamma_{\rm max})^{2-p} \sim 0.04$, and then $(\epsilon_e/\xi_e)^2 \epsilon_B^{1/2} \sim 1.25$, and then $\xi_e \lesssim 0.2$. The constraint on the microphysical parameters being very close in all cases, the exact value of p is then not of primary importance and the approximation $p = 2.0 \pm 0.1$ is then consistent.

The evolution of the peak frequency being consistent with an off-axis interpretation of the afterglow, we further test this scenario by deriving the viewing and half-opening angle of the jet. The jet break time is given by [176] for the ISM and [29] for the wind environments:

$$t_{\rm jet} \approx \begin{cases} 1.2\ (1+z) \left(\frac{E_{54}}{n_0}\right)^{1/3} \left(\frac{\Delta\theta}{0.1}\right)^{8/3}\ {\rm days} & (k=0) \\ \\ 6.25\ (1+z) \left(\frac{E_{54}}{A_*}\right) \left(\frac{\Delta\theta}{0.1}\right)^{4}\ {\rm days} & (k=2) \end{cases} \tag{5.17}$$

From Table 5.3 we read a post-break power-law decay index $b = 2.1 \pm 0.1$ ($e = 2.3 \pm 0.1$) if $t_{\rm jet} \sim t_{\rm peak}$ ($t_{\rm jet} = t_{\rm br_2}$). Both are consistent with being post-jet break decay indices. We therefore conservatively assume $t_{\rm jet} < 1\,{\rm day}$, which leads to:

$$\Delta\theta < \begin{cases} 0.055 \left(\frac{E_{54}}{n_0}\right)^{-1/8} \text{ rad} & (k=0) \\ \\ 0.045 \left(\frac{E_{54}}{A_*}\right)^{-1/4} \text{ rad} & (k=2) \end{cases} \tag{5.18}$$

Evaluating Eq. 9 of [134] at $t = t_{\rm peak}$, when $\gamma \sim 1/\theta$ we obtain:

$$\frac{1}{\gamma(t_{\rm peak})} \approx \theta = \begin{cases} 0.03 \left(\frac{E_{54}}{n_0}\right)^{-1/8} \text{ rad} & (k=0) \\ \\ 0.03 \left(\frac{E_{54}}{A_*}\right)^{-1/4} \text{ rad} & (k=2) \end{cases} \tag{5.19}$$

Using Eq. 5.14 for the ISM environment we finally have $\theta > 0.014 E_{k,54}^{-3/16}$ rad. From the comparison of Eq. 5.19 and Eq. 5.18 it is apparent that $\theta > \Delta\theta/2$. Moreover, the slope of the rising part of the re-brightening of the afterglow is ~ 1.8, which is in rough agreement with the rising slope of the re-brightening obtained from model 3 of [68] - see their Fig. 2 - for $\theta \sim 3\Delta\theta$. This is consistent with $\theta > \Delta\theta/2$.

The off-axis interpretation implies that the value of the observed gamma-ray isotropic energy $E_{\gamma,{\rm iso},\theta}$ corresponds to an actual on-axis input of $E_{\gamma,{\rm iso},0} \approx a^{-2} E_{\gamma,{\rm iso},\theta}$ if $\theta < \Delta\theta$ and $E_{\gamma,{\rm iso},0} \approx a^{-3} E_{\gamma,{\rm iso},\theta}$ if $\theta < \Delta\theta$. Since $E_{\gamma,{\rm iso},0} \sim 10^{53}$ erg, this may lead to very high energy output for this burst, which may be unphysical. It is therefore important to obtain limits on the Lorentz factor of the prompt emission, since $a^{-1} \approx 1 + \Gamma_0^2 \theta^2$. Lower limits to Γ_0 can be obtained following [106], requiring the medium to be optically thin to annihilation of photon pairs (Eq. 5.20) and to scattering of photons by pair-created electrons and positrons (Eq. 5.21)[8]:

$$\Gamma_{\min,\gamma\gamma} = \frac{\widehat{\tau}_\theta^{1/(2\beta_{\rm B}+2)} \left(\frac{150\text{ keV}}{m_e c^2}\right)^{(\beta_{\rm B}-1)/(2\beta_{\rm B}+2)}}{(1+z)^{(1-\beta_{\rm B})/(\beta_{\rm B}+1)}} \times \begin{cases} a^{-1/2} & \theta < \Delta\theta \\ (a_*)^{1/(2\beta_{\rm B}+2)}\, a^{-(\beta_{\rm B}+2)/(2(\beta_{\rm B}+1))} & \theta > \Delta\theta \end{cases} \tag{5.20}$$

$$\Gamma_{\min,{\rm e}^\pm} = \widehat{\tau}_\theta^{1/(\beta_{\rm B}+3)} (1+z)^{(\beta_{\rm B}-1)/(\beta_{\rm B}+3)} \times \begin{cases} a^{-2/(\beta_{\rm B}+3)} & \theta < \Delta\theta \\ (a_*)^{1/(\beta_{\rm B}+3)}\, a^{-3/(\beta_{\rm B}+3)} & \theta > \Delta\theta \end{cases} \tag{5.21}$$

where $\beta_{\rm B}$ is the high energy photon index of the prompt Band spectrum.

[8] See APPENDIX 5.8.1 for a complete derivation of Eq. 5.20 and 5.21

From [15], the Lorentz factor at the deceleration radius and at the peak of the re-brightening can be related by $\gamma(R_{\rm peak}) = \gamma(R_{\rm dec})(R_{\rm peak}/R_{\rm dec})^{-(3-k)/2}$. The Lorentz factor at the deceleration radius is a factor $g < 1$ of the Lorentz factor of the prompt emission Γ_0. Combining this with $a^{-1} = 1 + \Gamma_0^2\theta^2$ and $\theta = 1/\gamma(t_{\rm peak})$, we obtain the following expression for the parameter a:

$$a^{-1} = 1 + g^{-2}\left(\frac{R_{\rm peak}}{R_{\rm dec}}\right)^{3-k} . \qquad (5.22)$$

Since $g \lesssim 1/2$, and $R_{\rm dec} \lesssim R_{\rm peak}$, we have $a^{-1} \gtrsim 5$ which, when substituted in equation 5.20 and 5.21 and keeping the strongest constraint, implies $\Gamma_0 \gtrsim 46$. To consider the other extreme case, where the deceleration time is $\sim T_{\rm GRB}$, one should be careful in translating the ratio of radii to ratio of times: for a prompt emission with a single pulse, the duration of the GRB $T_{\rm GRB}$ is the duration of the pulse, which changes with the parameter a from on-axis to off-axis, as then does $t_{\rm dec}$. We can therefore use off-axis values of the time $t \sim R$ which means $R_{\rm peak}/R_{\rm dec} \sim t_{\rm peak}/t_{\rm dec} \sim t_{\rm peak}/T_{\rm GRB}$ in our case here. Since $t_{\rm peak} \sim 2\times10^4$ s and $T_{\rm GRB} = 264.3$ s (we identify the duration of the GRB with the T_{90} parameter), $a^{-1} \gtrsim 300$ for $k = 2$ (then $\Gamma_0 \gtrsim 230$) and $a^{-1} \gtrsim 1.7\times10^3$ ($\Gamma_0 \gtrsim 17\times10^3$) for $k = 0$. In the case of a prompt emission with several pulses, as it is the case for GRB 081028, each pulse duration increases by a factor a^{-1} from on-axis to off-axis, however the total duration of the burst does not increase much, approximately by a factor of order unity, since the enlargement of pulses is somewhat cancelled by their overlapping. In this case, the GRB duration to consider is the on-axis one, for which $t \propto R/\gamma^2 \propto R^{4-k}$; since $t_{\rm peak}$ is the limit between the on-axis and off-axis cases we can use $t_{\rm peak} \propto R_{\rm peak}^{4-k}$ and then $a^{-1} = 1 + g^{-2}\left(\frac{t_{\rm peak}}{T_{\rm GRB}}\right)^{(3-k)/(4-k)} \gtrsim 100$ (or $\Gamma_0 \gtrsim 136$) for $k = 0$ and $a^{-1} \gtrsim 36$ (or $\Gamma_0 \gtrsim 94$) for $k = 2$.

The lower limit on the value of a^{-1} thus ranges between ~ 5 and $\sim 10^2$ [9]: this implies values of the isotropic on-axis gamma-ray energy output to range between $E_{\gamma,{\rm iso},0} \sim 3\times10^{54}$ erg and $E_{\gamma,{\rm iso},0} \sim 10^{57}$ erg if $\theta < \Delta\theta$ and even greater values for $\theta > \Delta\theta$: between $E_{\gamma,{\rm iso},0} \sim 1.4\times10^{55}$ erg and $E_{\gamma,{\rm iso},0} \sim 10^{59}$ erg. Considering that $E_{\rm k,iso} \sim 10^{55}$ erg, for the lower limit of this window $a^{-1} \sim 5$ the efficiency of the prompt emission becomes $\epsilon_\gamma \sim 0.23$, which is a more usual value (it is in the middle of the efficiency distribution of FP06). However, the upper limit of the range of values for a^{-1} gives an efficiency of 99% (when $\theta < \Delta\theta$, and thus an even higher value for $\theta > \Delta\theta$), which is exceptionally high and very hard to reconcile with models of the prompt emission. This would suggest that the observed prompt emission is from a different component than the observed afterglow emission.

An alternative way of achieving a more reasonable gamma-ray efficiency is if the observed prompt gamma-ray emission is from material along our line of

[9] Since GRB 081028 is composed of at least two pulses, we consider the most relevant case, when the observed off-axis duration of the prompt emission is close to the on-axis one.

sight, which has $E_{\rm k,iso} \sim E_{\gamma,\rm iso}$, while the peak in the X-ray and optical light-curves at $\sim 2 \times 10^4$ s is from a narrow jet-component pointed away from us that has a significantly higher $E_{\rm k,iso}$. In this picture the afterglow emission of this material along our line of sight (and possibly also between our line of sight and the core of the off-axis jet component) could account for the very flat (almost constant flux) early optical emission (from the white light detection at 275 s, through the R-band detection at 1780 s, and the I-band detections at several thousand seconds). This early optical emission appears to be from a different origin than the contemporaneous X-ray emission, and is most likely afterglow emission, regardless of the origin of the prompt emission: the observed X-ray and optical emission in the time interval $1.8\,{\rm ks} \leq {\rm t} \leq 9.5\,{\rm ks}$ implies a spectral index $|\beta_{OX}| < 0.5$. Conversely, assuming $\beta_{OX} = 0.5$, the expected X-ray contribution of the on-axis component at these times is $\approx 3 \times 10^{-4}$ mJy which is lower than the observed X-ray flux for $t < 9\,{\rm ks}$ and comparable to the observed one at $t \sim 9\,{\rm ks}$.

5.6.5 *Count rate drop at 250 ks*

A run test applied to the XRT light-curve data with $t > 80\,{\rm ks}$ fit with Eq. 5.2 requires the introduction of a second component to model the partial switch-off and re-brightening of the source around 2×10^5 s (Fig. 5.3). While the significance of this drop is model dependent, the origins of a possible component able to account for $\sim 10\%$ of the total X-ray re-brightening must be discussed.

The temporal properties of the second re-brightening seem to point out to late energy injection to the forward shock: the decaying power-laws before and after the drop are roughly consistent with each other but shifted upwards in the count-rate axis. Since at this epoch the observed X-ray frequencies are above both the cooling and the injection frequencies, in the standard afterglow scenario the X-ray flux is $\propto E_{\rm iso}^{(p+2)/4}$ independently of the external density medium profile (see e.g. [140], their appendix B and C): the observed jump in flux would therefore require an increase of the energy in the forward shock by a factor of ~ 3. A density jump in the external medium density is an unlikely explanation, since in this wavelength regime the forward shock flux is found to be independent of the density parameter.

5.7 *Summary and conclusions*

The 0.3-10 keV X-ray emission of GRB 081028 consists of a flat phase up to ~ 300 s (the XRT is likely to have captured the prompt emission in the X-ray energy band) followed by a steep decay with flares superimposed extending to ~ 7000 s (component 1). The light-curve then shows a re-brightening which starts to rise at $t \sim 8000\,{\rm s}$ and peaks around 20 ks (component 2). The different spectral and temporal properties strongly characterise the XRT signal as due to two distinct *emission* components. However, their further characterisation as emission coming from *physically* distinct *regions* is model dependent.

The strong hard-to-soft evolution characterising the prompt and steep decay phase of GRB 081028 from trigger time to 1000 s is well modelled by a shifting Band function: the spectral peak energy evolves to lower values, decaying as $E_{\rm peak} \propto t^{-7.1\pm0.7}$ or $E_{\rm peak} \propto (t-t_0)^{-4.2\pm2.4}$ when the zero-time of the power-law is allowed to vary: the best fit constrains this parameter to be $t_0 = 109\pm89$ s. In either case our results are not consistent with the $\propto t^{-1}$ behaviour predicted by the HLE in its simplest formulation. While a more realistic version of this model might still account for the observed $E_{\rm peak}$ evolution, other possibilities must be investigated as well: the adiabatic expansion cooling of the γ-ray source predicts a steeper than observed light-curve decay and is therefore unlikely. While the peak is moving, a softening of both the low and high-energy portions of the spectrum is clearly detected. The failure of both the curvature effect and the adiabatic cooling argues against the abrupt switch-off of the GRB source after the prompt emission and suggest the continuation of the central engine activity during the steep decay. An off-axis explanation may reconcile the high latitude emission or the adiabatic expansion cooling models with the data. This will be explored in a further work.

GRB 081028 has afforded us the unprecedented opportunity to track a smoothly rising X-ray afterglow after the steep decay: the rising phase of the emission component later accounting for the shallow light-curve phase is usually missed, being hidden by the steep decay which is the tail of the prompt emission both from the spectral and from the temporal point of view. The peculiarity of GRB 081028 lies in a small overlap in time between the steep decay and the following re-brightening caused by an unusual delay of the onset of the second component of emission. Contemporaneous optical data allow the evolution of the SED during the re-brightening to be constrained: the spectral distribution is found to be best described by a photo-electrically absorbed smoothly broken power-law with a break frequency evolving from 1.6×10^{15} Hz downward to the optical band. The break frequency can be identified with the injection frequency of a synchrotron spectrum in the fast cooling regime evolving as $\nu_{\rm b} \propto t^{-2.6\pm0.2}$. The intrinsic optical absorption is found to satisfy $A_{\rm V,z} < 0.22$.

The observed break frequency scaling is inconsistent with the standard predictions of the onset of the forward shock emission even if this model is able to account for the temporal properties of the X-ray re-brightening (note that in this context the delay of the second emission component is due to a lower than usual fireball Lorentz factor or external medium density). Alternative scenarios have therefore been considered. While a dust scattering origin of the X-ray emission is ruled out since we lack observational evidence for a non-negligible dust extinction and strong spectral softening, a reverse shock origin cannot be excluded. However, this can be accomplished only by requiring non-standard burst parameters: the ejecta should have a tail of Lorentz factors decreasing to low values; ϵ_e should be near equipartition; only a small fraction $\xi_e \sim 10^{-2}$ of electrons should contribute to the emission.

The predictions of the off-axis model have been discussed in detail: according to this model a peak of emission is expected when the beaming cone widens enough to engulf the line of sight. The delayed onset of the second emission

component is not a consequence of unusual intrinsic properties of the GRB outflow but is instead an observational artifact, due to the off-axis condition. The observed evolution of $\nu_{\rm b}$ is consistent with the expected evolution of the injection frequency of a fast cooling synchrotron spectrum for $0 \lesssim k \lesssim 2$. We interpret the light-curve properties as arising from an off-axis view, with $\theta \sim 3\Delta\theta$ and $\theta \sim 0.03(\frac{E_{54}}{n_0})^{-1/8}$ for k=0 (or $\theta \sim 0.03(\frac{E_{54}}{A_*})^{-1/4}$ for k=2), θ being the angle from the outer edge of the jet and $\Delta\theta$ the jet opening angle.

In this scenario, the peculiarity of GRB 081028, or the reason why we do not observe more GRB 081028-like events, may be attributed to the following reasons. Since GRB 081028 is a particularly bright (and therefore rare) event when viewed on-axis (with high on-axis $E_{\rm iso}$ and $L_{\rm iso}$ values), it is detectable by an off-axis observer even at the cosmological distance implied by its redshift z = 3.038. In addition, GRB 081028 appears to be characterized by a particularly narrow jet, for which the ratio of the detectable off-axis solid angle to on-axis solid angle is larger than for wider (but otherwise similar) jets. Finally, GRB 081028 might have a peculiar angular structure that is not representative of most GRBs, which would undermine the drawing of statistical conclusions under the assumption of a similar angular structure for most or all GRB jets.

The radiative efficiency is one of the key parameters in GRB science: a precise estimate of this parameter would allow one to distinguish between different models put forward to explain the observed emission. For the on-axis model, with $\epsilon_\gamma \sim 10^{-2}$, the GRB 081028 efficiency turns out to be lower than the values obtained by FP06 and LZ04 for a sample of pre-*Swift* GRBs: this directly implies that instead of having released as much energy in the prompt emission as most bursts of the two samples, GRB 081028 has a much greater kinetic energy injected in the outflow. Figure 5.11 clearly shows that this conclusion is likely to be extended to other *Swift* bursts with secure $E_{\gamma,{\rm iso}}$ measurement. This picture changes if we consider the off-axis interpretation: if the deceleration time is much longer than the prompt duration the prompt and afterglow emission are consistent with originating from the same physical component and the efficiency of the burst is comparable to most bursts; if instead the deceleration time is close to the end of the prompt emission, then the on-axis isotropic energy output would imply an extremely high efficiency of 99% which is very hard to explain. This suggests that the prompt and afterglow emission come from different physical components.

GRB 081028 demonstrates the evolution of GRB spectral properties from the onset of the explosion to $\sim 10^6$ s after trigger and shows that this is likely to be attributed to two distinctly contributing components of emission. These can be constrained only by prompt, broad-band coverage and good time resolution observations.

5.8 APPENDIX

5.8.1 Derivation of equations 3.20 and 3.21

As for the main article, the convention of a subscript 0 (θ) for on-axis (off-axis) quantities is used. Following [106], their eq. 5 and 8, the lower limit to γ_0 due to photons annihilation reads:

$$\gamma_{\min,\gamma\gamma} \equiv \frac{\widehat{\tau_0}^{1/(2\beta_{\rm B}+2)}}{(1+z)^{(1-\beta_{\rm B})/(\beta_{\rm B}+1)}} \left(\frac{E_{\max}}{m_e c^2}\right)^{(\beta_{\rm B}-1)/(2\beta_{\rm B}+2)} \tag{5.23}$$

while considering the scattering of photons by pair-created electrons and positrons:

$$\gamma_{\min,{\rm e}^\pm} \equiv \widehat{\tau_0}^{1/(\beta_{\rm B}+3)} (1+z)^{(\beta_{\rm B}-1)/(\beta_{\rm B}+3)} \tag{5.24}$$

where: $E_{\max} = 150$ keV for BAT observations; β_B is the high energy photon index of the prompt spectrum; z is the redshift of the burst. From eq. 4 of [106], the dimensionless quantity $\widehat{\tau}$ can be re-written as:

$$\widehat{\tau_0} = (2.1 \times 10^{11}) \, \frac{(d_L/7\,{\rm Gpc})^2 (0.511)^{(1-\beta_{\rm B})} {\rm f}_{1,0}}{(\delta T_0/0.1\,{\rm s})(\beta_{\rm B}-1)} \tag{5.25}$$

where: d_L is the luminosity distance; δT_0 is the typical time scale of variability and $f_{1,0}$ is the on-axis number of photons per second per square centimeter per MeV at the energy of 1 MeV. The on-axis quantities must be now related to the observed off-axis ones. In particular from eq. 5.7 directly follows $\delta T_0 = a\,\delta T_\theta$ and $\nu_0 = \nu_\theta / a$. The fluence $\mathcal{F} = \int \frac{dtdEEdN}{dEdAdt} \propto EdN/dA$ while $f = \int \frac{dtdEdN}{dEdAdt} \propto dN/dA$. For a point source located at $\theta > \Delta\theta$ $dN/dA \propto d\Omega \propto \delta^2$: this implies $\mathcal{F}_0 = a^{-3}\mathcal{F}_\theta$, $f_0 = a^{-2} f_\theta$. When $\theta < \Delta\theta$ the size of the region significantly contributing to the observed emission increases as $\theta \propto a^{-1}$: this translates into $\mathcal{F}_0 = a^{-2}\mathcal{F}_\theta$, $f_0 = a^{-1} f_\theta$. From the fact that $\widehat{\tau} \propto \frac{f}{\delta T}$ and requiring the continuity of the function at $\Delta\theta$, it follows:

$$\widehat{\tau_0} = \begin{cases} a^{-2}\widehat{\tau_\theta} & \theta < \Delta\theta \\ a_*^{-2} \left(\frac{a}{a_*}\right)^{-3} \widehat{\tau_\theta} & \theta > \Delta\theta \end{cases} \tag{5.26}$$

where we remind the reader that $a_* \equiv a(\Delta\theta) = 1/(1+\Gamma_0^2 \Delta\theta^2)$.
Substituting this result into eq. 5.23, leads to:

$$\Gamma_{\min,\gamma\gamma} = \frac{\widehat{\tau_\theta}^{1/(2\beta_{\rm B}+2)} \left(\frac{150\ {\rm keV}}{m_e c^2}\right)^{(\beta_{\rm B}-1)/(2\beta_{\rm B}+2)}}{(1+z)^{(1-\beta_{\rm B})/(\beta_{\rm B}+1)}} \times \begin{cases} a^{-1/2} & \theta < \Delta\theta \\ (a_*)^{1/(2\beta_{\rm B}+2)} \, a^{-(\beta_{\rm B}+2)/(2\beta_{\rm B}+2)} & \theta > \Delta\theta \end{cases} \tag{5.27}$$

$$\Gamma_{\min,{\rm e}^\pm} = \widehat{\tau_\theta}^{1/(\beta_{\rm B}+3)} (1+z)^{(\beta_{\rm B}-1)/(\beta_{\rm B}+3)} \times \begin{cases} a^{-2/(\beta_{\rm B}+3)} & \theta < \Delta\theta \\ (a_*)^{1/(\beta_{\rm B}+3)} \, a^{-3/(\beta_{\rm B}+3)} & \theta > \Delta\theta \end{cases} \tag{5.28}$$

The prompt spectrum of GRB 081028 does not allow to constrain the high energy photon index $\beta_{\rm B}$, being consistent with a cut-off power-law (see Table 5.5). Using $\beta_{\rm B} = -2.5$ (value we observe around 600 s, observer frame), $f_1 = 1.6 \times 10^{-3}\,\mathrm{photons\,cm^{-2}s^{-1}\,MeV^{-1}}$. The observed evolution of $\beta_{\rm B}$ (see Sect. 5.5.6) implies a harder high energy spectrum at $t < 600\,\mathrm{s}$: using $\beta_{\rm B} = -2.1$ we have $f_1 = 3.6 \times 10^{-3}\,\mathrm{photons\,cm^{-2}s^{-1}\,MeV^{-1}}$. In the following $f_1 \approx 2 \times 10^{-3}\,\mathrm{photons\,cm^{-2}s^{-1}\,MeV^{-1}}$ will be used.

Equation 5.18 defines an upper limit to $\Delta\theta$ that translates into a lower limit to a_* considering that $a(\theta) \approx /(1+\gamma^2\theta^2) \approx (\gamma\theta)^{-2}$ for $\gamma\theta \gg 1$. Inserting this information in the equation above and using $\delta T_\theta = 70\,\mathrm{s}$ (variability time associated to the two pulses, Sect. 5.5.1), $d_{\rm L} = 17.4\,\mathrm{Gpc}$, $\beta_{\rm B} = 2.5$, $\widehat{\tau_\theta} \approx 6.8 \times 10^6$, we finally obtain eq. 5.20 and eq. 5.21.

5.8.2 Tables

Tmid (s)	**Exp** (s)	**mag obs**	**mag corr**			**Flux obs (mJy)**	**Flux corr (mJy)**	
WHITE								
275.2	147.4	20.86	20.70	+0.46	-0.32	$8.757 \cdot 10^{-3}$	$1.023 \cdot 10^{-2}$	$\pm 3.030 \cdot 10^{-3}$
663.1	19.4	> 21.24	> 20.87	–	–	$< 7.480 \cdot 10^{-3}$	$< 8.747 \cdot 10^{-3}$	–
5174.2	196.6	> 21.02	> 20.85	–	–	$< 7.619 \cdot 10^{-3}$	$< 8.910 \cdot 10^{-3}$	–
6580.5	139.6	> 20.38	> 20.21	–	–	$< 1.374 \cdot 10^{-2}$	$< 1.606 \cdot 10^{-2}$	–
101479.4	8890.0	22.94	22.77	+1.51	-0.61	$1.301 \cdot 10^{-3}$	$1.520 \cdot 10^{-3}$	$\pm 9.769 \cdot 10^{-4}$
124146.5	8872.8	21.46	21.29	+0.25	-0.21	$5.078 \cdot 10^{-3}$	$5.934 \cdot 10^{-3}$	$\pm 1.056 \cdot 10^{-3}$
V								
185.9	9.1	> 16.99	> 16.88	–	–	$< 5.811 \cdot 10^{-1}$	$< 6.430 \cdot 10^{-1}$	–
366.6	19.5	> 18.60	> 18.49	–	–	$< 1.319 \cdot 10^{-1}$	$< 1.460 \cdot 10^{-1}$	–
712.7	19.4	> 18.06	> 17.95	–	–	$< 2.169 \cdot 10^{-1}$	$< 2.400 \cdot 10^{-1}$	–
4149.8	196.6	> 18.86	> 18.75	–	–	$< 1.038 \cdot 10^{-1}$	$< 1.149 \cdot 10^{-1}$	–
5584.7	196.6	> 19.63	> 19.52	–	–	$< 5.108 \cdot 10^{-2}$	$< 5.6524 \cdot 10^{-2}$	–
11192.6	598.5	20.64	20.54	+0.53	-0.35	$2.016 \cdot 10^{-2}$	$2.225 \cdot 10^{-2}$	$\pm 7.752 \cdot 10^{-3}$
28542.1	598.5	19.82	19.71	+0.23	-0.19	$4.304 \cdot 10^{-2}$	$4.750 \cdot 10^{-2}$	$\pm 8.264 \cdot 10^{-3}$
45891.3	598.6	19.39	19.28	+0.16	-0.14	$6.392 \cdot 10^{-2}$	$7.054 \cdot 10^{-2}$	$\pm 8.643 \cdot 10^{-3}$
57502.6	598.6	19.51	19.40	+0.22	-0.18	$5.745 \cdot 10^{-2}$	$6.341 \cdot 10^{-2}$	$\pm 1.043 \cdot 10^{-2}$
101806.7	8961.6	> 19.94	> 19.83	–	–	$< 3.839 \cdot 10^{-2}$	$< 4.249 \cdot 10^{-2}$	–
156450.1	6146.6	> 19.65	> 19.55	–	–	$< 5.015 \cdot 10^{-2}$	$< 5.498 \cdot 10^{-2}$	–
B								
465.7	19.4	> 18.77	> 18.63	–	–	$< 1.261 \cdot 10^{-1}$	$< 1.435 \cdot 10^{-1}$	–
4969.6	196.6	> 21.54	> 21.40	–	–	$< 9.837 \cdot 10^{-3}$	$< 1.119 \cdot 10^{-2}$	–
6404.7	196.6	> 20.66	> 20.53	–	–	$< 2.212 \cdot 10^{-2}$	$< 2.493 \cdot 10^{-2}$	–
17796.8	506.1	20.34	20.20	+0.23	-0.19	$2.971 \cdot 10^{-2}$	$3.371 \cdot 10^{-2}$	$\pm 5.730 \cdot 10^{-3}$
35208.9	483.4	19.92	19.78	+0.18	-0.15	$4.377 \cdot 10^{-2}$	$4.966 \cdot 10^{-2}$	$\pm 6.686 \cdot 10^{-3}$
64072.7	474.4	20.80	20.66	+0.38	-0.28	$1.943 \cdot 10^{-2}$	$2.205 \cdot 10^{-2}$	$\pm 5.705 \cdot 10^{-3}$
101152.1	8814.4	> 21.54	> 21.41	–	–	$< 9.837 \cdot 10^{-3}$	$< 1.10886 \cdot 10^{-2}$	–
155772.9	6047.3	> 22.70	> 22.56	–	–	$< 3.380 \cdot 10^{-3}$	$< 3.845 \cdot 10^{-3}$	–
U								
613.8	19.5	> 19.24	> 19.07	–	–	$< 2.899 \cdot 10^{-2}$	$< 3.390 \cdot 10^{-2}$	–
16976.9	598.6	> 20.58	> 20.42	–	–	$< 8.438 \cdot 10^{-3}$	$< 9.778 \cdot 10^{-3}$	–
23578.2	511.4	> 19.97	> 19.80	–	–	$< 1.480 \cdot 10^{-2}$	$< 1.731 \cdot 10^{-2}$	–
37243.3	3516.9	21.00	20.83	+0.38	-0.28	$5.764 \cdot 10^{-3}$	$6.727 \cdot 10^{-3}$	$\pm 1.693 \cdot 10^{-3}$
66660.8	3671.5	> 20.63	> 20.47	–	–	$< 8.058 \cdot 10^{-3}$	$< 9.337 \cdot 10^{-3}$	–
123770.1	8692.4	> 21.08	> 20.91	–	–	$< 5.324 \cdot 10^{-3}$	$< 6.226 \cdot 10^{-3}$	–
155516.4	5699.7	> 20.48	> 20.31	–	–	$< 9.252 \cdot 10^{-3}$	$< 1.082 \cdot 10^{-2}$	–
UVW1								
416.4	19.5	> 22.03	> 21.80	–	–	$< 1.412 \cdot 10^{-3}$	$< 1.746 \cdot 10^{-3}$	–
589.5	19.4	> 18.68	> 18.45	–	–	$< 3.090 \cdot 10^{-2}$	$< 3.819 \cdot 10^{-2}$	–
5994.8	196.6	> 22.63	> 22.40	–	–	$< 8.128 \cdot 10^{-4}$	$< 1.005 \cdot 10^{-3}$	–
33415.1	885.6	> 21.83	> 21.60	–	–	$< 1.698 \cdot 10^{-3}$	$< 2.099 \cdot 10^{-3}$	–
40105.9	885.6	> 23.16	> 22.93	–	–	$< 4.988 \cdot 10^{-4}$	$< 6.165 \cdot 10^{-4}$	–
51671.4	885.6	> 22.86	> 22.63	–	–	$< 6.576 \cdot 10^{-4}$	$< 8.128 \cdot 10^{-3}$	–
65720.4	4231.4	> 22.19	> 21.96	–	–	$< 1.219 \cdot 10^{-3}$	$< 1.506 \cdot 10^{-3}$	–
386961.8	36503.7	> 24.37	> 24.14	–	–	$< 1.637 \cdot 10^{-4}$	$< 2.023 \cdot 10^{-4}$	–
733574.4	42008.6	> 23.92	> 23.69	–	–	$< 2.477 \cdot 10^{-4}$	$< 3.062 \cdot 10^{-4}$	–
UVM2								
564.5	19.4	> 19.44	> 19.17	–	–	$< 1.477 \cdot 10^{-2}$	$< 2.663 \cdot 10^{-3}$	–
5789.7	196.6	> 21.30	> 21.04	–	–	$< 2.663 \cdot 10^{-3}$	$< 3.383 \cdot 10^{-3}$	–
29392.5	771.3	> 21.80	> 21.53	–	–	$< 1.680 \cdot 10^{-3}$	$< 2.154 \cdot 10^{-3}$	–
54444.4	4565.2	> 23.48	> 23.22	–	–	$< 3.576 \cdot 10^{-4}$	$< 4.543 \cdot 10^{-4}$	–
68159.5	885.6	> 21.30	> 21.03	–	–	$< 2.663 \cdot 10^{-3}$	$< 3.415 \cdot 10^{-3}$	–

Tab. 5.1: continue....

Tmid (s)	**Exp** (s)	**mag obs**	**mag corr**			**Flux obs** (mJy)	**Flux corr** (mJy)	
UVW2								
515.3	19.5	> 21.77	> 21.47	–	–	$< 1.454 \cdot 10^{-3}$	$< 1.917 \cdot 10^{-3}$	–
5380.0	196.6	> 21.48	> 21.18	–	–	$< 1.900 \cdot 10^{-3}$	$< 2.504 \cdot 10^{-3}$	–
56593.0	885.6	> 20.96	> 20.65	–	–	$< 3.067 \cdot 10^{-3}$	$< 4.080 \cdot 10^{-3}$	–

Tab. 5.1: Swift-UVOT photometric set of GRB 081028. $3-\sigma$ upper limits are provided in cases of non-detection. Column 1: observations mid-time since BAT trigger; column 2: exposure time; columns 3 and 5: observed magnitudes and fluxes; columns 4 and 8: extinction corrected magnitudes and fluxes; columns 6 and 7 report the errors on the extinction corrected magnitudes, while column 9 lists the errors on the extinction corrected flux. Only the Galactic extinction correction has been applied to the data.

Tmid (s)	**Filter**	**Exp** (s)	**mag obs**	**Flux obs** (mJy)	**mag corr**	**Flux corr** (mJy)
CrAO						
1779.84	R	23x60	21.62 ± 0.07	$(6.922 \pm 0.446) \cdot 10^{-3}$	21.545 ± 0.07	$(7.418 \pm 0.478) \cdot 10^{-3}$
3585.60	I	30x60	21.32 ± 0.09	$(7.560 \pm 0.627) \cdot 10^{-3}$	21.264 ± 0.09	$(7.961 \pm 0.660) \cdot 10^{-3}$
5529.60	I	30x60	21.43 ± 0.09	$(6.832 \pm 0.566) \cdot 10^{-3}$	21.374 ± 0.09	$(7.193 \pm 0.596) \cdot 10^{-3}$
7473.60	I	30x60	21.20 ± 0.08	$(8.444 \pm 0.622) \cdot 10^{-3}$	21.144 ± 0.08	$(8.444 \pm 0.622) \cdot 10^{-3}$
9426.24	I	30x60	20.66 ± 0.05	$(1.389 \pm 0.064) \cdot 10^{-2}$	20.604 ± 0.05	$(1.462 \pm 0.067) \cdot 10^{-2}$
GROND						
20880.0	g'		19.9 ± 0.1	$(3.98 \pm 0.37) \cdot 10^{-2}$	19.79 ± 0.1	$(4.406 \pm 0.410) \cdot 10^{-2}$
20880.0	r'		19.3 ± 0.1	$(6.92 \pm 0.64) \cdot 10^{-2}$	19.22 ± 0.1	$(7.454 \pm 0.686) \cdot 10^{-2}$
20880.0	i'		19.2 ± 0.1	$(7.59 \pm 0.70) \cdot 10^{-2}$	19.14 ± 0.1	$(8.017 \pm 0.738) \cdot 10^{-2}$
20880.0	z'		19.1 ± 0.1	$(8.38 \pm 0.77) \cdot 10^{-2}$	19.05 ± 0.1	$(8.694 \pm 0.801) \cdot 10^{-2}$
20880.0	J		19.0 ± 0.15	$(9.12 \pm 1.26) \cdot 10^{-2}$	18.97 ± 0.15	$(9.359 \pm 1.293) \cdot 10^{-2}$
20880.0	H		18.7 ± 0.15	$(1.202 \pm 0.166) \cdot 10^{-1}$	18.68 ± 0.15	$(1.221 \pm 0.169) \cdot 10^{-1}$
20880.0	K		19.0 ± 0.15	$(9.12 \pm 1.26) \cdot 10^{-2}$	19.00 ± 0.15	$(9.135 \pm 0.502) \cdot 10^{-2}$
112680.	g'		21.26 ± 0.05	$(1.14 \pm 0.05) \cdot 10^{-2}$	21.15 ± 0.05	$(1.259 \pm 0.058) \cdot 10^{-2}$
112680.	r'		20.49 ± 0.05	$(2.31 \pm 0.10) \cdot 10^{-2}$	20.41 ± 0.05	$(2.491 \pm 0.115) \cdot 10^{-2}$
112680.	i'		20.24 ± 0.05	$(2.91 \pm 0.13) \cdot 10^{-2}$	20.18 ± 0.05	$(3.076 \pm 0.142) \cdot 10^{-2}$
112680.	z'		19.99 ± 0.05	$(3.66 \pm 0.17) \cdot 10^{-2}$	19.94 ± 0.05	$(3.830 \pm 0.176) \cdot 10^{-2}$
112680.	J		19.6 ± 0.1	$(5.25 \pm 0.48) \cdot 10^{-2}$	19.57 ± 0.1	$(5.386 \pm 0.496) \cdot 10^{-2}$
PAIRITEL						
41133.2	J	1875.67	17.78 ± 0.12	$(1.232 \pm 0.126) \cdot 10^{-1}$	17.752 ± 0.12	$(1.264 \pm 0.140) \cdot 10^{-1}$
41133.2	H	1875.67	16.91 ± 0.10	$(1.763 \pm 0.162) \cdot 10^{-1}$	16.893 ± 0.10	$(1.791 \pm 0.165) \cdot 10^{-1}$
41133.2	K_s	1875.67	16.34 ± 0.13	$(1.941 \pm 0.232) \cdot 10^{-1}$	16.3383 ± 0.13	$(1.944 \pm 0.233) \cdot 10^{-1}$
44006.0	J	1844.28	17.60 ± 0.11	$(1.453 \pm 0.147) \cdot 10^{-1}$	17.572 ± 0.11	$(1.492 \pm 0.151) \cdot 10^{-1}$
44006.0	H	1844.28	16.83 ± 0.10	$(1.898 \pm 0.174) \cdot 10^{-1}$	16.813 ± 0.10	$(1.928 \pm 0.178) \cdot 10^{-1}$
44006.0	K_s	1844.28	15.87 ± 0.10	$(2.993 \pm 0.276) \cdot 10^{-1}$	15.8683 ± 0.10	$(2.993 \pm 0.276) \cdot 10^{-1}$
NOT						
19680.	R		19.23 ± 0.03	$(6.255 \pm 0.200) \cdot 10^{-2}$	19.1545 ± 0.03	$(6.706 \pm 0.185) \cdot 10^{-2}$

Tab. 5.2: Ground-based photometric set of GRB 081028. Column 1: observations mid-time since BAT trigger; column 2: photometric filter used; column 3: exposure; column4 and 5: observed magnitude and flux; column 6 and 7: magnitues and fluxes corrected for Galactic reddening. There is no evidence for intrinsic optical extinction (see Sect. 5.5.5). GROND (PAIRITEL) data come from Clemens et al., 2008; Clemens et al., 2008b (Miller et al., 2008).

6. TIMING IN THE TIME DOMAIN OF SWIFT GAMMA RAY BURSTS

While waiting for gravitational waves and neutrino detections, the best probe of the early stages of the GRB explosions are the gamma-ray photons giving rise to the complex temporal structure of the GRB light-curves.

6.1 Abstract

The time variability in the afterglow and prompt light-curve can provide important clues to the nature of the source that powers the GRB emission and to its surrounding. The power spectrum analysis in the time domain is developed starting from the findings of [102]: unlike the Fourier transform this is suitable to study the rms variations at different time scales. A complete characterization of the output of the technique is performed. Although optimized to study the GRB signal, the time in the time domain (TTD) analysis is able to provide the variability information of any kind of short, non-repetitive, non-stationary signal. The timing analysis of 252 15-150 keV light-curves of Swift-detected events, reveals the existence of three classes of GRBs. Moreover, when the cosmological time dilation effect is considered, the distribution of the GRB characteristic variability time scales is found to cluster around 0.6-1 s. A showcase for the application of the TTD analysis to the GRB prompt emission is represented by the naked-eye GRB 080319B: this burst shows the presence of two characteristic variability time scales. Both undergo a remarkable evolution during the prompt emission and are strongly energy dependent. Different theoretical interpretations are discussed: none of them is able to account for all the observational findings. The TTD analysis provides an unprecedented description of the temporal properties of the prompt emission: a full interpretation of its meaning and a robust connection to the physics and related models will be the next step of the research.

6.2 Introduction

The *future* of the Gamma Ray Burst (GRB) prompt emission study relies on the detection of their counterparts in the gravitational wave and neutrino channels. At *present* the best probe of the early stages of the GRB explosion are still their

gamma-ray photons which reveal the temporal and spectral structure of GRB pulses.

GRBs are short a-periodic events with a temporal structure that represents a challenge for standard temporal analysis techniques: while $\sim 15\%$ of the GRBs consists of a single smooth FRED structure (Fast Rise Exponential Decay), the majority seems to be the result of the random superposition of a number of emission episodes. This means that, while the determination of the relevant timescales is known to be the essential ingredient to understand the underlying physical process, the temporal studies of the prompt emission phase are not yet able to describe and explain their basic temporal properties. In particular, the temporal structure of any burst profile is likely to be determined by the combination of several intrinsic (cooling mechanisms, jet profile, distance of the emitting region from the central engine, profiles of bulk Lorentz factor, etc) and extrinsic parameters (viewing angle effects, intervening absorption). An accurate study of the variability properties of GRB profiles is therefore of primary importance.

The present situation is even worse for the afterglow emission: in this case the low temporal resolution characterizing the optical, NIR and radio observations prevents any serious study of temporal variability in those wave-length ranges. A beautiful exception to this rule is given by GRB 080319B, where the optical prompt emission was tracked by the TORTORA camera (see [13] and references therein) with a ~ 1.3 s temporal resolution. I refer the reader to Guidorzi, Margutti et al., in preparation for further details. The timing technique described in this chapter can be applied to the early X-ray afterglow of *Swift* GRBs: for bright GRBs, the XRT provides the temporal information down to the 2 ms timescale. The variability information of the early X-ray afterglow can be extracted for the first time: to this topic is dedicated subsec. 6.7.4.

A primary purpose of this work is to quantify the degree of determinism underlying the observed variability history and heterogeneous appearances of the GRB signal in the time domain. This determinism, if present (as shown in Sec. 6.7), puts strong constraints on the possible physical mechanisms at work. This chapter is organized as follows: the limits of the standard timing approaches are described in Sec. 6.3, while the first application of the TTD analysis on GRB data and its basic formulation are treated in Sec. 6.4. A detailed picture of the output of the TTD is given in Sec. 6.5. Section 6.6 is instead dedicated to the application of the timing technique to the prompt emission of GRBs. The results are described in Sec. 6.7: particular attention is devoted to GRB 080319B in subsect. 6.7.3. Finally, the conclusions are drawn in Sec. 6.8.

A short review of the relevant timescales of the GRB physics according to the standard scenarios is given in the introduction chapter.

6.3 Limits of the standard timing approaches

The main challenges encountered in the temporal analysis are strongly related to the intrinsic short-term, non-repetitive, composite structure of the GRB signal. In particular, the temporal approaches that can be found in the GRB literature con be roughly divided into three categories: pulse fitting, peak finding algorithms and FFT-related (Fast Fourier Transform) approaches. The limits of each category of studies are outlined below.

Pulse fitting approaches: A great effort has been done trying to model the GRB pulses and to study their shapes and the distribution of the best fit parameters. These studies have found in the light-curve pulses the building blocks of the GRB light-curves. However: first, a universal pulse shape is assumed and the obtained results in part depend on the assumed shape ; second, the identification of long smooth structures (for example at low energies) or of spiky features that are not well fit by the assumed function is difficult and sometimes impossible[1]. Finally, the deconvolution of overlapping pulses is problematic: in most bright GRBs the pulses are bunched together and inevitably overlap while in most dimmer bursts the low signal-to-noise prevents any kind of pulse by pulse study. Examples of this kind of studies has been performed by [132] and [133].

Peak finding algorithms: Much of the GRB temporal analysis has been done trying to extract information directly from the count-rate light-curves. A number of automatic pulse selection algorithms appeared in the literature (see e.g. [158]): this approach has the advantage of an objective way of identifying pulses (at least of the ones with a high signal-to-noise ratio). The main difficulty is in overcoming the limitations imposed by the presence of noise and the overlap of neighboring pulses. This directly translates into a subjective identification of low signal-to-noise ratio pulses.

FFT related approaches: This category is meant to comprehend all the standard linear analysis tools that share the Fourier transform approach: ACF[2] studies, CCF[3] studies, PSD[4] studies in the frequency domain (see e.g. [18]). The main results of this category comprehend: quantification of the time lag of high energy photons with respect to low energy photons in the gamma-ray domain; discovery of two classes of GRBs: the long lag bursts and the GRB with a negligible time lag; discovery of the broad and the narrow ACF bursts classes: this property has not found a physical explanation, yet. However, this approach suffers from many limitations I list below. First, most inferences based on these tools would require stationary signals where the duration is much longer than the typical pulse width: a way to overcome this limitations is to estimate "average" behaviors. However, this automatically assumes that each burst is a single realization of the very same stochastic process and no GRB subclass exists (this

[1] Visual inspection suggests the presence of a broad, smooth component with short-term spikes superimposed in a few bursts. See e.g. [196] and [132].

[2] Auto Correlation Function

[3] Cross Correlation Function

[4] Power Spectral Density

is in contrast with the observations). This approach is shared by [10], [11] and [49]. Second, in spite of the wide usage of the FFT to quantify the variability timescales of GRB profiles, care must be used in the interpretation of the Fourier spectrum of an aperiodic signal in the time domain (see e.g. [103]): the discrete Fourier transform expresses a light-curve $x(t_k)$ into sine wave components in the frequency domain:

$$a(f_j) = \sum x(t_k) e^{-i2\pi f_j k \Delta t} \tag{6.1}$$

where $a(f_j)$ is the Fourier amplitude of sine wave components at frequency $f_j = j/(N\Delta t)$, $j = -N/2, ..., N/2 - 1$ and $x(t_k)$ represents the photon counts during a time interval $(t_k, t_k + \Delta t)$, $k = 1, 2, ...N$ with $t_k = (k-1)\Delta t$. The Fourier power density is defined as:

$$p_f(f_j) = |a(f_j)|^2 \tag{6.2}$$

This quantity is used to describe the variability power at different frequencies f_j: however, this does *not* represent the distribution of the variability power over timescales $1/f_j$: the power at a frequency f^* does not represent the variability power at a time scale $t^* = 1/f^*$ unless the signal is periodic with frequency f^*. The relation between the frequency and time domain for the Fourier transform is expressed by the Parseval's theorem which states that the *integral* of the Fourier power density over the *whole* frequency range is equal to the variability power of the same process in the time domain:

$$\sum p_f(f_j)\Delta f = \sum |r(t_k)|^2 \Delta t \tag{6.3}$$

where $r(t_k) = x(t_k)/\Delta t$ is the count rate at t_k and $\Delta f = 1/(N\Delta t)$. *Nothing is said about the power density distribution over the time domain* so that the rms variation versus timescale of a time series may differ substantially from its Fourier spectrum: this becomes immediately clear if a sinusoidal signal is taken as an example. In this case the Fourier spectrum is a δ function (or approximately a δ function if the discrete Fourier transform is used instead of the continuous one); this means that this spectrum has almost no power over frequencies different from the one related to the periodicity of the signal f^*. However, it is not true that the signal is variable *only* over a timescale $t_{var} = 1/f^*$: instead, the signal shows variability in the time domain over any timescale t_{var} with $t_{var} < f^*$. This is portrayed in Fig. 6.1. The Fourier PSD, while giving the complete information about the periodicity of this signal, is still not an accurate tool to represent the variability over different timescales of a time series: in principle, the power densities in the time domain can be derived from the Fourier spectrum only if ones perfectly knows the power density which is associated to each sinusoidal function and then sum them up weighting each contribution by the Fourier amplitude coefficient. (See also [28]).

The TTD can therefore be a complementary tool to characterize the variability of GRB sources in the gamma-ray and X-ray regime. Since any physical

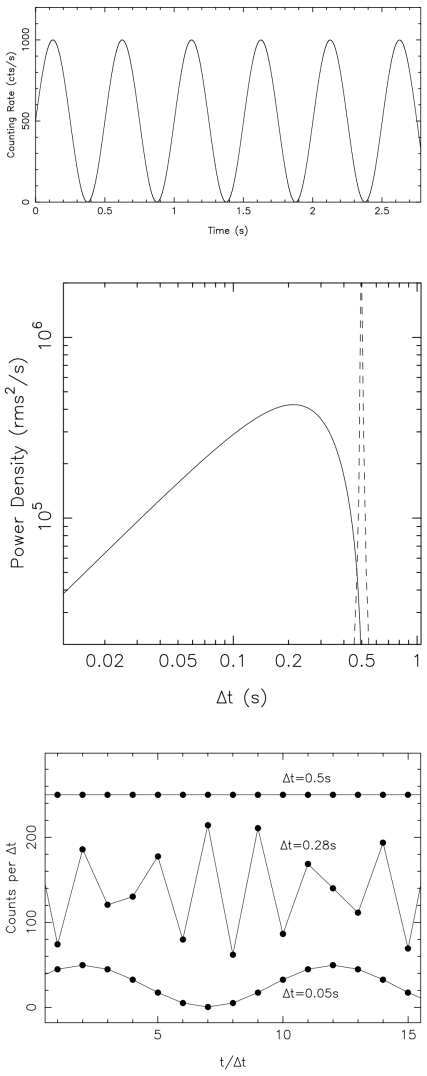

Fig. 6.1: Upper panel: sinusoidal signal used as input of the Fourier transform and temporal analysis in the time domain. *Middle panel*: dashed line: power density spectrum derived from the FFT of the sine signal and shifted downward of a factor of 100; solid line: variability spectrum as obtained by the temporal analysis technique described in this chapter. *Bottom panel*: resulting count rate light curves obtained re-binning the original sine signal over the indicated timescales. The signal shows clear variability over timescales which are different from the period of the sine wave. (Adapted from [103]).

process actually occurs in the time domain, the study of real variability amplitudes at different timescales could be useful in understanding a time-varying process.

6.4 The TTD technique in the literature

This section is dedicated to the description of the Timing in the Time Domain (TTD) technique as first formulated by [102] and [103] (SubSec. 6.4.1) and to the first application to GRB signals by [179] (SubSec. 6.4.2) before any fine tuning of the technique to the nature of the GRB signal. This describes the state of the art before the present work.

6.4.1 Basic formulation

The TTD analysis was first formulated by [102] and [103]. Given a counting series $x(k)$ I define $r(k)$ the corresponding counting rate series: these are obtained from a time history of observed photons with a time step Δt. The variation power $P(\Delta t)$ is defined as:

$$P(\Delta t) = \frac{Var(x)}{(\Delta t)^2} = \frac{\frac{1}{N}\sum_k (x(k) - \overline{x})^2}{(\Delta t)^2} = \frac{1}{N}\sum_k (r(k) - \overline{r})^2 \ \ [\mathrm{rms}^2] \qquad (6.4)$$

where $\overline{x} = \frac{\sum_k x(k)}{N} \equiv \overline{x}(\Delta t)$ and $\overline{r} = \frac{\sum_k r(k)}{N}$, which does not depend on the time step Δt. Note that the power on a time scale Δt does not receive any contribution from any time scale $< \Delta t$ (since any variability information is lost on those time scales for a signal which has been re-binned on Δt). On the contrary, any variability on time scales $> \Delta t$ contributes to the observed $P(\Delta t)$, so that this quantity can be viewed as the integral of the variability power for time scales $> \Delta t$. Re-binning the count rate light-curve over different time scales Δt_1, Δt_2, etc... it is possible to obtain the Power distribution of the signal over the different time scales. However, to extract the variability information from $P(\Delta t)$, a first time derivative of $P(\Delta t)$ is necessary. We name the new quantity the power density:

$$p(\Delta t) = \frac{dP(\Delta t)}{d\Delta t} \ \ [\mathrm{rms}^2 \mathrm{s}^{-1}] \qquad (6.5)$$

this is the rate of change of $P(\Delta t)$ with respect to the time step Δt. In practice, one expects the Power to be a decreasing function of the re-binning time Δt: this means that Eq. 6.5 defines a quantity which would be always negative. For this reason it is preferable to define $p(\Delta t) = -\frac{dP(\Delta t)}{d\Delta t}$. Second: in practice we do not have the knowledge of the continuous function $P(\Delta t)$: instead we have access to a particular sampling (over particular time scales) of the same function. The definition of the power density can be revised as follows, taking into consideration the two observations above: from two Powers, $P(\Delta t_1)$ and

$P(\Delta t_2)$, at two time scales Δt_1 and Δt_2 with $\Delta t_2 > \Delta t_1$, the power density at $\Delta t = \frac{\Delta t_1 + \Delta t_2}{2}$ is given approximately by:

$$p(\Delta t) = \frac{P(\Delta t_1) - P(\Delta t_2)}{(\Delta t_2 - \Delta t_1)} \quad (\mathrm{rms}^2 \mathrm{s}^{-1}) \tag{6.6}$$

For a pure Poisson noise distribution, the previous equation reduces to:

$$P_{\mathrm{noise}} = \frac{Var(x)}{(\Delta t)^2} = \frac{\overline{x}}{(\Delta t)^2} = \frac{r}{\Delta t} \quad (\mathrm{rms}^2) \tag{6.7}$$

where r is the expectation value of the counting rate which can be estimated by the global average of the observation. The noise power density at $\Delta t = \frac{\Delta t_1 + \Delta t_2}{2}$ is given by:

$$p_{\mathrm{noise}}(\Delta t) = \frac{P_{\mathrm{noise}}(\Delta t_1) - P_{\mathrm{noise}}(\Delta t_2)}{(\Delta t_2 - \Delta t_1)} = \frac{r}{\Delta t_1 \Delta t_2} \quad (\mathrm{rms}^2 \mathrm{s}^{-1}) \tag{6.8}$$

The signal power density (power density which is not due to the noise contribution) can be defined as

$$p_{\mathrm{signal}}(\Delta t) = p(\Delta t) - p_{\mathrm{noise}}(\Delta t) \tag{6.9}$$

Finally, the fractional power density is given by:

$$fpd(\Delta t) = \frac{p_{\mathrm{signal}}(\Delta t)}{r^2} \quad (\mathrm{rms/mean})^2 \mathrm{s}^{-1} \tag{6.10}$$

This technique was first applied to the X-ray signal coming from X-ray binaries [103] and to study the variability of Cygnus X-1 [102]. In both cases it was possible to divide the observation into different segments (M) each containing N successive counts. Each segment is treated as a realization of the same underlying process, so that if y is any of the quantities defined above (Power, density power, etc.), after obtaining M evaluation of y (one from each segment), the best estimate of the value of y for the timescale Δt is considered to be:

$$\overline{y}(\Delta t) = \frac{1}{M} \sum_i y_i(\Delta t) \tag{6.11}$$

The associated error is computed as:

$$\sigma(\overline{y}) = \sqrt{\sum_i \frac{(y_i - \overline{y})^2}{M(M-1)}} \tag{6.12}$$

This renormalization assures that the results are completely insensitive to the introduction of a constant multiplicative factor to the count rates.

These assumptions do not hold for GRBs.

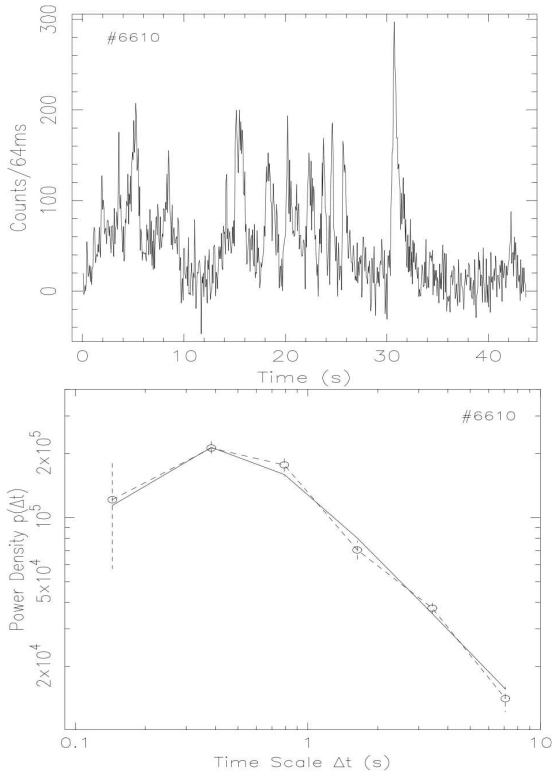

Fig. 6.2: Upper panel: time profile of the BATSE GRB 6610. *Lower panel*: corresponding signal power density as defined by 6.9. Solid line: best fit broken power law model. See the main text for details. Adapted from [179].

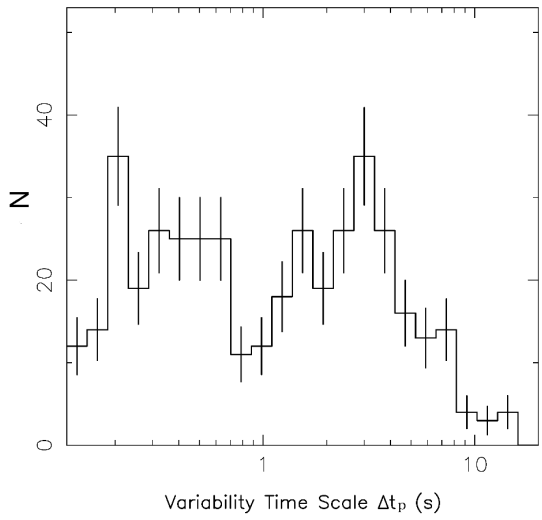

Fig. 6.3: Bimodal distribution of the characteristic variability time scale Δt_p . Adapted from [179].

6.4.2 The first application to GRB signals

The TTD technique as described above was first applied by [179] to a sample of 478 gamma-ray light-curves of GRBs detected by BATSE with a time resolution of 64 ms. The fundamental findings and limits of this first application are described below.

The study concentrated on bright, long bursts with $T_{100} > 15$ s. Since no redshift information is available for these GRBs, all the quantities were calculated in the observer frame. To limit the influence of the background each light-curve was cut using the T_{100} window: the T_{90} window was extended forward for $0.05T_{90}$ and backward of the same quantity. For each of the 478 GRB prompt light-curves, the signal power density of Eq. 6.9 was derived. Out of 478 PDS (Power Density Spectra), 63 keep rising until the smallest investigated time-scale, while the remaining PDS showed a clear peak of the type shown in Fig. 6.2. The main finding of this work was a bimodal distribution of the time-scales corresponding to the peak of the PDS (see Fig. 6.3): as shown in Sect. 6.5, these are characteristic time scales of variability of the GRB light-curves. This would imply the existence of two classes of GRBs in the variability plane: the first would comprise the slowly-varying GRB, with a typical Δt_p of a few seconds; the second family is made by GRB with prompt variability around $0.2 - 0.3$ s. The proposed physical explanation included: different size of the progenitor of the two groups; winds ejected at different distances or different distances between winds. I refer the reader to [179] for further details.

While particularly interesting, this study suffered from some limitations,

partly due to observational constraints and partly to the lack of characterization of the TTD technique. In particular:

1. No red-shift information was available for the 478 BATSE bursts, so that only observer frame quantities could be computed. In particular, the characteristic variability time scales could not be corrected for cosmological time dilation effects: this makes difficult the comparison of properties of different GRBs. The same bimodal distribution of Fig. 6.3 suffers from this limitation.

2. If the two classes of GRBs (the fast and the slow variable families) are physical, they are also likely to show other distinctive features: afterglow emission, host galaxies populations etc. This information was not available for the vast majority of the BATSE GRBs, but is now available thanks to the fast re-pointing capability of *Swift*.

3. The TTD was used by [179] in a unique energy band (the summed channels II and III which corresponds to $50 - 300$ keV observer frame). No study of the evolution of the variability of a GRB as a function of energy was done. However, the way the variability time scales are found to evolve with energy constitutes a precious characterization of the physical mechanism at work. (See Sect. 6.7.3).

4. The same can be said about the temporal evolution of the variability time scales. The TTD was applied by [179] to the entire burst profile: no study of the possible temporal evolution of the variability time scale was done. (See Sect. 6.7.3).

5. The power density was calculated at time scales Δt arranged at equal intervals in logarithmic space. This results in a poor time-resolution of the power density and of all the computed temporal quantities as shown in Fig. 6.2. The implication is a poor constrain on Δt_p and the necessity to fit the power density distribution with a broken power law as portrayed in Fig. 6.2, solid line: it is worth noting that, since the points of the power density distribution are not independent from one another, the acceptability of the fit could not be assessed using standard tools like the χ^2 minimization. Moreover, the poor temporal resolution did not allow the authors to appreciate the complete shape of the power density distributions: in particular, they were not able to find different variability times scales with different power in the same burst profile. Also in this case, the presence of more than one variability time scale in a single GRB adds important information to constrain the underlying physics.

6. A problem is the computation of the errors associated to each power density point: since the approach outlined at the end of Sect. 6.4.1 is not applicable to the GRBs because of their nature of short term, non-repetitive events, another approach is needed. [179] binned the power density with an approximately equal number of data points in each time scale bin and

derived the uncertainties accordingly. While in this way a smoothing of the power density distribution is achieved, the error bars do not reflect the significance of the variability detection.

7. The problem of the significance of the power associated to each particular time scale (or the probability that the observed power is due to a random fluctuation in the data) is never addressed in the paper.

8. The window of investigation was defined by [179] to the T_{100} to limit the contribution of the noise: however, the direct consequence was the impossibility to study the asymptotic behavior of the power density for time scales greater than the variability one. The time series of investigation can be instead extended to a greater time interval which comprehends consistent periods of noise if an accurate study of the power associated to the noise of that particular instrument is done. The work by [179] lacks of this study.

9. The authors limited their study to the power density. The definition of other quantities makes the results of the TTD analysis useful for other tools. See subsect. 6.5.6.

The present work is aimed at overcoming the limitations above, showing how simple and powerful the TTD analysis is when applied to the GRB data set.

6.5 Characterization of the TTD output

The previous section has shown the state of the art before the completion of this work. The aim of this Sect. is to fully characterize the output of the TTD analysis, with particular reference to the Fractional Power Density (fpd, defined in Eq. 6.10).

Generally speaking, the fpd is expected to show a peak in correspondence to a characteristic variability time scale Δt_{var}: in Fig. 6.1, middle panel, the power density is plotted. This quantity (which is the a re-normalized version of the fpd) shows a clear peak at ~ 0.2 s which corresponds to $T/4$ where T is the period of the sine wave. This behavior can be understood as follows: the fpd is basically minus the first time derivative of the Power. The Power is expected to decrease with the increase of smoothing time scale Δt, since the variability over every time scale $< \Delta t$ is washed out. If the variability of the signal is concentrated on a particular time scale Δt_{var}, a consistent decrease of the Power is expected as soon as the re-binning time scale matches the variability time scale: this means that its first time derivative with respect to Δt will experience a strong decrease or that the fpd, which is defined positive, will show an important peak. This is portrayed in Fig. 6.4.

This section is organized as follows: the shape of the fpd as expected from a Norris 2005 profile is described in subsect. 6.5.1, while subsect. 6.5.2 is dedicated to the description of the parameters to which the fpd is particularly sensitive and on which mostly depends. The asymptotic behavior of the fpd for

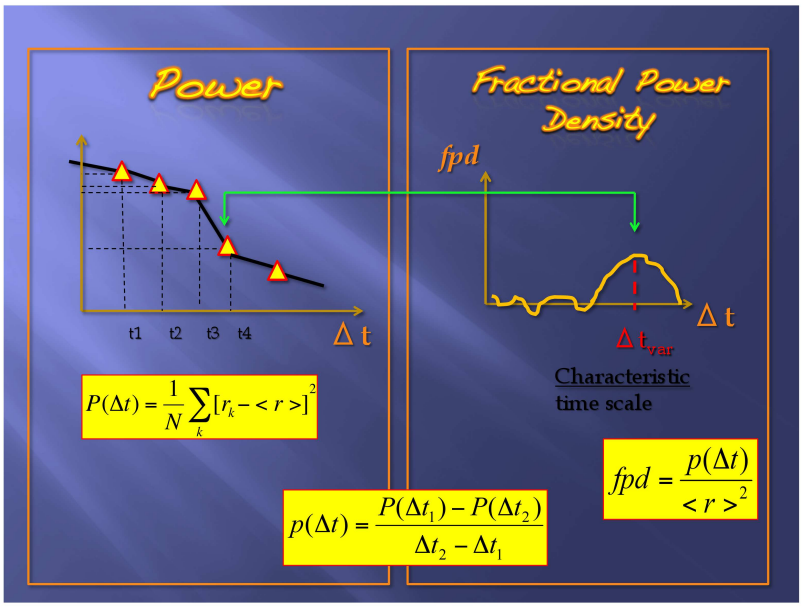

Fig. 6.4: Cartoon describing the link between the Power and the Fractional Power Density fpd: when the smoothing procedure encounters Δt_{var} which is the variability time scale of the signal, the Power experiences a sharp drop while the fpd shows a clear peak. This allows the identification of the characteristic time scale of variability of the signal.

time scales $\gg \Delta t_{var}$ is described in subsect. 6.5.3: this is particularly useful to characterize the tail of the prompt emission; power-law and exponential signals are analyzed in subsect. 6.5.4 and 6.5.5, respectively. A summary and a plot of the different features of the *fpd* shape can be found at the end of subsect. 6.5.5: this is essential to read the output of the TTD analysis. Finally, a new quantity, the Power Density Ratio is introduced and defined in subsection 6.5.6.

6.5.1 Fractional power density of a Norris 2005 profile

The typical *fpd* shape for a Norris 2005 profile is derived in this paragraph. This profile provides a good fit for both prompt pulses (both in the optical and in the gamma-ray range, see Guidorzi, Margutti, et al., in preparation and [133], respectively) and of X-ray flares (Chincarini et al., in prep.) and is therefore of particular interest. The functional shape is proportional to the inverse of the product of two exponentials, one increasing and the other one decreasing with time, as follows [133]:

$$I(t) = A\frac{\lambda}{\exp(\tau_1/t)\exp(t/\tau_2)} \quad \text{for t} > 0 \tag{6.13}$$

where $\mu = (\tau_1/\tau_2)^{1/2}$ and $\lambda = \exp(2\mu)$.
Three time scales describe the profile: the rise time, the decay time and the width of the pulse. The first exponential drives the rise at the pulse onset, while after the peak the second exponential becomes more and more dominant with time. The $1/e$ rise and decay times are defined by:

$$\tau_{\rm dec,rise} = \frac{1}{2}\tau_2\Big[(1+4\mu)^{1/2} \pm 1\Big] \tag{6.14}$$

while the width of the pulse between the two $1/e$ intensity points is given by:

$$w = \tau_2(1+4\mu)^{1/2} \tag{6.15}$$

Figure 6.5, left panel, shows the typical shape of a Norris 2005 profile; the respective *fpd* are plotted in the right panel. In particular: the three *fpd* converge to the same asymptotic behavior after the peak (the detailed analysis of this behavior is the subject of subsect. 6.5.3); almost symmetrical pulses give rise to an *fpd* with a single peak; if instead the pulse has a rise time which is very different from its decay time, then the *fpd* shows a flat phase between two timescales Δt_1 and Δt_2: this is because the analyzed signal actually contains two variability time scales, the first related to the sharp rise and the other to the smoother decay (blue solid line of Fig. 6.5).

The time scale of the peak of the *fpd* is found to be strongly correlated with the width of the pulses. The relation between the two quantities has been determined running a set of 1000 simulations with 1000 different Norris pulse profiles. In particular, τ_1 was allowed to vary between 1 and 100, with steps of 1; τ_2 was allowed to vary between 1 and 10, with steps of 1. These ranges has been chosen with reference to Fig. 1 of [133]. The width-*fpd* peak relation can be described by the law $\mathrm{Log[w]} = \mathrm{b} + \mathrm{Log[fpd_{peak}]}$ with best fit parameter $b = 0.081 \pm 0.021$ and inferred scatter $\sigma = 0.031$ (see Fig. 6.6).

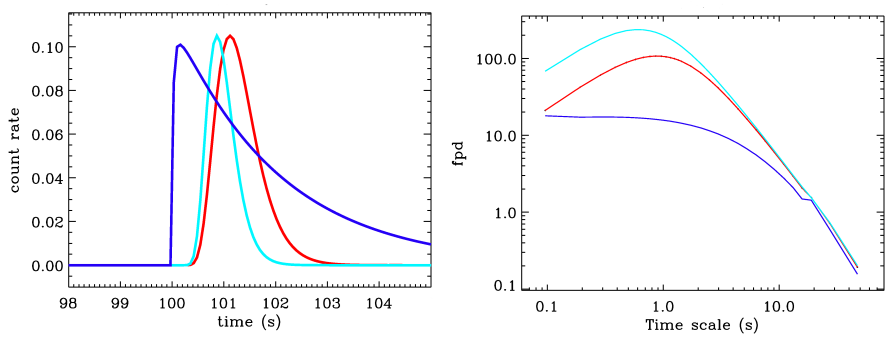

Fig. 6.5: *Left panel:* a set of 3 Norris 2005 profiles with equal amplitude but different time scales. Light blue solid line: $\tau_1 = 5$ s, $\tau_2 = 0.15$ s ($w = 0.74$ s); Red solid line: $\tau_1 = 5$ s, $\tau_2 = 0.25$ s ($w = 1.10$ s); Blue solid line: $\tau_1 = 0.01$ s, $\tau_2 = 2.0$ s ($w = 2.27$ s). *Right panel:* respective fpd plots.

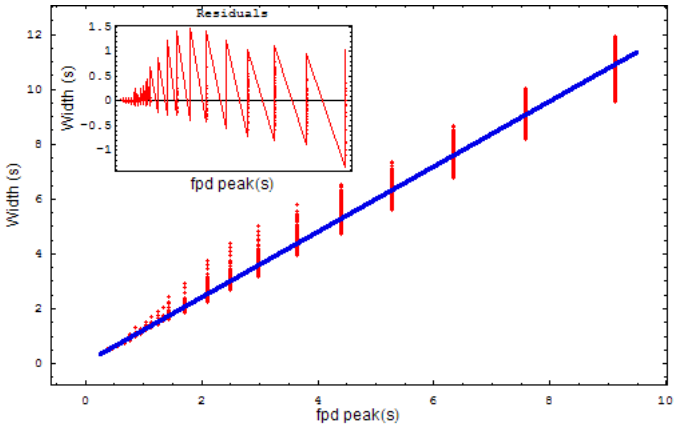

Fig. 6.6: Width-fpd peak relation for a Norris 2005 profile as determined by running a set of 1000 simulations. Blue solid line: best fit. *Inset:* residuals with respect to the best fit relation.

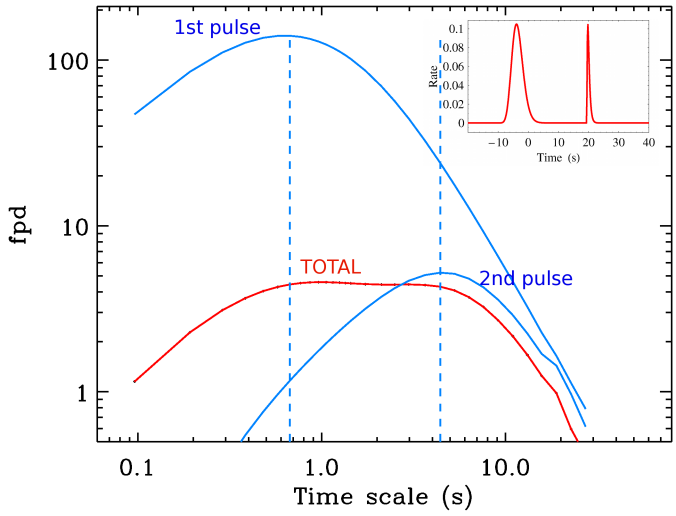

Fig. 6.7: Solid red line: fpd of a signal made of two pulses with equal amplitude but different widths. Light blue solid lines: fpd of each of the two pulses. The total fpd shows two peaks in correspondence of the original time scales of variability associated to each of the two pulses. *Inset*: input signal.

6.5.2 *Fractional power density dependence on overlap, width and amplitude of different pulses*

The fpd output is basically sensitive to three parameters: the pulse width, pulse amplitude and the overlap between different pulses. The effect of the three parameters is investigated below.

Width

With reference to Fig. 6.7, it is clear that from the fpd analysis it is possible to extract the information on the original time scales of variability: the signal is made of two pulses with equal amplitude but different widths. This is reflected by the presence of two peaks with equal amplitude in the fpd plot: the peak time scales are exactly at the expected positions (see Fig. 6.7).

Amplitude

Each fpd peak marks the position of a variability time scale. The relative importance of each time scale in a single profile is given by the amplitude of the fpd peak. Figure 6.8 shows a total fpd where it is still possible to see the two time scales of variability: the difference with respect to Fig. 6.7 is that the fpd is dominated by the smaller time scale of variability, since in the original profile a greater amplitude was associated to the pulse with the lower width.

Overlap

The overlap of neighboring pulses is the major limitation to any kind of temporal

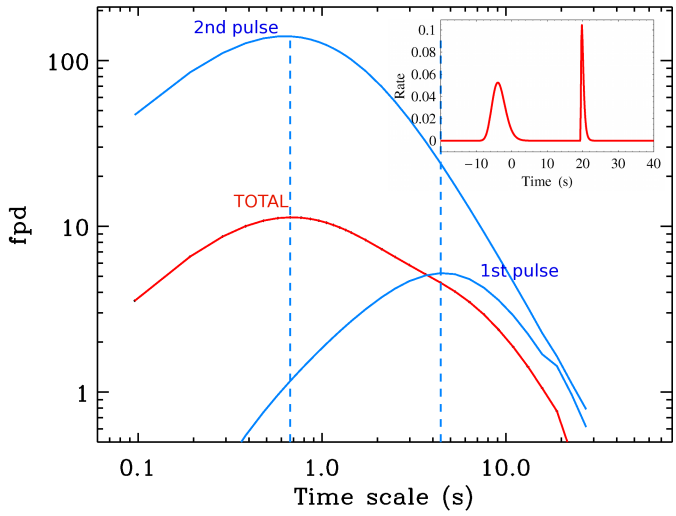

Fig. 6.8: Solid red line: fpd of a signal made of two pulses with different amplitudes and different widths. Light blue solid lines: fpd of each of the two pulses. The total fpd shows two peaks in correspondence of the original time scales of variability associated to each of the two pulses. The amplitude of the fpd peaks reflects the amplitudes of the original pulses *Inset*: input signal.

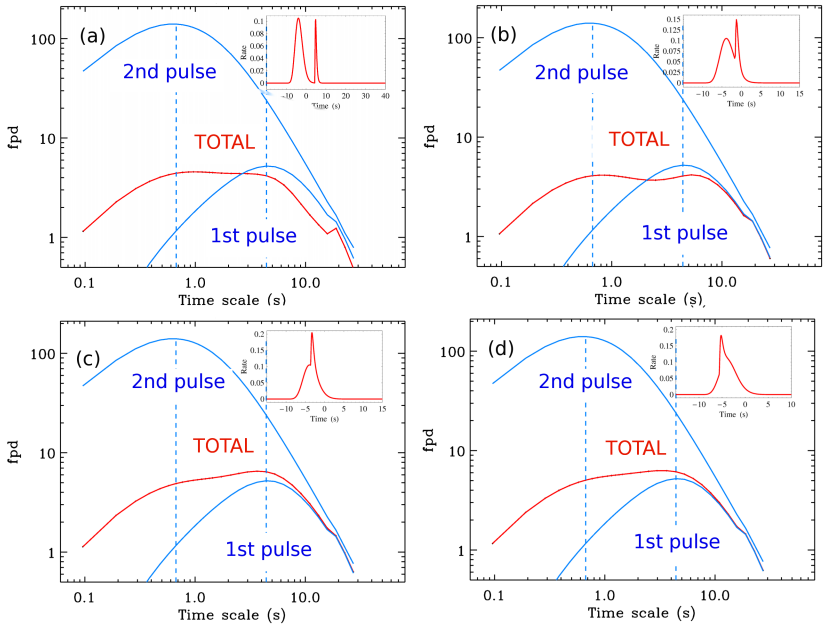

Fig. 6.9: Effect of the pulse overlap on the *fpd* shape. From panel (a) to (d) an increasing overlap affects the original signal composed of two pulses with equal amplitude but different width. *Inset*: analyzed signal.

analysis. The effects of the overlap is investigated in Fig. 6.9: from panel (a) to panel (d) it is possible to see how the fpd shape changes with an increasing degree of overlap between two structures characterized by two different time scales. Notably, even in the presence of the strong strong overlap portrayed in panel (d) the total fpd is still able to extract the information on the two time scales, with two fpd peaks of comparable amplitude (this is expected since the original pulses have the same amplitude). When a series of pulses is considered, (Fig. 6.10) the peak of the total fpd shifts to lower time scales (see panel (e)) and then starts to track the width of the entire profile (panels (c) and (f)) when the overlap makes the input signal to be a unique smooth structure as portrayed in panel (c).

In the absence of overlap the TTD analysis is completely insensitive to the relative position of the different pulses. The pulse width determines the position of the pdf peak; the pulse amplitude determines the amplitude of the fpd peak. The TTD analysis does a good job also in the presence of important overlap: however, a strong overlap of different pulses shifts the fpd peak.

A further test, is to compare the results of the TTD analysis of a real burst to the results of the pulse fitting technique: this is done for GRB 061126. I refer to subsection 6.6 for the details about the application of the TTD to real BAT data. Here the aim is to compare the results of the two analysis techniques to further show the capability of the TTD analysis.

From the fpd analysis (Fig. 6.11):

1. The fpd shows a doubled peaked structure, indication of the presence of two variability time scales: the first around 0.2 s and the second around 2 s. Only the second time scale is higher than 0.5 s, which is the time scale used to re-bin the data before fitting: any kind of variability on that time scale has been washed out by the re-binning procedure. This means that the fitting procedure will not be sensitive to the previous presence of this variability.

2. The fpd of the real data shows a perfect agreement with the fpd calculated from the best fit function for time scales greater than the re-binning time scale. Instead, the real data show an excess of power for $\Delta t < 0.5$ s which has been washed out by the re-binning procedure (which causes a loss of information).

From the best-fitting procedure (Fig. 6.12):

1. The GRB 061126 15-150 keV prompt profile can be modeled using a set of 11 Norris 2005 profiles. While the χ^2 is completely acceptable when calculated on the temporal profile of the burst re-binned on $\Delta t = 0.5$ s ($\chi^2/dof = 132.6/115$), a completely unacceptable χ^2 is obtained if calculated on the original 64 ms profile. This indicates the presence of non random fluctuations of the signal on time scales < 0.5 s, in perfect agreement with the fpd result. The fpd information is more complete and clearly indicate the other variability time scale.

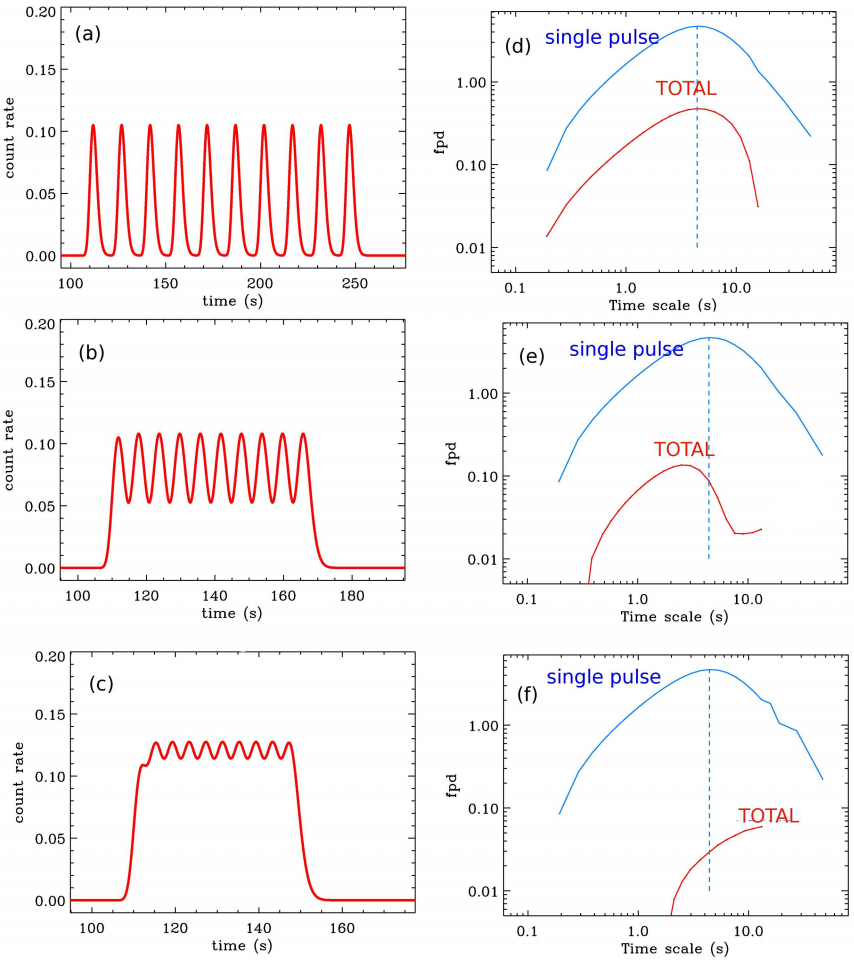

Fig. 6.10: Effect of the overlap of a series of pulses. Every pulse has a width $w = 5.2$ s. The Δt between peaks decreases from panel (a) to (c). In particular: $\Delta t \sim 15$ s for panel (a); $\Delta t \sim 6$ s for panel (b); $\Delta t \sim 4$ s for panel (c). Panel (d), (e), (f): *fpd* plot. Red solid line: *fpd* of the total signal; solid blue line: *fpd* of the single pulse. The vertical dashed line marks the position of the single pulse *fpd* peak.

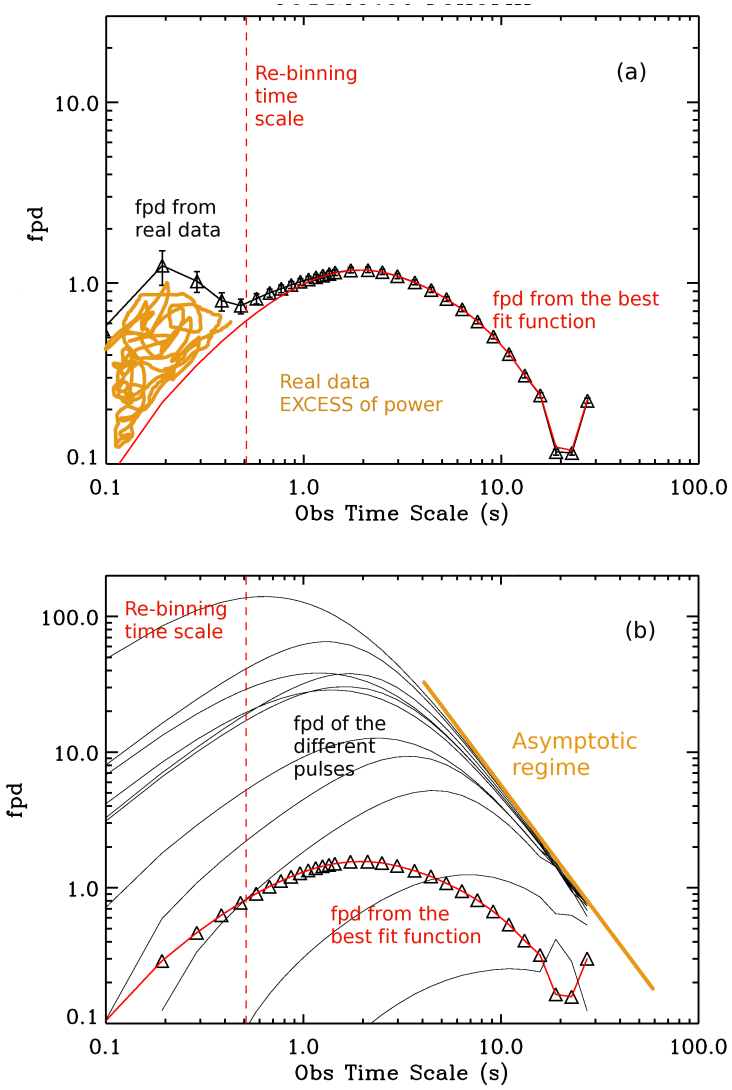

Fig. 6.11: *Upper panel:* solid red line: fpd of the best fit profile of GRB 061126; open triangles: fpd of the real data; vertical dashed line: time scale used to re-bin the data before the fitting procedure. *Lower panel:* open triangles: fpd of the best fit function of GRB 061126 15-150 keV prompt emission ; solid black lines: fpd of the different pulses. For large time scales the fpd reaches an asymptotic regime consisting of a power law with slope -2. See subsec. 6.5.3 for further details.

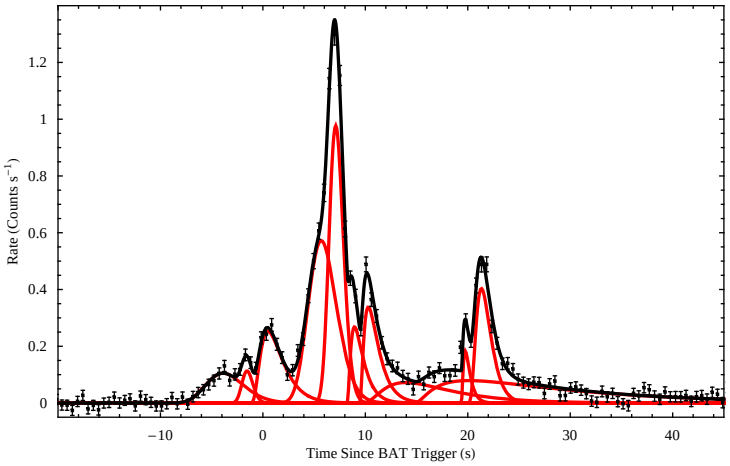

Fig. 6.12: 15-150 keV prompt profile of GRB 061126. Black solid line: best fit function, superposition of 11 Norris 2005 profiles ($\chi^2/dof = 132.6/115$, Pvalue=12%). The re-binning time scale is 0.5 s. Red solid line: Norris 2005 components.

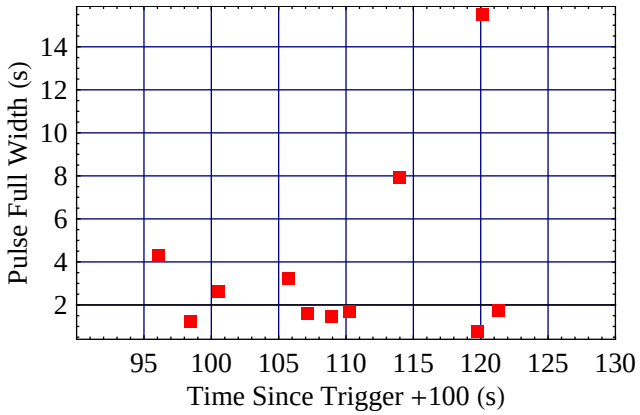

Fig. 6.13: Pulse full width at half maximum for the best-fit parameters of the GRB 061126 15-150 keV prompt emission. The majority of the pulses shows a width around 2 s.

2. The majority of the best-fit profiles shows a full width at half maximum around 2 s (Fig. 6.13) which is the variability time scale indicated by the fpd (the larger of the to variability time scales).

The two procedures give consistent results: the advantage of the fpd relies on a more complete piece of information delivered in a matter of minutes.

6.5.3 Asymptotic fpd behavior at time scales much greater than Δt_{var}

Fig. 6.11 suggests the presence of an asymptotic fpd behavior for time scales much greater than the characteristic time scale. In particular, it suggests that for $\Delta t \gg \Delta t_{var}$ the fpd scales as t^{-2}. This is mathematically proved below. From 6.4:

$$P(\Delta t) = \frac{1}{N}\sum_k (r(k) - \overline{r})^2 \tag{6.16}$$

If the duration of the signal is finite, then at a certain point, we will reach a re-binning time scale Δt^* for which the signal is completely contained in a single bin k^*, so that the previous formula can be rewritten as:

$$P(\Delta t) = \frac{1}{N}[(N-1)(0-\overline{r})^2 + (r(k^*) - \overline{r})^2] \tag{6.17}$$

where we should remind that $N = N(\Delta t)$. The fpd is the first time derivative of the previous quantity (with opposite sign):

$$fpd = -\frac{d}{d\Delta t}\Big[\frac{N-1}{N}(0-\overline{r})^2 + \frac{(r(k^*)-\overline{r})^2}{N}\Big] \sim -\frac{d}{d\Delta t}\Big[\frac{(r(k^*)-\overline{r})^2}{N}\Big] \tag{6.18}$$

for $(N-1) \sim N$. Since $\overline{r}$ does not depend on Δt, the first term in the first equation is constant and consequently gives no contribution to the fpd:

$$fpd = -\frac{d}{d\Delta t}\Big[\frac{r(k^*)^2 + \overline{r}^2 - 2\overline{r}r(k^*)}{N}\Big] = \frac{d}{d\Delta t}\Big[\frac{r(k^*)^2 - 2\overline{r}r(k^*)}{N}\Big] \tag{6.19}$$

If the time series contains a total of N_c counts, then $r(k^*) = \frac{N_c}{\Delta t}$; $N(\Delta t) \sim \frac{T_{tot}}{\Delta t}$. This means that:

$$fpd = -\frac{d}{d\Delta t}\Big[\frac{(\frac{N_c}{\Delta t})^2 - 2\overline{r}\frac{N_c}{\Delta t}}{\frac{T_{tot}}{\Delta t}}\Big] = -\frac{d}{d\Delta t}\Big[\frac{N_c^2}{T_{tot}\Delta t} - 2\overline{r}\frac{N_c}{T_{tot}}\Big] \tag{6.20}$$

Since the second term does not depend on Δt the previous equation reduces to:

$$fpd = \frac{N_c^2}{T_{tot}}\frac{1}{\Delta t^2} \tag{6.21}$$

It therefore possible to conclude that for $\Delta t \gg \Delta t_{var}$ we have:

$$fpd \sim \Delta t^{-2} \tag{6.22}$$

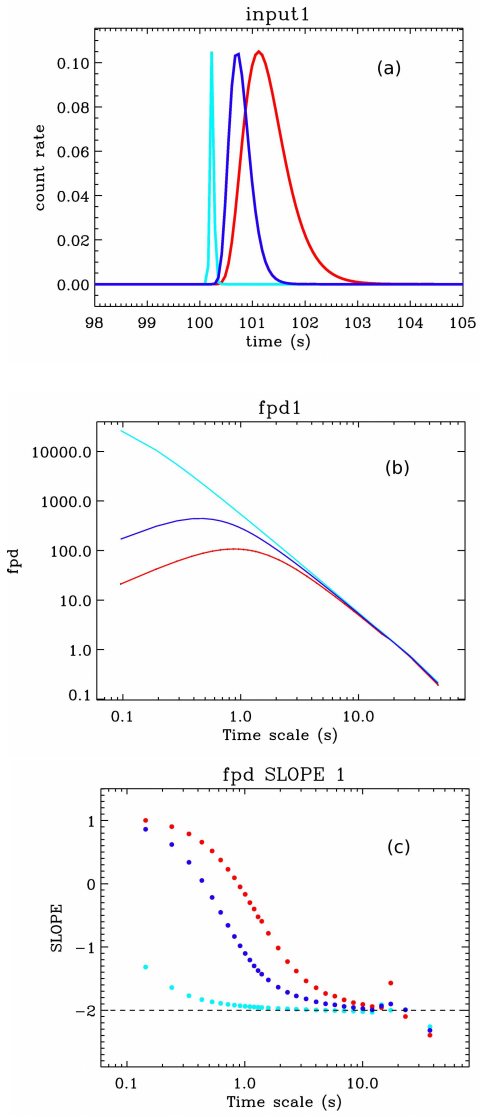

Fig. 6.14: *Upper panel*: Norris 2005 profiles with different widths which are used as input of the *fpd* analysis. *Middle panel*: *fpd* of the three signal profiles. *Lower panel:* slope of the *fpd*. The three *fpd* relaxes to a slope of -2 as expected.

This conclusion does not depend on the particular shape of the signal, as illustrated below. Figure 6.14 shows the asymptotic behavior of the fpd for $\Delta t \gg \Delta t_{var}$ for three Norris 2005 profiles with different widths. With reference to the lower panel, it is clear that the fpd reaches an asymptotic power law behavior with power law index of -2 as expected. In particular, the lower the duration of the signal, the sooner the asymptotic behavior is reached, as expected. Figure 6.15 shows the result for a step-like signal with duration of 0.5 s: as in the previous case, an asymptotic behavior with the fpd declining as a power-law signal with slope -2 is reached for high time scales, confirming the finding that the asymptotic behavior does not depend on the signal shape. Note that the contribution of the noise on these time scales is usually negligible, so that the results obtained on a clean signal are completely representative of what one would obtain from real data.

6.5.4 Fractional power density of a power-law signal

The fpd of a power-law signal is well approximated by a power-law with a power-law index which is linked to the original power law decay index of the signal by a relation which is plotted in Fig. 6.16. The error bars mark the range of slopes covered by the fpd evaluated over time scales from 0.01 s to 10 s: this is the range of time scales of study of the fpd of GRB prompt signals. The asymptotic regime is reached in the case of steep power law decays. From this plot it is possible to re-construct the behavior of the original signal from the slope of the fpd (note that the plotted relation holds only if the range of investigated time scale is exactly the same or very similar). In this way it is possible to reveal the presence of power law tails in prompt GRB signals.

6.5.5 Fractional power density of an exponential signal

Figure 6.17 shows the range of slopes of the fpd of an exponentially decaying signal of the form: $\sim Exp^{-t/t^*}$ where t^* is the e-folding time. The asymptotic behavior of a pure power law fpd with slope -2 is reached in the case of very low e-folding times.

Finally, a summary of the fpd shape characterization is portrayed in Fig. 6.18.

6.5.6 The Power Density Ratio (pdr)

I can define an other useful quantity, the Power Density Ratio (pdr), as follows:

$$pdr = \frac{p(\Delta t)}{p_{\rm noise}(\Delta t)} \tag{6.23}$$

This quantity is expected to show an asymptotic value of 1 for the time scales at which the variability is dominated by the noise (short time scales, as shown in Fig. 6.18): the rise of this function above 1 indicates the presence of intrinsic variability of the signal. This is illustrated in Fig. 6.19 for GRB 060124 in the

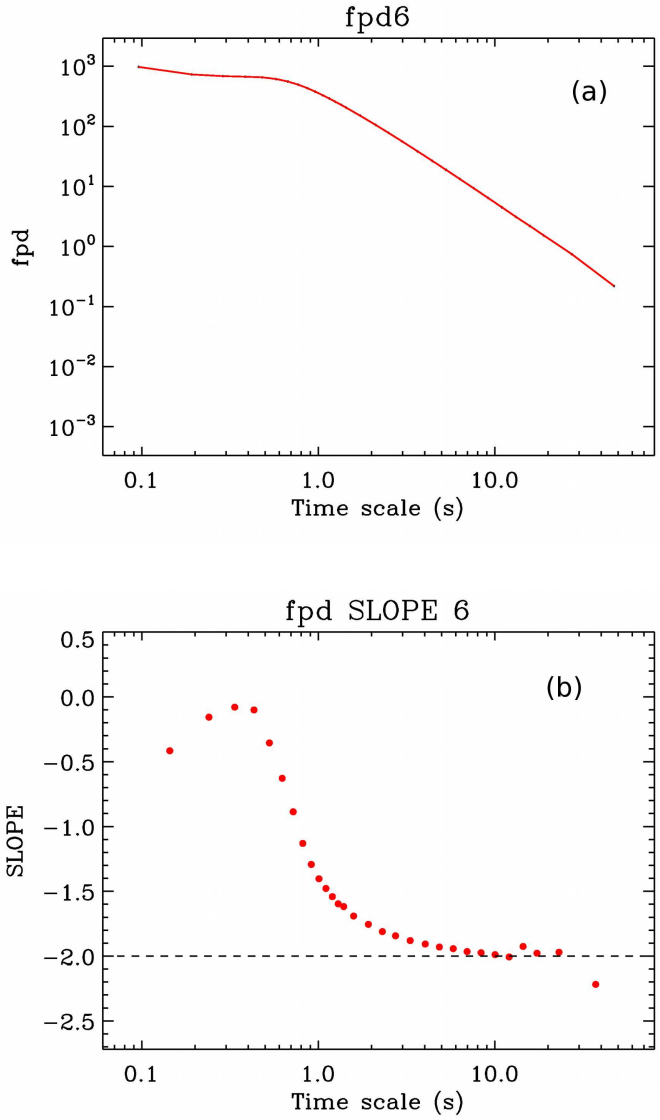

Fig. 6.15: Upper panel: fpd of a step like function with duration 0.5 s. *Lower panel*: fod slope. The fpd slope relaxes to -2 for time scales much greater than Δt_{var}.

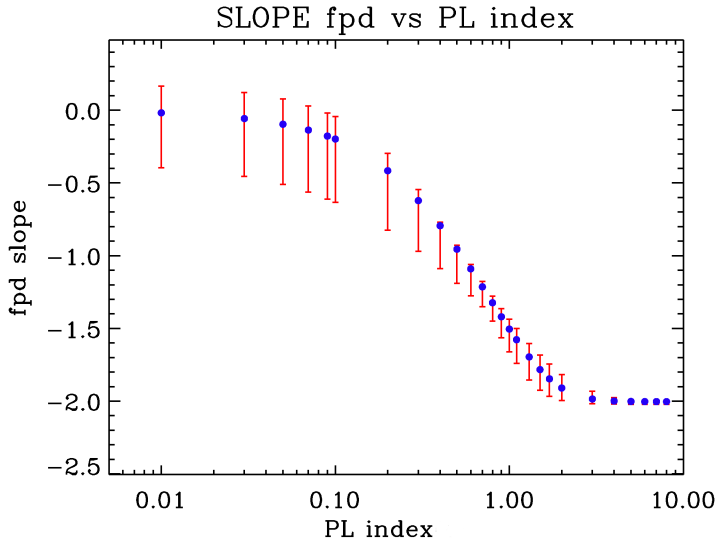

Fig. 6.16: Slope of the fpd versus power law index of the original power law signal. The error bars mark the range of slopes covered by the fpd evaluated on time scales from 0.01 up to 10 s.

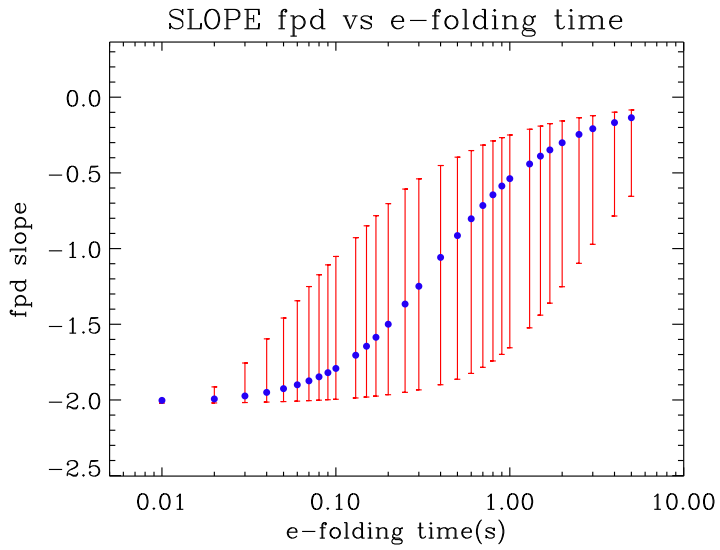

Fig. 6.17: Slope of the fpd versus e-folding time of an original exponential signal. The error bars mark the range of slopes covered by the fpd evaluated on time scales from 0.01 up to 10 s.

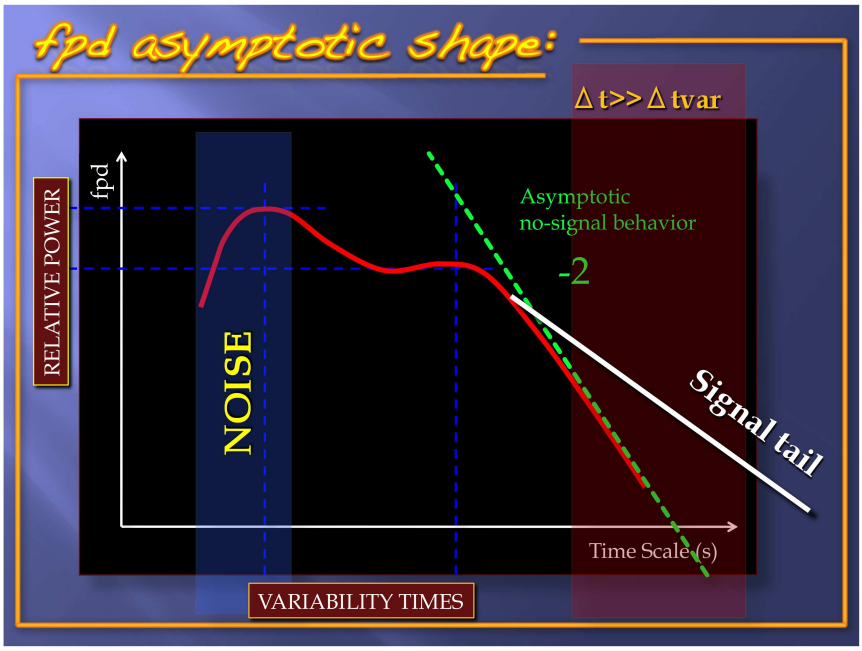

Fig. 6.18: Cartoon showing the basic features of an *fpd* plot.

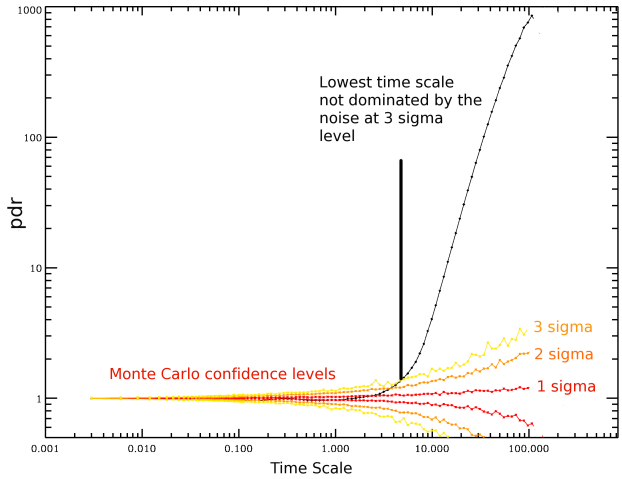

Fig. 6.19: Power Density Ratio (*pdr*) calculated for GRB 060124 in the 0.3-10 keV energy range. See 6.7.4 for the details of the application of the TTD to XRT data. Black solid line: *pdr*; solid lines in color: 1, 2 and 3 sigma confidence intervals for a signal which is pure noise with a mean count rate equal to the observed one.

X-ray regime: while for $\Delta t < 5$ s the variability of the signal is dominated by random fluctuations, starting from 5 s the signal shows intrinsic variability at the 3 sigma confidence level. This is calculated by running a set of Monte Carlo simulations starting from a signal which consists of random fluctuations around the mean observed count rate, as described in Sect. 6.6. The evaluation of this quantity therefore provides a way to calculate the minimum re-binning time scale over which a particular signal is not dominated by the noise. The output is an alternative to the Haar wavelet activity which has been used by [198] to study the presence of flickering in the first 1 s of the GRB prompt light-curves on millisecond timescales. See also [131].

6.6 *Application to real data: a sample of 252 GRBs detected by* Swift-*BAT*

The TTD analysis has been applied to all the GRBs detected by *Swift*-BAT in the time period April 2005 - June 2008. I require each light-curve to contain the complete 15-150 keV data set of the event, without data-gaps. This requirement excludes from the analysis: GRB 050820A; GRB 060218; GRB 060906; GRB 071010A; GRB 071112C and GRB 071122[5]. The following bursts have instead a very low-significance signal: GRB 050925, GRB 051105A, GRB 060502B, GRB 060801, GRB 070729, GRB 070809, GRB 070810B and GRB 070913. They are not part of the current data set of analysis. The final sample comprises 252 *Swift*-detected events.

For each event, a 64 ms light-curve is extracted in the 15-150 keV energy band together with 4 light-curves in the 15-25 keV, 25-50 keV, 50-100 keV and 100-150 keV energy bands with the same resolution. BAT data have been processed using standard Swift-BAT analysis tools within HEASOFT. Standard screening and filtering criteria have been applied. In particular, each event recorded by BAT is mask-tagged using the BATMASKWTEVT at the source position. The BAT detector quality map is obtained by processing the nearest-in-time enable/disable map of the detectors. Mask-weighted, background subtracted light-curves are obtained. The light-curves used in this work belong to the BAT archive in Merate developed by P. Romano and C. Guidorzi.

For each light-curve the interval of time of analysis has been selected as follows: a peak finding algorithm is first run to scan the complete data set recorded and search for fluctuations which are significant at a minimum 7σ level re-binning over all the possible re-binning time scales. The first and the last peak appearing in the light-curve and satisfying the requirement above are then selected. Starting from the first significant peak, and going backward in time, the first bin of the light-curve with a negative signal is recorded: I call the corresponding time t_1. t_2 instead corresponds to the first bin with negative signal after the last significant peak in the light-curve. The interval of time of

[5] GRB 060505 was detected in service mode and not in burst mode and is equally excluded from the sample.

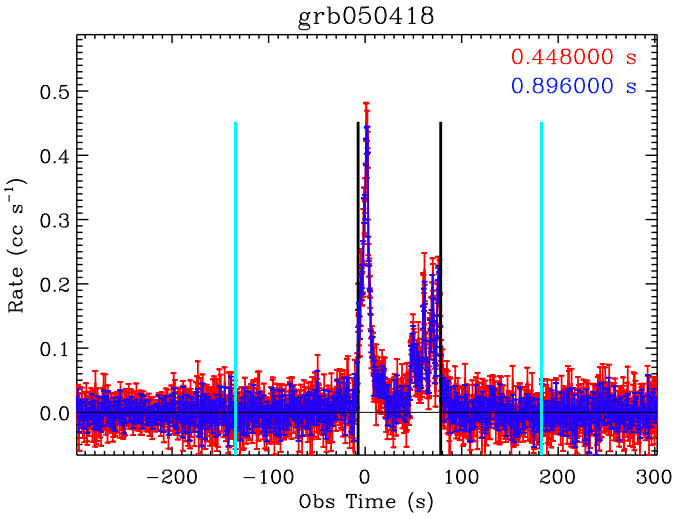

Fig. 6.20: BAT light-curve of GRB 050418. Blue (red) points: light-curve re-binned over $\Delta t = 0.896$ s ($\Delta t = 0.448$ s). The black vertical lines mark the position of the first and last bin time with signal significant at the 7σ level. Light-blue vertical lines: $t_1 - 100$ s (on the left) and $t_2 + 100$ s (on the right).

investigation is defined to start at $t_1 - 100$ s and to finish at $t_2 + 100$ s. An example is shown in Fig. 6.20.

This section describes the application of the TTD analysis to the prompt high-energy signal of *Swift* GRBs and is organized as follows. The application of the technique to real data requires some modifications to the basic formulation described in Sect. 6.4.1: an ad hoc study of the noise allows the extraction of the variability information on short time scales (this is done in subsect. 6.6.1). Moreover, some improvements to the basic formulation allow the technique to become insensitive to the position of the origin of the re-binning: since the origin of the re-binning is a completely arbitrary choice, it is desirable that the output does not depend on that parameter (see sebsect. 6.6.3). A way to improve the time resolution during the variability time search is described in subsect. 6.6.2, while the problem of the computation of the errors of the *fpd* and *pdr* is addressed in subsect. 6.6.4. Finally, the products of the TTD analysis for each burst is described in subsect. 6.6.5.

6.6.1 Noise power subtraction

The starting 64 ms light-curves contain a mask-weighted background subtracted signal: for this reason it is not possible to reconstruct the originally detected counts. This means that the basic formulation of subsect. 6.4.1 cannot be directly applied: in particular, Eq. 6.8 must be modified to account for the modification of the underlying statistics of the noise. However, [165] showed

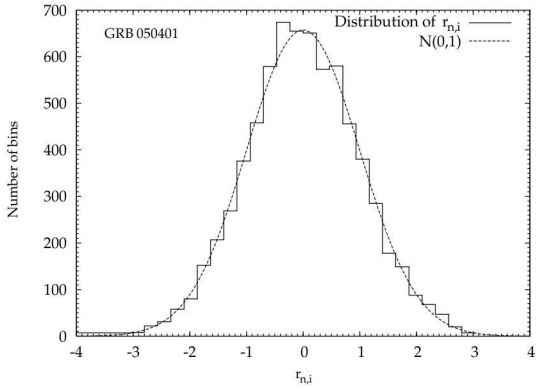

Fig. 6.21: Distribution of the normalized rates $r_{n,i}$ in the case of GRB 050401. The distribution is well fitted by a standardized Gaussian. From [165].

that the statistical noise of BAT mask-tagged light-curves is well modeled by a standardized Gaussian distribution. Every rate r_i can be therefore considered as a random variable with variance σ_i. The power associated to the noise of BAT data is subsequently calculated as follows:

$$P_{\rm noise}(\Delta t) = \frac{\sum_i \sigma_i^2}{N} \tag{6.24}$$

This definition assure to have an fpd which is equal to 0 (or an pdr which is 1) for a BAT time series that consists of pure noise.

6.6.2 Temporal resolution of the variability time scale search

One of the limits of the previous application of the TTD analysis is the limited time resolution in the search for the characteristic time scale of variability. In the previous application by [179], the time scales of investigation were logarithmically spaced: this assured that the portion of the signal analyzed was always the same, going from one time scale to the next; however, a byproduct of this approach is the poor time resolution: any quantity is in fact evaluated at a certain Δt^* and at $2 \times \Delta t^*$ with nothing in between. This procedure has been revised as described below.

Given a starting binning time of the light-curve $\Delta t_{\rm start}$ the Power is evaluated on any time scale which is an integer multiple of $\Delta t_{\rm start}$ from 1 to 15. Starting from $15 \times \Delta t_{\rm start}$, the Power is evaluated on time scales which can be expressed as $k \times \Delta t_{\rm start}$ where k is the integer part of a^b where $a = 1.2$ and $b = 16, 17, 18, 19, ...$ The light-curve is re-binned on each of these time scales. This procedure is not able to assure that the analyzed portion of the light-curve is always the same: for this reason, a given re-binning result is thrown away (and no temporal quantity is calculated on that time scale) if more than 5%

of the entire light-curve is not part of the re-binned signal. This requirement assures that any re-binned version of the signal is representative of the entire original signal.

6.6.3 Dependence on the re-binning origin

The variance of the rate calculated on a particular time scale is function of the origin of the re-binning procedure. For this reason, for each time scale, one should work out the fpd and pdr for any possible choice of the origin of the re-binning. However, from a practical point of view, this is computationally time consuming: a good compromise is to calculate the two quantities for 100 randomly chosen positions of the origin of the re-binning procedure. Any fpd or pdr value quoted in this work is the mean of these 100 measurements: this assures the independence from something which is completely arbitrary and avoid sharp transitions of the fpd or pdr from one time scale to the previous one (or the next one).

6.6.4 Significance of a variability time scale

Since GRBs are non-repetitive signals, the errors affecting each temporal quantity cannot be evaluated as described by Eq. 6.12. The significance of each point of any quantity of the TTD analysis is assessed through Monte Carlo simulations: in particular, for each event, for each energy band of investigation, a set of 1000 simulation is run. The complete procedure is described below.

I start from the observed mask-weighted time-tagged BAT light-curves. From each light-curve the normalized integral distribution is derived. What we observe is a single realization of a process we do not know. We do not have a model to feed the Monte Carlo procedure. Instead of assuming a particular model, I prefer to start from the observations. A random realization of the observed signal is constructed randomly choosing a number between 0 and 1 and then taking the corresponding time in the integral distribution: this procedure is repeated N^* times, where N^* is the integer number which is nearest to $\sum_i r_i \Delta t_i$ (r_i is the rate observed in the time bin i). In this way I am able to build a realization of the observed distribution, which will be a second order realization of the original process. The second order realizations are able to re-construct the mean of the observed signal, but will have a variance which is expected to be twice the observed one. I define $V(1)$ the variance of the observed signal which is a first order realization of the original process, while $V_i(2)$ is the variance of the simulation i which is a second order realization of the original (and unknown) process. Since the power is sensitive to the variance of the rate, I renormalize the variance of the simulated signals over each time scale dividing by the median of the distribution of $V_i(2)/V(1)$: only in this way the obtained values of the different temporal quantities can be considered to represent the TTD output of a random variation of the observed signal. A set of 1000 Monte Carlo simulations is run: this means that for each temporal quantity (fpd or pdr for example) and for each time scale, a distribution of 1000 values of that

quantity is provided by the simulations: the $1\,\sigma$, $2\,\sigma$ and $3\,\sigma$ confidence intervals (CI) are derived for each time scale starting from this distribution (with the $3\,\sigma$ CI defined by the two extreme values observed in 1000 realizations). The results are shown in Fig. 6.22.

6.6.5 BAT-analysis products

The TTD analysis has been applied to the total 15-150 keV signal of 252 BAT GRBs. To evaluate the evolution of the variability time scale with energy, the signal has been split into 4 different energy bands: 15-25 keV; 25-50 keV; 50-100 keV and 100-150 keV. For each of the 5 light-curves, I calculate the fpd and the pdr and evaluate the corresponding uncertainties using the method of subsect. 6.6.4. Figures 6.22, Fig. 6.23 and Fig. 6.24 show the results for GRB 050326 taken as example. The light-curve of GRB 050326 is shown in Fig. 6.25.

6.7 Results

The inspection of the fpd plots of the 252 GRBs allows the identification of 3 different classes of events: fpd plots with a unique peak; fpd plots with more than one peak and fpd plots with a power law shape. This is illustrated in subsect. 6.7.1. The time scale to which is associated the maximum of the variability power is studied in subsect. 6.7.2. Subsection 6.7.3 instead describes the results obtained for the exceptional burst GRB 080319B and shows the capability of the power spectrum in the time domain for a burst with good quality data. Finally, the first application to X-ray data is described in subsect. 6.7.4.

6.7.1 Fractional power density shape

From a morphological point of view, the fpd plots can be divided into 3 classes.

Single peak fpd

Nearly half of the GRBs shows an fpd with a unique peak: these events are characterized by a unique variability time scale. While this is obvious for a GRB consisting of a single pulse (see e.g. GRB 060912A of Fig. 6.26), it is interesting to note that a single variability time scale is also shared by some multi spike GRBs: GRB 050326 and GRB 080411 (Fig. 6.26) are two examples.

Multiple peak fpd

Other GRBs ($\sim 40\%$), are not dominated by a single variability time scale: instead, their fpd profile shows the presence of more than one peak, revealing that more than one variability time scale is present in the data. In GRB 060607A (Fig. 6.27) two time scales, the first lying ~ 0.7 s and the second around 8 s are associated to comparable powers; in other cases there is evidence for more than 2 variability time scales (see e.g. GRB 071020 in Fig. 6.27). A show case is represented by GRB 080319B: this is extensively treated in subsect. 6.7.3.

Power law fpd

From Sect. 6.5.3, we know that the fpd is expected to reach an asymptotic

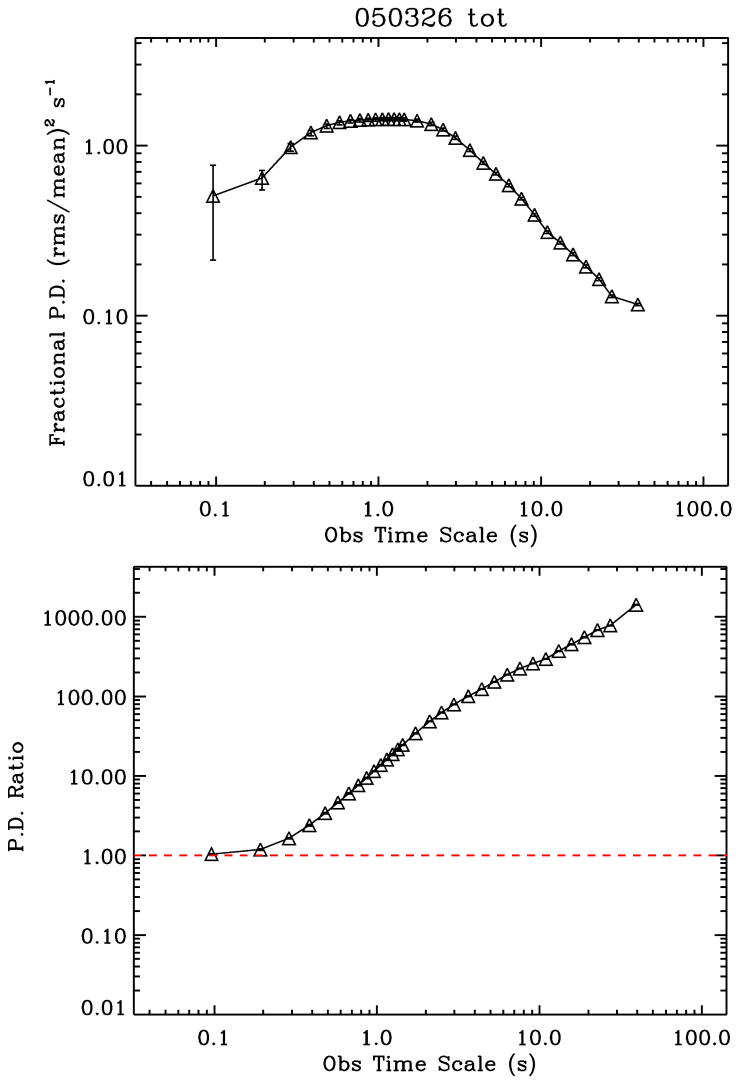

Fig. 6.22: *Upper panel*: *fpd* of GRB 050326 calculated in the 15-150 keV energy band. A double peaked structure indicating the presence of two time scales of variability can be seen, with $\Delta t_{var1} \sim 0.4$ s and $\Delta t_{var2} \sim 2.5$ s. *Lower panel*: *pdr* of the same signal. For time scales ~ 0.1 s the consistency of the *pdr* with 1 indicates that the variability of the signal is dominated by noise fluctuations. In both panels the errors are provided at 1σ significance.

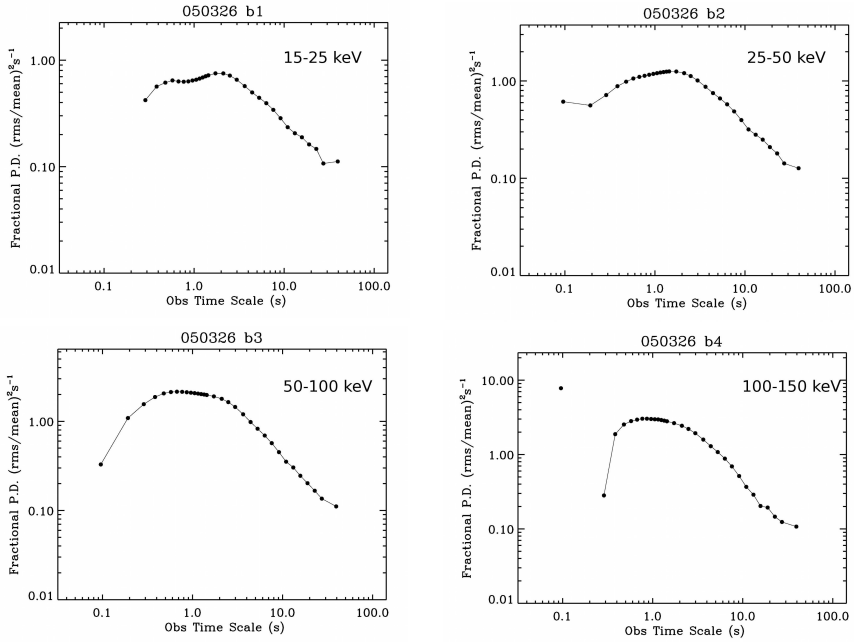

Fig. 6.23: Fractional power density of GRB 050326 calculated in 4 different energy bands. The presence of two different variability time scales is now clear and each time scale can be further characterized using its energy dependence.

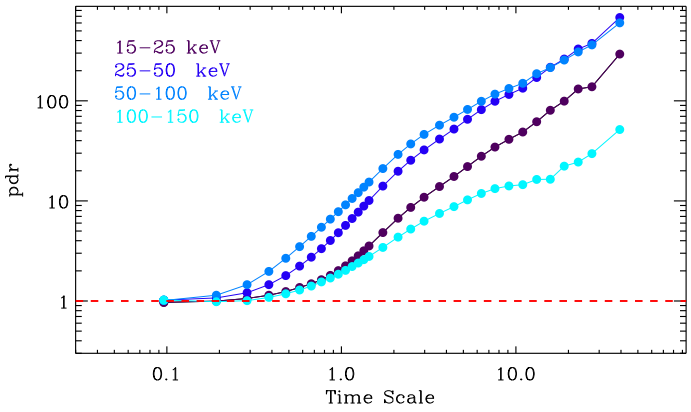

Fig. 6.24: Power density ratio of GRB 050326 analyzed in different energy bands.

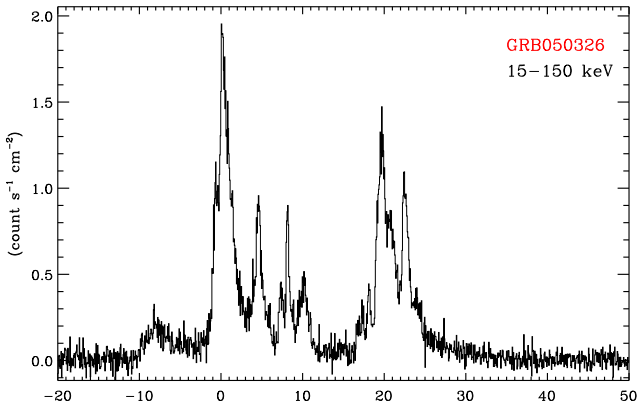

Fig. 6.25: 15-150 keV light-curve of GRB 050326. The re-binning time scale is 64 ms.

behavior for time scales much greater than Δt_{var}. The asymptotic behavior is a power law declining with a power law index of -2. In the case of GRB 050925, the duration of the signal is so small that the asymptotic behavior is reached on the analyzed time scales (see Fig. 6.28). In the case of GRB 050717 the presence of a visible signal tail prevents the fpd from reaching the asymptotic slope -2: instead, the fpd declines following a power law of index ~ -0.8. The vast majority of short GRBs belongs to this class.

While the 1-peak and multiple peak fpd constitutes two separate classes, the presence of the fpd power law tail can co-exist with a single or a multiple peak in the fpd, so that there is an overlap between the first two classes and the third. This is because the fpd peak localize the variability time scale, while the power law decay of the function clarifies how the source switches off: abruptly (-2 behavior on the investigated time scales) or following a power law decline with a long tail (fpd with power law index > -2).

6.7.2 Maximum variability time scale

Among the 252 GRBs I select the subsample of GRBs with an fpd shape defined by points whose value differs from 0 at a minimum $3\,\sigma$ significance level. In particular, I require the absolute peak of the fpd to have a minimum $3\,\sigma$ significance. Among the selected GRBs, I furthermore require to have a measure of Δt_{var} and disregard the events for which only an upper limit can be quoted due to the presence of a minimum time scale of investigation ($\sim$ 0.2 s). This procedure restricts the sample to 75 events (the ones with the best statistics). The maximum variability time scale is the time scale over which the signal shows the maximum variability power and is calculated from the absolute maximum of the fpd function. The aim is to test if there is evidence for a universal time scale of variability to further characterize the GRB population

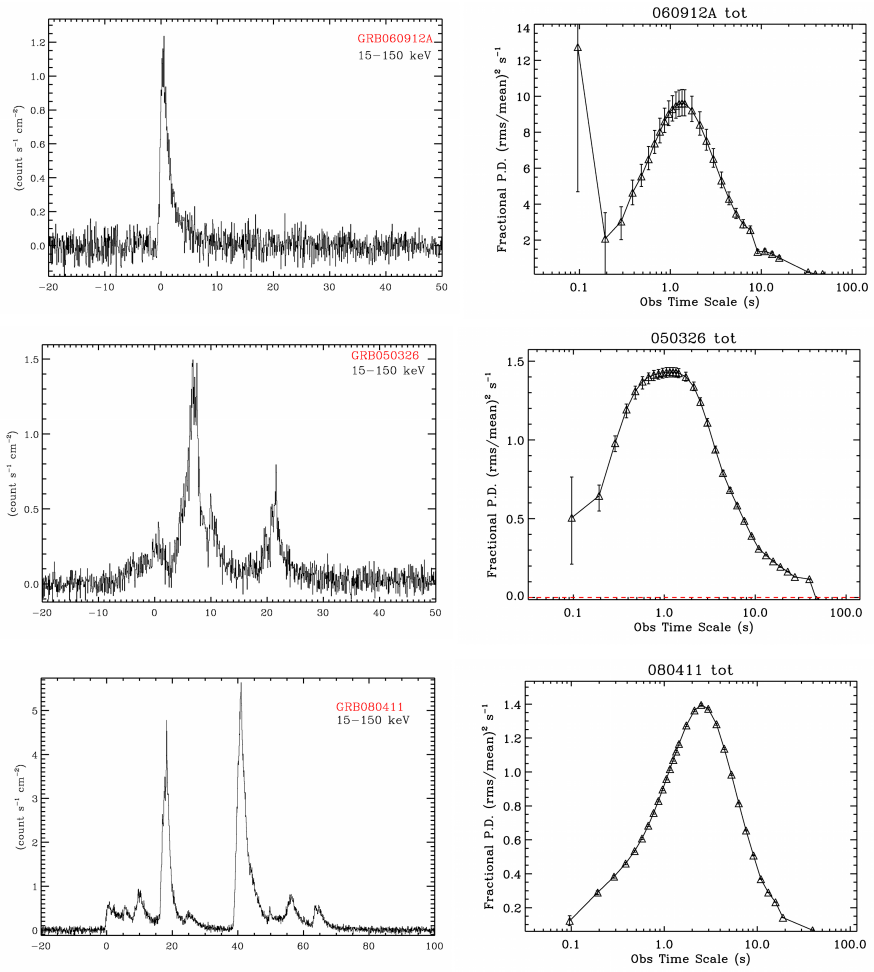

Fig. 6.26: Examples of GRBs characterized by an *fpd* with a single peak. *Left panels:* 15-150 keV BAT light-curves. The binning time is chosen to be 0.064 s. *Right panels:* *fpd* of the three bursts. Errors are provided at the $1\,\sigma$ confidence level.

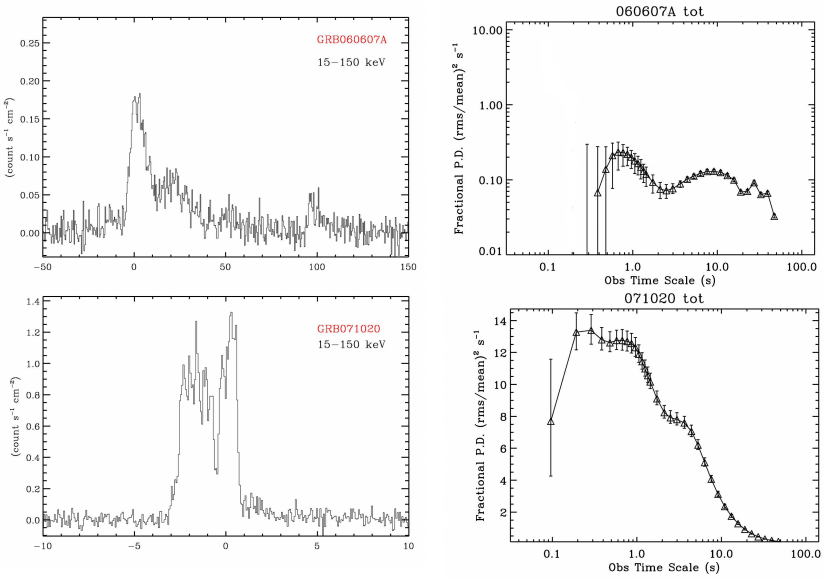

Fig. 6.27: Examples of GRBs characterized by an fpd with multiple peaks. *Left panels:* 15-150 keV BAT light-curves. The binning time is 0.064 s and 0.448 s for GRB 071020 and GRB 060607A, respectively. *Right panels:* fpd of the two bursts. Errors are provided at the $1\,\sigma$ confidence level.

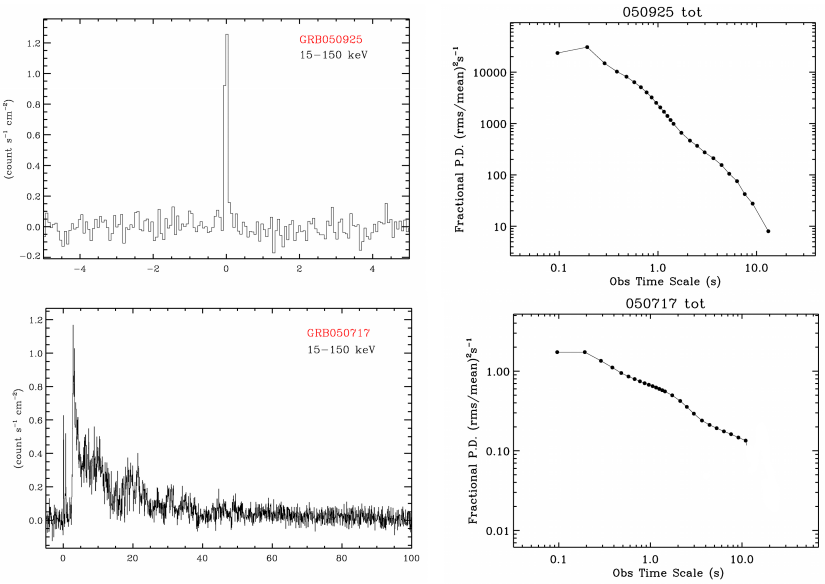

Fig. 6.28: Examples of GRBs characterized by a power law fpd. *Left panels:* 15-150 keV BAT light-curves. The binning time is 0.064 s. *Right panels:* fpd of the two bursts. Errors are provided at the $1\,\sigma$ confidence level.

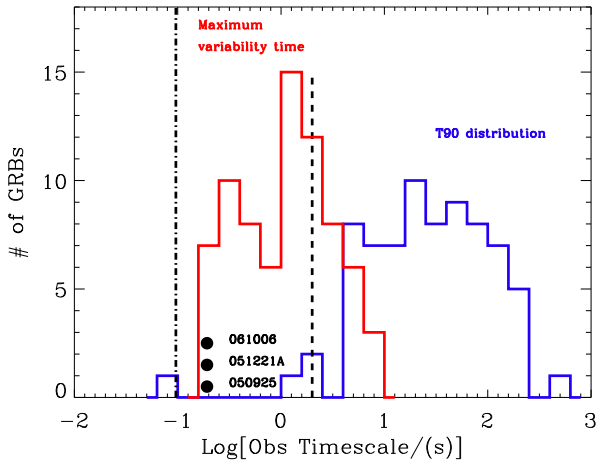

Fig. 6.29: Blue histogram: distribution of the observed T_{90} parameter of the GRBs of the sample as obtained from the GCNs. Red line: distribution of the observed maximum variability time scale. The black dots mark the position of the maximum variability time scale of the short GRBs belonging to the sample. Vertical dashed line: 2 s region; vertical dot dashed line: minimum variability time scale that can be appreciate starting from a 64 ms binned light-curve.

from the temporal variability point of view.

The results are listed in Table 6.1: this table provides the redshift information when available. The investigated time scales before and after the fpd peak are listed as t_i and t_f, respectively: this provides a reasonable confidence interval of time scales that contains the peak of the fpd. In the following plots, the Δt_{var} error bars extend from t_i to t_f.

The distribution of the maximum variability time scale is shown in Fig. 6.29 in the observed frame and in Fig. 6.30 in the source rest frame. Three short GRBs are part of the sample: GRB 050925; GRB 051221A and GRB 061006. They all show the minimum reported $\Delta t_{var} = 0.192$ s in the observer frame; however, when the cosmological time dilation is taken into account (see Fig. 6.30) a limited fraction of *long* GRBs show an intrinsic maximum variability time scale shorter than the ones corresponding to short GRBs. In particular, GRB 071020, GRB 080607 and GRB 060927 have a rest frame $\Delta t_{var} < 0.12$ s. The distribution of the observed Δt_{var} shows a hint of bimodality which is strengthened by the rest frame calculation: a first group of GRBs (comprising the short ones) are characterized by a rest frame $\Delta t_{var} < 0.3$ s while the second group has $\Delta t_{var} > 0.5$ s (rest frame). A bimodal distribution was also found by [179]. The redshift information is available for 29 events out of the 75 GRBs of Fig. 6.29: notably, Fig. 6.30 shows that 15 of them (56 % of the long GRBs of

GRB	**z**	Δt_{var} (s)	t_i (s)	t_f (s)	**GRB**	**z**	Δt_{var} (s)	t_i (s)	t_f (s)
050117	-9.000	0.576	0.480	0.672	060825	-9.000	0.960	0.864	1.056
050124	-9.000	0.960	0.864	1.056	060904B	0.703	4.416	3.648	5.280
050128	-9.000	0.480	0.384	0.576	060904A	-9.000	0.288	0.192	0.384
050219B	-9.000	0.576	0.480	0.672	060908	1.884	2.496	2.112	2.976
050319	3.240	0.960	0.864	1.056	060912A	0.937	1.344	1.248	1.440
050326	-9.000	1.152	1.056	1.248	060927	5.467	0.576	0.480	0.672
050401	2.900	0.576	0.480	0.672	061004	-9.000	1.440	1.344	1.728
050416B	-9.000	1.440	1.344	1.728	061006	0.438	0.192	0.096	0.288
050418	-9.000	4.416	3.648	5.280	061021	-9.000	2.112	1.728	2.496
050502B	-9.000	2.496	2.112	2.976	061121	1.314	1.344	1.248	1.440
050525A	0.606	1.440	1.344	1.728	061126	1.159	2.112	1.728	2.496
050603	2.821	0.384	0.288	0.480	061222A	-9.000	0.480	0.384	0.576
050607	-9.000	3.648	3.649	4.418	070220	-9.000	0.576	0.480	0.672
050713A	-9.000	4.416	3.648	5.280	070318	0.836	6.336	5.280	7.583
050715	-9.000	2.976	2.496	3.649	070328	-9.000	1.440	1.344	1.728
050801	-9.000	1.440	1.344	1.728	070506	2.310	2.976	2.496	3.648
050820B	-9.000	0.480	0.384	0.576	070508	-9.000	0.192	0.096	0.288
050822	-9.000	3.648	2.976	4.416	070509	-9.000	5.280	4.416	6.336
050922C	2.198	2.112	1.728	2.496	070521	-9.000	0.288	0.192	0.384
050925	-9.000	0.192	0.096	0.288	070616	-9.000	1.152	1.056	1.248
051221A	0.546	0.192	0.096	0.288	070714A	-9.000	1.152	1.056	1.248
060111A	-9.000	9.122	7.585	10.946	070808	-9.000	2.976	2.496	3.648
060117	-9.000	0.288	0.192	0.384	070911	-9.000	1.056	0.960	1.152
060206	4.048	3.648	2.976	4.416	070917	-9.000	1.056	0.960	1.152
060210	3.910	3.648	2.976	4.416	071003	-9.000	1.728	1.440	2.112
060306	-9.000	0.384	0.288	0.480	071020	2.145	0.288	0.192	0.384
060322	-9.000	0.768	0.672	0.864	071117	1.331	1.728	1.440	2.112
060418	1.489	1.248	1.152	1.344	080229A	-9.000	0.384	0.288	0.480
060421	-9.000	0.384	0.288	0.480	080319C	1.950	2.112	1.728	2.496
060428A	-9.000	5.281	4.417	6.337	080409	-9.000	1.440	1.344	1.728
060510A	-9.000	0.768	0.672	0.864	080411	1.030	2.496	2.112	2.976
060526	3.210	1.056	0.960	1.152	080413B	1.100	1.728	1.440	2.112
060614	0.125	0.192	0.096	0.288	080413A	2.433	2.976	2.496	3.648
060708	-9.000	0.864	0.768	0.960	080426	-9.000	0.192	0.096	0.288
060714	2.710	2.112	1.728	2.496	080430	0.767	4.416	3.648	5.280
060719	-9.000	2.496	2.112	2.976	080605	1.640	0.384	0.288	0.480
060813	-9.000	6.336	5.280	7.583	080607	3.036	0.384	0.288	0.480
					080613B	-9.000	0.192	0.096	0.288

Tab. 6.1: List of GRBs for which it was possible to extract the information on the maximum variability time scale. From left to right: GRB name; time scale corresponding to the peak of the fpd (Δt_{var}); maximum time scale of evaluation of the fpd preceding the fpd peak (t_i); minimum time scale of evaluation of the fpd after the fpd peak. The redshift information is extracted from the Gamma-ray burst Coordinates Network (GCN): -9 indicates that this information is not available. Observer frame quantities have been listed.

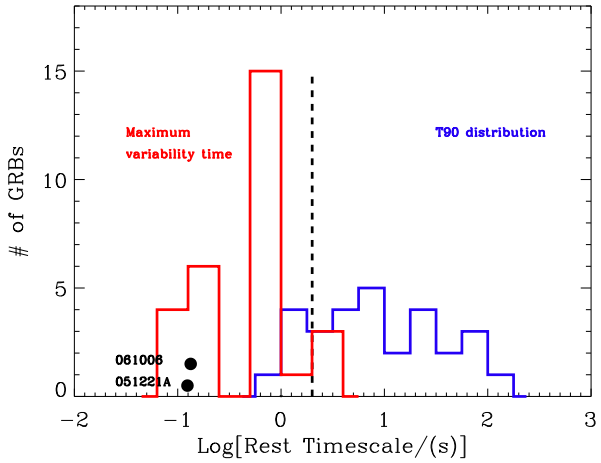

Fig. 6.30: Rest frame version of Fig. 6.29. The vertical dashed line marks the 2 s region of the plane.

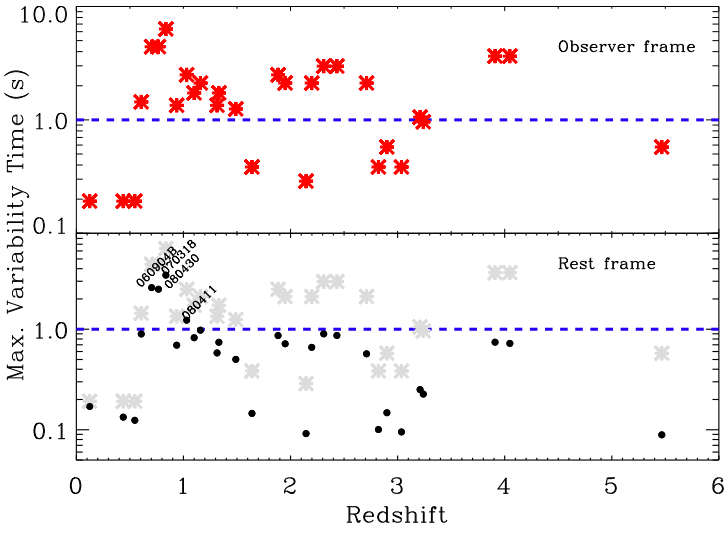

Fig. 6.31: Maximum variability time scale Δt_{var} as a function of redshift. *Upper panel:* Observer frame values. *Lower panel:* black dots: rest frame quantities; grey stars: observer frame quantities. In both panels the blue dashed line marks the 1s time scale taken as a reference value. The bimodality of Fig. 6.30 is also apparent.

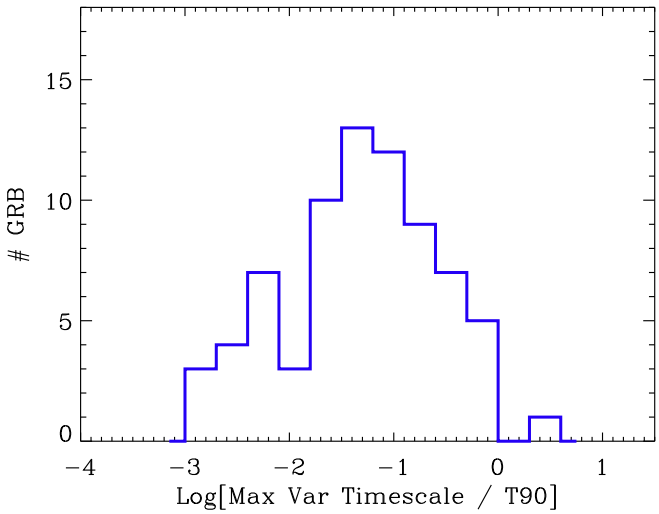

Fig. 6.32: Histogram of the distribution of the ratio between the maximum variability time and the duration of the GRB.

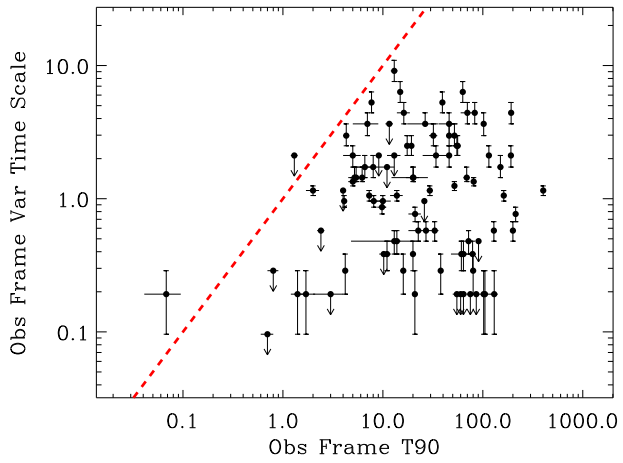

Fig. 6.33: Maximum variability time vs T_{90} for the population of analyzed GRBs. Observer frame quantities are used. Red dashed line: locus of the points for which the maximum variability time scale equals the duration of the GRB.

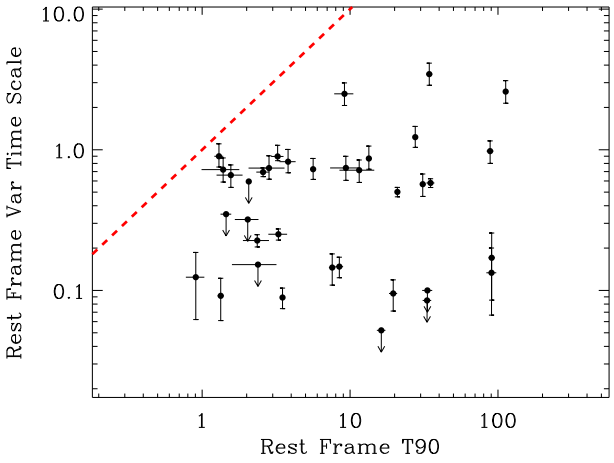

Fig. 6.34: Rest frame version of Fig. 6.33.

the sample) share a rest frame maximum variability time in the range $0.6 - 1$ s. *I therefore identify* $\Delta t \sim (0.6 - 1)$ *s as a characteristic variability time scale of long GRBs in the source rest frame.* This is in agreement with previous pulse fitting studies which found the distribution of the pulse widths to be a lognormal centered at ~ 1 s, observer frame (see e.g. [128]).

There is no evidence for a redshift evolution of Δt_{var} once corrected for the cosmological time dilation effect as apparent from Fig. 6.31. The intrinsic variability time is below 1 s except for GRB 080430, GRB 060904B and GRB 070318: it is interesting to note that these three GRBs have a 15-150 keV prompt emission which consists of a single smooth fast rise exponential decay pulse. The bimodality of the distribution of the rest frame variability times (see Fig. 6.30) can be seen as well from the lower panel of this figure. However, the different distances of the emitting sources together with the expansion of the Universe have complicated effects on the observed time scales: these effects go beyond the simple (1+z) correction. In particular: the detected signal is a strong function of the threshold of the instrument, which means that more distant events will be recorded with lower statistics: this would tend to increase the minimum detectable variability time scale; at the same time, the time delation acts in the opposite direction, allowing the observer to appreciate particulars on smaller rest frame time scales; finally, we record the signal coming from different sources in the same *observer frame* energy band: high-z GRBs will be therefore imaged in intrinsically higher energy band, where the variability is known to shift to lower time scales (see e.g. [50]: $w \propto E^{-0.4}$ where w is the width of the autocorrelation function). The quantification of these effects is non trivial, and is beyond the scope of the present work. This will be the subject of an upcoming work. With these limitations in mind, it is interesting to note that 90% of the analyzed

events has a rest frame maximum variability time which is < 1 s.

The GRB prompt emission is usually classified using the T_{90} parameter: Fig. 6.32 shows the wide dynamical range of the $\Delta t_{var}/T_{90}$ ratio: from 10^{-3} up to 1. The two time scales are not correlated, as shown by Fig. 6.33 and Fig. 6.34: the duration and the variability time are likely to be determined by two independent physical parameters.

6.7.3 The naked-eye burst: 080319B

GRB 080319B triggered *Swift* on March 19, 2008: fortuitous circumstances provided exceptional broad-band coverage of the prompt emission and allowed the access to a regime not yet probed. The burst direction was already in the BAT (15-150 keV) field of view ~ 1000 s before the trigger (which occurred at $T_0 = 06:12:49$ UT) and was independently detected by Konus Wind (KW) in the 20 keV - 15 MeV energy band. Both instruments revealed a complex, energy dependent temporal behavior, with many clearly separated pulses above 70 keV and smoother structures at lower energies (Fig. 6.35). While the exceptional quality of the gamma-ray data assure the possibility to do a systematic study of the temporal (this work; Guidorzi, Margutti et al., in preparation) and spectral properties of the burst, its peculiarity lies in the detected prompt optical emission which reached the 5th magnitude: this burst could have been observed in a dark sky by a naked eye for a few tens of seconds. But the exceptional brightness of the event is only a part of the story: GRB 080319B happened only 10 degrees away from GRB 080319A, also detected by *Swift* less than 30 minutes earlier. The fortuitous location of the second burst of the day (GRB 080319B) allowed several wide field telescopes to detect the optical counterpart of the event instantly: in particular, GRB 080319B was already in the field of view of the TORTORA camera mounted on REM [123] from before the time of the explosion. This, together with the high temporal resolution of TORTORA (down to 0.1 s), allowed the community to capture the prompt emission of GRB 080319B in exquisite detail from the optical to the gamma-ray: an unprecedented data set was collected.

The long lasting afterglow of the event was then followed by a number of ground based facilities from the optical to the radio wave-lenght regime, while *Swift* continued to monitor the burst in the X-ray and UV domain. I refer the reader to [159] for a complete summary of the observational follow-up of GRB 080319B and for a possible interpretation of the observed afterglow emission. Alternative interpretations can be found in [96], [142], [22], [205]. In this subsection I concentrate on the temporal properties of the prompt emission in the gamma-ray energy band. A summary of the proposed theoretical interpretations is given at the end of the subsection, while in the following the results of the application of the TTD technique are shown (see [115]).

The fpd of GRB 080319B as defined by Eq. 6.10 (after accounting for the noise contribution of the BAT detector) has been calculated for the entire 15-150 keV profile (Fig. 6.36) and for each individual channel as well (Fig. 6.38). In both cases a separate analysis for the two parts of the time profile indicated

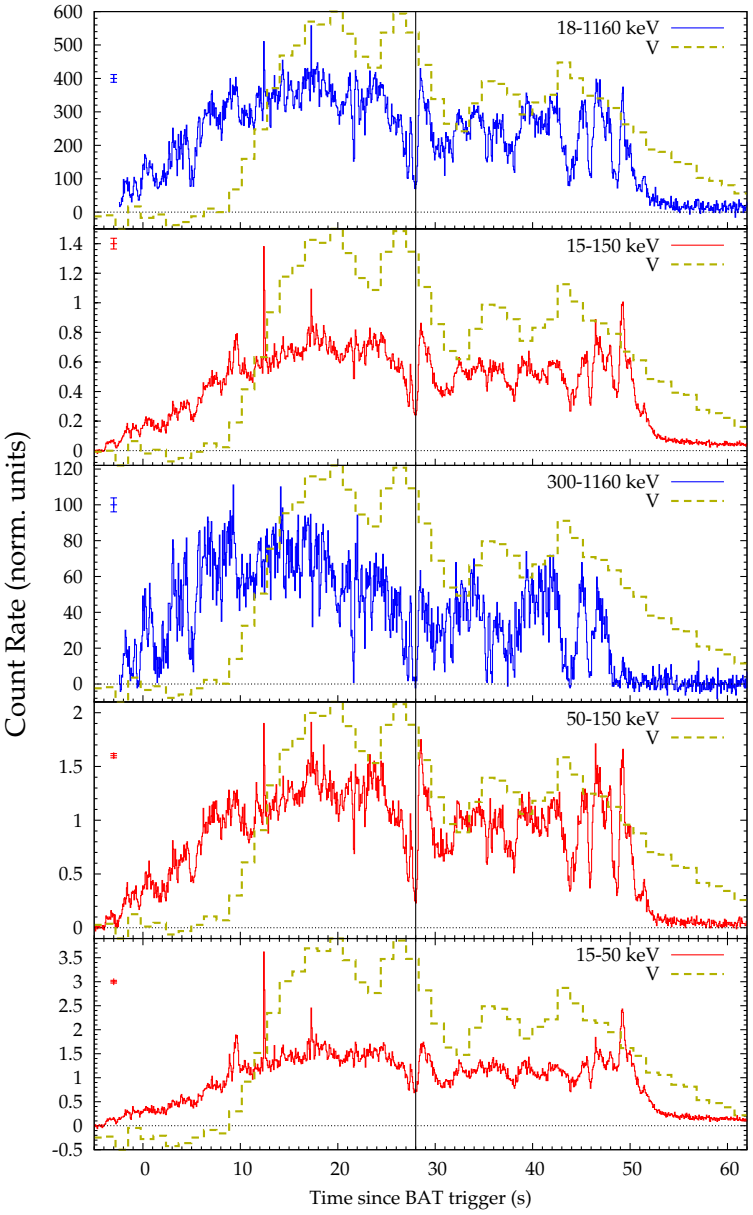

Fig. 6.35: Prompt profile of GRB 080319B in different energy bands. From top to bottom the solid line shows the gamma-ray band burst temporal profile, while the dashed line shows the optical observations by TORTORA. In particular: the red (blue) line refers to BAT (Konus-Wind) observations. The vertical black solid line splits the burst profile at 28 s: the first and the second half of the burst show in fact different characteristic variability time scales. Arbitrary flux units have been used. Observer frame quantities are used. (From Guidorzi, Margutti et al., in preparation).

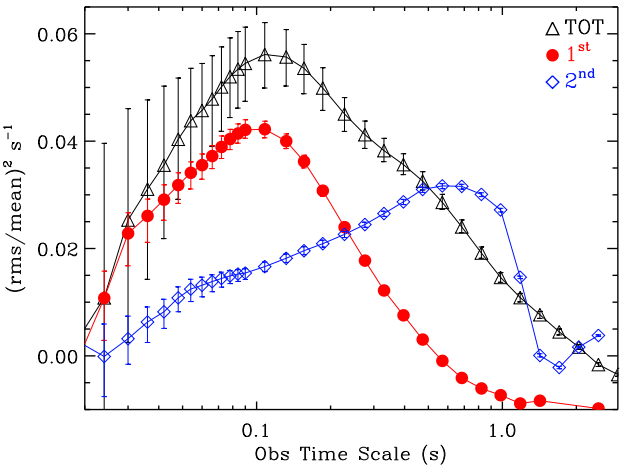

Fig. 6.36: Fractional power density (or power spectrum in the time domain) of the total 15-150 keV BAT light-curve. Black triangles: total light curve; red circles: first light-curve part ($t < 28$) s; blue diamonds: second light-curve part ($t > 28$ s). The two parts are clearly characterized by different variability time scales. From Guidorzi, Margutti et al., in preparation.

in Fig. 6.35 with a solid line has been done. With reference to Fig. 6.36, it is apparent that the bursts is dominated by a variability time $\Delta t_{var} \sim 0.1$ s, but shows different variability features when the first half is compared to the second half of the burst[6]: the characteristic time scale of variability shifts from ~ 0.1 s to ~ 1 s[7]. A continuous evolution towards longer time scales of variability is indeed expected if the variability time is the angular time ($t_{ang} = R/2c\Gamma^2$, see the introduction chapter) and we have either a deceleration or an expansion of the radius of emission (or both of them). To test this possibility I time sliced the temporal profile of the burst using windows of 40 s and shifting each window with respect to the previous one of 3.5 s. The fpd has then been applied to each window, leading to the result displayed in Fig. 6.37: from black to red, the window shifts from the beginning to the end of the observed gamma-ray emission. It is apparent that the power associated to the shorter time scale and typical of the first half of the signal gradually disappears; on the contrary, the power tracking the longer time scale gradually rises. Notably, there is no continuous shift of the power with the time-scale: instead these

[6] I have chosen 28 s observer frame as dividing line between the two behaviors. However, the conclusions are not sensitive to the exact location of the dividing line, provided that it is in the range 20-40 s after trigger.

[7] The presence of the very soft spike around 12 s has been investigated as possible source of the 0.1 s variability time scale: while contributing to the power associated to this time scale, the first half of the burst is still dominated by the 0.1 s time scale even when a period of pure noise fluctuations is substituted to the very short spike.

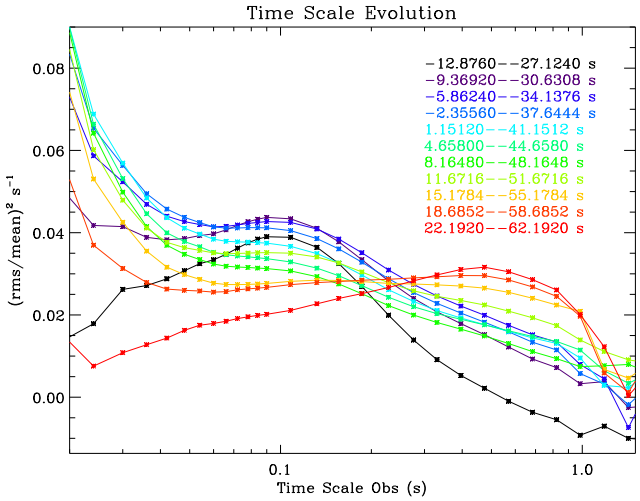

Fig. 6.37: Time resolved analysis of GRB 080319B prompt emission in the 15-150 keV energy range. The fpd is shown as a function of the observed time-scale. Color coding corresponds to a 40 s long window of analysis moving along the GRB profile by steps of 3.5 s. Observer frame time intervals are listed. This plot shows the presence of two variability time scales characterizing different light-curve portions. See the main text for details. From [115].

results indicate the presence of only two variability timescales: ~ 0.1 s and ~ 1 s, in sharp contrast with the naive expectation of a variability time dominated by the angular time. An interesting possibility is that these two time scales are associated to two different physical phenomena and that the gamma-ray emission of GRB 080319B is dominated by the first in the first half and by the second in the second half. I further characterize the variability of GRB 080319B investigating the energy dependence of the two variability time scales (if any). From Fig. 6.38: the lowest energy channel is dominated by the power around ~ 0.1 s while the presence of the longer variability time scale becomes more important for higher energy channels.

Finally, Fig. 6.39 portrayes the results for an energy resolved analysis of the first and second half high energy temporal profile of GRB 080319B. It clearly shows that *there are two variability time scales: the shorter around* 0.1 *s and the longer* ~ 1 *s. Both are strong function of energy and time from trigger.*

I list below the basic information one can extract from this plot:

1. The lowest energy band is dominated by the 0.1 s variability time: when split into two parts, this time scale dominates the first one. In the 25-50 keV channel the evolution is qualitatively the same as that detected in the softest one, the unique difference being less power associated to the 0.1 s time scale;

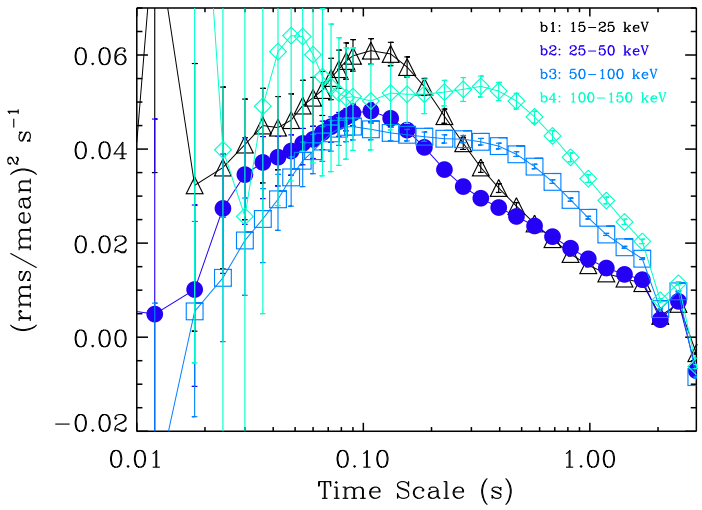

Fig. 6.38: Energy resolved analysis of GRB 080319B prompt emission. The fpd is calculated in different energy bands as a function of the observed time scale. Triangles: 15-25 keV; circles: 25-50 keV; squares: 50-100 keV; diamonds: 100-150 keV. The presence of different variability time scales in different energy channels is apparent. From [115].

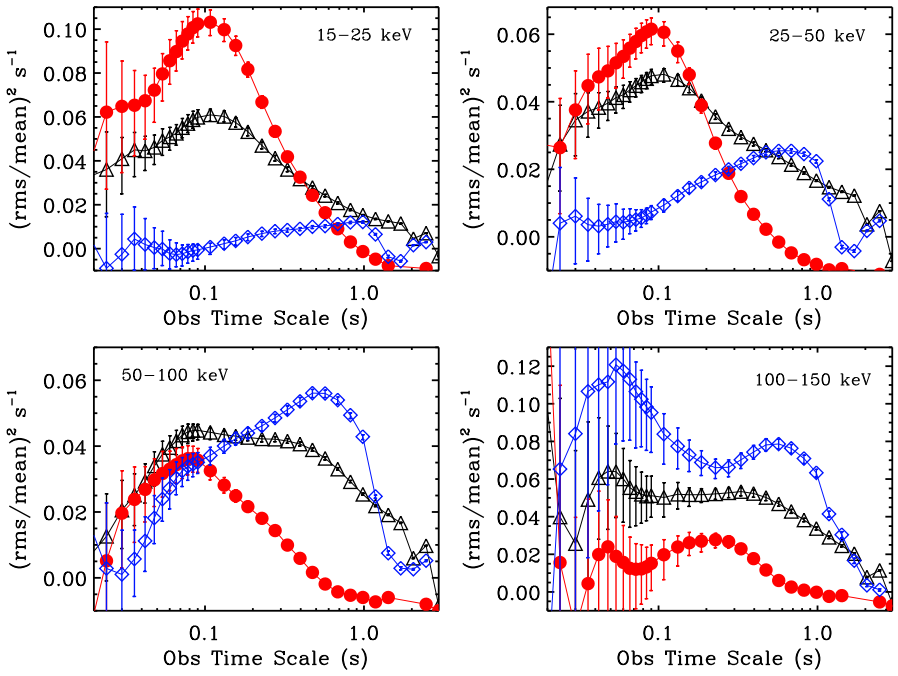

Fig. 6.39: Fractional power density at different energies for BAT data. The black triangles red circles and blue diamonds refer to the total, the first and second parts of the prompt light-curve. The evolution of the variability time scales both with energy and with time can be easily seen. From Guidorzi, Margutti et al., in preparation.

2. The power associated to the longer time scale increases with energy, even if it is present in the second half of the burst from the softest channel.

3. For energies above $\sim 50keV$, the two bottom panels of the figure show the presence of both time scales in the second part. A similar results has been later confirmed by an FFT study as shown below (see Fig. 6.40). Actually, both time scales are present along the entire profile.

4. With reference to the two bottom panels of the figure: while the shorter time scale around 0.1 s does not evolve with time, being around 0.1 s both in the first and in the second half of the burst, the ~ 1 s variability time scale evolve to higher values from the first to the second half.

This strongly suggests that the detected emission is the superposition of two independent contributions with different variability time scales: the 0.1 *s time scale is present in the entire 15-150 keV signal; dominates the first half of the emission and it does not evolve with time; the* ~ 1 *s variability time scale is peculiar of the high energy portion of the spectrum (energies higher than* ~ 50 *keV); dominates the second half of the emission and evolves to higher values with time.* An intriguing possibility is that the 28 s marks the beginning of the afterglow emission: this possibility is tested in Guidorzi, Margutti et al., in preparation.

The different behavior of the prompt emission in the first and the second half of the profile is also suggested by the FFT analysis of the same profile as shown by Fig. 6.40 and is confirmed by the [186] analysis of the spectral lag: the intrinsic gamma-ray spectral lag (time lag measured between gamma-ray energy channels) increases for $t >\sim 28$ s, while the extrinsic lag (time lag between the gamma-ray and optical photons detected by TORTORA) is either zero or negative in this time interval; the intrinsic time-resolved spectral lag is maximum for $t > 28$ s while the extrinsic time-resolved spectral lag is maximum for $t < 28$ s: this leads to effectively separating the burst into two emission episodes partitioned roughly around 28 s, consistent with the scenario of the TTD analysis. Other observational results on the time structure of GRB 080319B are summarized below (this summary has been updated at the end of September 2009):

1. *Time lag:* presence of a positive time lag between optical and gamma-ray photons: the bulk of harder photons precede the softer ones all the way down to the optical. The time lag is of the order of a few seconds ([185], Guidorzi, Margutti et al., in preparation).

2. *Intrinsic and extrinsic time lag:* the data show both an intrinsic (between gamma-ray channels) and extrinsic (gamma versus optical) time lag. A time resolved computation of the time lag divides the first to the second half of the prompt profile as explained above: in particular the extrinsic lag of the second part clusters around zero ([185], Guidorzi, Margutti et al., in preparation).

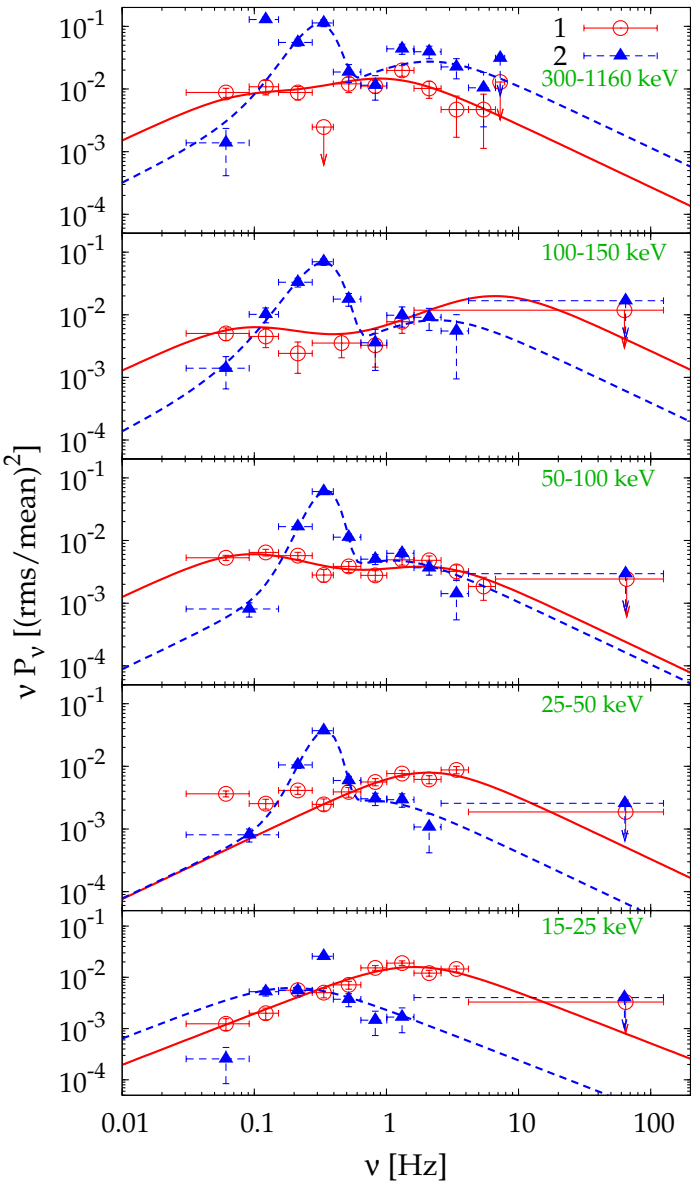

Fig. 6.40: νF_ν Fourier spectra of the first (empty circles) and second (filled triangles) parts of the 15-150 keV BAT profile and of the hardest KW channel. 2σ upper limits are provided. From Guidorzi, Margutti et al., in preparation.

3. *Correlation γ-optical:* the gamma-ray and optical profiles are correlated on a time scale of a few seconds. The correlation is not completely due to the rising and decaying phase of the two profiles ([159]) and it is strengthened if a rigid shift of the gamma ray profile is done forward in time (following the results of the time lag analysis). The γ-optical correlation is almost completely due to the first half of the emission (Guidorzi, Margutti et al., in preparation).

4. *Degree of variability:* the optical light-curve is significantly less variable than the high energy signal (Guidorzi, Margutti et al., in preparation).

5. *Optical-γ:* the temporal properties of the softer gamma-ray are similar to the optical ones only in the second half of the profile. The first half of the profile is dominates by the 0.1 s variability time scale which is lacking in the optical (Guidorzi, Margutti et al., in preparation).

6. *Periodicity:* a marginal evidence for a transient periodic feature was reported by [13] between 36.7 s and 53.3 s with a period of 1.13 s. The significance of this feature is limited: $\sim 1\%$.

A variety of interpretations has been put forward. A brief summary is given below:

- [159] explain the gamma-ray photons as due to IC of the optical ones which were instead produced by synchrotron (the same explanation is favored by [96]): the global scenario is therefore a SSC mechanism produced in the very same region of emission. The delay of the optical photons with respect to the gamma-ray ones would be due to the $\nu_{opt} < \nu_a$ regime [159]: however, the the two frequencies cannot differ too much since we observe a large optical flux (which would have otherwise been absorbed), [96]. The high degree of variability of the gamma-ray signal with respect to the optical one cannot be explained, since the gamma-ray should be a re-processed version of the original optical flux. Moreover, the gamma-ray signal arrives *before* the optical one.

- The SSC scenario has been criticized by [150] and [221]: the synchrotron self absorption and the very large detected optical flux pose strong constraints on the source of the optical emission: a way out is if the origin of the prompt optical emission lies at very large radii, but this is inconsistent with the internal shock scenario. Alternatively, a very large random Lorentz factor of the electrons is required. The authors conclude that the SSC could not have produced the gamma-rays and that even the possibility of gamma-ray and optical photons generated by synchrotron emission by two populations of electrons within the same emitting region is excluded. Instead the suggested scenario requires two different emitting regions for the gamma-ray and the optical photons, with the optical flux generated at larger distance by the external shocks and the high energy component generated by internal shocks: this explains the observed delay between the two emissions and the smaller variability in the optical profile.

- According to [209] the prompt gamma and optical radiation of GRB 080319B was due to synchrotron emission produced in the same region by forward and reverse shocks, respectively, provided that the Lorentz factors of the two shocks are different enough. It is unclear how and if the observed temporal propertied can be naturally explained within this scenario.

- Finally, [48] suggest an alternative scenario where the gamma and optical flux are generated from *different* regions. In particular, the optical flux is the result of the neutron decay of an ultra relativistic shell caught up by a later proton shell: this encounter gives rise to shocks that are less efficient than the previous proton- proton shell interaction (which give origin to the prompt gamma-rays) and produces softer radiation which can be shown to peak in the optical range. This explains the gamma-optical lag: it is unclear how this can also explain the correlation between the two profiles.

None of these models is able to account for all the particulars found by the different temporal analysis techniques.

To conclude, the complex coupling between the optical and the gamma-ray profile produced essentially two configurations: the *different region* and the *same region* scenarios. The former is favored by [13], [221], [48] and [150]: the optical photons are created at a larger distance. This explains the time lag and lower variability of the optical versus gamma-ray profile; the latter is favored by [96], [209] and [185]: this interpretation is lead observationally by the strong coupling of the two signals especially in the second half of the temporal profile. Both emissions are produced at large radii to overcome the self-absorption problem. This scenario has some problems in explaining the observed time-lag and different degree of variability of the two emissions.

6.7.4 Temporal variability of GRB early X-ray afterglows

The main complication in the application of the TTD analysis to XRT data arises from the way the data are collected: XRT observations are organized into segments. Each segment contains more orbits of observation, each one with a maximum duration of $\sim$ 1800 s. This means that at least every 1800 s there is an orbital data gap of the same extension. Moreover, inside each orbit a time bin can have a fractional exposure lower than one. The second source of problems is the presence of pile-up that strongly modifies the statistics of the original photons. I refer the reader to the XRT catalogue chapter for the technical language used in this subsection.

Both problems can be overcome considering XRT-WT mode observations (which are entirely collected during the first orbit of observation) with fractional exposure equal 1 and excluding the region of the CCD affected by pile-up. This operation assures a data set with a minimum temporal resolution of $\sim$ 2 ms.

The TTD has been applied to a sample consisting of the 28 brightest early ($t_{max} < 3000$ s) X-ray afterglows detected by *Swift*-XRT up to March 2008 whose light curves are not affected by data gaps (Table 6.2). For each GRB $0.3 - 10$ keV light curve, I calculated the *pdr* has defined in subsec. 6.5.6,

080319B	070616	061121	060814	060526	060210	060105
080310	070419B	061007	060729	060510B	060202	051117A
080212	070328	060904B	060614	060418	060124	050730
071031	070129	060904A	060607A	060218	060111A	050724

Tab. 6.2: The 28 brightest early ($t_{max} < 3000$ s) X-ray afterglows detected by Swift-XRT up to March 2008 whose light curves are not affected by data gaps.

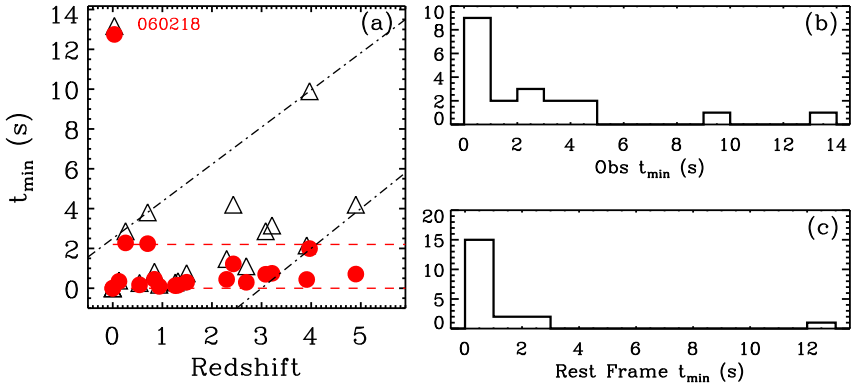

Fig. 6.41: (a) Minimum detectable variability time scale t_{min} as a function of redshift: empty triangles: observed values; filled circles: redshift corrected values. No evolution of the t_{min} parameter is apparent when the cosmological time dilation is properly considered (black dot-dashed lines vs. red dashed lines). Right panel:observed (b) and redshift corrected (c) t_{min} distributions.

equation 6.23. The minimum detectable variability time scale is defined as the shortest time-scale showing a pdr above the 3σ level expected from a pure Poisson noise distribution estimated via Monte Carlo simulations. For each light-curve a set of 1000 simulations is run.

The results are shown in Fig. 6.41: most of early X-ray afterglows has $t_{min} < 1$ s. A definite exception is GRB 060218 with $t_{min} > 10$ s. While no evolution with redshift is detected (Fig. 6.41), t_{min} shows instead a clear trend with energy: the softer the energy band, the longer the variability time scale (see Fig. 6.42). Observational effects would eventually work against this and therefore can only strengthen this conclusion.

6.8 Conclusion

The present chapter has described the use of the TTD on GRB data: this technique has to be thought as a complementary approach with respect to the standard methods of temporal analysis. Given the lack of a proper characterization of the technique in the literature, this work is first aimed at offering an as complete as possible picture of the output of the TTD as a function of the known

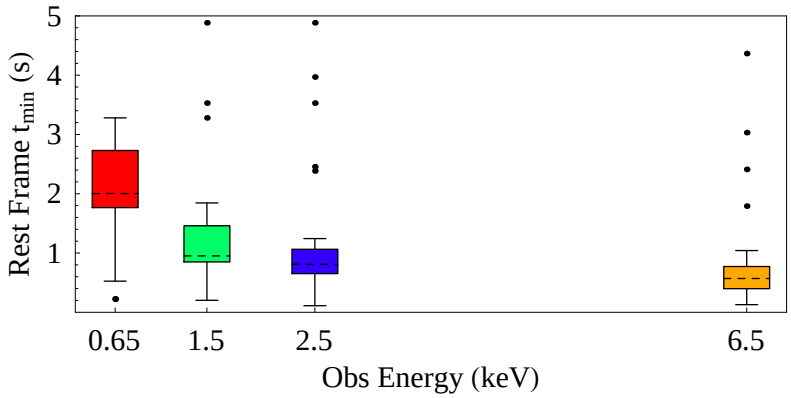

Fig. 6.42: Box-and-whisker plot showing the rest frame minimum time scale of variability as a function of the observed energy band of light curve extraction. Dashed lines: median values. Box edges:quantiles 40% and 60%. The thick black lines mark the data set extension excluding outliers (filled black circles).

properties of the input signal. This is the first step which is required before any kind of scientific discussion of the results can take place and it is performed in Sect. 6.5. For this reason many implications of the found results are still to be discussed on the modeling ground: the presence of different variability classes (sebsec. 6.7.1) has to be understood by cross correlating this new classification with other standard classification schemes of GRB sources and comparing the variability measure other burst parameters (e.g. spectral peak energy, isotropic energy, luminosity etc.), with particular reference to those describing the multi-wavelength afterglow. This will be the subject of a forthcoming work.

GRB 080319B with its high-level statistics offers the possibility to exploit the full capability of the TTD analysis as shown in subsec. 6.7.3. This analysis reveals the presence of two different variability time scales probably connected to different emission components overlapping in time[8]. The two time scales dominates in different energy bands and their evolution or non-evolution with time can be appreciated. In general, the TTD analysis has been shown to be able to: quantify the variability time scales; quantify their evolution during the prompt emission; do an energy-resolved study of the variability properties of the prompt emission. A similar analysis can be applied to all the GRBs with comparable statistics: I estimate a few percent of the total number of GRBs to be suitable to this study (see e.g. GRB 070616 or GRB 091024). Even if limited in number, these case-studies could reveal precious information about the prompt emission mechanism as for GRB 080319B.

A much larger sample is instead suitable to quantify the time scale of max-

[8] It is interesting to note that the same conclusion is reached starting from the spectral analysis of Fermi-LAT detected sources: see e.g. [1].

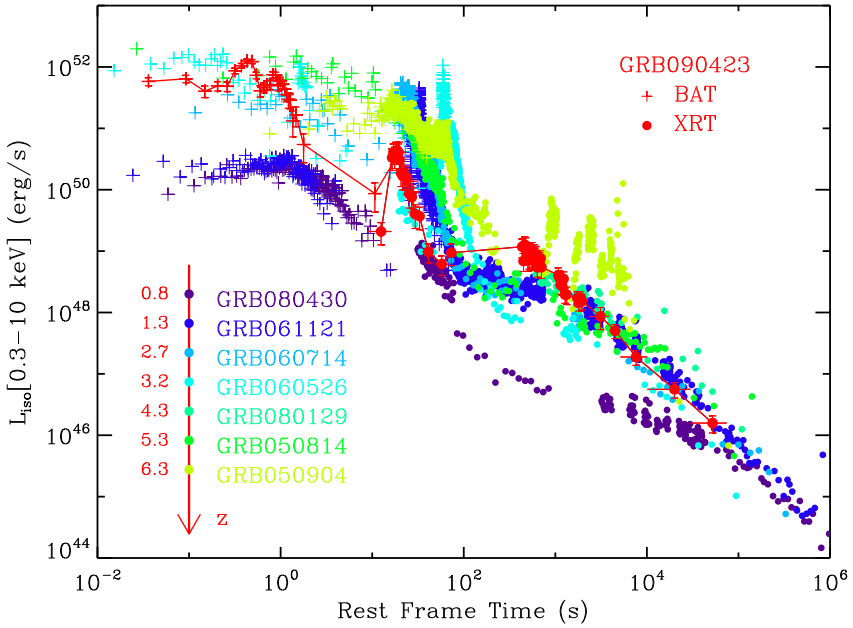

Fig. 6.43: BAT and XRT light curve of GRB 090423 (red data) in the source rest-frame. The light curve of GRB 090423 is compared with seven GRBs in the redshift interval $0.8 - 6.3$. The bursts are selected among those showing a canonical three-phase behaviour (steep decayplateaunormal decay) in the X-ray light curve and without spectral break between BAT and XRT, allowing the spectral calibration of the BAT signal into the 0.3-10 keV energy band. The light curve of GRB 090423 does not show any distinguishing features as compared to lower redshift bursts, implying that the physical mechanism that causes the GRB and its interaction with the circum-burst medium are similar at $z = 8.1$ and at lower redshifts: GRB 090423 is the furthest GRB observed to date and the most distant object of the Universe observed ever as of November 2009. From [174].

imum variability of the detected signal Δt_{var} (subsec. 6.7.2): Δt_{var} shows a hint for a bimodal distribution with half of the sample lying in the 0.6-1 s rest frame bin. This timescale is therefore identified as the typical variability time scale of GRB sources in the hard X-ray range in the host galaxy rest frame. The possible alternative of a burst profile which is the result of noise processes on a continuum of timescales is not favored by the analysis. The absence of a redshift evolution of the rest frame variability time scale strongly calls for a mechanism of GRB production which is independent of the cosmological evolution of the Universe at the first level of approximation: a similar conclusion is independently reached from the comparison of the X-ray luminosity light-curves of high-z and low-z GRBs during the afterglow phase, as shown in Fig. 6.43: their similarity suggests a common burst environment if we believe the standard external shock scenario. The variability time scale does not correlate with the T_{90} parameter: the duration and the variability are likely to be determined by two independent physical parameters during the emission.

BIBLIOGRAPHY

[1] Abdo, A. A., Ackermann, M., Asano, K., et al., 2009, ApJ submitted, Astro-ph/0910.4192

[2] Amati, L., 2006, MNRAS, 372, 233

[3] Amati, L. and Guidorzi, C. and Frontera, F. et al., 2008, MNRAS, 391, 577

[4] Antonelli, L. A., Piro, L., Vietri, M. et al., 2000, ApJ, 545, L39

[5] Arnett, D. W., "Supernova & Nucleosynthesis, 1996, Edit. J.P. Ostriker, Princeton University Press, Princeton, New Jersey"

[6] Arnett, D. W., 1988, ApJ, 331, 377

[7] Band, D., Matteson, J., Ford, L. et al., 1993, ApJ, 413, 281

[8] Barthelmy, S. D., Barbier, L. M., Cummings, J. R. et al., 2005, SSRv, 120, 143

[9] Barthelmy, W. H., Baumgartner, L. M., Cummings, J. R. et al., 2008, GCN8428

[10] Beloborodov, A. M, Stern, B. E & Svensson, R., 1998, ApJ, 508, L25

[11] Beloborodov, A. M, Stern, B. E & Svensson, R., 1998, ApJ, 535, 158

[12] Berger, E., Foley, R., Simcoe, R. et al., 2008, GCN8434

[13] Beskin, G., Karpov, S., Bondar, S., et al., 2009, Science submitted (astro-ph/0905.4431)

[14] Beuermann, K., Hessman, F. V., Reinsch, K., et al. 1999, A&A, 352, L26

[15] Blandford, R. D. & McKee, C. F., 1976, PhFl, 19, 1130

[16] Blondin, J. M. & Ellison, D. C., 2001, ApJ, 557, 782

[17] Bloom, J. S., Prochaska, J. X., Lee, W., et al., 2009, Astro-ph/0905.1965

[18] Borgonovo, L., Frontera, F., Guidorzi, C., et al., 2007, A&A, 465, 765

[19] Borozdin, K. N. & Trudolyubov, S. P., 2003, ApJ, 583, L57

[20] Böttcher, M., Astro-ph/0312538.

[21] Bloom, J. S., Starr, D. L., Blake, C. H. et al., 2006, ASP Conf. Ser. 351, 751

[22] Bloom, J. S., Perley, D. A., Li, W., et al., 2009, ApJ, 691, 723

[23] Burrows, D. N., & Racusin, J., 2006, Nuovo Cim., 121B:1273-1287, Astro-ph/0702633

[24] Burrows, D. N., Hill, J. E., Nousek, J. A. et al., 2005, SSRv, 120, 165

[25] Butler, N. R., Marshall, H. L., Ricker, G. R., et al., 2003, ApJ, 597, 1010.

[26] Campana, S., Lazzati, D., Ripamonti, E., et al., 2007, ApJ, 654, L17

[27] Cannizzo, J., Barthelmy, S. D., Beardmore, A. P.., et al., 2008, GCN Report 119.2

[28] Chang, H. & Yi, I., ApJ, 542, L17

[29] Chevalier, R. A. & Li, Z.-Y., ApJ, 2000, 536, 195

[30] Chincarini, G., Moretti, A., Romano, P. et al., 2007, ApJ, 671, 1903

[31] Costa, E., Frontera, F., Heise, J. et al., 1997, Nature, 387, 783

[32] Churazov, E., Gilfanov, M., Forman, W. et al., 1996, ApJ, 471, 673

[33] Clemens,C., Loew, S., & Greiner, J., 2008, GCN8424

[34] Clemens,C., Kruehler, T., & Greiner, J., 2008b, GCN8442

[35] Covino, S., Malesani, D., Tagliaferri, G., et al, 2006, Nuovo Cim.,121B:1171-1176, Astro-ph/0612643

[36] Dickey J. M. & Lockman F. J., 1990, ARA&A, 28, 215-261

[37] Dai, Z. G. & Lu, T. 2002, ApJ, 565, L87

[38] Barniol Duran, R. and Kumar, P., 2009, MNRAS, 395, 955

[39] Dutra, C. M., Ahumada, A. V., Clariá, J. J. et al., 2003, A&A, 408, 287

[40] Dwarkadas, V. V., 2005, ApJ, 630, 892 Astro-ph/0403195

[41] Eichler, D. & Granot, J., 2006, ApJ, 641, L5

[42] Evans, P. A., Beardmore, A. P., Page, K. L., et al., 2007, A&A, 469, 379

[43] Evans, P. A., Goad, M. R., Osborne, J. P. et al., 2008, GCN8427

[44] Evans, P. A., Beardmore, A. P., Page, K. L. et al., 2009, MNRAS, 397, 1177

[45] Evans, P. A. Goad, M. R. Osborne, J. P. et al. 2009b, GCN Circ. 8796

[46] Falcone, A. D. Morris, D. Racusin, J. et al. 2007, ApJ, 671, 1921

[47] Fan, Y. and Piran, T., 2006, MNRAS, 369, 197

[48] Fan, Y. Z., Zhang, B & Wei, D. M., 2009, Ph. Rev., 79, 1301

[49] Fenimore, E. E., int't Zand, J. J. M., Norris, J. P. et al., 1995, ApJ, 448, L101

[50] Fenimore, E. E., Madras, C. D., Nayakshin, S., 1996, ApJ, 473, 998

[51] Frail, D. A., Kulkarni, S. R., Sari, R. et al. 2001, ApJ, 537, 191

[52] Fugazza, D., D'Avanzo, P., Malesani, D., et al., 2006, GCN circ 5513

[53] Gehrels, N.,Chincarini, G., Giommi, P. et al., 2004, ApJ, 611, 1005

[54] Gehrels, N., Ramirez-Ruiz, E., Fox, D. B., 2009, ARA&A, 47, 567

[55] Genet, F., Daigne, F., & Mochkovitch, R., 2007, MNRAS, 381, 732

[56] Genet, F. and Granot, J., 2009, MNRAS submitted, arXiv0901.0680

[57] Ghirlanda, G., Nava, L., Ghisellini, G. et al., A&A, 496, 585

[58] Ghisellini, G., Lazzati, D., Rossi, E. & Rees, M. J., 2002, A& A, L33

[59] Goad, M. R., Tyler, L. G., Beardmore, A. P., 2007, A&A, 476, 1401

[60] Goad, M. R., Page, K. L., Godet, O. et al., 2007, A&A, 468, 103

[61] Godet, O., Page, K. L., Osborne, J. et al., 2007, A&A, 471, 385

[62] Godet, O., Beardmore, A. P., Abbey, A. F., et al., A&A, 494, 775

[63] Greiner, J., Bornemann, W., Clemens, C. et al., 2008, PASP, 120, 405

[64] Granot, J. & Sari, R., 2001, AAS, 1991, 6121

[65] Granot, J. & Königl, A., 2001, ApJ, 560, 145

[66] Granot, J. et al., 2001, in "GRBs in the Afterglow Era", ed. E. Costa, F. Frontera & J. Hjorth (Berlin: Springer), 312

[67] Granot, J. &Sari, R., 2002, ApJ, 568, 820

[68] Granot, J., Panaitescu, A., Kumar, P. et al., 2002, 570, L61

[69] Granot, J., Nakar, E. & Piran, T., 2003, Nature, 426, 138

[70] Granot, J. 2005, ApJ, 631, 1022

[71] Granot, J. & Kumar, P., 2006, MNRAS, 366, L13

[72] Granot, J., Königl, A. & Piran, T., 2006, MNRAS, 370, 1946

[73] Granot, J., 2008, Astro-ph/0811.1657, "070228: The Next Decade of Gamma-Ray Burst Afterglows" conference proceedings

[74] Grupe, D. Nousek, J. A. vanden Berk, D. E. et al. 2007, AJ, 133, 2216

[75] Guidorzi, C. and Frontera, F. and Montanari, E. et al., 2005, MNRAS, 363, 315

[76] Guidorzi, C., Baumgartner, W. H., Beardmore, A. P. et al., 2008, GCN8421

[77] Guidorzi, C., Margutti, R. & Mao, J., 2008b, GCN8429

[78] Guidorzi, C., Barthelmy, S. D., Schady, P. et al., GCN Report 176

[79] Guidorzi, C. Clemens, C. Kobayashi, S. et al. 2009, A&A, 499, 439

[80] Hill et al., 2004, Proceeding of SPIE, Vol. 5165, pp. 217-231.

[81] Hoversten, E. A. & Sakamoto, T. 2009, GCN Circ. 8799

[82] Huang, Y. F., Gou, L. J., Dai, Z. G. & Lu, T., 2000, ApJ, 543, 90

[83] Ioka, K. Kobayashi, S. & Zhang, B. 2005, ApJ, 631, 429

[84] Ioka, K., Toma K., Yamazaki, R. et al., 2006, A&A, 458, 7I

[85] Kalberla, P. M. W., Burton, W. B., Hartmann, D. et al., 2005, A&A, 440, 775

[86] Kaneko, Y., Preece, R. D., Briggs, M. S. et al., 2006, ApJS, 166, 298

[87] Klebesadel, R. W., Strong, I. B., Olson, R. A., 1973, ApJ, 182, 85L

[88] Klotz, A., Boër, M., Eysseric, J. et al., 2008, PASP, 120, 1298

[89] Kobayashi, S., Piran, T.,& Sari, R., 1997, ApJ, 490, 92

[90] Kobayashi, S., & Sari, R., 2001, ApJ, 551, 934

[91] Kouveliotou, C., Meegan, C. A., Fishman, G. J., 1993, ApJ, 413, 101L

[92] Kulkarni, S. R. & Kasliwal, M. M., 2009, Astro-ph/0903.0218

[93] Kumar, P. & Panaitescu, A., 2000, ApJ, 541L, 51

[94] Kumar, P. & Piran, T. 2000, ApJ, 535, 152

[95] Kumar, P., Narayan, R. & Johnson, J. L., 2008, MNRAS, 388, 1729

[96] Kumar, P., & Panaitescu, A., 2008b, MNRAS, 391, L19

[97] Lamb, D. Q., Donaghy, T. Q. & Graziani, C., 2005, ApJ, 620, 355L

[98] Lazzati, D., 2002, Astro-ph/0211174

[99] Lazzati, D., Ramirez-Ruiz, E., Rees, M. J., 2002, ApJ, 572, L57

[100] Rybicki, G. B., Lightman, A. P., 1979, Radiative Processes in Astrophysics, John Wiley & Sons

[101] Lazzati, D. Rossi, E. Covino, S. et al. 2002, A&A, 396, L5

[102] Li, T.-P., 2001, ChJAA, 1, 313

[103] Li, T. P. and Muraki, Y. et al., 2001, ApJ, 578, 374L

[104] Liang, E. W., Zhang, B., O'Brien, P. T. et al., 2006, ApJ, 646, 351

[105] Liang, E.-W. and Zhang, B.-B. and Zhang, B., 2007, ApJ, 670, 565

[106] Lithwick, Y. & Sari, R, 2001, ApJ, 555L, 54

[107] Lloyd-Ronning, N. M. and Zhang, B., 2004, ApJ, 613, 477

[108] Lyutikov, M., 2009, Astro-ph/0911.0349, to appear in: "The shocking universe" conference proceedings

[109] Mclaughlin, G. C., Wijers, R. A. M., Brown, G. E. & Bethe, H. A., 2002, ApJ, 567,454

[110] Madau, P., 1995, ApJ, 441, 18

[111] Mangano, V., Holland, S. T., Malesani, D. et al., 2007, A&A, 470, 105

[112] Mangano, V., La Parola, V., Cusumano et al., 2007b, ApJ, 654, 403

[113] Marrkwardt, C. B., Barbier, L., Barthelmy, S. D., et al. 2006, GCN 5520

[114] Markwardt, C. B., Evans, P. A., Goad, M. et al., 2007, GCN Report 42.3

[115] Margutti, R., Guidorzi, C., Chincarini et al., 2008, AIPC, 1065, 259

[116] Mazzali, P., Deng, J., Tominaga, N., et al., 2003, ApJ, 599, L95

[117] Mazzali, P., Deng, J., Pian, E., et al., 2006, ApJ, 645, 1323

[118] Mazzali, P., Deng, J., Nomoto, K., et al., 2006, Nature, 442, 1018

[119] Medvedev, M. V., 2006, ApJ, 651, 9L

[120] Meszaàros, P. Rees, M. J. & Wijers, R. A. M. J. ApJ, 1998, 499, 301

[121] Meszaàros, P., 2006, Rep. Prog. Phys., 69, 2259

[122] Miller, A. A., Cobb, B. E., Bloom, J. S. et al., 2008, GCN8499

[123] Molinari, E., et al., 2006, Nuovo Cimento B, 121, 1525

[124] Molinari, E. Vergani, S. D. Malesani, D. et al. 2007, A&A, 469, 13

[125] Moretti et al., 2005, Proceeding of SPIE, Vol. 5898, pp. 360-368.

[126] Moretti, A., Margutti, R., Pasotti, F., 2008, A&A, 478, 409

[127] Morrison, R., & McCammon, D., 1983, ApJ 270, 119

[128] Nakar, E., & Piran, T., 2002, MNRAS, 331, 40

[129] Nakar, E. & Granot, J., MNRAS, 380, 1744

[130] Nomoto, K., Maeda, K., Mazzali, P.A., et al. Astro-ph/0308136

[131] ,Norris, J. P., Scargle, J. D., Kouveliotou, C., et al., 1994, 424, 540

[132] Norris, J. P. Nemiroff, R. J. Bonnell, J. T. et al. 1996, ApJ, 459, 393

[133] Norris, J. P., Bonnell, J. T., Kazanas, D. et al., 2005, ApJ, 627, 324

[134] Nousek, J. A., Kouveliotou, C., Grupe, D. et al., 2006, ApJ, 642, 389

[135] O'Brien, P. T., Willingale, R., Osborne, J. et al., 2006, ApJ, 647, 1213

[136] Olofsson, G., Fynbo, J. P. U., & Jakobsson, P., 2008, GCN8425

[137] Paczyński, B. 1998, ApJ, 494, L45

[138] Pagani, C., Morris, D. C., Kobayashi, S., et al., 2006, ApJ, 645, 1315

[139] Page, K. L., Willingale, R., O'Brien, P. T., et al., 2009, MNRAS, 395, 328

[140] Panaitescu, A. & Kumar, P., 2000, ApJ, 543, 66

[141] Panaitescu, A., Mészáros, P., Burrows, D., 2006, MNRAS, 369, 2059

[142] , S. B., Castro-Tirado, A. J., Jelínek, M. et al., 2009, A&A, 504, 45

[143] Patat, F., 2001, ApJ, 555

[144] van Paradijs, J., Groot, P. J.,Galama, T., et al., 1997, Nature, 386, 686

[145] Pei, Y. C., ApJ, 395, 130

[146] Peng, Z. Y., Ma, L., Zhao, X. H. et al., ApJ, 2009, 698, 417

[147] Perna, R., Lazzati, D. & Fiore, F., 2003, ApJ, 585, 775

[148] Piran, T., 1999, Phys. Rev., 314, 575

[149] Piran, T., 2004, Rev. Mod. Phys., 76, 1143

[150] Piran, T., Sari, R. & Zou, Y., 2009, MNRAS, 393, 1107

[151] Piro, L., Costa, E., Feroci, M., et al., 1999, A&AS., 138, 431

[152] Piro, L., Garmire, G., Garcia, M., et al., 2000, Science, 290, 955

[153] Pozdnyakov, L. A., Sobol, I. M. & Sunyaev, R. A. 1983

[154] Pozdnyakov, L. A., Sobol, I. M., Sunyaev, R. A., 1979, A&A, 75, 214

[155] Poole, T. S., Breeveld, A. A., Page, M. J. et al., 2008, MNRAS, 383, 627

[156] Protassov, R., van Dyk, D. A., Connors, A. et al., 2002, ApJ, 571, 545

[157] Qin, Y.-P., 2009, ApJ, 691, 811

[158] Quilligan, F., McBreen, B., Hanlon, L., et al., 2002, A&A, 385, 377

[159] Racusin, J. l., Karpov, S. V., Sokolowski, M. et al., 2008, Nature, 455, 183

[160] Ramirez-Ruiz, E., Merloni, A. & Rees, M. J., 2001, MNRAS, 324, 1147

[161] Reeves, J. N., Watson, D., Osborne, J. P., et al., 2002, Nature, 416, 512

[162] Reeves, J. N., Watson, D., Osborne, J. P., et al., 2003, A&A, 403, 463

[163] Rees, M. J. & Meszaros, P. 1998, ApJ, 496, L1

[164] Reichart, D. E. and Lamb, D. Q. and Fenimore, E. E. et al., 2001, ApJ, 552, 57

[165] Rizzuto, D., Guidorzi, C., Romano, P. et al., 2007, MNRAS, 379, 619

[166] Romano, P., Campana, S., Chincarini, G. et al., 2006, A&A, 456, 917

[167] Roming, P. W. A., Kennedy, T. E., Mason, K. O. et al., SSRv, 120, 95

[168] Rumyantsev, V., Biryukov, V. & Pozanenko, A., 2008, GCN8455

[169] Rutledge, R. E. & Sako, M., 2003, MNRAS, 339, 600

[170] Sakamoto, T. Lamb, D. Q. Kawai, N. et al. 2005, ApJ, 629, 311

[171] Sakamoto, T. Hullinger, D. Sato, G. et al. 2008, ApJ, 679, 570

[172] Sakamoto, T. Sato, G. Barbier, L. et al. 2009, ApJ, 693, 922

[173] Sako, M., Harrison, F. A., Rutledge, R. E., 2005, ApJ, 623, 973S.

[174] Salvaterra, R., Della Valle, M., Campana, S., et al., 2009, Nature in press

[175] Sari, R. and Piran, T. and Narayan, R., 1998, ApJ, 497L, 17S

[176] Sari, R., Piran, T. &Halpern, J. P., 1999, ApJ, 519, L17

[177] Sari, R. & Piran, T., 1999b, ApJ, 520, 641

[178] Sari, R. & Esin, A. A., 2001, ApJ, 548, 787

[179] Shen, R. F. & Song, L. M., 2003, PASJ, 55, 345

[180] Shen, R. F., Willingale, R., Kumar, P. et al., 2009, MNRAS, 393, 598.

[181] Schlegel, D. J., Finkbeiner, D. P. & Davis, M., 1998, ApJ, 500, 525

[182] Shady, P. & Guidorzi, C., 2008, GCN8431

[183] Shao, L. &Dai, Z. G., ApJ, 2007, 660, 1319

[184] Soderberg, A., Grindlay, J. E., Bloom, J. S., et al., 2009, Astro-ph/0902.3674

[185] Stamatikos, M. Barthelmy, S. D. Baumgartner, W. H. et al. 2009, GCN Circ. 8800

[186] Stamatikos09b, M., Ukwatta,T. N., Sakamoto, T., et al., 2009, AIPC, 1133, 356

[187] Starling, R. L. C., O'Brien, P. T., Willingale, R. et al., 2008, MNRAS, 384, 504

[188] Syunyaev, R.A. & Titarchuk, L.G. 1980, A&A , 86, 121

[189] Tagliaferri, G., Goad, M., Chincarini, G. et al., 2005, Nature, 436, 985

[190] Tavecchio, F., Ghisellini, G., & Lazzati, D., 2004, A&A, 415, 443

[191] Teeseling, van A., Fischer, A. & Beuermann, ASP Conference Series, Vol. 157,1999, 309-316

[192] Vaughan, S., Goad, M. R., Beardmore, A. P., et al., 2006, ApJ, 638, 920

[193] Vedrenne, G., Atteia, J. L., 2009, Gamma Ray Bursts: the brightest explosions in the universe, Springer, Chichester, UK

[194] Verner, D. A., & Yakovlev, D. G., 1995, A&A Suppl. Ser., 109, 125

[195] Verner, D. A., & Ferland, G. J., 1996, ApJ, 103, 467

[196] Vetere, L., Massaro, E., Costa, E., et al., 2006, A&A, 447, 499

[197] Vietri, M., Ghisellini, G., Lazzati, D., Fiore, F. & Stella, L., 2001, ApJ, 550, L43

[198] Walker, K. C., & Schaffer, B. E., ApJ, 2000, 537, 264

[199] Wang, X. & Loeb, A. 2000, ApJ, 535, 788

[200] Watson, D., Reeves, J. N., Hjorth, J., et al., 2003, ApJ, 595, L29

[201] Willingale, R. and O'Brien, P. T. and Osborne, J. P. et al., 2007, ApJ, 662, 1093

[202] Willis, A. J., 1991, IAUC, 143, 265

[203] Woosley, S. E. 1993, ApJ, 405, 273

[204] Woosley, S. E. & Weaver, T. A., 1995, ApJS, 101, 181

[205] Wozniak, P. R., Vestrand, W. T., Panaitescu, A. D., et al., 2009, ApJ, 691, 495

[206] Yonetoku, D., Tanabe, S., Murakami, T. et al., 2008, PASJ, 60, 351

[207] Yoshida, A., Namiki, M., Otani, C., et al., 1999, A&AS, 138, 433

[208] Yoshida, A., Namiki, M., Yonetoku, D., et al., 2001, ApJ, 557, L27

[209] ,Yu,Y. W.,Wang, X. Y. & Dai, Z. G., 2009, ApJ, 692, 1662

[210] Zhang, B. , 2002 , ApJ, 571, 876

[211] Zhang, B., et al. 2004, ApJ, 601, L119

[212] Zhang, B. & Meszaros, P., 2004, Int. J. Mod. Phys. A, 19, 2385

[213] Zhang, B., Fan, Y.Z., Dyks, J., et al., 2006, ApJ, 642, 354

[214] Zhang, B.-B. and Liang, E.-W. and Zhang, B., ApJ, 666, 1002

[215] Zhang, B., Zhang, B .B., Liang, E. W, et al., 2007, 655, L25

[216] Zhang, B. and Liang, E. and Page, K. L. et al., 2007, ApJ, 655, 989

[217] Zhang, B. 2007, ChJAA, 7, 1

[218] Zhang, B.-B., Zhang, B., Liang & Wang, X. Y., 2009, ApJ, 690, L10

[219] Zhang, & MacFadyen, A., 2009, ApJ, 698, 1261

[220] Zhao, X. & Bai, J. M., 2006, ApJ, 635, L1

[221] Zou, Y. C., Piran, T. & Sari, R., 2009, ApJ, 692, 92L